UNIVERSITY OF CALIFORNIA SAN DIEGO

Engineered nanosensors for detecting protease activity in traumatic brain injury

A Dissertation submitted in partial satisfaction of the requirements
for the degree Doctor of Philosophy

in

Bioengineering

by

Julia A. Kudryashev

Committee in charge:

Professor Ester J. Kwon, Chair
Professor Karen L. Christman
Professor Vivian Hook
Professor Sameer B. Shah
Professor Yingxiao Wang

2022

The Dissertation of Julia A. Kudryashev is approved, and it is acceptable in quality and form for publication on microfilm and electronically.

University of California San Diego

2022

DEDICATION

This dissertation is dedicated to my advisor, who took a chance on mentoring me as her first graduate student, extended incredible amounts of patience and understanding as I progressed through my PhD, and whose mentoring style I hope to emulate in my future career.

To my parents, who supported me through the highs and lows of this journey with delicious food, sage advice, and financial support. I hope I continue to make you proud.

To my labmates, who aided me in the long days of animal work, talked through experiments with me, and motivated me to keep going even when the going was tough.

To my friends, who helped me to maintain a healthier work-life balance and provided some much-needed emotional support.

To my cats, who helped me weather the initial lock-downs of the pandemic and provided a source of comfort and company while analyzing experiments and writing this dissertation.

TABLE OF CONTENTS

LIST OF FIGURES

LIST OF TABLES

LIST OF ABBREVIATIONS

ABN	Activity-based nanosensor
AUC	Area under the curve
BBB	Blood-brain barrier
CCI	Controlled cortical impact
CNS	Central nervous system
DLS	Dynamic light scattering
ELISA	Enzyme-linked immunoassay
ECM	Extra-cellular matrix
FRET	Förster resonance energy transfer
HA	Hyaluronic acid
HApep	Hyaluronic acid-targeting peptide
LFA	Lateral flow assay
LOD	Limit of detection
LSFM	Light sheet fluorescence microscopy
ROC	Receiver operating characteristic
TBI	Traumatic brain injury
TBI-ABN	Activity-based nanosensor for traumatic brain injury

ACKNOWLEDGEMENTS

Chapter 1, in full, has been submitted for publication of the material as it may appear in Engineering Biomaterials for Neural Applications, and is reproduced with permission from Springer Nature. Kudryashev, Julia. A.; Madias, Marianne I.; Kwon, Ester J. Bioresponsive nanomaterials for CNS disease. Springer Nature, 2022. The dissertation author was one of the primary researchers and authors of this paper.

Chapter 2, in full, is reprinted with permission from Kudryashev, Julia A.; Waggoner, Lauren E.; Leng, Hope T.; Mininni, Nicholas H.; Kwon, Ester J. An Activity-Based Nanosensor for Traumatic Brain Injury. ACS Sensors. 2020, 5 (3), 686–692. Copyright 2020 American Chemical Society. The dissertation author was the primary researcher and author of this paper.

Chapter 3, in full, is reprinted with permission from Kandell, Rebecca M.; Kudryashev, Julia A.; Kwon, Ester J. Targeting the Extracellular Matrix in Traumatic Brain Injury Increases Signal Generation from an Activity-Based Nanosensor. ACS Nano 2021, 15 (12), 20504–20516. Copyright 2021 American Chemical Society. The dissertation author was one of the primary researchers and authors of this paper.

Chapter 4, in full, is currently being prepared for submission for publication of the material. Kudryashev, Julia A.; Madias, Marianne I.; Kandell, Rebecca M.; Lin, Queenie X.; Kwon, Ester J. The dissertation author was the primary researcher and author of this material.

VITA

2017 Bachelor of Science in Bioengineering, Massachusetts Institute of Technology

2022 Doctor of Philosophy in Bioengineering, University of California San Diego

PUBLICATIONS

Kudryashev, J. A.*, Madias, M. I.*, & Kwon, E. J. (2022) Bioresponsive nanomaterials for CNS disease. *Engineering biomaterials for neural applications*. Springer Nature. Work to be published.

Kandell, R. M.*, **Kudryashev, J. A.***, & Kwon, E. J. (2021). Targeting the extracellular matrix in traumatic brain injury increases signal generation from an activity-based nanosensor. *ACS nano*, *15*(12), 20504-20516. https://doi.org/10.1021/acsnano.1c09064

Kudryashev, J. A., Waggoner, L. E., Leng, H. T., Mininni, N. H., & Kwon, E. J. (2020). An Activity-Based Nanosensor for Traumatic Brain Injury. *ACS sensors*, *5*(3), 686-692. https://doi.org/10.1021/acssensors.9b01812

Ishida, K., Xu, H., Sasakawa, N., Lung, M. S. Y., **Kudryashev, J. A.**, Gee, P., & Hotta, A. (2018). Site-specific randomization of the endogenous genome by a regulatable CRISPR-Cas9 *piggyBac* system in human cells. *Scientific Reports*, *8*, 310. http://doi.org/10.1038/s41598-017-18568-4

ABSTRACT OF THE DISSERTATION

Engineered nanosensors for detecting protease activity in traumatic brain injury

by

Julia A. Kudryashev

Doctor of Philosophy in Bionengineering

University of California San Diego, 2022

Professor Ester J. Kwon, Chair

Traumatic brain injury (TBI) affects over 2.8 million people annually in the United States and leads to the hospitalization of ~300,000 patients per year. Current methods of diagnosis for TBI are either subjective and poor at discriminating mild TBI (Glasgow Coma Scale) or take extensive time and resources to run (computed tomography and magnetic resonance imaging). These diagnostic modalities also do not capture information on the biological processes driving the pathology of secondary injury, where there is a window of opportunity to prevent further damage with treatment. As a supplement to these diagnostics, the blood or cerebrospinal fluid can be sampled for biomarkers in the form of breakdown

products which are released during degenerative processes after TBI. Many of these biomarkers are produced by ectopic proteases including the calcium-dependent protease calpain-1, which is implicated in cellular death and worsened prognosis after TBI. Thus, the measurement of calpain-1 activity may help to diagnose injury progression and inform patient prognosis after TBI.

To diagnose secondary injury in TBI, we developed an activity-based nanosensor for TBI (TBI-ABN) which can detect activity from the protease calpain-1. The nanosensor is comprised of a FRET peptide conjugated to a 40 kDa 8-arm PEG scaffold, and can produce a fluorescent signal once it is specifically cleaved by active calpain-1. In a mouse model of TBI, systemically administered TBI-ABNs were found to accumulate and activate in the injured brain tissue as assessed by fluorescence in brain tissue slices. Next, we investigated whether adding active targeting to components of the brain extracellular matrix, such as hyaluronic acid, could improve the sensitivity of TBI-ABNs. We conjugated hyaluronic acid-targeting peptides to TBI-ABNs and found that the activation of sensor in injured brain tissue was increased by approximately 2.8- and 6.6-fold when targeting peptides were added at moderate and high valencies, respectively, compared to non-targeted nanosensor within brain tissue homogenates. Finally, we redesigned the TBI-ABN to release a synthetic biomarker into the blood or urine after systemic administration for a minimally-invasive measurement of protease activity after TBI. The synthetic biomarker could be quantified both via fluorescence and immunoassays to detect calpain-1 activity in TBI. These nanosensors are the first demonstrations of protease activity measurement in the context of TBI and have potential both as tools to study protease activation in the injured brain and as diagnostics to identify the biological processes taking place after injury.

INTRODUCTION

Traumatic brain injury

Traumatic brain injury (TBI), caused by a mechanical insult to the brain, affects over 2.8 million people annually in the United States and leads to the hospitalization of ~300,000 patients per year.[1] Rapid triage of patients requiring surgery is essential, as mortality decreases by 50% if patients receive surgery within 4 hours of arrival at a hospital.[2] Patients with TBI experience symptoms that affect both physical and cognitive function, including dysfunction of motor control, loss of memory, or emotional dysregulation. In patients who experience multiple head injuries without adequate time to recover in between, these symptoms can progress into neurodegeneration or chronic traumatic encephalitis.[3] The rapid and sensitive detection of TBI in patients is critical for decreasing mortality in severe injury and for detecting the progression of neurodegeneration with repeated injury.

Current clinical diagnostic modalities

Current methods to diagnose and prognosticate TBI rely either on presentation of symptoms or on imaging for structural deformations. The Glasgow Coma Scale (GCS) is one of the most commonly used methods of diagnosis; it grades a patient's severity of TBI based on their visual, verbal and motor responses.[4] It is a useful scale for initial patient stratification; however, the GCS score is assigned based on potentially subjective observations of the patient, scores may be affected by outside factors such as pre-existing conditions or by sedation of the patient, and it is less specific for patients with milder forms of TBI where differences in injury can be more difficult to discriminate.[5] Computed tomography (CT) head scans are commonly used to diagnose anatomical pathologies such as contusions and swelling in the acute stage of

injury, but are limited in their ability to detect more diffuse or microscopic injuries.[6] Magnetic resonance imaging (MRI) is commonly used in the chronic stages of injury to identify diffuse damage and progression of injury.[7] Both imaging modalities require dedicated facilities, expensive equipment, and trained personnel- and are thus time- and resource-intensive to run. There is an opportunity to supplement these diagnostic modalities with rapid and sensitive diagnostics that provide information on the biological activity driving TBI pathology, and allow for an objective, quantitative triage of patients.

Pathology and treatment of TBI

After the primary impact, the brain undergoes a series of biological cascades known as secondary injury. In this secondary stage, injured tissue experiences sustained protease activity, inflammation, excitotoxicity, and neuronal death.[4] These processes begin minutes after injury and may persist for months, progressing to chronic pathologies including reactive glial scarring, white matter degeneration, and diffuse microbleeding.[8] Standard treatments for TBI- such as reducing intracranial pressure, inducing hypothermia, or removing blood clots- are palliative in nature and do not address the underlying processes driving secondary damage.[9] A number of more targeted small molecule therapies against secondary injury have been developed, but results have been inconsistent in the transition from animal models to clinical studies.[10] A notable recent example is the application of progesterone in acute TBI as a part of two large-scale phase 3 trials: SYNAPSE and PROTECT III. Despite promising results in earlier trials, no notable improvement in outcome was seen in TBI patients when they were treated with progesterone within 4-8 hours of injury.[11,12] One factor in the difficulty of translating treatments is the lack of a clear quantitative outcome of treatment. Many trials, including SYNAPSE and

PROTECT III, tend to measure patient outcome based on score changes in the GCS, which has a low discriminative ability for small changes in TBI and cannot discriminate pathoanatomical features of TBI.[5] A potential strategy to improve the development of TBI therapies is through the direct, quantitative sampling of pathological activity in patients before and after treatment.

Protease activity in TBI

Soon after the initial injury, imbalances in cellular metabolism, neurotransmitter release, and ionic homeostasis lead to the production of reactive oxygen species, spreading neuroinflammation, and cell death.[13] These pathologies in turn contribute to the sustained activation of endogenous proteases which further drive secondary injury. Numerous proteases have been implicated in the progression of secondary injury, including calpain-1, calpain-2, MMP9, MMP2, cathepsin B, and caspase 3.[14–17] These proteases generate breakdown products which leak into the blood and cerebrospinal fluid after TBI, and which have been the focus of recent studies into diagnostic and prognostic biomarker panels for TBI.[18] Calpain-1, for example, is a calcium-dependent cysteine protease ubiquitously expressed throughout the body including the central nervous system. During TBI, it is responsible for generating breakdown products from cytoskeletal proteins including: αII-spectrin, tau, and neurofilaments.[19] The serum levels of these breakdown products have the potential to prognosticate a delayed recovery after a mild TBI,[20] and to diagnose patients who received a TBI.[21,22] Matrix metalloproteinase 9 (MMP9) is a zinc-dependent protease which activates and cleaves extracellular matrix components in pathological conditions including TBI. Its pathological activity has been associated with blood-brain barrier (BBB) breakdown, exacerbation of cerebral edema, and progression of neuronal death in the acute stages of TBI. MMP9 levels have been shown to increase within 6 hours of a

TBI,[23] and elevated MMP9 plasma levels have been associated with increased mortality in the first few days after severe TBI.[24] Valuable information on the progression of TBI in patients could be gained through the direct sampling of pathological activity from proteases such as calpain-1 and MMP9.

Activity-Based Nanosensors

Protease-responsive nanosensors, more recently known as activity-based nanosensors (ABNs), are gaining significance for their ability to be engineered in response to specific biological stimuli, allowing for the capture of pathological processes that cannot be detected by conventional molecular quantification methods.[25] ABNs can be tuned and applied to measure activity upstream of breakdown product accumulation, allowing the user to bypass the rate-limited production and transport of native products and detect pathologies at earlier time points.[26,27] There are notable examples of activity-based sensors in cancer: fluorescently activated polymers can identify tumor margins during surgical resection[28,29] and urinary sensors can detect and stratify tumors.[30–32] Based on these advances in cancer, measuring protease activity with an activity-based nanosensor to diagnose TBI is a promising strategy.

The nanoscale property of ABNs is critical to their application in acute TBI; in the uninjured brain, the presence of tight junctions and enhanced efflux of materials has made drug delivery across the blood-brain barrier (BBB) a formidable challenge. However, the BBB is locally dysregulated immediately after a TBI; this pathological hallmark allows for the delivery of nanoscale materials into the injured tissue.[33,34] Previous studies have shown that intravenously-injected nanoscale materials up to 500 nm in diameter may passively accumulate in the injured tissue in the first 24 hours after a TBI.[35,36] Similar observations have been seen in

the extravasation of native blood proteins in multiple injury models and in postmortem patient samples.[34,37–39] This property is reminiscent of the enhanced permeation and retention (EPR) effect seen for nanoparticles against some tumors.[40] Thus, the ability of nanoscale materials to passively accumulate into injured brain tissue makes them uniquely suited for delivering sensors and therapeutics against TBI.

References

(1) CDC. Surveillance Report of Traumatic Brain Injury-Related Emergency Department Visits, Hospitalizations, and Deaths—United States, 2014; 2019.

(2) Kim, Y. J. The Impact of Time from ED Arrival to Surgery on Mortality and Hospital Length of Stay in Patients With Traumatic Brain Injury. J. Emerg. Nurs. **2011**, 37 (4), 328–333. https://doi.org/10.1016/j.jen.2010.04.017.

(3) Singla, A.; Leineweber, B.; Monteith, S.; Oskouian, R. J.; Tubbs, R. S. The Anatomy of Concussion and Chronic Traumatic Encephalopathy: A Comprehensive Review. Clin. Anat. **2019**, 32 (3), 310–318. https://doi.org/10.1002/ca.23313.

(4) Maas, A. I. R.; Stocchetti, N.; Bullock, R. Moderate and Severe Traumatic Brain Injury in Adults. Lancet Neurol. **2008**, 7 (8), 728–741. https://doi.org/10.1016/S1474-4422(08)70164-9.

(5) Saatman, K. E.; Duhaime, A.-C.; Bullock, R.; Maas, A. I. R.; Valadka, A.; Manley, G. T. Classification of Traumatic Brain Injury for Targeted Therapies. J. Neurotrauma **2008**, 25 (7), 719–738. https://doi.org/10.1089/neu.2008.0586.

(6) Hofman, P. A. M.; Stapert, S. Z.; Kroonenburgh, M. J. P. G. van; Jolles, J.; Kruijk, J. de; Wilmink, J. T. MR Imaging, Single-Photon Emission CT, and Neurocognitive Performance after Mild Traumatic Brain Injury. Am. J. Neuroradiol. **2001**, 22 (3), 441–449.

(7) Edlow, B. L.; Rosenthal, E. S. Diagnostic, Prognostic, and Advanced Imaging in Severe Traumatic Brain Injury. Curr. Trauma Rep. **2015**, 1 (3), 133–146. https://doi.org/10.1007/s40719-015-0018-7.

(8) Bramlett, H. M.; Dietrich, W. D. Long-Term Consequences of Traumatic Brain Injury: Current Status of Potential Mechanisms of Injury and Neurological Outcomes. J. Neurotrauma **2014**, 32 (23), 1834–1848. https://doi.org/10.1089/neu.2014.3352.

(9) Fong, R.; Konakondla, S.; Schirmer, C. M.; Lacroix, M. Surgical Interventions for Severe Traumatic Brain Injury. J. Emerg. Crit. Care Med. **2017**, 1 (10). https://doi.org/10.21037/jeccm.2017.09.03.

(10) Pearn, M. L.; Niesman, I. R.; Egawa, J.; Sawada, A.; Almenar-Queralt, A.; Shah, S. B.; Duckworth, J. L.; Head, B. P. Pathophysiology Associated with Traumatic Brain Injury: Current Treatments and Potential Novel Therapeutics. Cell. Mol. Neurobiol. **2017**, 37 (4), 571–585. https://doi.org/10.1007/s10571-016-0400-1.

(11) Skolnick, B. E.; Maas, A. I.; Narayan, R. K.; van der Hoop, R. G.; MacAllister, T.; Ward, J. D.; Nelson, N. R.; Stocchetti, N. A Clinical Trial of Progesterone for Severe Traumatic Brain Injury. http://dx.doi.org/10.1056/NEJMoa1411090. https://www.nejm.org/doi/10.1056/NEJMoa1411090?url_ver=Z39.88-2003&rfr_id=ori%3Arid%3Acrossref.org&rfr_dat=cr_pub++0www.ncbi.nlm.nih.gov (accessed 2020-05-25). https://doi.org/10.1056/NEJMoa1411090.

(12) Wright, D. W.; Yeatts, S. D.; Silbergleit, R.; Palesch, Y. Y.; Hertzberg, V. S.; Frankel, M.; Goldstein, F. C.; Caveney, A. F.; Howlett-Smith, H.; Bengelink, E. M.; Manley, G. T.; Merck, L. H.; Janis, L. S.; Barsan, W. G. Very Early Administration of Progesterone for Acute Traumatic Brain Injury. N. Engl. J. Med. **2014**, 371 (26), 2457–2466. https://doi.org/10.1056/NEJMoa1404304.

(13) Walker, K. R.; Tesco, G. Molecular Mechanisms of Cognitive Dysfunction Following Traumatic Brain Injury. Front. Aging Neurosci. **2013**, 5. https://doi.org/10.3389/fnagi.2013.00029.

(14) Zhang, Z.; Larner, S. F.; Liu, M. C.; Zheng, W.; Hayes, R. L.; Wang, K. K. W. Multiple AlphaII-Spectrin Breakdown Products Distinguish Calpain and Caspase Dominated Necrotic and Apoptotic Cell Death Pathways. Apoptosis **2009**, 14 (11), 1289–1298. https://doi.org/10.1007/s10495-009-0405-z.

(15) Boutté, A. M.; Hook, V.; Thangavelu, B.; Sarkis, G. A.; Abbatiello, B. N.; Hook, G.; Jacobsen, J. S.; Robertson, C. S.; Gilsdorf, J.; Yang, Z.; Wang, K. K. W.; Shear, D. A. Penetrating Traumatic Brain Injury Triggers Dysregulation of Cathepsin B Protein Levels Independent of Cysteine Protease Activity in Brain and Cerebral Spinal Fluid. J. Neurotrauma **2020**, 37 (13), 1574–1586. https://doi.org/10.1089/neu.2019.6537.

(16) Abdul-Muneer, P. M.; Pfister, B. J.; Haorah, J.; Chandra, N. Role of Matrix Metalloproteinases in the Pathogenesis of Traumatic Brain Injury. Mol. Neurobiol. **2016**, 53 (9), 6106–6123. https://doi.org/10.1007/s12035-015-9520-8.

(17) Baudry, M.; Bi, X. Calpain-1 and Calpain-2: The Yin and Yang of Synaptic Plasticity and Neurodegeneration. Trends Neurosci. **2016**, 39 (4), 235–245. https://doi.org/10.1016/j.tins.2016.01.007.

(18) Wang, K. K.; Yang, Z.; Zhu, T.; Shi, Y.; Rubenstein, R.; Tyndall, J. A.; Manley, G. T. An Update on Diagnostic and Prognostic Biomarkers for Traumatic Brain Injury. Expert Rev. Mol. Diagn. **2018**, 18 (2), 165–180. https://doi.org/10.1080/14737159.2018.1428089.

(19) Saatman, K. E.; Creed, J.; Raghupathi, R. Calpain as a Therapeutic Target in Traumatic Brain Injury. Neurotherapeutics **2010**, 7 (1), 31–42. https://doi.org/10.1016/j.nurt.2009.11.002.

(20) Gan, Z. S.; Stein, S. C.; Swanson, R.; Guan, S.; Garcia, L.; Mehta, D.; Smith, D. H. Blood Biomarkers for Traumatic Brain Injury: A Quantitative Assessment of Diagnostic and Prognostic Accuracy. Front. Neurol. **2019**, 10 (APR), 446–446. https://doi.org/10.3389/fneur.2019.00446.

(21) Siman, R.; Giovannone, N.; Hanten, G.; Wilde, E. A.; McCauley, S. R.; Hunter, J. V.; Li, X.; Levin, H. S.; Smith, D. H. Evidence That the Blood Biomarker SNTF Predicts Brain Imaging Changes and Persistent Cognitive Dysfunction in Mild TBI Patients. Front. Neurol. **2013**, 4, 190–190. https://doi.org/10.3389/fneur.2013.00190.

(22) Siman, R.; Shahim, P.; Tegner, Y.; Blennow, K.; Zetterberg, H.; Smith, D. H. Serum SNTF Increases in Concussed Professional Ice Hockey Players and Relates to the Severity of Postconcussion Symptoms. J. Neurotrauma **2015**, 32 (17), 1294–1300. https://doi.org/10.1089/neu.2014.3698.

(23) Jia, F.; Pan, Y.; Mao, Q.; Liang, Y.; Jiang, J. Matrix Metalloproteinase-9 Expression and Protein Levels after Fluid Percussion Injury in Rats: The Effect of Injury Severity and Brain Temperature. J. Neurotrauma **2010**, 27 (6), 1059–1068. https://doi.org/10.1089/neu.2009.1067.

(24) Simon, D.; Evaldt, J.; Nabinger, D. D.; Fontana, M. F.; Klein, M. G.; Gomes, J. do A.; Regner, A. Plasma Matrix Metalloproteinase-9 Levels Predict Intensive Care Unit Mortality Early after Severe Traumatic Brain Injury. Brain Inj. **2017**, 31 (3), 390–395. https://doi.org/10.1080/02699052.2016.1259501.

(25) Thorek, D. L. J.; Watson, P. A.; Lee, S. G.; Ku, A. T.; Bournazos, S.; Braun, K.; Kim, K.; Sjostrom, K.; Doran, M. G.; Lamminmaki, U.; Santos, E.; Veach, D.; Turkekul, M.; Casey, E.; Lewis, J. S.; Abou, D. S.; van Voss, M. R. H.; Scardino, P. T.; Strand, S.-E.; Alpaugh, M. L.; Scher, H. I.; Lilja, H.; Larson, S. M.; Ulmert, D. Internalization of Secreted Antigen-Targeted Antibodies by the Neonatal Fc Receptor for Precision Imaging of the Androgen Receptor Axis. Sci. Transl. Med. **2016**, 8 (367), 367ra167-367ra167. https://doi.org/10.1126/scitranslmed.aaf2335.

(26) Hori, S. S.; Gambhir, S. S. Mathematical Model Identifies Blood Biomarker-Based Early Cancer Detection Strategies and Limitations. Sci. Transl. Med. **2011**, 3 (109), 109ra116-109ra116. https://doi.org/10.1126/scitranslmed.3003110.

(27) Kwong, G. A.; Dudani, J. S.; Carrodeguas, E.; Mazumdar, E. V.; Zekavat, S. M.; Bhatia, S. N. Mathematical Framework for Activity-Based Cancer Biomarkers. Proc. Natl. Acad. Sci. U. S. A. **2015**, 112 (41), 12627–12632. https://doi.org/10.1073/pnas.1506925112.

(28) Urano, Y.; Sakabe, M.; Kosaka, N.; Ogawa, M.; Mitsunaga, M.; Asanuma, D.; Kamiya, M.; Young, M. R.; Nagano, T.; Choyke, P. L.; Kobayashi, H. Rapid Cancer Detection by Topically Spraying a -Glutamyltranspeptidase-Activated Fluorescent Probe. Sci. Transl. Med. **2011**, 3 (110), 110ra119-110ra119. https://doi.org/10.1126/scitranslmed.3002823.

(29) Whitley, M. J.; Cardona, D. M.; Lazarides, A. L.; Spasojevic, I.; Ferrer, J. M.; Cahill, J.; Lee, C.-L.; Snuderl, M.; Blazer III, D. G.; Hwang, E. S.; Greenup, R. A.; Mosca, P. J.; Mito, J. K.; Cuneo, K. C.; Larrier, N. A.; O'Reilly, E. K.; Riedel, R. F.; Eward, W. C.; Strasfeld, D. B.; Fukumura, D.; Jain, R. K.; Lee, W. D.; Griffith, L. G.; Bawendi, M. G.; Kirsch, D. G.; Brigman, B. E. A Mouse-Human Phase 1 Co-Clinical Trial of a Protease-Activated Fluorescent Probe for Imaging Cancer. Sci. Transl. Med. **2016**, 8 (320), 320ra4-320ra4. https://doi.org/10.1126/scitranslmed.aad0293.

(30) Kwong, G. A.; von Maltzahn, G.; Murugappan, G.; Abudayyeh, O.; Mo, S.; Papayannopoulos, I. A.; Sverdlov, D. Y.; Liu, S. B.; Warren, A. D.; Popov, Y.; Schuppan, D.; Bhatia, S. N. Mass-Encoded Synthetic Biomarkers for Multiplexed Urinary Monitoring of Disease. Nat. Biotechnol. **2013**, 31 (1), 63–70. https://doi.org/10.1038/nbt.2464.

(31) Kwon, E. J.; Dudani, J. S.; Bhatia, S. N. Ultrasensitive Tumour-Penetrating Nanosensors of Protease Activity. Nat. Biomed. Eng. **2017**, 1 (4), 0054–0054. https://doi.org/10.1038/s41551-017-0054.

(32) Dudani, J. S.; Ibrahim, M.; Kirkpatrick, J.; Warren, A. D.; Bhatia, S. N. Classification of Prostate Cancer Using a Protease Activity Nanosensor Library. Proc. Natl. Acad. Sci. U. S. A. **2018**, 115 (36), 8954–8959. https://doi.org/10.1073/pnas.1805337115.

(33) Price, L.; Wilson, C.; Grant, G. Blood–Brain Barrier Pathophysiology Following Traumatic Brain Injury. In Translational Research in Traumatic Brain Injury; Laskowitz, D., Grant, G., Eds.; CRC Press/Taylor and Francis Group: Boca Raton, FL, 2016; pp 85–96. https://doi.org/10.1201/b18959-5.

(34) Hicks, R. R.; Baldwin, S. A.; Scheff, S. W. Serum Extravasation and Cytoskeletal Alterations Following Traumatic Brain Injury in Rats. Mol. Chem. Neuropathol. **1997**, 32 (1–3), 1–16. https://doi.org/10.1007/BF02815164.

(35) Bharadwaj, V. N.; Lifshitz, J.; Adelson, P. D.; Kodibagkar, V. D.; Stabenfeldt, S. E. Temporal Assessment of Nanoparticle Accumulation after Experimental Brain Injury: Effect of Particle Size. Sci. Rep. **2016**, 6 (1), 29988–29988. https://doi.org/10.1038/srep29988.

(36) Kwon, E. J.; Skalak, M.; Lo Bu, R.; Bhatia, S. N. Neuron-Targeted Nanoparticle for SiRNA Delivery to Traumatic Brain Injuries. ACS Nano **2016**, 10 (8), 7926–7933. https://doi.org/10.1021/acsnano.6b03858.

(37) Habgood, M. D.; Bye, N.; Dziegielewska, K. M.; Ek, C. J.; Lane, M. A.; Potter, A.; Morganti-Kossmann, C.; Saunders, N. R. Changes in Blood-Brain Barrier Permeability to Large and Small Molecules Following Traumatic Brain Injury in Mice. Eur. J. Neurosci. **2007**, 25 (1), 231–238. https://doi.org/10.1111/j.1460-9568.2006.05275.x.

(38) Hay, J. R.; Johnson, V. E.; Young, A. M. H.; Smith, D. H.; Stewart, W. Blood-Brain Barrier Disruption Is an Early Event That May Persist for Many Years After Traumatic Brain Injury in Humans. J. Neuropathol. Exp. Neurol. **2015**, 74 (12), 1147–1157. https://doi.org/10.1097/nen.0000000000000261.

(39) Liu, H. M.; Sturner, W. Q. Extravasation of Plasma Proteins in Brain Trauma. Forensic Sci. Int. **1988**, 38 (3–4), 285–295. https://doi.org/10.1016/0379-0738(88)90174-0.

(40) Boyd, B. J.; Galle, A.; Daglas, M.; Rosenfeld, J. V.; Medcalf, R. Traumatic Brain Injury Opens Blood–Brain Barrier to Stealth Liposomes via an Enhanced Permeability and Retention (EPR)-like Effect. J. Drug Target. **2015**, 23 (9), 847–853. https://doi.org/10.3109/1061186X.2015.1034280.

CHAPTER 1. BIORESPONSIVE NANOMATERIALS FOR CNS DISEASE

1.1. Abstract

Diseases of the central nervous system (CNS) affect millions of people worldwide and disease burden is increasing with an aging population. Yet, there are few medicines available to diagnose and treat neurological disorders and progress on developing new medicines has been limited. One major challenge is the narrow therapeutic window of payloads that act in the CNS – significant transport barriers restrict bioavailability yet the CNS is sensitive to toxicity. Bioresponsive nanomaterials can be engineered to activate based on context and encode sophisticated functions. Contexts that activate bioresponsive nanomaterials can be specific to the temporal and spatial dynamics of healthy and pathological biological processes, and thus offer approaches to increase efficacy of payloads while mitigating off-target effects. In this chapter, environment cues specific to CNS diseases or within subcellular compartments will be discussed and examples of bioresponsive nanomaterials that have been engineered to respond to these cues will be presented.

1.2. Introduction

A major challenge in the development of CNS medicines is the narrow therapeutic window. Systemically administered therapeutics have limited bioavailability to the CNS due to transport barriers such as the blood-brain barrier (BBB), requiring large doses that can lead to off-target toxicity. One approach to navigate this narrow therapeutic window is through local, controlled release of drugs. An example of this approach that has achieved clinical translation for the treatment of malignant gliomas is the Gliadel® Wafer, a 1 mm thick, 1.45 cm diameter disc

comprised of chemotherapeutic formulated with a mixture of synthetic polymers. Gliadel® Wafers are designed to be implanted in the surgical cavity created by tumor resection and slowly degrade for the controlled release of chemotherapeutic over 3 weeks. While the local implantation of a controlled release formulation is an approach that can be effective when there is surgical access to the brain (e.g., resection of brain cancers, removal of blood clots/control of bleeding, or relieving pressure after brain injury caused by traumatic injury or stroke), there are many neurological disorders where surgical intervention is not the standard of care. In addition, surgical access to the brain is typically acute and may not be appropriate for medicines that require chronic delivery. As an alternative strategy to local implantation to achieve desirable pharmacokinetics, materials have been engineered to switch between inactive and active states based on cues to control on- vs. off-target activity. This class of materials, referred to as "stimuli-responsive" or "smart" materials, has been engineered to respond to a wide range of stimuli and in ideal cases responses can be controlled spatially and temporally within a living organism. Activating stimuli can be broadly separated into human-controlled, externally generated stimuli (e.g., heat, magnetic fields, or ultrasound) and biologically-generated, endogenous stimuli (e.g., acidity, redox potential, or enzyme activity).[1–3] While aspects of spatial and/or temporal control of externally generated stimuli can be user-controlled, application requires a priori knowledge of the disease location and timescales. In contrast, endogenous stimuli arise from specific pathologies and/or natural biological compartments, and therefore materials that respond to these stimuli can behave autonomously to their environment once delivered into the body. Due to the biological nature of these endogenous stimuli, materials that are responsive in these contexts are referred to as "bioresponsive" materials.

Some of the earliest applications of bioresponsive materials have been for drug delivery.[4] One of the first examples of a pH-responsive delivery system was a pH-degradable polymer of vinyl acetate-maleic anhydride, which released drug with the ionization of carboxyl sidechains in physiological solutions.[5] Another notable example of a pH-responsive polymer is Carbopol® (polyacrylic acid), which undergoes a sol-gel transition and becomes mucoadhesive when placed in solutions above pH 5.5.[6] Carbopol is a component of multiple FDA-approved drug delivery systems in applications in the eye, nose, stomach and vagina.[4,6,7] Since initial designs, many advances have been made in developing bioresponsive materials that are tailored to disease-associated microenvironments such as wound beds, tumors, and atherosclerosis.[2,3,8] For example, injectable MMP-responsive hydrogels have been developed which can release MMP-specific inhibitors in response to elevated MMP activity within infarcted myocardial tissue.[9] In a porcine model of myocardial infarction, these hydrogels were found to attenuate post-infarction tissue remodeling with limited off-targeted effects after direct injection into the infarcted tissue. One prominent class of bioresponsive materials that have been FDA-approved or currently in clinical trials are antibody-drug conjugates that are protease-responsive for the treatment of cancer. Adcetris®, which was first approved for clinical use to treat lymphoma in 2011, is an anti-CD30 antibody which releases drug intracellularly via cathepsin-B-cleavable linkages between the antibody and the cargo.[10] The protease-responsive linker was found to reduce off-target toxicity of antibody-drug conjugates in tumor xenograft mice compared to treatment with conjugates containing pH-sensitive hydrazone bonds.[10] In the Probody™ antibody system by CytomX, of which multiple conjugates are currently undergoing clinical trials, the antibody's binding site is masked with a blocking domain through a protease-cleavable linker.[11] The inclusion of this protease-sensitive masking domain drastically reduced off-target toxicity of monoclonal

antibody therapies such as EGFR-targeted cetuximab; in healthy non-human primates, the safety factor of cetuximab was increased by 3- to 15-fold when it was modified with a masking domain connected via a uPA- and matriptase-cleavable linker.[12] These examples show how bioresponsive materials have been leveraged to improve the therapeutic efficacy of drugs by tuning elements to respond to disease-associated protease activity.

Materials with dimensions on the nanometer length scale have unique and emergent physical and biological properties that have been exploited to create tools, diagnostics, and therapeutics in numerous disease contexts, including cancer, infections, and CNS diseases.[13,14] The material composition of these "nanomaterials" can be varied, and includes metals, ceramics, synthetic polymers, biomolecules, and composites thereof. Since the FDA approval of Doxil in 1995, an increasing number of nanomaterial drug delivery systems have been translated into the clinic over the past decades.[15,16] One reason for why nanomaterials are attractive platforms for drug delivery is that they can widen the therapeutic window. For example, Doxil is a lipid/polymer formulation of the chemotherapeutic doxorubicin which was designed to mitigate off-target effects through altering drug biodistribution based on physicochemical properties. Encapsulation of doxorubicin in the interior of the ~100 nm liposome resulted in decreased cardiotoxicity and nephrotoxicity compared to free drug.[17,18] Nanomaterials can also increase the efficacy of therapeutics. Nucleic acid drugs are charged, labile macromolecules that require intracellular localization to be active, usually to the cytosol or nucleus. Due to the physicochemical properties of nucleic acids, transport to intracellular compartments is negligible without a delivery carrier. The first synthetic nanomaterial for nucleic acid delivery approved by the FDA was patisiran, approved in 2018 for the intravenous delivery of siRNA to treat hereditary transthyretin-mediated amyloidosis, a rare life-threatening disease caused by

mutations in transthyretin.[19] In 2020, similar lipid nanoparticle designs were granted emergency approval by the FDA as mRNA-based vaccines for COVID-19.[20] A crucial component to these lipid nanoparticle technologies is an ionizable lipid that can become protonated in the endosomal-lysosomal pathway to mediate cargo release into the cytoplasm.[21]

This chapter will focus on the discussion of bioresponsive nanomaterials engineered for CNS diseases. Nanomaterials are useful platforms to create bioresponsive systems because they are often supramolecular assemblies, which allows for the design of sophisticated, multi-component systems. Bioresponsive nanomaterials ~10-200 nm in size can be assembled from ~1-5 nm stimuli-responsive elements that collectively lead to a state change across the greater nanomaterial structure. At the molecular level, the stimuli-responsive elements that make up the fundamental building blocks in the greater nanomaterial structure can be categorized to have two types of responses: cleavage of covalent bonds or changes in physicochemical properties (Figure 1.1). Depending on the organization of these fundamental building blocks in the greater nanomaterial structure, a large diversity of responses can be engineered. Systems can directly respond to stimuli (Figure 1.2) or translate stimuli to nanomaterial state changes that trigger programmable functions (Figure 1.3).

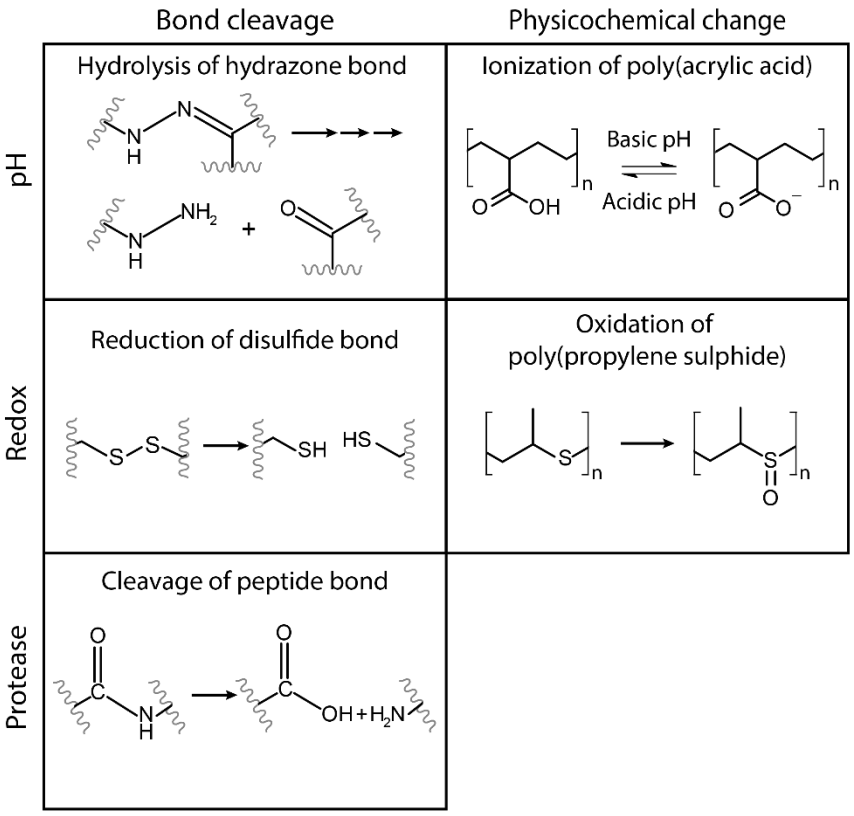

Figure 1.1: Fundamental stimuli-responsive elements in bioresponsive nanomaterials.

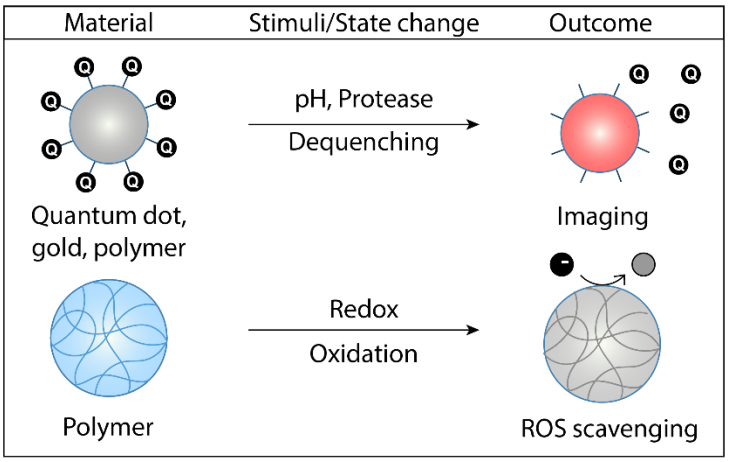

Figure 1.2: Bioresponsive nanomaterials that directly respond to stimuli.

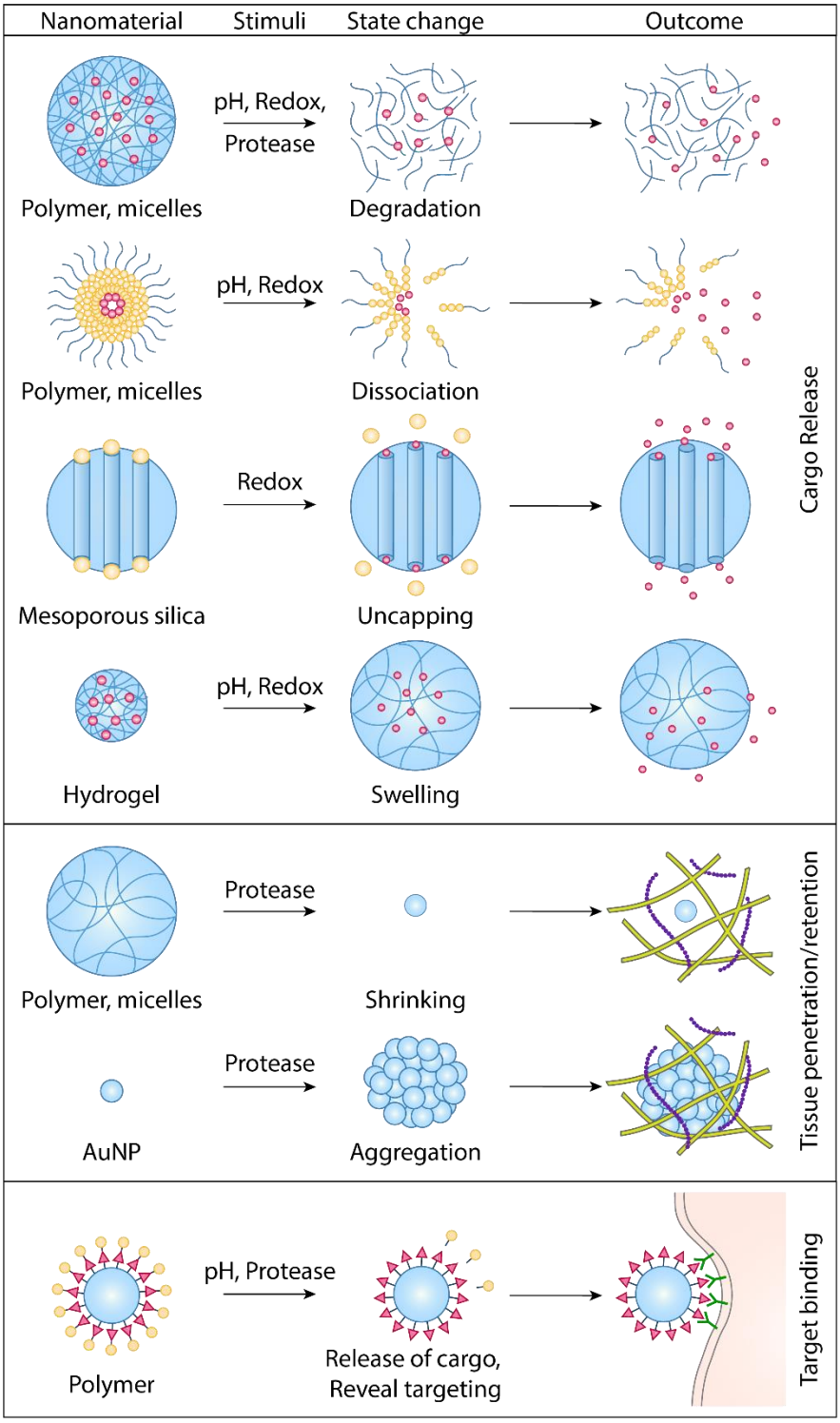

Figure 1.3: Bioresponsive nanomaterials that translate stimuli to a state change.

Because of the major transport barriers to and within the brain and the narrow therapeutic window of CNS therapeutics, numerous bioresponsive nanomaterial systems have been developed to improve delivery by responding to environmental cues present in biological barriers and/or in disease-specific contexts. The blood-brain barrier (BBB) is a major biological barrier for systemically-delivered nanomaterials and is estimated to exclude >99% of all therapeutics,[22,23] although disease-specific dysregulation of BBB function may be exploited for therapeutic delivery.[24] Due to the major bottleneck presented by the BBB, bioresponsive systems have been engineered to utilize endogenous transcellular transport pathways (Figure 1.4).

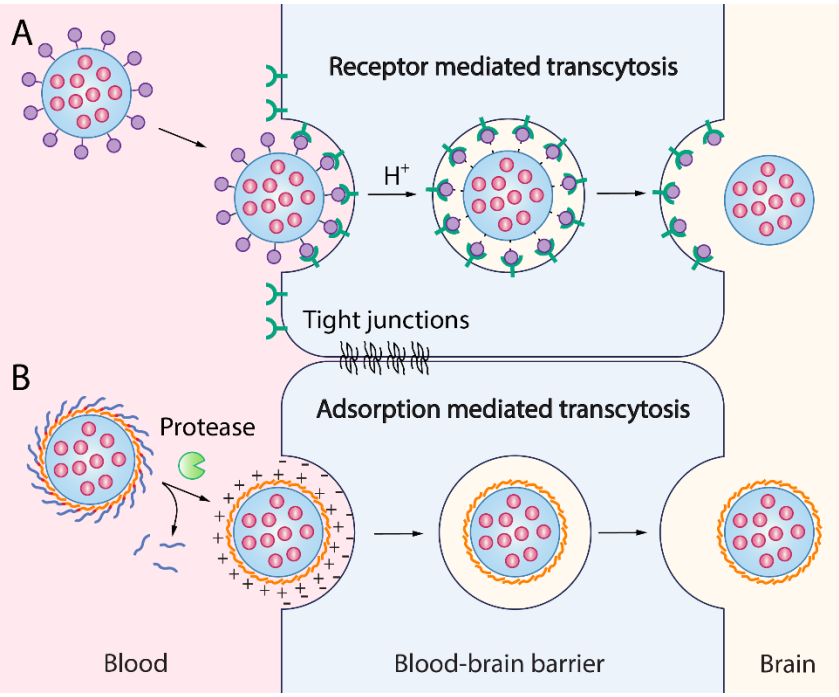

Figure 1.4: Bioresponsive nanomaterials that traverse the blood-brain barrier through transcellular pathways.

Bioresponsive nanomaterials designed for the CNS can also capitalize on environmental cues that change depending on disease-associated pathological processes or subcellular compartments. Environmental cues exploited by bioresponsive nanomaterials designed for the CNS broadly include pH, redox potential, and enzymatic activity, and changes in these cues can arise in CNS diseases such as brain injuries, neurodegenerative diseases, and cancer. Subcellular compartments such as the endosome or the cytosol also have distinct chemical environments that can be exploited by bioresponsive nanomaterials. In this chapter, the BBB and major environmental cues that are perturbed in CNS disease (pH, redox, proteases, electrical impulses, and hypoxia) will be discussed. For each cue or context present in the CNS, examples of bioresponsive nanomaterials will be presented (Table 1.1).

Table 1.1: Examples of bioresponsive nanomaterials applied to CNS pathologies.

Cue	Disease	Nanomaterial	Chemistry of Response	State Change	Outcome	Refs
pH	Cancer	Polymer micelle	Cleavage of hydrazone bond between cargo and micelle in tumor microenvironment	Dissociation of micelle	Cargo release of vinblastine derivative in a mouse glioma model	25
	Cancer	Polymer micelle	Cleavage of boronate ester bond between targeting ligands in tumor microenvironment	Dissociation of micellar network, exposure of targeting ligands against glioma cells	Enhanced levels and specificity of accumulation in a mouse glioma model	26
	Cancer	Polymer/iron oxide nanoparticle	Protonation of block co-polymer in tumor microenvironment	Shrinking of NPs	Prolonged blood circulation time, enhanced accumulation in tumor, extended MRI time window in a rat glioma model	27
	Cancer	Polymer micelle	Protonation of block co-polymer in tumor microenvironment	Dissociation of micelle, dequenching of fluorescent dye	Enhanced levels and specificity of PET cargo uptake in tumor cells, imaging of tumor in a mouse glioma model	28
	Chronic pain	Polymer micelle	Protonation of block co-polymer in endosome	Dissociation of micelle	Release of therapeutic to inhibit pain signaling initiated in the endosome in a rat model of chronic pain	29
	Cancer	Gold nanoparticle	Cleavage of hydrazone bonds between cargo and nanoparticle in endosome		Cargo release of chemotherapeutic doxorubicin, decreased off-target toxicity in a mouse glioma model	30
	Cancer	Poly-L-lysine dendrigraft	Cleavage of diamino ketal linker between Tf and dendrigraft in endosome	Release of dendrigraft from Tf-TfR complex	Increased BBB exocytosis and accumulation in tumor, cargo release of doxorubicin in a mouse glioma model	31
			Cleavage of imine linker between doxorubicin cargo and dendrigraft			

Table 1.1: Examples of bioresponsive nanomaterials applied to CNS pathologies, continued.

Cue	Disease	Nanomaterial	Chemistry of Response	State Change	Outcome	Refs
Redox	Stroke	Polymer nanoparticle	ROS-mediated oxidation of sulfide groups in inflammatory microenvironment	ROS scavenging, swelling of NP, shedding of PEG surface layer	Decreased neuroinflammation in a mouse stroke model	32
	TBI	Polymer nanoparticle	ROS-mediated oxidation of thioether groups in inflammatory microenvironment	ROS scavenging	Decreased tissue levels of ROS in a mouse TBI model	33
	Spinal cord injury	Polymer nanoparticle	ROS-mediated oxidation of thioether groups in inflammatory microenvironment	ROS scavenging	Decreased inflammation, improvement in motor skills in a rat spinal cord injury model	34
	Alzheimer's disease	Mesoporous silica capped with gold nanoparticle or IgG	H_2O_2-mediated oxidation and cleavage of boronate ester linker between AuNP/IgG and mesoporous silica	Uncapping of MSN pores	Cargo release of metal chelator clioquinol and decreased cytotoxicity in vitro in PC12 cells	35,36
	Alzheimer's disease	Polymer micelle	H_2O_2-mediated oxidation and cleavage of phenylboronic groups in inflammatory microenvironment	Destabilization of hydrophobic core	Cargo release of curcumin in a mouse AD model	37
	Stroke	Polymer micelle	H_2O_2-mediated oxidation and cleavage of phenylboronic groups in inflammatory microenvironment	Destabilization of hydrophobic core	Cargo release of rapamycin in a rat stroke model	38
	Stroke	Polymer nanoparticle with RBC membrane shell	H_2O_2-mediated oxidation and cleavage of phenylboronic groups in intracellular space	Destabilization of hydrophobic core	Cargo release of NR2B9C in a rat stroke model	39
	Cancer	Polymer micelle	H_2O_2-mediated oxidation and cleavage of phenylboronic groups in intracellular space	Destabilization of hydrophobic core	Cargo release of siRNA in a mouse glioma model	40
	Cancer	Polymer nanocapsule	GSH-mediated reduction and cleavage of cystamine disulfide crosslinker in intracellular space	Degradation of nanocapsule	Cargo release of siRNA in a mouse glioblastoma model	41

Table 1.1: Examples of bioresponsive nanomaterials applied to CNS pathologies, continued.

Cue	Disease	Nanomaterial	Chemistry of Response	State Change	Outcome	Refs
Redox	Stroke	Gold nanoparticle	ROS and hyaluronidase-mediated degradation of hyaluronic acid linker between FAM and AuNP in inflammatory microenvironment	Dequenching of FAM	Imaging of ROS levels in the brain in a rat stroke model	42
Protease	Cancer	Peptide/polymer micelle	MMP-2/9-mediated cleavage of PLGLAG peptide linker between protamine and TAT peptide	Activation of cell-penetrating peptide TAT	Increased delivery of paclitaxel cargo to tumor, reduced CPP-mediated off-target accumulation in a mouse glioblastoma model	43
	Stroke	Polymer nanoparticle with platelet membrane shell	Thrombin-mediated cleavage of a LTPRGWRLGGC peptide linker between rtPA and TAT peptide	Dissociation of NP, activation of cell-penetrating peptide TAT	Cargo release of rtPA at blood clot and ZL006e in ischemic brain, increased BBB transport and accumulation in ischemic tissue in a rat stroke model	44
			pH-mediated degradation of dextran core in ischemic tissue	Degradation of NP		
	Cancer	Gold nanoparticle	Legumain-mediated cleavage of a AANCK peptide for exposure of 1,2-thiolamino group on peptide-functionalized AuNP	Aggregation of gold via click cycloaddition between 1,2-thiolamino group and CABT on separate AuNPs	Increased retention and specificity of doxorubicin cargo delivery in a mouse glioma model	45
			pH-mediated cleavage of hydrazone bonds between cargo and surface of AuNP in endosome			
	Alzheimer's disease	Peptide/polymer micelle	Legumain-mediated cleavage of a AANCK peptide for exposure of 1,2-thiolamino group on peptide-functionalized micelle	Aggregation of micelles via click cycloaddition between 1,2-thiolamino group and CABT on separate micelles	Increased retention of paclitaxel, donepezil and insulin cargos in a mouse AD model	46

Table 1.1: Examples of bioresponsive nanomaterials applied to CNS pathologies, continued.

Cue	Disease	Nanomaterial	Chemistry of Response	State Change	Outcome	Refs
Protease	Stroke	Peptide/polymer micelle	Thrombin-mediated cleavage of a norleucine-TPRSFL peptide linker or MMP-9-mediated cleavage of a LGRMGLPGK peptide linker between PEG and PCL blocks	Removal of PCL to restructure and shrink micelles or removal of PEG to destabilize and aggregate micelles	Enhanced delivery of glyburide cargo to ischemic brain tissue with shrinking thrombin-responsive micelles in a mouse stroke model	47
	Cancer	Peptide/polymer micelle	Neutrophil elastase-mediated cleavage of a RLQLKL peptide linker between PEG and PCL blocks	Removal of PCL to restructure and shrink micelles	Enhanced delivery of doxorubicin cargo in a mouse metastatic tumor model	48
	Cancer	Polymer micelle with prodrug gene	MMP-2-mediated cleavage of PLGLAG peptide linkers between promelittin and vector sequences	Cargo activation of promelittin to melittin	Activation of melittin in tumor with limited off-target toxicity in a mouse metastatic tumor model	49
	Cancer	Polymer/peptide nanocapsule	MMP-2-mediated cleavage of VPLGVRTK peptide crosslinker	Degradation of nanocapsule	Delivery of antibody cargo across BBB in a glioma mouse model	50
	Cancer	Quantum dot	MMP-2-mediated cleavage of PLGVR peptide linker between low molecular weight protamine and QSY21	Dequenching of quantum dot	Imaging of tumor in a mouse glioma model	51
	TBI	Polymer/peptide conjugate	Calpain-1-mediated cleavage of QEVYGAMP linker between quencher and fluorophore	Dequenching of FRET peptide	Imaging of calpain-1 activity in a mouse TBI model	52
electric field	Epilepsy	Polymer hydrogel nanoparticle	Ionization of sulfonate groups during seizure	Swelling of NPs	Cargo release of anti-seizure drug phenytoin sodium in a mouse seizure model	53
hypoxia	Cancer	Polymer/lipid micelle	Hypoxic reduction of nitro groups to amino groups on metronidazole core in intracellular space	Destabilization of hydrophobic core	Enhanced delivery of doxorubicin cargo and sensitized tumor to radiotherapy in a mouse glioma model	54

1.3. Blood-brain barrier targeting strategies

A significant challenge in the development of therapies for CNS pathologies has been the effective delivery of intravenously injected agents into the brain. The blood-brain barrier (BBB) is a physical and functional barrier that is estimated to exclude ~100% of macromolecules and greater than 98% of small molecules from the brain. Major components of the barrier include tight junctions between cells, low rates of transcytosis across cells, and the expression of efflux pumps.[23] In recent decades, nanomaterials have emerged as a promising approach to create drug delivery systems that cross the BBB due to their ability to be rationally designed, oftentimes independently from their drug cargo. Numerous strategies have been devised to facilitate the transport of nanomaterials across the BBB, including targeting BBB receptors for receptor-mediated endocytosis, activating transporters for carrier-mediated transport, and changing nanomaterial surface charge or lipophilicity to target adsorptive-mediated endocytosis (Figure 1.4).[55–57] These delivery strategies help widen the therapeutic window by increasing the bioavailability of cargo in the brain, thereby reducing the administered dosage necessary to achieve therapeutic efficacy.

In order to exploit receptor-mediated transcytosis, nanomaterials are typically modified with ligands that specifically target endocytotic receptors present on the BBB. Ligands presented on nanomaterial structures are typically multi-valent, leading to an increase in the overall binding strength of the nanomaterial, termed avidity. The functionalized nanomaterial is endocytosed after binding to receptors on the luminal side of the BBB, after which it can then be released into the brain parenchyma on the abluminal side or trafficked into a lysosome for degradation (Figure 1.4A).[57] Transferrin receptor-mediated endocytosis has been one of the most well-studied pathways for exploitation by drug delivery, however, the binding avidity of materials must be

finely tuned to optimize transport. As an example of this challenge, in a study of systemically administered transferrin antibodies, antibodies with a high affinity for the transferrin receptor were found to have limited transport into the brain parenchyma despite a high level of uptake into the BBB. The high-affinity interaction of these antibodies with their receptor leads to a high fraction of antibodies remaining bound to transferrin receptors within the endosome and minimal release into the brain parenchyma. Simultaneously, tightly bound antibodies also reduce the number of available transferrin receptors for additional antibody binding.[58] This delivery traffic jam was resolved by engineering antibodies with moderate binding affinity for the transferrin receptor, which promoted release into the parenchyma at the cost of lower initial receptor binding in the lumen.

As an alternate strategy to the precise balancing of receptor binding affinity, a nanomaterial can undergo a stimulus-triggered state change between high avidity and low avidity binding to membrane receptors to maintain both a high rate of uptake into the BBB and a high rate of release into the brain. This strategy was first demonstrated with gold nanoparticles (AuNPs) which were functionalized with transferrin via pH-cleavable linkages to improve receptor-mediated transcytosis across the BBB in mice.[59] During endocytosis, the acidic environment within the endosome cleaves the diamino ketal linkers between the AuNP and transferrin, triggering a release of the AuNP from the transferrin/transferrin receptor complex. Thus, the AuNPs have a high avidity for the transferrin receptor on the luminal side to promote entry into the BBB, then undergo a pH-induced dissociation on the abluminal side to promote release from the BBB. In another technology which built upon the pH-triggered change for transferrin receptor avidity, a glucose analog which acted as an additional targeting ligand against glucose transporter 1 (GLUT1) was incorporated to increase the rate of nanomaterial

exocytosis into the brain parenchyma.[31] After internalization via the transferrin receptor, pH-mediated cleavage of the transferrin ligand in the endosome allowed dissociation from the transferrin receptor complex and an increased rate of exocytosis. The glucose analog could then promote subsequent uptake by GLUT1-expressing glioma cells. In a C6 glioma mouse model, nanoparticles modified with glucose analog, pH-cleavable transferrin, and pH-triggered doxorubicin release increased doxorubicin delivery to the glioma, increased the specificity of delivery to glioma over healthy brain tissue, and led to prolonged survival times in mice compared to nanoparticles modified with glucose analog and non-cleavable transferrin and nanoparticles modified with only pH-cleavable transferrin.

Adsorptive-mediated endocytosis is receptor-independent, and is instead based on physicochemical properties. In order to exploit adsorptive-mediated endocytosis, nanomaterials have been functionalized with positive charges to promote electrostatic interactions with negatively charged proteoglycans on the luminal side of the BBB (Figure 1.4B).[57] Cationic, amphipathic cell-penetrating peptides (CPPs) such as transcriptional activator (TAT) peptide are one category of materials used to facilitate receptor-independent endocytosis of nanomaterial across the BBB. While this strategy can improve intracellular delivery of nanomaterials, the charge-based interactions mediated by CPPs can also lead to non-specific targeting to multiple cell types, increased clearance from the liver, and increased systemic toxicity with intravenous administration.[60] In responsive materials, these drawbacks can be tempered with the incorporation of a domain which masks CPP activity with a neutralizing negative charge or steric hindrance.[60] Masking domains are linked to the CPP via a cleavable moiety so that the CPP is inert in circulation until the mask is removed by local tissue- and/or disease-specific cues, revealing CPPs and triggering electrostatic interaction with the cell membrane. This strategy was

used to improve drug delivery to ischemic brain tissue in stroke with a CPP-functionalized nanoplatelet which could activate CPP in the proximity of a blood clot.[44] A ~167 nm nanoplatelet was engineered from a dextran core, a platelet membrane shell, and surface coating of a CPP which was masked by thrombolytic recombinant tissue plasminogen activator (rtPA) via a thrombin-cleavable linker. After systemic administration in a rat stroke model, the nanoplatelet could first localize to the thrombus, where active thrombin was available to cleave peptide linkers on the surface. Cleavage triggered both release of therapeutic rtPA to induce proteolytic degradation of the blood clot and exposure of the CPP on the nanoplatelet surface for entry into the BBB. With the exposed CPP, the nanoplatelet could transcytose across the BBB into the ischemic penumbra, where the acidic microenvironment then degraded the dextran core to prompt the release of a second payload of neuroprotectant ZL006e into the parenchyma. Compared to nanoplatelets with non-cleavable peptides and free drug, systemically administered activatable nanoplatelets were able to cross the BBB more efficiently in rats with stroke and led to a >2-fold decrease in brain infarct volume, greater decrease in brain ROS levels, and improvement in neurological scores with minimal off-target toxicity. Thus, receptor-independent adsorptive-mediated transcytosis could be exploited by the thrombin-mediated unveiling of CPP in proximity to disease-associated BBB.

1.4. pH

1.4.1. pH in CNS Pathology

pH gradients occur within the body at the tissue and cellular level in both healthy and disease conditions. While the normal pH of blood is slightly alkaline at ~7.4, the pH in other tissues can be more acidic or basic depending on the specific needs for biological function. At

the cellular level, in comparison to the slightly alkaline extracellular pH (7.3-7.4), cytosolic pH is more acidic (pH 7.2) due to cellular metabolism, often leading to local acidosis in disease states where cellular metabolism is dysregulated.[61,62] In the brain, extracellular pH is measured to be 7.1-7.3 in microelectrode recordings in animal models.[63,64] In CNS pathologies such as gliomas and ischemic stroke, hypoxia and acidosis in the tissue microenvironment can lead to abnormal pH gradients that can be exploited by engineered nanomaterials. Cancer cells have a unique 'reversed' pH gradient where their intracellular pH is above normal (>7.2) and extracellular pH is lower (~6.7-7.1).[65] High intracellular pH aids in tumor cell proliferation and evasion of apoptosis, while low extracellular pH promotes cell-matrix remodeling and increases the activity of acid-activated proteases. This pH gradient is a result of the increased expression and activity of passive and active plasma membrane transporters that release lactate and H^+ ions in the tumor microenvironment.[66] The extracellular accumulation of protons in the tumor microenvironment can be further exacerbated by dysregulated tumor vasculature and poor lymphatic drainage. Extracellular pH can be heterogeneous throughout the tumor,[67] and differential pH is hypothesized to decrease over time as the tumors progress.[68] An acidic extracellular environment can also occur in ischemic stroke and in TBI. After vessel blockage in the brain, the lack of effective perfusion directly causes local tissue acidosis. Hypoperfused tissue rapidly becomes hypoxic and the resulting anaerobic metabolism leads to the accumulation of lactic acid.[69] In this process, both intracellular and extracellular H^+ concentrations increase; local pH in the peri-infarct penumbra ranges from 6.5-6.9 and can be as low as 6.0 in the ischemic core.[70] Ischemic tissue acidosis leads to increased risk of cell dysfunction and cell death due to activation of pH-sensitive ion channels linked to intracellular Ca^{2+} accumulation and cytotoxic edema.[70] Within TBI, acidic extracellular pH (pH < 7.1) tends to reverse or normalize in the subsequent days

following injury.[71–73] In some cases, however, the acidic extracellular space may be sustained due to metabolic dysfunction, which has correlated with worse outcomes and increased mortality.[71,72]

Intracellularly, vesicles of the endolysosomal pathway acidify to pH 4.5-6.5 as they mature, providing an opportunity for pH-responsive nanomaterials to facilitate endolysosomal escape into the cytosol where many payloads are active. Nanoparticles in circulation that interact with the endothelial membrane of the BBB are often taken up into endocytic vesicles termed early endosomes. These vesicles are sorted and can either be recycled to the membrane for exocytosis of its contents back into the blood or mature into late endosomes for further processing to lysosomes for degradation. During maturation of the endosome to lysosomes, the pH decreases creating the acidic environment required for optimal activity of degradative lysosomal enzymes.[74] In the context of therapeutic nanomaterials, entrapment in the endolysosomal pathway leads to loss of efficacy for cargo that are active in the cytoplasm or require transcytosis across the endothelium into the brain parenchyma. In particular, endolysosomal escape is a critical aspect for drug delivery systems for nucleic acids that are labile and require translocation to the cytosol or nucleus. In the context of CNS pathology, pH-sensitive molecules have been incorporated in nanomaterials to deliver nucleic acid therapeutics targeting gliomas.[75,76]

1.4.2. pH-Responsive Technologies

Two common building blocks used to engineer pH-responsive nanomaterials are ionizable side groups and acid-cleavable bonds. The pKa values of ionizable side groups in pH-sensitive nanomaterials are in physiological pH ranges and can reversibly change charge state

based on the pH of the local environment. This charge state change can lead to nanomaterial swelling with increased ionization or shrinking with decreased ionization due to the osmotic pressure created by counter ions.[77] Acid-sensitive bonds have increased degradation rates in lower pH environments and cleavage can lead to irreversible nanomaterial dissociation or cargo release. To date, pH-responsive nanomaterial technologies in the brain have been largely applied to cancer due to the acidic extracellular environment and to achieve intracellular release in the acidic lysosome.

Nanomaterials responsive to extracellular pH

The local acidic environments present in pathophysiological conditions provide an opportunity for the design of pH-sensitive nanomaterials that selectively activate in sites of disease while remaining inert in healthy, off-target contexts. Block copolymers with hydrophobic and hydrophilic domains can form micelles in aqueous conditions with hydrophobic domains oriented in the center of the micelle and hydrophilic domains oriented to the aqueous environment. In order to achieve pH-responsive drug release from polymeric micelles for the treatment of glioblastoma, acid-labile hydrazone bonds have been used to link chemotherapeutic drug to the carrier.[25] Hydrazone bonds undergo hydrolysis at pH levels lower than 6.8, however, the rate of hydrolysis can change based on how acyl hydrazones are prepared; acyl hydrazones prepared from aliphatic ketones are much more sensitive to hydrolysis compared to those prepared from aromatic aldehydes. pH-sensitive drug release was compared between two different polymer micelles tuned to be sensitive to either mildly acidic conditions in the tumor extracellular environment (~pH 6.9) or more acidic conditions in the endolysosomal environment (pH <6.5) depending on if acyl hydrazones were prepared from an aliphatic ketone or aromatic

aldehyde, respectively. Drug was conjugated to the hydrophobic segment of the block co-polymer so that it would be sequestered in the hydrophobic center of the micelle until acid-labile hydrolysis and subsequent disassembly of the micelle released the drug. In both orthotopic glioblastoma xenograft and syngeneic mouse models, treatment of mice with micelles that were sensitive to extracellular pH extended median survival time compared to treatment of mice with micelles that were sensitive to intracellular pH, non-responsive drug-loaded micelles, or free drug.

Using pH as a trigger to "reveal" ligands can be one approach to satisfy different design criteria of sequential delivery barriers encountered by intravenously delivered nanomaterials. In one example of this strategy, nanomaterials were designed to first overcome the BBB and then target brain tumor cells in technology described as sequential targeting in crosslinking (STICK).[26] These nanomaterials were functionalized with two different targeting ligands: the first targeting ligand, maltobionic acid, targeted GLUT1 receptors on the BBB, while the second targeting ligand, carboxyphenylboronic acid, targeted sialic acid on brain tumor cells. A ~140 nm nanomaterial structure was assembled from crosslinking polymer micelles displaying the two targeting ligands via pH-sensitive boronate ester bonds. The nanomaterial was designed to transcytose across the BBB into the tumor via maltobionic acid on the nanomaterial surface and dissociate into individual micelles in the acidic extracellular pH in the tumor microenvironment. Micelles then could penetrate into the tumor due to their reduced size and bind to tumor cells through the carboxyphenylboronic acid groups previously sequestered in the interior of the greater nanomaterial structure. When applied to an orthotopic glioma mouse model, STICK nanomaterials transported in greater amounts into gliomas after intravenous delivery compared to nanomaterials with only a single targeting group. STICK nanoparticles loaded with

chemotherapeutic drug extended the median survival time of mice compared to saline control, liposomal carriers, and single targeted carriers without pH-sensitive crosslinks. These results demonstrate that using pH as a trigger to reveal secondary moieties for sequential targeting can be an effective strategy for delivery of therapeutics across the multiple delivery barriers present in the CNS.

pH activation can also lead to a physical state change such as swelling or shrinking. Changes in nanomaterial size can affect retention and diffusion within target tissues – applicable to both diagnostic and therapeutic payloads. In order to achieve size changes that could improve pharmacokinetic profiles of an MRI contrast agent, a nanomaterial was created from a thermo- and pH-sensitive polymer which could swell in acidic conditions.[27] Iron oxide nanoparticles were loaded into nanogels comprised of thermosensitive poly(*N*-isopropylacrylamide) which was co-polymerized with pH-sensitive acrylic acid to form poly(*N*-isopropylacrylamide-*co*-acrylic acid) (MPNA) nanogels. Acrylic acid takes on different degrees of ionization and hydrophilicity based on pH; in circulation at a physiological pH of 7.4, the nanogels were hydrophilic and swollen (~95.5 nm) while in the acidic tumor environment became hydrophobic and shrunken (~85 nm), promoting uptake by tumor cells. In a rat model of glioma, the swelling response of systemically administered lactoferrin-targeted MPNA nanogels led to a longer circulation half-life and extended the MRI time window in the tumor from 2 hours to 6 hours compared to lactoferrin-targeted iron oxide nanoparticles alone.

Nanomaterials responsive to pH have also been used to improve contrast agents for positron emission tomography (PET). While PET can be used to image through the skull, the conventional PET metabolic tracer ^{18}F-fluorodeoxyglucose (FDG) is unable to be used for gliomas due to the background signal caused by naturally high uptake of glucose in healthy brain

tissue. To address this loss of contrast-to-noise ratio needed for imaging, pH-sensitive micelles were modified to chelate the positron-emitting radionuclide ^{64}Cu.[28] Micelles that are neutrally charged in normal physiologic pH ~7.4 were engineered to convert into polycationic unimers at pH <6.9, which can subsequently be internalized by cancer cells through electrostatic interaction. Due to internalization of the contrast agent by tumor cells, the signal could be retained and detected for up to 24 hours compared to contrast agents that remain extracellular. This nanomaterial was able to detect tumor volumes of 10-20 mm^3 in the brain and outperformed non-responsive nanomaterial as well as FDG by over an order of magnitude.

Nanomaterials responsive to intracellular pH

Numerous drugs have therapeutic targets within the cell and therefore trafficking drugs to the correct intracellular compartment is crucial for efficacy. In chronic pain, the G protein-coupled receptor neurokinin 1 receptor (NK_1R) localizes from the plasma membrane to endosomes, resulting in signaling that maintains pain. In order to inhibit NK_1R signaling specific to chronic pain, the NK_1R antagonist aprepitant was formulated into micelles made with pH-sensitive block co-polymers for specific release of drug in the acidified endosome.[29] At neutral pH, the 2-[N,N-(diisopropylamino)ethyl] methacrylate–co–di(ethylene glycol) methylether methacrylate (DIPMA-co-DEMGA) core is hydrophobic and can sequester hydrophobic cargo aprepitant, whereas at pH <6.1, the tertiary amine of DIPMA protonates, leading to electrostatic repulsion and disassembly of the micelle and subsequent release of drug. Intrathecal administration of aprepitant formulated in pH-sensitive micelles elicited similar levels of nociception relief at one third the dose compared to pH-insensitive micelles or free aprepitant in a sural nerve spared rat model. In addition, pH-sensitive micelles achieved a ~2-fold longer

duration of chronic pain relief when compared to aprepitant administered as free drug or in pH-insensitive micelles, demonstrating that bioresponsive nanomaterials can increase the efficacy of drug.

Chemotherapeutic drugs targeting gliomas are highly cytotoxic, necessitating carriers that are stable in circulation to limit off target toxicity in the bloodstream. Additionally, the large majority of nanoparticles become trapped in endolysosomal compartments in endothelial cells of the BBB and are degraded before reaching the tumor microenvironment. The endosomal-lysosomal lumen is maintained to pH ~4.5-6.5, and this drastic pH gradient provides an opportunity to leverage pH-sensitive nanomaterials for the selective release of cargo within the endolysosome. In order to achieve intracellular specific release of the chemotherapeutic doxorubicin, Ruan et al. used hydrazone bonds to anchor doxorubicin onto gold nanoparticles (AuNPs).[30] The AuNP surface was also modified with polyethylene glycol (PEG) to improve blood circulation and low density lipoprotein receptor related protein 1 (LRP-1) ligand angiopep-2 to increase BBB targeting and tumor penetration. Doxorubicin release kinetics were much faster at pH <6 compared to pH 6.8 or 7.4 and treatment of a mouse model of glioma with pH-sensitive targeting AuNPs demonstrated improved survival times and tumor penetration compared to free drug.

1.5. Redox

1.5.1. Redox in CNS Pathology

Natural redox states in the body are a balance of reducing molecules such as glutathione (GSH) and free radicals such as reactive oxygen species (ROS). These molecules help mediate oxidation and reduction reactions for normal cellular function, such as the reduction of disulfides

during protein folding.[78] Intracellular glutathione levels in most cells range from 1-2 mM.[79] ROS levels in healthy brain tissue are not well-defined due to limitations in real-time measurement but are estimated to be between 25-50 μM for H_2O_2.[80] Dysregulation of cellular metabolism in disease states can lead to the decrease or accumulation of these molecules and thus perturbation of redox states at both the tissue and cellular level. Inflammation and hypoxia, associated with pathophysiological conditions such as traumatic brain injury (TBI), ischemic stroke, and Alzheimer's disease,[81] are common causes for imbalances in reducing molecules and free radicals. The brain is particularly vulnerable to excess ROS because it is rich in lipids that can undergo ROS-mediated lipid peroxidation,[82] and there are low endogenous levels of antioxidant molecules and enzymes available to buffer elevated ROS in pathological conditions.[83]

Neuroinflammation is present across numerous CNS diseases, including injuries, stroke, and neurodegenerative disease. During neuroinflammation, ROS such as superoxide (O_2^-), hydrogen peroxide (H_2O_2), and nitric oxide (NO) are produced by reactive astrocytes and microglia, creating local increases in ROS levels.[84,85] Additional major sources implicated in excess ROS generation are the electron transport chain in mitochondria and the cell membrane enzyme complex NADPH oxidase (NOX).[82] At acute time points after ischemic stroke, hypoxia created by obstructed cerebral blood flow leads to an initial increase in ROS levels due to a decrease in the electron-transport rate in mitochondria, and cerebral reperfusion leads to a secondary burst of elevated ROS levels connected to upregulation of NOX expression.[86] The increase in ROS levels after ischemic stroke occurs rapidly within the first 24 hours of injury, followed by a gradual decrease to baseline levels over a number of days.[87–89] Traumatic injury to the CNS has been shown to activate glutamate receptors and increase intracellular accumulation of Ca^{2+} in neurons.[90] These are implicated in the mitochondrial dysfunction of the electron

transport chain that produces excess ROS following TBI.[91] Additionally, the activation of NOX produces ROS that contributes to neuronal death.[22] ROS levels have also been found to increase rapidly in injured brain tissue after TBI followed by a gradual return to baseline levels.[92] In Alzheimer's disease, the aggregation of amyloid beta (Aβ) protein can induce oxidative stress in the brain and has been tied to elevated lipid peroxidation and low levels of endogenous antioxidants.[93]

At the cellular level, an abundance of reducing molecules such as GSH can change redox potential; GSH levels are two or three orders of magnitude higher in the cytosol of healthy cells than in the extracellular fluid.[79,94] In tumor tissues such as gliomas, GSH concentrations in the cytosol can be elevated even higher to meet the demands of malignant cell proliferation.[95,96] Nanomaterial therapeutics can be designed to take advantage of these intracellular reducing environments for cytosolic delivery of cargo.

1.5.2. Redox-Responsive Technologies

Building blocks used to engineer redox-responsive nanomaterials are reducible/oxidizable functional groups and redox-cleavable linkers. Functional groups containing sulfides, thioethers, or phenylboronic groups can be oxidized, and lead to consumption of the ROS and/or changes in the hydrophobicity of the nanomaterial. Redox-sensitive linkers, for example, disulfide bonds, boronate esters, and hyaluronic acid, have accelerated degradation in reducing or oxidizing environments. Similar to acid-sensitive linkers, redox-sensitive linkers can lead to irreversible nanomaterial dissociation or cargo release. These state changes can be capitalized on for drug delivery based on change in redox potential of the extracellular environment in CNS diseases or within subcellular compartments. Due to the redox potential

created by inflammation, many redox-responsive nanomaterial technologies have been applied to acute brain injuries.

ROS scavenging

Elevated ROS levels are particularly harmful in the lipid-rich environment of the CNS due to ROS-mediated lipid peroxidation, and therefore scavenging of ROS is a therapeutic approach in CNS disease. ROS-responsive nanomaterials can directly scavenge ROS through the incorporation of sulfides or thioethers. Upon exposure to ROS, these functional groups are oxidized into more polar groups such as sulfoxides and sulfones, consuming the ROS in the process. To mitigate increased ROS levels following ischemic stroke, Rajkovic et al. synthesized ROS scavenging PEGylated poly(propylene sulfide) (PPS) nanoparticles that swell and shed their PEG surface layer when exposed to ROS due to their high density of sulfide groups.[32] These nanoparticles were responsive to multiple types of ROS, including hydrogen peroxide (H_2O_2), superoxide (O_2-), and nitric oxide (NO). Intravenous administration in a mouse model of ischemic stroke 30 minutes after reperfusion demonstrated that PPS nanoparticles accumulate in the ischemic brain region, and decrease infarct volume, neuronal loss, and the number of activated microglia compared to saline control. In an application of thioether-mediated ROS scavenging in TBI, core-crosslinked nanoparticles were synthesized with polysorbate 80 and a high proportion of thioether groups.[33] Core-crosslinked thioether polysorbate 80 nanoparticles accumulated in the injured brain of a mouse model of TBI, decreased tissue levels of ROS, and decreased neuroinflammation compared to the clinically-tested antioxidant therapy, PEG-super oxide dismutase. Thioether-based ROS scavenging can also be applied in spinal cord injury. Nanoparticles made from polymer with a high density of thioether groups were encapsulated in a

PEG-lipid shell to create a ROS-scavenging nanoparticle.[34] Intravenous administration of these nanoparticles to rats with spinal cord injury improved locomotor activity at lower doses compared to treatment with the corticosteroid methylprednisolone. Analysis of tissue demonstrated that ROS-scavenging nanoparticles could decrease ROS and inflammatory cytokine levels and mitigate demyelination in the injury.

Redox-mediated nanomaterial degradation

Aβ aggregation is hypothesized to be an important hallmark in the progression of Alzheimer's disease. Treatments for Alzheimer's disease under investigation include metal chelators to mitigate metal ion-induced Aβ aggregation. However, because metal ions are important in normal function in healthy tissues throughout the body, non-specific delivery of metal chelators can have significant off-target effects. In order to selectively chelate metal ions in the brain to prevent metal-induced Aβ aggregation in Alzheimer's disease, nanomaterials that are H_2O_2-responsive for controlled release of the metal chelator clioquinol (CQ) were engineered.[35] Metal chelators were loaded into the 2.57 nm sized pores of mesoporous silica nanoparticles (MSN) and pores were capped with 10 nm AuNPs via redox-sensitive boronate ester bonds to create a MSN-CQ-AuNP construct that released chelator in response to redox potential. In an in vitro model of Alzheimer's disease created by co-incubation of PC12 cells with Aβ-Cu^{2+} complexes, treatment with MSN-CQ-AuNPs led to a decrease in cell DNA fragmentation and a restoration of ROS to physiological levels. Redox-responsive nanoparticles were less cytotoxic in vitro and in vivo when compared to non-responsive nanoparticles or free chelator drug. A similar system was designed where pores were capped with IgG via H_2O_2-sensitive arylboronic esters.[36] These examples demonstrate the ability of MSN pore drug loading

to protect against off-target cytotoxicity of metal chelators and provide anti-Aβ aggregation therapeutic effect through redox-sensitive uncapping of MSNs.

ROS-responsive boronic esters have also been applied to ligand-targeted nanomaterials. Receptor for advanced glycation end-products (RAGE) mediates the transport of plasma Aβ into the brain and is upregulated in the BBB, neurons, and microglia during Alzheimer's disease progression.[37] To exploit elevated RAGE and mitigate Aβ accumulation and ROS in Alzheimer's disease, a RAGE-targeted polymeric micelle system was engineered to dissociate in response to ROS and release curcumin, a compound that targets Aβ aggregation. To target RAGE, a targeting peptide was modified onto PEG in a polylysine-PEG co-block polymer. The ROS-responsive element was the modification of the epsilon amines of the polylysine-PEG with hydrophobic phenylboronic groups. In the presence of H_2O_2, ROS-mediated oxidation initiated self-immolation of the phenylboronic groups, revealing the primary amines and switching the material from amphiphilic to hydrophilic. In the intact micellar structure, hydrophobic curcumin was loaded in the core with phenylboronic-capped lysines and ROS-mediated degradation led to disassembly of the micelle through loss of the hydrophobic phenylboronic groups and subsequent curcumin release. Administration of these responsive micelles in a mouse model of Alzheimer's disease over 3 months resulted in decreased oxidative stress, Aβ plaques, and microglial activation compared to non-peptide targeting micelles, non-drug loaded micelles, and free drug. The same approach was also adapted for the treatment of ischemic stroke, where the fibrin-binding peptide CREKA was functionalized onto phenylboronic ester-modified PEG-polylysine micelles loaded with mTOR inhibitor rapamycin.[38] In a rat model of stroke, these micelles facilitated decreases in ROS levels and M2 microglia repair, leading to decreased brain infarct area and significantly higher neuron density compared to non-targeted, non-drug loaded,

and free drug controls. While these systems use synthetic PEG to increase blood circulation times, alternative systems use biological red blood cell membranes to encapsulate ROS-responsive boronic ester-containing cores to evade the immune system and prolong blood circulation.[39] Modification of red blood cell membranes with stroke homing peptide showed enhanced active targeting to the ischemic area in a rat model of stroke compared to non-targeting and free drug controls, resulting in improved function in neurological testing and decreased infarct volume after injury.

Nucleic acids such as small interfering RNA (siRNA) have the potential to drug gene candidates in glioblastoma that have been challenging to inhibit with traditional small molecule therapeutics. However, nucleic acids as drugs are difficult to deliver due to their high charge density, large size, and instability in the biological milieu. This has necessitated drug delivery carriers for the clinical translation of nucleic acid drugs, such as the lipid nanoparticle systems in FDA-approved patisiran.[97] The delivery of nucleic acid by nanomaterials requires balancing the need to protect labile cargo extracellularly and the need for efficient release of cargo intracellularly in order to allow interaction with the biological machinery of the cell.[98] Responsive materials are one potential solution to satisfy these conflicting design criteria. One redox-responsive carrier for siRNA has been engineered through self-assembly of nucleic acids with polymers functionalized with guanidinium and phenylboronic ester; assemblies are stabilized by the electrostatic interactions and hydrogen bonding of guanidinium and hydrophobic interactions of phenylboronic ester.[40] The elevated ROS in glioblastoma cells mediates degradation of the phenylboronic ester, and the loss of the hydrophobic interactions destabilizes the complex to release siRNA for subsequent engagement of RISC machinery and degradation of target mRNA in the cytosol. Only nanocomplexes that included phenylboronic

ester led to the release of siRNA in the presence of H_2O_2. These nanocomplexes led to silencing of gene targets when delivered to mice bearing orthotopic implants of glioblastoma cells.

In order to exploit the reducing environment created by elevated GSH levels in gliomas, nanomaterials can be crosslinked with disulfide bonds for release of therapeutic cargo in the glioma microenvironment. To create a nanomaterial that would disassemble in reducing environments, a capsule was directly polymerized onto siRNA molecules using a disulfide crosslinker resulting in a 25 nm construct.[41] In vitro, release of siRNA from the nanocapsule was accelerated in the presence of GSH and silencing was improved 2-fold over capsules without disulfide crosslinking. These nanocapsules were modified with the peptide ligand angiopep-2 to target the LRP-1 overexpressed on the BBB and glioblastoma cells. In mice bearing orthotopic glioblastoma xenografts, disulfide crosslinked nanocapsules formed around therapeutic siRNA led to a significantly decreased tumor size and increased survival by ~2-fold over non-reducible nanocapsules.

ROS-responsive nanomaterials have also been used for imaging applications for CNS disease. Hyaluronic acid is a natural polymer that can be degraded by hyaluronidase or ROS. An imaging construct for ischemic stroke was engineered through the immobilization of fluorophore-conjugated hyaluronic acid onto the surface of gold nanoparticles.[42,99] The fluorophore fluorescence is quenched by gold nanoparticles when in close proximity through nanoparticle surface energy transfer (NSET). Degradation of hyaluronic acid led to dissociation of fluorophores from the gold surface and dequenching of fluorescence.[99] Ex vivo imaging of nanoparticles directly injected into the brain in a rat stroke model revealed that maximal levels of ROS accumulation occurs 24 hours after injury. These responsive nanoparticles could also be

imaged in live animals and had a 3-fold increase in signal when applied to stroke models compared to healthy controls.[42]

1.6. Proteases

1.6.1. Proteases in CNS Pathology

Proteases are enzymes which can recognize and hydrolytically cleave specific sequences within other proteins. There are currently over 800 known proteases within the human genome which are involved in all aspects of cellular function including protein processing, transcriptional control, and signal amplification.[100,101] In pathophysiological conditions, proteases can be ectopically expressed or activated. Proteases are often direct participants in pathological processes; for example, caspases play essential roles in cellular apoptosis and thrombin regulates blood coagulation, and therefore incorporation of elements responsive to disease-associated proteases can increase nanomaterial specificity. This strategy has been explored in cancer nanomedicine, where many protease-responsive nanomaterials have been designed to respond to matrix metalloprotease 2 (MMP-2) and MMP-9, which are upregulated across multiple cancers.[102–104] The engineering design from these past works have been applied to technologies designed to function in CNS pathologies, where proteases such as MMP-2, MMP-9, neutrophil elastase, legumain, thrombin, and calpain are abnormally activated in brain cancers, neuroinflammation, TBI, and stroke.[24,105,106]

MMP-2 and MMP-9 are zinc-dependent proteases that break down components of the extracellular matrix (ECM) and are upregulated in brain cancers as part of cellular proliferation and neuroinflammation, and in acute brain injuries as part of neuroinflammation and repair.[105,107–109] MMP-2 and -9 are expressed in inactive zymogen form, pro-MMP-2 and -9,

that become activated after proteolytic processing. In brain tumors, MMP-2 and -9 are both produced by glial and endothelial cells, while MMP-9 is also expressed by infiltrating immune cells.[107] MMP-9 tends to be elevated at the proliferating margins of malignant gliomas, and the increased expression of MMP-2 and MMP-9 in gliomas has been linked to increased malignancy in human patients.[108,109] In the first 24 hours after injury or stroke, MMP-9 is upregulated in and secreted by brain endothelial cells, neurons, astrocytes, and infiltrating leukocytes both within the injured tissue and around the injury periphery, and this activity can be sustained through 96 hours after injury.[105,110–114] The increased expression of MMP-9 has been associated with increased levels of edema and hemorrhage in the brain after stroke, and with higher mortality rates in patients with severe TBI.[115] While MMP-9 has been implicated in BBB breakdown and neuroinflammation in acute stages of injury, its sustained activation weeks after injury is also proposed to facilitate neurovascular remodeling and repair.[116]

In addition to MMPs, proteases such as the serine protease neutrophil elastase and asparagine endopeptidase legumain can be released by invading leukocytes during neuroinflammation in cancer, injury, and stroke. Neutrophil elastase, secreted by neutrophils, targets many components of the ECM including collagen I-IV, fibronectin, proteoglycans, and cadherin, and its increased levels have been linked to increased malignancy in tumors[117] and BBB breakdown and cell death in TBI and stroke.[118,119] Within acute injuries, neutrophil elastase elevation initiates from 2 hours after injury and can remain elevated through 24 hours after injury.[118,119] Legumain is secreted by macrophages, microglia, and neurons.[120] Its substrates include pro-MMP-2, cathepsins, tau, myelin basic protein, and fibronectin.[121] In cancer, legumain has been found to have an increased expression in many solid tumors including those in the CNS, and its overexpression has been linked to increased tumor invasiveness and

metastasis.[122] Legumain activity and expression is also increased under acidic conditions such as in ischemic tissue after stroke,[123] and its increased activity is associated with increased hyperphosphorylation of tau in Alzheimer's disease.[124]

In both TBI and stroke, a combination of BBB disruption, excitotoxicity, cell death, and neuroinflammation during secondary injury lead to the sustained activation of injury-associated proteases including thrombin and calpain.[105,125–128] Thrombin is a serine protease which plays a central part in the coagulation cascade. When the BBB is dysregulated during TBI and stroke, thrombin can extravasate from the blood into the brain parenchyma and can contribute to further BBB disruption, neuronal cell death, and inflammation.[127,129,130] Calpains are calcium-dependent cysteine proteases which activate within hours of injury through an excitotoxicity-triggered influx of calcium ions into neurons, and which can remain active for days post-injury.[128,131,132] Calpains are produced by neurons, astrocytes, and endothelial cells in the brain, cleave a variety of cytoskeletal proteins, and contribute to both apoptotic and necrotic cell death.[133] While calpains are typically intracellular, ectopic release into the extracellular microenvironment during inflammation and cell death has been observed.[134]

While the above proteases were discussed in the context of specific CNS diseases, similarities in protease activation can be observed across diseases due to their association with pathological processes shared among diseases. For example, the inflammation triggered by cancer, neurodegeneration, and brain injury leads to the infiltration of leukocytes which become a source for MMP-9, neutrophil elastase, and legumain, although the timescale and magnitude may differ across diseases. There are also similarities in elevated MMP-9 expression for neurovascular remodeling during the reparative 'wound healing' stages of brain injury and in

proliferating areas of tumors.[107,135] As a result, the same proteases may be used as activators for protease-responsive technologies across CNS pathologies that share pathological hallmarks.

1.6.2. Protease-Responsive Technologies

The building blocks used to engineer protease-responsive nanomaterials are based on peptide sequences that are protease substrates. Peptide substrates can be the endogenous sequence found in nature or de novo sequences identified in screens, and significant efforts have been made to tune these sequences using synthetic libraries and/or chemical modifications.[100,136] Similar to acid- or redox-sensitive linkers, protease-sensitive peptide linkers can lead to irreversible nanomaterial degradation or dissociation. These state changes lead to activated targeting groups or diagnostic signal, changes in nanomaterial size, and released therapeutic payloads in the extracellular environment in CNS diseases.

Activation of targeting

Protease-cleavable linkages can be introduced into nanomaterials to produce a step-wise unveiling of targeting domains at the target tissue in a similar manner to the targeting activation discussed for pH- and redox-responsive materials. With non-specific cell-targeting domains such as CPPs, spatial and temporal activation of targeting in the diseased tissue can reduce off-target accumulation and increase specificity of cargo delivery.[60] In order to introduce specificity towards glioblastoma cells, MMP-2 or -9-sensitive linkers have been used to charge shield a cationic CPP surface.[43] PEG-poly(ε-caprolactone) (PEG-PCL) nanoparticles functionalized with low molecular weight protamine CPP were masked with a polyanionic peptide via MMP-2 or MMP-9 substrates. In the tumor microenvironment, removal of the polyanionic peptide by

tumor-associated proteases enable entry of nanomaterials into tumor cells and subsequent delivery of a chemotherapeutic paclitaxel payload. In a C6 glioblastoma mouse model, these nanomaterials exhibited increased accumulation in the tumor and led to a prolonged survival time in treated mice compared to nanomaterials with unmasked CPPs and free paclitaxel. In off-target organs, activatable nanoparticles had a similar accumulation as nanoparticles without CPPs due to their similar charge profiles, while the positively charged nanoparticles with unmasked CPPs had a higher accumulation in the lung and liver and a faster blood clearance rate. The masking agent itself can also act as a therapeutic payload once it is released, as was demonstrated with the nanoplatelet system which was discussed in Section 2.[44] In proximity of a blood clot in ischemic stroke, active thrombin cleaves a linkage between thrombolytic rtPA and a CPP on the nanoplatelet surface. The CPP, which had been masked by rtPA, could then induce adsorptive-mediated transcytosis of the nanoplatelet across the BBB, while the rtPA remained in the proximity of the blood clot to proteolytically activate plasmin for dissolution of the clot. In both of these examples, protease-mediated unveiling of CPP allowed for selective entry of nanomaterials into target cells while minimizing CPP-mediated nonspecific accumulation.

Protease-mediated nanomaterial aggregation

Protease-cleavable domains can also be introduced to induce nanomaterial aggregation by activating reactive groups for crosslinking between adjacent nanomaterials or by changing the arrangement of hydrophobic and hydrophilic polymer blocks for destabilization of micellar structures. Once a nanomaterial has entered the brain parenchyma, an increase in effective nanomaterial size achieved by swelling or aggregation can increase tissue retention. Conversely, a decrease in nanomaterial size may be desirable to promote diffusive transport of the material

deeper into the brain parenchyma due to known size-dependent penetration through the brain extracellular space.[137]

In an example of protease-mediated nanomaterial aggregation, two complementary sets of AuNPs were designed to aggregate after cleavage by legumain in the glioma microenvironment.[45] One set of AuNPs was functionalized with a peptide that would expose a functional cysteine once it was cleaved by legumain. The other set of AuNPs was functionalized with 2-cyano-6-aminobenzothiazole (CABT), a group which reacts with the 1,2-thiolamino groups on the exposed cysteine to form a covalent bond through click cycloaddition. With this system, legumain cleavage led to nanomaterial aggregation with effective nanomaterial size increasing an order of magnitude from ~35.6 to 309.6 nm. These AuNPs were modified with doxorubicin through pH-dependent linkages and administered to mice carrying an orthotopic C6 glioma, where there was an increased accumulation of AuNPs in the tumor site, higher specificity of targeting to the tumor over healthy brain tissue, and a greatly prolonged survival time in mice treated with activatable AuNPs over non-activatable AuNPs. This increased accumulation was attributed to a reduced efflux of aggregated AuNPs from the brain, and this same peptide-CABT chemistry was later applied to enhance the brain retention of legumain-activated micelles in Alzheimer's Disease.[46]

To improve the delivery efficiency of therapeutics to ischemic brain tissue in stroke, a nanomaterial system composed of hydrophobic PCL and hydrophilic PEG block co-polymers modified with peptide substrates was designed to shrink or expand in size upon cleavage of a thrombin or MMP-9 peptide.[47] Nanomaterials could either undergo micellar collapse and aggregation to expand from ~100 nm to ~1100 nm in size, or restructure and shrink from ~218 nm to 79 nm in size based on placement of the protease substrate linker within the competing

hydrophobic and hydrophilic domains of the block co-polymers. Ultimately, thrombin-responsive shrinking nanoparticles were used to enhance the delivery of therapeutic glyburide payloads to the ischemic brain tissue of mice with stroke by 9-fold and 4.5-fold compared to non-responsive and expandable nanoparticles, respectively. This same approach was applied to create nanoparticles which shrink in response to upregulated neutrophil elastase in metastatic brain cancer.[48]

Release or activation of cargo

Locally activated proteases in cancer and stroke have been used to selectively degrade nanocarriers and release or activate cargo in target brain tissue. This strategy can help to avoid off-target toxicity by delivering an inert "prodrug" form of therapeutic that can be activated at the target tissue of interest. Selective activation is especially important for highly cytotoxic anticancer molecules such as melittin, which can induce widespread systemic toxicity if administered directly into the bloodstream. To promote delivery of melittin into metastatic brain tumors while limiting off-target toxicity, a genetically encoded prodrug form of melittin was designed to be activated by MMP-2.[49] Polymeric poly(lactone-*co*-β-amino ester) nanomaterials were designed to carry a gene payload that encoded for secretory promelittin, which is nontoxic until it is cleaved by tumor-associated MMP-2 to form cytolytic melittin. When applied to in vitro cell cultures, the promelittin was activated and cytotoxic against 231BR cells which expressed MMP-2, but inactive and nontoxic towards normal human astrocyte cells which did not express MMP-2. This specific cargo activation combined with selective targeting of the nanomaterials against tumors led to a reduction in tumor size without significant off-target

toxicity and enhanced the survival of mice with metastatic brain cancer compared to saline and nanoparticle-only controls.

Protease-mediated activation has also been used to add stepwise functionality in nanomaterials to restore the function of cargo which requires targeting or protective components for delivery. To enhance the delivery of a large protein cargo into gliomas, cargo was ensheathed in an MMP-2-responsive nanocapsule comprised of choline and acetylcholine analogs that could facilitate active transport across the BBB.[50] Once the ~25 nm nanocapsule crossed into tumor tissue, upregulated MMP-2 could cleave the peptide linkers holding the nanocapsule together and release an antibody drug payload. In vitro, this antibody payload was unable to bind to its target cells until it was released from its nanocapsule by MMP-2, necessitating the degradation of the capsule for function. In an orthotopic xenograft glioma mouse model, repeated treatment with nanocapsule-mediated delivery of nimotuzumab and trastuzumab antibodies led to a larger reduction in tumor size and lengthened survival in mice compared to free antibody, indicating that the responsive nanocapsule could successfully deliver its cargo into the tumor without compromising its function.

Activity-based nanosensors as diagnostics

The measurement of abnormal protease activity is useful to understand the spatial and temporal progression of pathological processes due to the integral role proteases play in disease progression. Since proteases function by cleaving peptide substrates, changes in disease-associated protease activity can be directly sampled with probes which produce a measurable signal upon cleavage by the target protease. Fluorescence-based Förster Resonance Energy Transfer (FRET) sensors are the most utilized modality and involve an energy transfer between a

donor and acceptor molecule when they are separated by a distance of 20-60 Å.[138] When the acceptor group is a quencher, the emitted fluorescence from the donor fluorophore is not visible until the quencher is separated in physical distance. One such system was based on quantum dots modified with negatively-charged heparin used to electrostatically self-assemble positively-charged protamine modified with quencher via a MMP-2-cleavable substrate.[51] The resulting nanomaterial was 204 nm and in the presence of MMP-2, quencher could be cleaved from protamine, leading to physical separation from the quantum dot core and dequenching of fluorescent signal. This system was used in combination with brain-specific ligand targeting and was used to visualize orthotopic U87 glioma xenografts in mice after intravenous administration. Activity-based nanosensors can also help to diagnose pathological activity in the brain and further understand proteolytic contributions to CNS pathology. To measure the activity of calpain-1, a protease implicated in neuronal breakdown in TBI, a FRET-substrate for calpain-1 was attached to a ~10 nm polymeric PEG core.[52] After intravenous delivery in a controlled cortical impact mouse model of TBI, this nanosensor could accumulate into injured brain tissue after passing through the damaged BBB. Once in the injured tissue, nanosensor signal could be detected in response to locally activated calpain-1 in the injured tissue. This signal revealed changes in calpain activity that were otherwise difficult to capture by measuring changes in calpain-1 expression alone.

1.7. Other cues

1.7.1. Electrical Impulses

Seizure-induced abnormalities in the electrical impulses between neurons provide an opportunity for the endogenous stimulation of electro-responsive nanomaterials. Electro-responsive materials for drug delivery are typically constructed from conducting polymers which

can induce changes in charge or hydrophobicity throughout the material under an electric field,[139] and one form of electro-responsive drug delivery involves hydrogels which can swell and release a payload under electro-induced osmotic pressure.[140] This concept was applied to improve drug delivery for seizures using electro-responsive hydrogel nanoparticles that can swell and release an antiepileptic drug payload in response to endogenous electric fields during epileptic seizures.[53] The hydrogel nanoparticles were functionalized with sulfonate groups which ionize under electric fields; when tested under an external electric field in vitro, the nanoparticles rapidly swelled from ~102 nm to 388 nm under increasing currents of 50 to 500 μA. In a chemically-induced seizure rat model, these responsive nanoparticles released drug in the brain upon seizure induction in a severity-dependent manner. By contrast drug concentrations did not increase in response to seizure induction after non-responsive nanoparticles or free drug administration, indicating that the payload release from responsive nanomaterials was induced by the seizures. Treatment with electro-responsive nanoparticles decreased severity and frequency of seizures and increased the latency to seizures in both electrically- and chemically-induced seizure rat models compared to matching doses of non-responsive nanoparticles and free drug.

1.7.2. Hypoxia

Hypoxic regions, or regions with low levels of oxygen (<2%), are a hallmark of solid tumors and ischemic stroke and thus are another possible cue that can enhance the specificity of responsive nanomaterials. Physiological brain pO_2 is 33.8 ± 2.6 mmHg (4.4 ± 0.3%), and mean pO_2 decreases with brain depth.[86,141] To introduce responsiveness to hypoxia, nitroaromatic compounds such as 5-nitroimidazole and its derivative metronidazole can be introduced into nanomaterials. Under hypoxic conditions, these compounds react with

intracellular nitroreductases and undergo a step-wise reduction of nitro (NO_2) groups to amine (NH_2) groups to switch between a hydrophobic to a hydrophilic state.[142] To both increase the specificity of anticancer drug delivery and sensitize glioma cells to radiotherapy, a hypoxia-responsive nanoparticle was engineered with a polymerized metronidazole hydrophobic core co-loaded with doxorubicin surrounded by an angiopep-2-functionalized lipid shell.[54] The polymerized metronidazole served a dual function in the nanoparticles: the conversion of NO_2 groups to more hydrophilic NH_2 groups in hypoxic environments prompts the release of hydrophobic doxorubicin, and the radical intermediates of the metronidazole sensitize the tumor cell to radiotherapy by inducing DNA damage. In an orthotopic C6 glioma mouse model, hypoxia-responsive metronidazole nanoparticles more effectively delivered the doxorubicin and sensitized tumors to radiotherapy, leading to a decrease in tumor growth by ~3.5-5-fold compared to non-responsive doxorubicin-loaded PLGA nanoparticles.

1.8. Conclusion

In the past decade, significant advances have been made in the understanding of CNS disease etiology and the design of engineered bioresponsive nanomaterials. While there has been successful translation of bioresponsive nanomaterials as imaging agents for surgical cancer resection and lipid nanoparticles for nucleic acid delivery,[143,144] there have yet to be bioresponsive nanomaterials translated for CNS disease due to similar obstacles that prevent the clinical translation of traditional CNS-specific small molecules. One existing challenge in the advancement of bioresponsive nanomaterials for CNS applications is the identification of biological stimuli that are unique to disease contexts. Although one of the advantages of bioresponsive nanomaterials is reduction of off-target delivery, certain pathological conditions

may involve generation of stimuli in tissues other than the brain; for example, MMPs are also elevated in the blood of patients following stroke and TBI.[145,146] Due to the redundancy of biological stimuli, engineered nanomaterials will likely require multiple mechanisms to achieve specificity. For example, many of the discussed bioresponsive nanomaterials incorporate tissue-specific ligand targeting and disease-specific payloads in addition to their response to stimuli. Self-regulating bioresponsive nanomaterial systems under the control of negative feedback loops can further improve specificity, mimicking examples of endogenous biological homeostasis such as the clotting cascade.

Disease-specific environmental cues in the brain are complex and can be spatially heterogenous and temporally dynamic. Designing bioresponsive nanomaterials for this complex and dynamic environment is an ongoing challenge. To create specific responses based on the temporal and spatial dependence of environmental cues, building blocks can be combined into a single nanomaterial to create Boolean logic gates[147] that require the presence of two stimuli to activate. Alternatively, when cues are spatially separated, nanomaterials can be designed to have sequential activation as they encounter stimuli.[148] However, this design requires knowledge of the sequence of cues a priori. When the order or timescales of endogenous stimuli are unknown or when the stimuli are heterogeneously distributed throughout a diseased tissue, nanomaterials could alternatively be designed to activate in an 'OR' configuration either by including multiple responses within a single nanomaterial or by delivering a mixture of different bioresponsive nanomaterials. In addition, CNS disease physiology, and thus the environmental cues, can vary based on a number of patient-specific biological factors, including race, age, and sex, which has implications for bioresponsive nanomaterial design.[149,150] For example, it has been proposed that estrogen has neuroprotective effects by reducing ROS through its antioxidant activity and

regulation of antioxidant genes[151–153] and epidemiological studies show that premenopausal females are less likely to suffer from neurodegeneration, whereas postmenopausal females have increased risk on par or exceeding that of males, indicating that ROS-sensitive strategies can be sex- and age-dependent.[154,155] The interaction of nanomaterials and the injured brain has also been found to be sex-dependent, with increased nanoparticle extravasation into the brain of female vs. male mice after intravenous delivery 24 hours post-injury.[156] There remains a significant gap in knowledge on the impact of biological factors on the interaction of bioresponsive nanomaterials and the CNS.

Going forward, the design and implementation of bioresponsive nanomaterials would benefit from a precision medicine approach. While there are general classes of responsive materials specific to CNS diseases, such as pH-responsive nanomaterials for cancer and ROS-responsive nanomaterials for acute brain injuries, in the clinical scenario there are limitations in the ability to implement effective disease-directed responsive materials without knowledge of the molecular underpinnings of the disease in specific patients at specified times. Currently, information on the environmental cues such as pH, redox, and protease activity, is largely unknown at the time of diagnosis and as discussed above, it is known that these cues can be dependent on multiple factors including the severity of disease, time of treatment, age, and sex.[157] Future clinical translation may therefore benefit from matching a patient's underlying molecular status with appropriate bioresponsive nanomaterials rather than applying a "one-size-fits-all" approach for each disease.[158] At the same time, lessons learned from past clinical successes support simple engineering designs that can be reproducibly manufactured at scale and have well-defined mechanisms of actions. Nevertheless, efficacy and safety are the major hurdles

to the successful translation of medicines into the CNS, and bioresponsive nanomaterials have the potential to decouple the double-edged sword of potency and off-target effects.

1.9. Acknowledgements

Chapter 1, in full, has been submitted for publication of the material as it may appear in Engineering Biomaterials for Neural Applications, and is reproduced with permission from Springer Nature. Kudryashev, Julia. A.; Madias, Marianne I.; Kwon, Ester J. Bioresponsive nanomaterials for CNS disease. Springer Nature, 2022. The dissertation author was one of the primary researchers and authors of this paper.

1.10. References

(1) Mura, S.; Nicolas, J.; Couvreur, P. Stimuli-Responsive Nanocarriers for Drug Delivery. *Nat. Mater.* **2013**, *12* (11), 991–1003. https://doi.org/10.1038/nmat3776.

(2) Blum, A. P.; Kammeyer, J. K.; Rush, A. M.; Callmann, C. E.; Hahn, M. E.; Gianneschi, N. C. Stimuli-Responsive Nanomaterials for Biomedical Applications. *J. Am. Chem. Soc.* **2015**, *137* (6), 2140–2154. https://doi.org/10.1021/ja510147n.

(3) Lu, Y.; Aimetti, A. A.; Langer, R.; Gu, Z. Bioresponsive Materials. *Nat. Rev. Mater.* **2016**, *2* (1), 1–17. https://doi.org/10.1038/natrevmats.2016.75.

(4) Hoffman, A. S. Stimuli-Responsive Polymers: Biomedical Applications and Challenges for Clinical Translation. *Adv. Drug Deliv. Rev.* **2013**, *65* (1), 10–16. https://doi.org/10.1016/j.addr.2012.11.004.

(5) Heller, J.; Baker, R. W.; Gale, R. M.; Rodin, J. O. Controlled Drug Release by Polymer Dissolution. I. Partial Esters of Maleic Anhydride Copolymers—Properties and Theory. *J. Appl. Polym. Sci.* **1978**, *22* (7), 1991–2009. https://doi.org/10.1002/app.1978.070220720.

(6) Lin, H.-R.; Sung, K. C. Carbopol/Pluronic Phase Change Solutions for Ophthalmic Drug Delivery. *J. Controlled Release* **2000**, *69* (3), 379–388. https://doi.org/10.1016/S0168-3659(00)00329-1.

(7) Agrawal, M.; Saraf, S.; Saraf, S.; Dubey, S. K.; Puri, A.; Gupta, U.; Kesharwani, P.; Ravichandiran, V.; Kumar, P.; Naidu, V. G. M.; Murty, U. S.; Ajazuddin; Alexander, A. Stimuli-Responsive In Situ Gelling System for Nose-to-Brain Drug Delivery. *J. Controlled Release* **2020**, *327*, 235–265. https://doi.org/10.1016/j.jconrel.2020.07.044.

(8) Cook, A. B.; Decuzzi, P. Harnessing Endogenous Stimuli for Responsive Materials in Theranostics. *ACS Nano* **2021**, *15* (2), 2068–2098. https://doi.org/10.1021/acsnano.0c09115.

(9) Purcell, B. P.; Lobb, D.; Charati, M. B.; Dorsey, S. M.; Wade, R. J.; Zellars, K. N.; Doviak, H.; Pettaway, S.; Logdon, C. B.; Shuman, J. A.; Freels, P. D.; Gorman III, J. H.; Gorman, R. C.; Spinale, F. G.; Burdick, J. A. Injectable and Bioresponsive Hydrogels for On-Demand Matrix Metalloproteinase Inhibition. *Nat. Mater.* **2014**, *13* (6), 653–661. https://doi.org/10.1038/nmat3922.

(10) Doronina, S. O.; Toki, B. E.; Torgov, M. Y.; Mendelsohn, B. A.; Cerveny, C. G.; Chace, D. F.; DeBlanc, R. L.; Gearing, R. P.; Bovee, T. D.; Siegall, C. B.; Francisco, J. A.; Wahl, A. F.; Meyer, D. L.; Senter, P. D. Development of Potent Monoclonal Antibody Auristatin Conjugates for Cancer Therapy. *Nat. Biotechnol.* **2003**, *21* (7), 778–784. https://doi.org/10.1038/nbt832.

(11) Kavanaugh, W. M. Antibody Prodrugs for Cancer. *Expert Opin. Biol. Ther.* **2020**, *20* (2), 163–171. https://doi.org/10.1080/14712598.2020.1699053.

(12) Desnoyers, L. R.; Vasiljeva, O.; Richardson, J. H.; Yang, A.; Menendez, E. E. M.; Liang, T. W.; Wong, C.; Bessette, P. H.; Kamath, K.; Moore, S. J.; Sagert, J. G.; Hostetter, D. R.; Han, F.; Gee, J.; Flandez, J.; Markham, K.; Nguyen, M.; Krimm, M.; Wong, K. R.; Liu, S.; Daugherty, P. S.; West, J. W.; Lowman, H. B. Tumor-Specific Activation of an EGFR-Targeting Probody Enhances Therapeutic Index. *Sci. Transl. Med.* **2013**. https://doi.org/10.1126/scitranslmed.3006682.

(13) Kwon, E. J.; Lo, J. H.; Bhatia, S. N. Smart Nanosystems: Bio-Inspired Technologies That Interact with the Host Environment. *Proc. Natl. Acad. Sci.* **2015**, *112* (47), 14460–14466. https://doi.org/10.1073/pnas.1508522112.

(14) Shi, J.; Kantoff, P. W.; Wooster, R.; Farokhzad, O. C. Cancer Nanomedicine: Progress, Challenges and Opportunities. *Nat. Rev. Cancer* **2017**, *17* (1), 20–37. https://doi.org/10.1038/nrc.2016.108.

(15) Anselmo, A. C.; Mitragotri, S. Nanoparticles in the Clinic. *Bioeng. Transl. Med.* **2016**, *1* (1), 10–29. https://doi.org/10.1002/btm2.10003.

(16) Attenello, F. J.; Mukherjee, D.; Datoo, G.; McGirt, M. J.; Bohan, E.; Weingart, J. D.; Olivi, A.; Quinones-Hinojosa, A.; Brem, H. Use of Gliadel (BCNU) Wafer in the Surgical Treatment of Malignant Glioma: A 10-Year Institutional Experience. *Ann. Surg. Oncol.* **2008**, *15* (10), 2887. https://doi.org/10.1245/s10434-008-0048-2.

(17) Safra, T.; Muggia, F.; Jeffers, S.; Tsao-Wei, D. D.; Groshen, S.; Lyass, O.; Henderson, R.; Berry, G.; Gabizon, A. Pegylated Liposomal Doxorubicin (Doxil): Reduced Clinical Cardiotoxicity in Patients Reaching or Exceeding Cumulative Doses of 500 Mg/M2. *Ann. Oncol.* **2000**, *11* (8), 1029–1034. https://doi.org/10.1023/A:1008365716693.

(18) Lyass, O.; Hubert, A.; Gabizon, A. A. Phase I Study of Doxil-Cisplatin Combination Chemotherapy in Patients with Advanced Malignancies. *Clin. Cancer Res.* **2001**, *7* (10), 3040–3046.

(19) Adams, D.; Gonzalez-Duarte, A.; O'Riordan, W. D.; Yang, C.-C.; Ueda, M.; Kristen, A. V.; Tournev, I.; Schmidt, H. H.; Coelho, T.; Berk, J. L.; Lin, K.-P.; Vita, G.; Attarian, S.; Planté-Bordeneuve, V.; Mezei, M. M.; Campistol, J. M.; Buades, J.; Brannagan, T. H.; Kim, B. J.; Oh, J.; Parman, Y.; Sekijima, Y.; Hawkins, P. N.; Solomon, S. D.; Polydefkis, M.; Dyck, P. J.; Gandhi, P. J.; Goyal, S.; Chen, J.; Strahs, A. L.; Nochur, S. V.; Sweetser, M. T.; Garg, P. P.; Vaishnaw, A. K.; Gollob, J. A.; Suhr, O. B. Patisiran, an RNAi Therapeutic, for Hereditary Transthyretin Amyloidosis. *N. Engl. J. Med.* **2018**, *379* (1), 11–21. https://doi.org/10.1056/NEJMoa1716153.

(20) Polack, F. P.; Thomas, S. J.; Kitchin, N.; Absalon, J.; Gurtman, A.; Lockhart, S.; Perez, J. L.; Pérez Marc, G.; Moreira, E. D.; Zerbini, C.; Bailey, R.; Swanson, K. A.; Roychoudhury, S.; Koury, K.; Li, P.; Kalina, W. V.; Cooper, D.; Frenck, R. W.; Hammitt, L. L.; Türeci, Ö.; Nell, H.; Schaefer, A.; Ünal, S.; Tresnan, D. B.; Mather, S.; Dormitzer, P. R.; Şahin, U.; Jansen, K. U.; Gruber, W. C. Safety and Efficacy of the BNT162b2 MRNA Covid-19 Vaccine. *N. Engl. J. Med.* **2020**, *383* (27), 2603–2615. https://doi.org/10.1056/NEJMoa2034577.

(21) Kulkarni, J. A.; Witzigmann, D.; Chen, S.; Cullis, P. R.; van der Meel, R. Lipid Nanoparticle Technology for Clinical Translation of SiRNA Therapeutics. *Acc. Chem. Res.* **2019**, *52* (9), 2435–2444. https://doi.org/10.1021/acs.accounts.9b00368.

(22) Daneman, R. The Blood–Brain Barrier in Health and Disease. *Ann. Neurol.* **2012**, *72* (5), 648–672. https://doi.org/10.1002/ana.23648.

(23) Pardridge, W. M. The Blood-Brain Barrier: Bottleneck in Brain Drug Development. *NeuroRX* **2005**, *2* (1), 3–14. https://doi.org/10.1602/neurorx.2.1.3.

(24) Kandell, R. M.; Waggoner, L. E.; Kwon, E. J. Nanomedicine for Acute Brain Injuries: Insight from Decades of Cancer Nanomedicine. *Mol. Pharm.* **2021**, *18* (2), 522–538. https://doi.org/10.1021/acs.molpharmaceut.0c00287.

(25) Quader, S.; Liu, X.; Toh, K.; Su, Y.-L.; Maity, A. R.; Tao, A.; Paraiso, W. K. D.; Mochida, Y.; Kinoh, H.; Cabral, H.; Kataoka, K. Supramolecularly Enabled PH- Triggered Drug Action at Tumor Microenvironment Potentiates Nanomedicine Efficacy against Glioblastoma. *Biomaterials* **2021**, *267*, 120463. https://doi.org/10.1016/j.biomaterials.2020.120463.

(26) Wu, H.; Lu, H.; Xiao, W.; Yang, J.; Du, H.; Shen, Y.; Qu, H.; Jia, B.; Manna, S. K.; Ramachandran, M.; Xue, X.; Ma, Z.; Xu, X.; Wang, Z.; He, Y.; Lam, K. S.; Zawadzki, R. J.; Li, Y.; Lin, T.-Y. Sequential Targeting in Crosslinking Nanotheranostics for Tackling the Multibarriers of Brain Tumors. *Adv. Mater.* **2020**, *32* (14), 1903759. https://doi.org/10.1002/adma.201903759.

(27) Jiang, L.; Zhou, Q.; Mu, K.; Xie, H.; Zhu, Y.; Zhu, W.; Zhao, Y.; Xu, H.; Yang, X. PH/Temperature Sensitive Magnetic Nanogels Conjugated with Cy5.5-Labled Lactoferrin for MR and Fluorescence Imaging of Glioma in Rats. *Biomaterials* **2013**, *34* (30), 7418–7428. https://doi.org/10.1016/j.biomaterials.2013.05.078.

(28) Huang, G.; Zhao, T.; Wang, C.; Nham, K.; Xiong, Y.; Gao, X.; Wang, Y.; Hao, G.; Ge, W.-P.; Sun, X.; Sumer, B. D.; Gao, J. PET Imaging of Occult Tumours by Temporal Integration of Tumour-Acidosis Signals from PH-Sensitive 64 Cu-Labelled Polymers. *Nat. Biomed. Eng.* **2020**, *4* (3), 314–324. https://doi.org/10.1038/s41551-019-0416-1.

(29) Ramírez-García, P. D.; Retamal, J. S.; Shenoy, P.; Imlach, W.; Sykes, M.; Truong, N.; Constandil, L.; Pelissier, T.; Nowell, C. J.; Khor, S. Y.; Layani, L. M.; Lumb, C.; Poole, D. P.; Lieu, T.; Stewart, G. D.; Mai, Q. N.; Jensen, D. D.; Latorre, R.; Scheff, N. N.; Schmidt, B. L.; Quinn, J. F.; Whittaker, M. R.; Veldhuis, N. A.; Davis, T. P.; Bunnett, N. W. A PH-Responsive Nanoparticle Targets the Neurokinin 1 Receptor in Endosomes to Prevent Chronic Pain. *Nat. Nanotechnol.* **2019**, *14* (12), 1150–1159. https://doi.org/10.1038/s41565-019-0568-x.

(30) Ruan, S.; Yuan, M.; Zhang, L.; Hu, G.; Chen, J.; Cun, X.; Zhang, Q.; Yang, Y.; He, Q.; Gao, H. Tumor Microenvironment Sensitive Doxorubicin Delivery and Release to Glioma Using Angiopep-2 Decorated Gold Nanoparticles. *Biomaterials* **2015**, *37*, 425–435. https://doi.org/10.1016/j.biomaterials.2014.10.007.

(31) Ruan, S.; Qin, L.; Xiao, W.; Hu, C.; Zhou, Y.; Wang, R.; Sun, X.; Yu, W.; He, Q.; Gao, H. Acid-Responsive Transferrin Dissociation and GLUT Mediated Exocytosis for Increased

Blood–Brain Barrier Transcytosis and Programmed Glioma Targeting Delivery. *Adv. Funct. Mater.* **2018**, *28* (30), 1802227. https://doi.org/10.1002/adfm.201802227.

(32) Rajkovic, O.; Gourmel, C.; d'Arcy, R.; Wong, R.; Rajkovic, I.; Tirelli, N.; Pinteaux, E. Reactive Oxygen Species-Responsive Nanoparticles for the Treatment of Ischemic Stroke. *Adv. Ther.* **2019**, *2* (7), 1900038. https://doi.org/10.1002/adtp.201900038.

(33) Yoo, D.; Magsam, A. W.; Kelly, A. M.; Stayton, P. S.; Kievit, F. M.; Convertine, A. J. Core-Cross-Linked Nanoparticles Reduce Neuroinflammation and Improve Outcome in a Mouse Model of Traumatic Brain Injury. *ACS Nano* **2017**, *11* (9), 8600–8611. https://doi.org/10.1021/acsnano.7b03426.

(34) Zhang, T.; Lin, F.; Liu, W.; Liu, Y.; Guo, Z.; Xiao, C.; Zhuang, X.; Chen, X. Reactive Oxide Species-Scavenging Lipid-Polymer Nanoparticles for Neuroprotection after Spinal Cord Injury. *Appl. Mater. Today* **2021**, *24*, 101109. https://doi.org/10.1016/j.apmt.2021.101109.

(35) Yang, L.; Yin, T.; Liu, Y.; Sun, J.; Zhou, Y.; Liu, J. Gold Nanoparticle-Capped Mesoporous Silica-Based H2O2-Responsive Controlled Release System for Alzheimer's Disease Treatment. *Acta Biomater.* **2016**, *46*, 177–190. https://doi.org/10.1016/j.actbio.2016.09.010.

(36) Geng, J.; Li, M.; Wu, L.; Chen, C.; Qu, X. Mesoporous Silica Nanoparticle-Based H2O2 Responsive Controlled-Release System Used for Alzheimer's Disease Treatment. *Adv. Healthc. Mater.* **2012**, *1* (3), 332–336. https://doi.org/10.1002/adhm.201200067.

(37) Lu, Y.; Guo, Z.; Zhang, Y.; Li, C.; Zhang, Y.; Guo, Q.; Chen, Q.; Chen, X.; He, X.; Liu, L.; Ruan, C.; Sun, T.; Ji, B.; Lu, W.; Jiang, C. Microenvironment Remodeling Micelles for Alzheimer's Disease Therapy by Early Modulation of Activated Microglia. *Adv. Sci.* **2019**, *6* (4), 1801586. https://doi.org/10.1002/advs.201801586.

(38) Lu, Y.; Li, C.; Chen, Q.; Liu, P.; Guo, Q.; Zhang, Y.; Chen, X.; Zhang, Y.; Zhou, W.; Liang, D.; Zhang, Y.; Sun, T.; Lu, W.; Jiang, C. Microthrombus-Targeting Micelles for Neurovascular Remodeling and Enhanced Microcirculatory Perfusion in Acute Ischemic Stroke. *Adv. Mater.* **2019**, *31* (21), 1808361. https://doi.org/10.1002/adma.201808361.

(39) Lv, W.; Xu, J.; Wang, X.; Li, X.; Xu, Q.; Xin, H. Bioengineered Boronic Ester Modified Dextran Polymer Nanoparticles as Reactive Oxygen Species Responsive Nanocarrier for Ischemic Stroke Treatment. *ACS Nano* **2018**, *12* (6), 5417–5426. https://doi.org/10.1021/acsnano.8b00477.

(40) Zheng, M.; Liu, Y.; Wang, Y.; Zhang, D.; Zou, Y.; Ruan, W.; Yin, J.; Tao, W.; Park, J. B.; Shi, B. ROS-Responsive Polymeric SiRNA Nanomedicine Stabilized by Triple Interactions for the Robust Glioblastoma Combinational RNAi Therapy. *Adv. Mater.* **2019**, *31* (37), 1903277. https://doi.org/10.1002/adma.201903277.

(41) Zou, Y.; Sun, X.; Wang, Y.; Yan, C.; Liu, Y.; Li, J.; Zhang, D.; Zheng, M.; Chung, R. S.; Shi, B. Single SiRNA Nanocapsules for Effective SiRNA Brain Delivery and Glioblastoma Treatment. *Adv. Mater.* **2020**, *32* (24), 2000416. https://doi.org/10.1002/adma.202000416.

(42) Hyun, H.; Lee, K.; Min, K. H.; Jeon, P.; Kim, K.; Jeong, S. Y.; Kwon, I. C.; Park, T. G.; Lee, M. Ischemic Brain Imaging Using Fluorescent Gold Nanoprobes Sensitive to Reactive Oxygen Species. *J. Controlled Release* **2013**, *170* (3), 352–357. https://doi.org/10.1016/j.jconrel.2013.06.002.

(43) Gu, G.; Xia, H.; Hu, Q.; Liu, Z.; Jiang, M.; Kang, T.; Miao, D.; Tu, Y.; Pang, Z.; Song, Q.; Yao, L.; Chen, H.; Gao, X.; Chen, J. PEG-Co-PCL Nanoparticles Modified with MMP-2/9 Activatable Low Molecular Weight Protamine for Enhanced Targeted Glioblastoma Therapy. *Biomaterials* **2013**, *34* (1), 196–208. https://doi.org/10.1016/j.biomaterials.2012.09.044.

(44) Xu, J.; Wang, X.; Yin, H.; Cao, X.; Hu, Q.; Lv, W.; Xu, Q.; Gu, Z.; Xin, H. Sequentially Site-Specific Delivery of Thrombolytics and Neuroprotectant for Enhanced Treatment of Ischemic Stroke. *ACS Nano* **2019**, *13* (8), 8577–8588. https://doi.org/10.1021/acsnano.9b01798.

(45) Ruan, S.; Hu, C.; Tang, X.; Cun, X.; Xiao, W.; Shi, K.; He, Q.; Gao, H. Increased Gold Nanoparticle Retention in Brain Tumors by in Situ Enzyme-Induced Aggregation. *ACS Nano* **2016**, *10* (11), 10086–10098. https://doi.org/10.1021/acsnano.6b05070.

(46) Ren, J.; Jiang, F.; Wang, M.; Hu, H.; Zhang, B.; Chen, L.; Dai, F. Increased Cross-Linking Micelle Retention in the Brain of Alzheimer's Disease Mice by Elevated Asparagine Endopeptidase Protease Responsive Aggregation. *Biomater. Sci.* **2020**, *8* (23), 6533–6544. https://doi.org/10.1039/D0BM01439G.

(47) Guo, X.; Deng, G.; Liu, J.; Zou, P.; Du, F.; Liu, F.; Chen, A. T.; Hu, R.; Li, M.; Zhang, S.; Tang, Z.; Han, L.; Liu, J.; Sheth, K. N.; Chen, Q.; Gou, X.; Zhou, J. Thrombin-Responsive, Brain-Targeting Nanoparticles for Improved Stroke Therapy. *ACS Nano* **2018**, *12* (8), 8723–8732. https://doi.org/10.1021/acsnano.8b04787.

(48) Zhang, S.; Deng, G.; Liu, F.; Peng, B.; Bao, Y.; Du, F.; Chen, A. T.; Liu, J.; Chen, Z.; Ma, J.; Tang, X.; Chen, Q.; Zhou, J. Autocatalytic Delivery of Brain Tumor–Targeting, Size-

Shrinkable Nanoparticles for Treatment of Breast Cancer Brain Metastases. *Adv. Funct. Mater.* **2020**, *30* (14), 1910651. https://doi.org/10.1002/adfm.201910651.

(49) Zhou, Y.; Zhang, S.; Chen, Z.; Bao, Y.; Chen, A. T.; Sheu, W. C.; Liu, F.; Jiang, Z.; Zhou, J. Targeted Delivery of Secretory Promelittin via Novel Poly(Lactone-Co-β-Amino Ester) Nanoparticles for Treatment of Breast Cancer Brain Metastases. *Adv. Sci.* **2020**, *7* (5), 1901866. https://doi.org/10.1002/advs.201901866.

(50) Han, L.; Liu, C.; Qi, H.; Zhou, J.; Wen, J.; Wu, D.; Xu, D.; Qin, M.; Ren, J.; Wang, Q.; Long, L.; Liu, Y.; Chen, I.; Yuan, X.; Lu, Y.; Kang, C. Systemic Delivery of Monoclonal Antibodies to the Central Nervous System for Brain Tumor Therapy. *Adv. Mater.* **2019**, *31* (19), 1805697. https://doi.org/10.1002/adma.201805697.

(51) Wang, Y.; Lin, T.; Zhang, W.; Jiang, Y.; Jin, H.; He, H.; Yang, V. C.; Chen, Y.; Huang, Y. A Prodrug-Type, MMP-2-Targeting Nanoprobe for Tumor Detection and Imaging. *Theranostics* **2015**, *5* (8), 787–795. https://doi.org/10.7150/thno.11139.

(52) Kudryashev, J. A.; Waggoner, L. E.; Leng, H. T.; Mininni, N. H.; Kwon, E. J. An Activity-Based Nanosensor for Traumatic Brain Injury. *ACS Sens.* **2020**, *5* (3), 686–692. https://doi.org/10.1021/acssensors.9b01812.

(53) Wang, Y.; Ying, X.; Chen, L.; Liu, Y.; Wang, Y.; Liang, J.; Xu, C.; Guo, Y.; Wang, S.; Hu, W.; Du, Y.; Chen, Z. Electroresponsive Nanoparticles Improve Antiseizure Effect of Phenytoin in Generalized Tonic-Clonic Seizures. *Neurotherapeutics* **2016**, *13* (3), 603–613. https://doi.org/10.1007/s13311-016-0431-9.

(54) Hua, L.; Wang, Z.; Zhao, L.; Mao, H.; Wang, G.; Zhang, K.; Liu, X.; Wu, D.; Zheng, Y.; Lu, J.; Yu, R.; Liu, H. Hypoxia-Responsive Lipid-Poly-(Hypoxic Radiosensitized Polyprodrug) Nanoparticles for Glioma Chemo- and Radiotherapy. *Theranostics* **2018**, *8* (18), 5088–5105. https://doi.org/10.7150/thno.26225.

(55) Liu, Y.; Lu, W. Recent Advances in Brain Tumor-Targeted Nano-Drug Delivery Systems. *Expert Opin. Drug Deliv.* **2012**, *9* (6), 671–686. https://doi.org/10.1517/17425247.2012.682726.

(56) Khan, A. R.; Yang, X.; Fu, M.; Zhai, G. Recent Progress of Drug Nanoformulations Targeting to Brain. *J. Controlled Release* **2018**, *291*, 37–64. https://doi.org/10.1016/J.JCONREL.2018.10.004.

(57) Furtado, D.; Björnmalm, M.; Ayton, S.; Bush, A. I.; Kempe, K.; Caruso, F. Overcoming the Blood–Brain Barrier: The Role of Nanomaterials in Treating Neurological Diseases. *Adv. Mater.* **2018**, *30* (46), 1801362. https://doi.org/10.1002/adma.201801362.

(58) Yu, Y. J.; Zhang, Y.; Kenrick, M.; Hoyte, K.; Luk, W.; Lu, Y.; Atwal, J.; Elliott, J. M.; Prabhu, S.; Watts, R. J.; Dennis, M. S. Boosting Brain Uptake of a Therapeutic Antibody by Reducing Its Affinity for a Transcytosis Target. *Sci. Transl. Med.* **2011**, *3* (84), 84ra44-84ra44. https://doi.org/10.1126/scitranslmed.3002230.

(59) Clark, A. J.; Davis, M. E. Increased Brain Uptake of Targeted Nanoparticles by Adding an Acid-Cleavable Linkage between Transferrin and the Nanoparticle Core. *Proc. Natl. Acad. Sci.* **2015**, *112* (40), 12486–12491.

(60) Aguilera, T. A.; Olson, E. S.; Timmers, M. M.; Jiang, T.; Tsien, R. Y. Systemic in Vivo Distribution of Activatable Cell Penetrating Peptides Is Superior to That of Cell Penetrating Peptides. *Integr. Biol.* **2009**, *1* (5–6), 371–381. https://doi.org/10.1039/b904878b.

(61) Gerweck, L. E.; Seetharaman, K. Cellular PH Gradient in Tumor versus Normal Tissue: Potential Exploitation for the Treatment of Cancer. *Cancer Res.* **1996**, *56* (6), 1194–1198.

(62) *Brain pH in Focal Cerebral Ischemia and the Protective Effects of Barbiturate Anesthesia - Robert E. Anderson, Thoralf M. Sundt, 1983*. https://journals.sagepub.com/doi/abs/10.1038/jcbfm.1983.76 (accessed 2021-07-05).

(63) Zhou, J.; Zhang, L.; Tian, Y. Micro Electrochemical PH Sensor Applicable for Real-Time Ratiometric Monitoring of PH Values in Rat Brains. *Anal. Chem.* **2016**, *88* (4), 2113–2118. https://doi.org/10.1021/acs.analchem.5b03634.

(64) Chesler, M. Regulation and Modulation of PH in the Brain. *Physiol. Rev.* **2003**, *83* (4), 1183–1221. https://doi.org/10.1152/physrev.00010.2003.

(65) Webb, B. A.; Chimenti, M.; Jacobson, M. P.; Barber, D. L. Dysregulated PH: A Perfect Storm for Cancer Progression. *Nat. Rev. Cancer* **2011**, *11* (9), 671–677. https://doi.org/10.1038/nrc3110.

(66) Corbet, C.; Feron, O. Tumour Acidosis: From the Passenger to the Driver's Seat. *Nat. Rev. Cancer* **2017**, *17* (10), 577–593. https://doi.org/10.1038/nrc.2017.77.

(67) Harris, R. J.; Yao, J.; Chakhoyan, A.; Raymond, C.; Leu, K.; Liau, L. M.; Nghiemphu, P. L.; Lai, A.; Salamon, N.; Pope, W. B.; Cloughesy, T. F.; Ellingson, B. M. Simultaneous PH-Sensitive and Oxygen-Sensitive MRI of Human Gliomas at 3 T Using Multi-Echo Amine Proton Chemical Exchange Saturation Transfer Spin-and-Gradient Echo Echo-Planar Imaging (CEST-SAGE-EPI). *Magn. Reson. Med.* **2018**, *80* (5), 1962–1978. https://doi.org/10.1002/mrm.27204.

(68) Korenchan, D. E.; Flavell, R. R. Spatiotemporal PH Heterogeneity as a Promoter of Cancer Progression and Therapeutic Resistance. *Cancers* **2019**, *11* (7), 1026. https://doi.org/10.3390/cancers11071026.

(69) Siesjö, B. K. Pathophysiology and Treatment of Focal Cerebral Ischemia. Part I: Pathophysiology. *J. Neurosurg.* **1992**, *77* (2), 169–184. https://doi.org/10.3171/jns.1992.77.2.0169.

(70) M Tóth, O.; Menyhárt, Á.; Frank, R.; Hantosi, D.; Farkas, E.; Bari, F. Tissue Acidosis Associated with Ischemic Stroke to Guide Neuroprotective Drug Delivery. *Biology* **2020**, *9* (12), E460. https://doi.org/10.3390/biology9120460.

(71) Timofeev, I.; Nortje, J.; Al-Rawi, P. G.; Hutchinson, P. J.; Gupta, A. K. Extracellular Brain Ph with or without Hypoxia Is a Marker of Profound Metabolic Derangement and Increased Mortality after Traumatic Brain Injury. *J. Cereb. Blood Flow Metab.* **2013**, *33* (3), 422–427. https://doi.org/10.1038/jcbfm.2012.186.

(72) Ellingson, B. M.; Yao, J.; Raymond, C.; Chakhoyan, A.; Khatibi, K.; Salamon, N.; Villablanca, J. P.; Wanner, I.; Real, C. R.; Laiwalla, A.; McArthur, D. L.; Monti, M. M.; Hovda, D. A.; Vespa, P. M. PH-Weighted Molecular MRI in Human Traumatic Brain Injury (TBI) Using Amine Proton Chemical Exchange Saturation Transfer Echoplanar Imaging (CEST EPI). *NeuroImage Clin.* **2019**, *22*, 101736. https://doi.org/10.1016/j.nicl.2019.101736.

(73) Yokota, H.; Yamamoto, Y.; Naoe, Y.; Fuse, A.; Sato, H.; Unemoto, K.; Kurokawa, A. Measurements of Cortical Cellular PH by Intracranial Tonometer in Severe Head Injury. *Crit. Care Med.* **2000**, *28* (9), 3275–3280.

(74) Alberts, B.; Johnson, A.; Lewis, J.; Raff, M.; Roberts, K.; Walter, P. Transport from the Trans Golgi Network to Lysosomes. *Mol. Biol. Cell 4th Ed.* **2002**.

(75) MacKay, J. A.; Li, W.; Huang, Z.; Dy, E. E.; Huynh, G.; Tihan, T.; Collins, R.; Deen, D. F.; Szoka, F. C. HIV TAT Peptide Modifies the Distribution of DNA Nanolipoparticles

Following Convection-Enhanced Delivery. *Mol. Ther. J. Am. Soc. Gene Ther.* **2008**, *16* (5), 893–900. https://doi.org/10.1038/mt.2008.36.

(76) Kim, A. J.; Woodworth, G. F.; Boylan, N. J.; Suk, J. S.; Hanes, J. Highly Compacted PH-Responsive DNA Nanoparticles Mediate Transgene Silencing in Experimental Glioma. *J. Mater. Chem. B* **2014**, *2* (46), 8165–8173. https://doi.org/10.1039/C4TB00559G.

(77) Rizwan, M.; Yahya, R.; Hassan, A.; Yar, M.; Azzahari, A. D.; Selvanathan, V.; Sonsudin, F.; Abouloula, C. N. PH Sensitive Hydrogels in Drug Delivery: Brief History, Properties, Swelling, and Release Mechanism, Material Selection and Applications. *Polymers* **2017**, *9* (4), 137. https://doi.org/10.3390/polym9040137.

(78) Ellgaard, L.; Sevier, C. S.; Bulleid, N. J. How Are Proteins Reduced in the Endoplasmic Reticulum? *Trends Biochem. Sci.* **2018**, *43* (1), 32–43. https://doi.org/10.1016/j.tibs.2017.10.006.

(79) Forman, H. J.; Zhang, H.; Rinna, A. Glutathione: Overview of Its Protective Roles, Measurement, and Biosynthesis. *Mol. Aspects Med.* **2009**, *30* (1–2), 1–12. https://doi.org/10.1016/j.mam.2008.08.006.

(80) L. O'Riordan, S.; Laughlin, K. M.; P. Lowry, J. In Vitro Physiological Performance Factors of a Catalase-Based Biosensor for Real-Time Electrochemical Detection of Brain Hydrogen Peroxide in Freely-Moving Animals. *Anal. Methods* **2016**, *8* (42), 7614–7622. https://doi.org/10.1039/C6AY02190E.

(81) Adibhatla, R. M.; Hatcher, J. F. Lipid Oxidation and Peroxidation in CNS Health and Disease: From Molecular Mechanisms to Therapeutic Opportunities. *Antioxid. Redox Signal.* **2010**, *12* (1), 125–169. https://doi.org/10.1089/ars.2009.2668.

(82) Li, W.; Yang, S. Targeting Oxidative Stress for the Treatment of Ischemic Stroke: Upstream and Downstream Therapeutic Strategies. *Brain Circ.* **2016**, *2* (4), 153–163. https://doi.org/10.4103/2394-8108.195279.

(83) Rodrigo, R.; Fernández-Gajardo, R.; Gutiérrez, R.; Matamala, J. M.; Carrasco, R.; Miranda-Merchak, A.; Feuerhake, W. Oxidative Stress and Pathophysiology of Ischemic Stroke: Novel Therapeutic Opportunities. *CNS Neurol. Disord. Drug Targets* **2013**, *12* (5), 698–714. https://doi.org/10.2174/18715273113120050015.

(84) Bordt, E. A.; Polster, B. M. NADPH Oxidase- and Mitochondria-Derived Reactive Oxygen Species in Proinflammatory Microglial Activation: A Bipartisan Affair? *Free Radic. Biol. Med.* **2014**, *76*, 34–46. https://doi.org/10.1016/j.freeradbiomed.2014.07.033.

(85) Simon, D. W.; McGeachy, M. J.; Bayır, H.; Clark, R. S. B.; Loane, D. J.; Kochanek, P. M. The Far-Reaching Scope of Neuroinflammation after Traumatic Brain Injury. *Nat. Rev. Neurol.* **2017**, *13* (3), 171–191. https://doi.org/10.1038/nrneurol.2017.13.

(86) Chen, R.; Lai, U. H.; Zhu, L.; Singh, A.; Ahmed, M.; Forsyth, N. R. Reactive Oxygen Species Formation in the Brain at Different Oxygen Levels: The Role of Hypoxia Inducible Factors. *Front. Cell Dev. Biol.* **2018**, *6*, 132. https://doi.org/10.3389/fcell.2018.00132.

(87) Selakovic, V.; Korenic, A.; Radenovic, L. Spatial and Temporal Patterns of Oxidative Stress in the Brain of Gerbils Submitted to Different Duration of Global Cerebral Ischemia. *Int. J. Dev. Neurosci.* **2011**, *29* (6), 645–654. https://doi.org/10.1016/j.ijdevneu.2011.02.009.

(88) Yang, J.; Qi, J.; Xiu, B.; Yang, B.; Niu, C.; Yang, H. Reactive Oxygen Species Play a Biphasic Role in Brain Ischemia. *J. Invest. Surg.* **2019**, *32* (2), 97–102. https://doi.org/10.1080/08941939.2017.1376131.

(89) Kapoor, M.; Sharma, S.; Sandhir, R.; Nehru, B. Temporal Changes in Physiological and Molecular Markers in Various Brain Regions Following Transient Global Ischemia in Rats. *Mol. Biol. Rep.* **2019**, *46* (6), 6215–6230. https://doi.org/10.1007/s11033-019-05060-7.

(90) Azbill, R. D.; Mu, X.; Bruce-Keller, A. J.; Mattson, M. P.; Springer, J. E. Impaired Mitochondrial Function, Oxidative Stress and Altered Antioxidant Enzyme Activities Following Traumatic Spinal Cord Injury. *Brain Res.* **1997**, *765* (2), 283–290. https://doi.org/10.1016/s0006-8993(97)00573-8.

(91) Rodríguez-Rodríguez, A.; Egea-Guerrero, J. J.; Murillo-Cabezas, F.; Carrillo-Vico, A. Oxidative Stress in Traumatic Brain Injury. *Curr. Med. Chem.* **2014**, *21* (10), 1201–1211. https://doi.org/10.2174/09298673216661312171533l0.

(92) Smith, S. L.; Andrus, P. K.; Zhang, J.-R.; Hall, E. D. Direct Measurement of Hydroxyl Radicals, Lipid Peroxidation, and Blood–Brain Barrier Disruption Following Unilateral Cortical Impact Head Injury in the Rat. *J. Neurotrauma* **1994**, *11* (4), 393–404. https://doi.org/10.1089/neu.1994.11.393.

(93) Manoharan, S.; Guillemin, G. J.; Abiramasundari, R. S.; Essa, M. M.; Akbar, M.; Akbar, M. D. The Role of Reactive Oxygen Species in the Pathogenesis of Alzheimer's Disease, Parkinson's Disease, and Huntington's Disease: A Mini Review. *Oxid. Med. Cell. Longev.* **2016**, *2016*, 8590578. https://doi.org/10.1155/2016/8590578.

(94) Wu, G.; Fang, Y.-Z.; Yang, S.; Lupton, J. R.; Turner, N. D. Glutathione Metabolism and Its Implications for Health. *J. Nutr.* **2004**, *134* (3), 489–492. https://doi.org/10.1093/jn/134.3.489.

(95) Gamcsik, M. P.; Kasibhatla, M. S.; Teeter, S. D.; Colvin, O. M. Glutathione Levels in Human Tumors. *Biomark. Biochem. Indic. Expo. Response Susceptibility Chem.* **2012**, *17* (8), 671–691. https://doi.org/10.3109/1354750X.2012.715672.

(96) Kennedy, L.; Sandhu, J. K.; Harper, M.-E.; Cuperlovic-Culf, M. Role of Glutathione in Cancer: From Mechanisms to Therapies. *Biomolecules* **2020**, *10* (10), E1429. https://doi.org/10.3390/biom10101429.

(97) Wood, H. FDA Approves Patisiran to Treat Hereditary Transthyretin Amyloidosis. *Nat. Rev. Neurol.* **2018**, *14* (10), 570–570. https://doi.org/10.1038/s41582-018-0065-0.

(98) Lo, J. H.; Kwon, E. J.; Zhang, A. Q.; Singhal, P.; Bhatia, S. N. Comparison of Modular PEG Incorporation Strategies for Stabilization of Peptide–SiRNA Nanocomplexes. *Bioconjug. Chem.* **2016**, *27* (10), 2323–2331. https://doi.org/10.1021/acs.bioconjchem.6b00304.

(99) Lee, H.; Lee, K.; Kim, I. K.; Park, T. G. Synthesis, Characterization, and in Vivo Diagnostic Applications of Hyaluronic Acid Immobilized Gold Nanoprobes. *Biomaterials* **2008**, *29* (35), 4709–4718. https://doi.org/10.1016/j.biomaterials.2008.08.038.

(100) Rawlings, N. D.; Barrett, A. J.; Thomas, P. D.; Huang, X.; Bateman, A.; Finn, R. D. The MEROPS Database of Proteolytic Enzymes, Their Substrates and Inhibitors in 2017 and a Comparison with Peptidases in the PANTHER Database. *Nucleic Acids Res.* **2018**, *46* (D1), D624–D632. https://doi.org/10.1093/nar/gkx1134.

(101) López-Otín, C.; Bond, J. S. Proteases: Multifunctional Enzymes in Life and Disease. *J. Biol. Chem.* **2008**, *283* (45), 30433–30437. https://doi.org/10.1074/jbc.R800035200.

(102) Jiang, T.; Olson, E. S.; Nguyen, Q. T.; Roy, M.; Jennings, P. A.; Tsien, R. Y. Tumor Imaging by Means of Proteolytic Activation of Cell-Penetrating Peptides. *Proc. Natl. Acad. Sci.* **2004**, *101* (51), 17867–17872. https://doi.org/10.1073/pnas.0408191101.

(103) Harris, T. J.; Maltzahn, G. von; Derfus, A. M.; Ruoslahti, E.; Bhatia, S. N. Proteolytic Actuation of Nanoparticle Self-Assembly. *Angew. Chem. Int. Ed.* **2006**, *45* (19), 3161–3165. https://doi.org/10.1002/anie.200600259.

(104) Wong, C.; Stylianopoulos, T.; Cui, J.; Martin, J.; Chauhan, V. P.; Jiang, W.; Popović, Z.; Jain, R. K.; Bawendi, M. G.; Fukumura, D. Multistage Nanoparticle Delivery System for Deep Penetration into Tumor Tissue. *Proc. Natl. Acad. Sci.* **2011**, *108* (6), 2426–2431. https://doi.org/10.1073/pnas.1018382108.

(105) Lo, E. H.; Wang, X.; Cuzner, M. L. Extracellular Proteolysis in Brain Injury and Inflammation: Role for Plasminogen Activators and Matrix Metalloproteinases. *J. Neurosci. Res.* **2002**, *69* (1), 1–9. https://doi.org/10.1002/jnr.10270.

(106) Rosenberg, G. A. Matrix Metalloproteinases and Their Multiple Roles in Neurodegenerative Diseases. *Lancet Neurol.* **2009**, *8* (2), 205–216. https://doi.org/10.1016/S1474-4422(09)70016-X.

(107) Rao, J. S. Molecular Mechanisms of Glioma Invasiveness: The Role of Proteases. *Nat. Rev. Cancer* **2003**, *3* (7), 489–501. https://doi.org/10.1038/nrc1121.

(108) Forsyth, P. A.; Wong, H.; Laing, T. D.; Rewcastle, N. B.; Morris, D. G.; Muzik, H.; Leco, K. J.; Johnston, R. N.; Brasher, P. M. A.; Sutherland, G.; Edwards, D. R. Gelatinase-A (MMP-2), Gelatinase-B (MMP-9) and Membrane Type Matrix Metalloproteinase-1 (MT1-MMP) Are Involved in Different Aspects of the Pathophysiology of Malignant Gliomas. *Br. J. Cancer* **1999**, *79* (11), 1828–1835. https://doi.org/10.1038/sj.bjc.6990291.

(109) Wang, M.; Wang, T.; Liu, S.; Yoshida, D.; Teramoto, A. The Expression of Matrix Metalloproteinase-2 and-9 in Human Gliomas of Different Pathological Grades. *Brain Tumor Pathol.* **2003**, *20* (2), 65–72. https://doi.org/10.1007/BF02483449.

(110) Rosell Anna; Ortega-Aznar Arantxa; Alvarez-Sabín José; Fernández-Cadenas Israel; Ribó Marc; Molina Carlos A.; Lo Eng H.; Montaner Joan. Increased Brain Expression of Matrix Metalloproteinase-9 After Ischemic and Hemorrhagic Human Stroke. *Stroke* **2006**, *37* (6), 1399–1406. https://doi.org/10.1161/01.STR.0000223001.06264.af.

(111) Tejima, E.; Zhao, B.-Q.; Tsuji, K.; Rosell, A.; van Leyen, K.; Gonzalez, R. G.; Montaner, J.; Wang, X.; Lo, E. H. Astrocytic Induction of Matrix Metalloproteinase-9 and Edema in Brain Hemorrhage. *J. Cereb. Blood Flow Metab.* **2007**, *27* (3), 460–468. https://doi.org/10.1038/sj.jcbfm.9600354.

(112) Gidday, J. M.; Gasche, Y. G.; Copin, J.-C.; Shah, A. R.; Perez, R. S.; Shapiro, S. D.; Chan, P. H.; Park, T. S. Leukocyte-Derived Matrix Metalloproteinase-9 Mediates Blood-Brain Barrier Breakdown and Is Proinflammatory after Transient Focal Cerebral Ischemia. *Am. J. Physiol.-Heart Circ. Physiol.* **2005**, *289* (2), H558–H568. https://doi.org/10.1152/ajpheart.01275.2004.

(113) Justicia, C.; Panés, J.; Solé, S.; Cervera, Á.; Deulofeu, R.; Chamorro, Á.; Planas, A. M. Neutrophil Infiltration Increases Matrix Metalloproteinase-9 in the Ischemic Brain after Occlusion/Reperfusion of the Middle Cerebral Artery in Rats. *J. Cereb. Blood Flow Metab.* **2003**, *23* (12), 1430–1440. https://doi.org/10.1097/01.WCB.0000090680.07515.C8.

(114) Vilalta, A.; Sahuquillo, J.; Poca, M. A.; De Los Rios, J.; Cuadrado, E.; Ortega-Aznar, A.; Riveiro, M.; Montaner, J. Brain Contusions Induce a Strong Local Overexpression of MMP-9. Results of a Pilot Study. In *Acta Neurochirurgica Supplements*; Steiger, H.-J., Ed.; Acta Neurochirurgica Supplementum; Springer: Vienna, 2009; pp 415–419. https://doi.org/10.1007/978-3-211-85578-2_81.

(115) Simon, D.; Evaldt, J.; Nabinger, D. D.; Fontana, M. F.; Klein, M. G.; Gomes, J. do A.; Regner, A. Plasma Matrix Metalloproteinase-9 Levels Predict Intensive Care Unit Mortality Early after Severe Traumatic Brain Injury. *Brain Inj.* **2017**, *31* (3), 390–395. https://doi.org/10.1080/02699052.2016.1259501.

(116) Zhao, B.-Q.; Wang, S.; Kim, H.-Y.; Storrie, H.; Rosen, B. R.; Mooney, D. J.; Wang, X.; Lo, E. H. Role of Matrix Metalloproteinases in Delayed Cortical Responses after Stroke. *Nat. Med.* **2006**, *12* (4), 441–445. https://doi.org/10.1038/nm1387.

(117) Sato, T.; Takahashi, S.; Mizumoto, T.; Harao, M.; Akizuki, M.; Takasugi, M.; Fukutomi, T.; Yamashita, J. Neutrophil Elastase and Cancer. *Surg. Oncol.* **2006**, *15* (4), 217–222. https://doi.org/10.1016/j.suronc.2007.01.003.

(118) Semple, B. D.; Trivedi, A.; Gimlin, K.; Noble-Haeusslein, L. J. Neutrophil Elastase Mediates Acute Pathogenesis and Is a Determinant of Long-Term Behavioral Recovery after Traumatic Injury to the Immature Brain. *Neurobiol. Dis.* **2015**, *74*, 263–280. https://doi.org/10.1016/j.nbd.2014.12.003.

(119) Stowe, A. M.; Adair-Kirk, T. L.; Gonzales, E. R.; Perez, R. S.; Shah, A. R.; Park, T. S.; Gidday, J. M. Neutrophil Elastase and Neurovascular Injury Following Focal Stroke and Reperfusion. *Neurobiol. Dis.* **2009**, *35* (1), 82–90. https://doi.org/10.1016/j.nbd.2009.04.006.

(120) Ma, L.; Shen, Y.-Q.; Khatri, H. P.; Schachner, M. The Asparaginyl Endopeptidase Legumain Is Essential for Functional Recovery after Spinal Cord Injury in Adult Zebrafish. *PLoS ONE* **2014**, *9* (4). https://doi.org/10.1371/journal.pone.0095098.

(121) Dall, E.; Brandstetter, H. Structure and Function of Legumain in Health and Disease. *Biochimie* **2016**, *122*, 126–150. https://doi.org/10.1016/j.biochi.2015.09.022.

(122) Liu, C.; Sun, C.; Huang, H.; Janda, K.; Edgington, T. Overexpression of Legumain in Tumors Is Significant for Invasion/Metastasis and a Candidate Enzymatic Target for Prodrug Therapy. *Cancer Res.* **2003**, *63* (11), 2957–2964.

(123) Ishizaki, T.; Erickson, A.; Kuric, E.; Shamloo, M.; Hara-Nishimura, I.; Inácio, A. R. L.; Wieloch, T.; Ruscher, K. The Asparaginyl Endopeptidase Legumain after Experimental Stroke. *J. Cereb. Blood Flow Metab.* **2010**, *30* (10), 1756–1766. https://doi.org/10.1038/jcbfm.2010.39.

(124) Basurto-Islas, G.; Grundke-Iqbal, I.; Tung, Y. C.; Liu, F.; Iqbal, K. Activation of Asparaginyl Endopeptidase Leads to Tau Hyperphosphorylation in Alzheimer Disease*. *J. Biol. Chem.* **2013**, *288* (24), 17495–17507. https://doi.org/10.1074/jbc.M112.446070.

(125) Knoblach, S. M.; Faden, A. I. Proteases in Traumatic Brain Injury. In *Proteases In The Brain*; Lendeckel, U., Hooper, N. M., Eds.; Proteases In Biology and Disease; Springer-Verlag: Berlin/Heidelberg, 2005; Vol. 3, pp 79–108. https://doi.org/10.1007/0-387-23101-3_4.

(126) Vafadari, B.; Salamian, A.; Kaczmarek, L. MMP-9 in Translation: From Molecule to Brain Physiology, Pathology, and Therapy. *J. Neurochem.* **2016**, *139*, 91–114. https://doi.org/10.1111/jnc.13415.

(127) Xi, G.; Reiser, G.; Keep, R. F. The Role of Thrombin and Thrombin Receptors in Ischemic, Hemorrhagic and Traumatic Brain Injury: Deleterious or Protective? *J. Neurochem.* **2002**, *84* (1), 3–9. https://doi.org/10.1046/j.1471-4159.2003.01268.x.

(128) Liu, J.; Liu, M. C.; Wang, K. K. W. Calpain in the CNS: From Synaptic Function to Neurotoxicity. *Sci. Signal.* **2008**, *1* (14), re1–re1. https://doi.org/10.1126/stke.114re1.

(129) Chen Bo; Cheng Qun; Yang Kai; Lyden Patrick D. Thrombin Mediates Severe Neurovascular Injury During Ischemia. *Stroke* **2010**, *41* (10), 2348–2352. https://doi.org/10.1161/STROKEAHA.110.584920.

(130) Chen, B.; Friedman, B.; Whitney, M. A.; Winkle, J. A. V.; Lei, I.-F.; Olson, E. S.; Cheng, Q.; Pereira, B.; Zhao, L.; Tsien, R. Y.; Lyden, P. D. Thrombin Activity Associated with Neuronal Damage during Acute Focal Ischemia. *J. Neurosci.* **2012**, *32* (22), 7622–7631. https://doi.org/10.1523/JNEUROSCI.0369-12.2012.

(131) Saatman, K. E.; Creed, J.; Raghupathi, R. Calpain as a Therapeutic Target in Traumatic Brain Injury. *Neurotherapeutics* **2010**, *7* (1), 31–42. https://doi.org/10.1016/j.nurt.2009.11.002.

(132) Bevers, M. B.; Neumar, R. W. Mechanistic Role of Calpains in Postischemic Neurodegeneration. *J. Cereb. Blood Flow Metab. Off. J. Int. Soc. Cereb. Blood Flow Metab.* **2008**, *28* (4), 655–673. https://doi.org/10.1038/sj.jcbfm.9600595.

(133) Zhang, Z.; Larner, S. F.; Liu, M. C.; Zheng, W.; Hayes, R. L.; Wang, K. K. W. Multiple AlphaII-Spectrin Breakdown Products Distinguish Calpain and Caspase Dominated Necrotic and Apoptotic Cell Death Pathways. *Apoptosis* **2009**, *14* (11), 1289–1298. https://doi.org/10.1007/s10495-009-0405-z.

(134) Levesque, S.; Wilson, B.; Gregoria, V.; Thorpe, L. B.; Dallas, S.; Polikov, V. S.; Hong, J. S.; Block, M. L. Reactive Microgliosis: Extracellular-Calpain and Microglia-Mediated Dopaminergic Neurotoxicity. *Brain* **2010**, *133* (3), 808–821. https://doi.org/10.1093/brain/awp333.

(135) Zhao Bing-Qiao; Tejima Emiri; Lo Eng H. Neurovascular Proteases in Brain Injury, Hemorrhage and Remodeling After Stroke. *Stroke* **2007**, *38* (2), 748–752. https://doi.org/10.1161/01.STR.0000253500.32979.d1.

(136) Zhang, X.-X.; Eden, H. S.; Chen, X. Peptides in Cancer Nanomedicine: Drug Carriers, Targeting Ligands and Protease Substrates. *J. Controlled Release* **2012**, *159* (1), 2–13. https://doi.org/10.1016/j.jconrel.2011.10.023.

(137) Nance, E. A.; Woodworth, G. F.; Sailor, K. A.; Shih, T.-Y.; Xu, Q.; Swaminathan, G.; Xiang, D.; Eberhart, C.; Hanes, J. A Dense Poly(Ethylene Glycol) Coating Improves Penetration of Large Polymeric Nanoparticles Within Brain Tissue. *Sci. Transl. Med.* **2012**, *4* (149), 149ra119-149ra119. https://doi.org/10.1126/scitranslmed.3003594.

(138) Selvin, P. R. The Renaissance of Fluorescence Resonance Energy Transfer. *Nat. Struct. Biol.* **2000**, *7* (9), 730–734. https://doi.org/10.1038/78948.

(139) Svirskis, D.; Travas-Sejdic, J.; Rodgers, A.; Garg, S. Electrochemically Controlled Drug Delivery Based on Intrinsically Conducting Polymers. *J. Controlled Release* **2010**, *146* (1), 6–15. https://doi.org/10.1016/j.jconrel.2010.03.023.

(140) Ge, J.; Neofytou, E.; Cahill, T. J.; Beygui, R. E.; Zare, R. N. Drug Release from Electric-Field-Responsive Nanoparticles. *ACS Nano* **2012**, *6* (1), 227–233. https://doi.org/10.1021/nn203430m.

(141) Carreau, A.; Hafny-Rahbi, B. E.; Matejuk, A.; Grillon, C.; Kieda, C. Why Is the Partial Oxygen Pressure of Human Tissues a Crucial Parameter? Small Molecules and Hypoxia. *J. Cell. Mol. Med.* **2011**, *15* (6), 1239–1253. https://doi.org/10.1111/j.1582-4934.2011.01258.x.

(142) Edwards, D. I. Nitroimidazole Drugs-Action and Resistance Mechanisms I. Mechanism of Action. *J. Antimicrob. Chemother.* **1993**, *31* (1), 9–20. https://doi.org/10.1093/jac/31.1.9.

(143) Whitley, M. J.; Cardona, D. M.; Lazarides, A. L.; Spasojevic, I.; Ferrer, J. M.; Cahill, J.; Lee, C.-L.; Snuderl, M.; Blazer, D. G.; Hwang, E. S.; Greenup, R. A.; Mosca, P. J.; Mito, J. K.; Cuneo, K. C.; Larrier, N. A.; O'Reilly, E. K.; Riedel, R. F.; Eward, W. C.; Strasfeld, D. B.; Fukumura, D.; Jain, R. K.; Lee, W. D.; Griffith, L. G.; Bawendi, M. G.; Kirsch, D. G.; Brigman, B. E. A Mouse-Human Phase 1 Co-Clinical Trial of a Protease-Activated Fluorescent Probe for Imaging Cancer. *Sci. Transl. Med.* **2016**, *8* (320), 320ra4-320ra4. https://doi.org/10.1126/scitranslmed.aad0293.

(144) Akinc, A.; Maier, M. A.; Manoharan, M.; Fitzgerald, K.; Jayaraman, M.; Barros, S.; Ansell, S.; Du, X.; Hope, M. J.; Madden, T. D.; Mui, B. L.; Semple, S. C.; Tam, Y. K.; Ciufolini, M.; Witzigmann, D.; Kulkarni, J. A.; van der Meel, R.; Cullis, P. R. The Onpattro Story and the Clinical Translation of Nanomedicines Containing Nucleic Acid-Based Drugs. *Nat. Nanotechnol.* **2019**, *14* (12), 1084–1087. https://doi.org/10.1038/s41565-019-0591-y.

(145) Horstmann, S.; Kalb, P.; Koziol, J.; Gardner, H.; Wagner, S. Profiles of Matrix Metalloproteinases, Their Inhibitors, and Laminin in Stroke Patients. *Stroke* **2003**, *34* (9), 2165–2170. https://doi.org/10.1161/01.STR.0000088062.86084.F2.

(146) Vilalta, A.; Sahuquillo, J.; Rosell, A.; Poca, M. A.; Riveiro, M.; Montaner, J. Moderate and Severe Traumatic Brain Injury Induce Early Overexpression of Systemic and Brain Gelatinases. *Intensive Care Med.* **2008**, *34* (8), 1384–1392. https://doi.org/10.1007/s00134-008-1056-1.

(147) Badeau, B. A.; Comerford, M. P.; Arakawa, C. K.; Shadish, J. A.; DeForest, C. A. Engineered Modular Biomaterial Logic Gates for Environmentally Triggered Therapeutic Delivery. *Nat. Chem.* **2018**, *10* (3), 251–258. https://doi.org/10.1038/nchem.2917.

(148) Badeau, B. A.; DeForest, C. A. Programming Stimuli-Responsive Behavior into Biomaterials. *Annu. Rev. Biomed. Eng.* **2019**, *21* (1), 241–265. https://doi.org/10.1146/annurev-bioeng-060418-052324.

(149) Hajipour, M. J.; Aghaverdi, H.; Serpooshan, V.; Vali, H.; Sheibani, S.; Mahmoudi, M. Sex as an Important Factor in Nanomedicine. *Nat. Commun.* **2021**, *12* (1), 2984. https://doi.org/10.1038/s41467-021-23230-9.

(150) Wood, T.; Nance, E. Disease-Directed Engineering for Physiology-Driven Treatment Interventions in Neurological Disorders. *APL Bioeng.* **2019**, *3* (4), 040901. https://doi.org/10.1063/1.5117299.

(151) Tower, J.; Pomatto, L. C. D.; Davies, K. J. A. Sex Differences in the Response to Oxidative and Proteolytic Stress. *Redox Biol.* **2020**, *31*, 101488. https://doi.org/10.1016/j.redox.2020.101488.

(152) Malorni, W.; Campesi, I.; Straface, E.; Vella, S.; Franconi, F. Redox Features of the Cell: A Gender Perspective. *Antioxid. Redox Signal.* **2007**, *9* (11), 1779–1802. https://doi.org/10.1089/ars.2007.1596.

(153) Simpkins, J. W.; Dykens, J. A. Mitochondrial Mechanisms of Estrogen Neuroprotection. *Brain Res. Rev.* **2008**, *57* (2), 421–430. https://doi.org/10.1016/j.brainresrev.2007.04.007.

(154) Appelros, P.; Stegmayr, B.; Terént, A. Sex Differences in Stroke Epidemiology. *Stroke* **2009**, *40* (4), 1082–1090. https://doi.org/10.1161/STROKEAHA.108.540781.

(155) Guevara, R.; Gianotti, M.; Oliver, J.; Roca, P. Age and Sex-Related Changes in Rat Brain Mitochondrial Oxidative Status. *Exp. Gerontol.* **2011**, *46* (11), 923–928. https://doi.org/10.1016/j.exger.2011.08.003.

(156) Bharadwaj, V. N.; Copeland, C.; Mathew, E.; Newbern, J.; Anderson, T. R.; Lifshitz, J.; Kodibagkar, V. D.; Stabenfeldt, S. E. Sex-Dependent Macromolecule and Nanoparticle Delivery in Experimental Brain Injury. *Tissue Eng. Part A* **2020**, *26* (13–14), 688–701. https://doi.org/10.1089/ten.tea.2020.0040.

(157) Zagni, E.; Simoni, L.; Colombo, D. Sex and Gender Differences in Central Nervous System-Related Disorders. *Neurosci. J.* **2016**, *2016*, 1–13. https://doi.org/10.1155/2016/2827090.

(158) Mitchell, M. J.; Billingsley, M. M.; Haley, R. M.; Wechsler, M. E.; Peppas, N. A.; Langer, R. Engineering Precision Nanoparticles for Drug Delivery. *Nat. Rev. Drug Discov.* **2021**, *20* (2), 101–124. https://doi.org/10.1038/s41573-020-0090-8.

CHAPTER 2. AN ACTIVITY-BASED NANOSENSOR FOR TRAUMATIC BRAIN INJURY

2.1. Abstract

Currently, traumatic brain injury (TBI) is detected by medical imaging; however, medical imaging requires expensive capital equipment, is time- and resource-intensive, and is poor at predicting patient prognosis. To date, direct measurement of elevated protease activity has yet to be utilized to detect TBI. In this work, we engineered an activity-based nanosensor for TBI (TBI-ABN) that responds to increased protease activity initiated after brain injury. We establish that a calcium-sensitive protease, calpain-1, is active in the injured brain hours within injury. We then optimize the molecular weight of a nanoscale polymeric carrier to infiltrate into injured brain tissue with minimal renal filtration. A calpain-1 substrate that generates a fluorescent signal upon cleavage was attached to this nanoscale polymeric carrier to generate an engineered TBI-ABN. When applied intravenously to a mouse model of TBI, our engineered sensor is observed to locally activate in the injured brain tissue. This TBI-ABN is the first demonstration of a sensor that responds to protease activity to detect TBI.

2.2. Introduction

Traumatic brain injury (TBI) affects over 2.8 million people annually in the United States and leads to the hospitalization of ~300 000 patients per year.[1] Among TBI patients who require surgical intervention, there is a 50% lower mortality rate and decreased length of stay if they receive surgery within 4 h of hospital admission,[2] indicating the importance of rapid diagnosis and triage to improve outcomes. However, current diagnosis is achieved by medical imaging, typically computed tomography (CT) and magnetic resonance imaging (MRI), both of which are

time- and resource-intensive and have a limited ability to predict patient prognosis.[3] Moreover, while medical imaging can identify macroscopic structural deformations in the brain, it currently does not yield information on the destructive biological activity that may unfold after injury. This secondary injury, which may include sustained protease activity, inflammation, excitotoxicity, and neuronal death, begins immediately after the primary injury and may lead to chronic neurodegeneration and a poorer patient prognosis.[4] Thus, a diagnostic that yields information on biological activity may inform improved clinical care.

Breakdown products shed into the blood and cerebrospinal fluid have been recently investigated as biomarkers to detect pathological processes in TBI.[5] These breakdown products originate from the degradation of nervous tissue as part of a prolonged secondary injury that begins within minutes after TBI.[6] To date, there is only one TBI biomarker-based diagnostic on the market; it is based on two separate enzyme-linked immunosorbent assays (ELISAs) to measure serum levels of the breakdown products glial fibrillary acidic protein (GFAP) and ubiquitin C-terminal hydrolase L1 (UCH-L1).[7] However, measurement of these biomarkers relies on the generation, stability, and transport of these byproducts;[8] direct measurement of degradative activity may be more representative of disease and therefore provide information that is more actionable for intervention. Calpain-1, a calcium-dependent protease expressed in neurons, glia, and endothelial cells within the brain, undergoes sustained activation after TBI due to pathological elevations of intracellular calcium.[6,9,10] Calpain-1 activity generates many breakdown products that are currently under investigation as biomarkers for TBI, including myelin basic protein, neurofilaments, and αII-spectrin.[5] Calpain-1 inhibition has been under investigation as a treatment for TBI,[11] and its byproducts can potentially predict patient prognosis after mild and severe TBI,[12,13] highlighting the importance of calpain-1 in the injury

sequelae and its prognostic potential. Thus, the detection of calpain-1 protease activity is a promising candidate for TBI diagnosis.

To explore the potential of activity-based sensors to detect TBI, our goal was to engineer a vascularly administered sensor that can accumulate in the injured brain tissue and produce a signal in response to calpain-1 activity (Figure 2.1A). A similar activity-based sensor strategy has been demonstrated for the sensitive detection of cancer and liver fibrosis in previous works,[14,15] but has yet to be applied to any brain disorders. First, we established increased calpain-1 activity that is independent of calpain-1 expression levels in the first few hours after TBI in mice, validating the need for a sensor of enzyme activity rather than enzyme levels. To engineer a diagnostic that can be delivered into the vasculature, we exploit the size-dependent accumulation of nanoscale polymeric carriers into the site of injury, where the blood–brain barrier (BBB) is compromised and allows extravasation of nanoscale materials. To detect calpain-1 activity, we engineered a fluorescent resonance energy-transfer (FRET) peptide, which activates in the presence of active calpain-1. Combining the peptide and carrier, we engineered a TBI activity-based nanosensor (TBI-ABN). This TBI-ABN activates at the site of injury in a mouse model of brain injury after intravenous administration. To our knowledge, TBI-ABN is the first demonstration of an activity-based sensor for TBI.

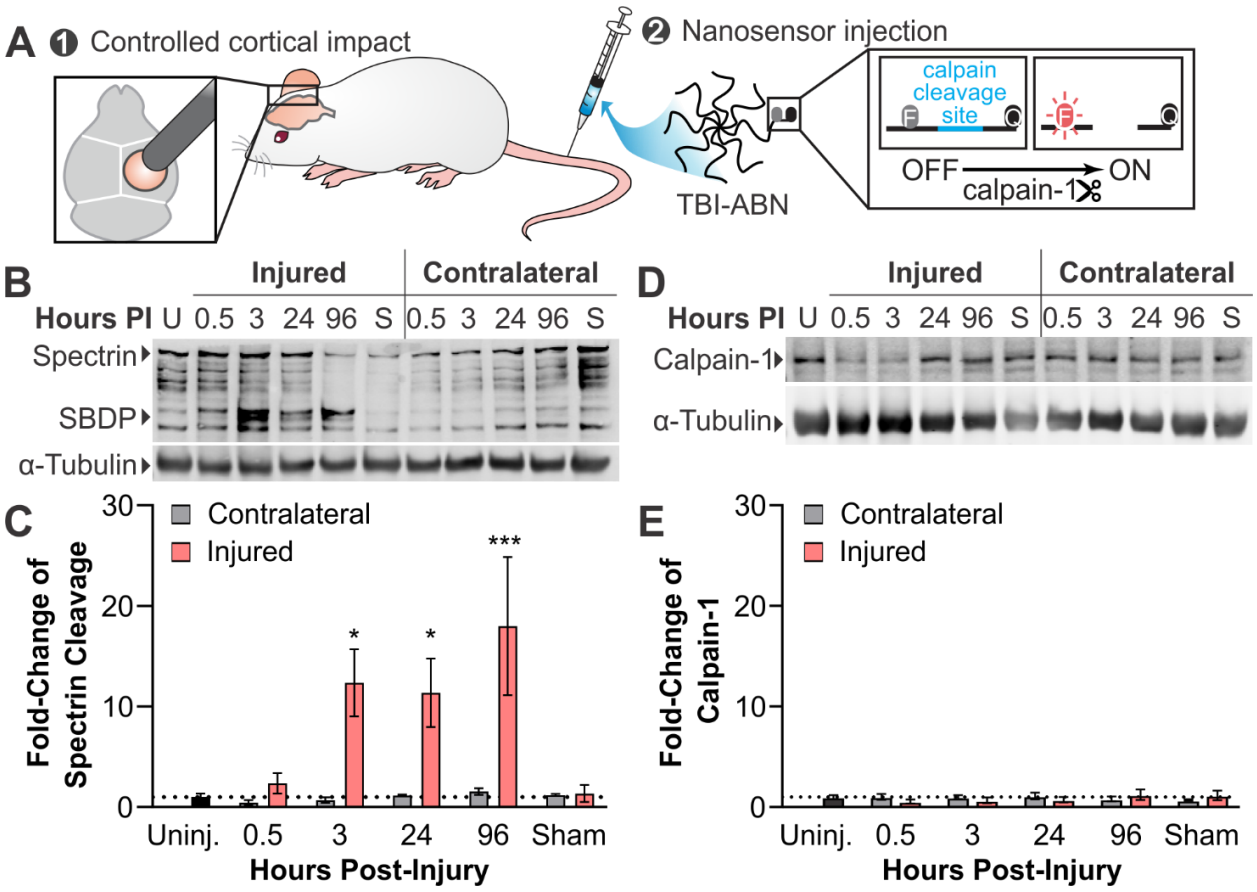

Figure 2.1: Design of a TBI activity-based nanosensor. (A) Overview of TBI-ABN design. (B) Time course post injury (PI) of αII-spectrin cleavage in controlled cortical impact (CCI)-injured cortices. (C) Quantification of calpain-1-specific 145 and 150 kDa αII-spectrin breakdown products (SBDP), normalized to α-tubulin and untreated control (n = 3, mean ± standard error (SE), $*p < 0.05$, $***p < 0.001$, two-way analysis of variance (ANOVA), and Dunnett's post hoc test against uninjured control). (D) Time course and (E) quantification of 80 kDa calpain-1 denoted by the arrow, normalized to α-tubulin and untreated control (n = 3, mean ± SE). Uninjured (U) mice received no surgery. Sham (S) mice received a craniotomy and no injury.

2.3. Results and Discussion

2.3.1. Calpain-1 Locally Activates in a Mouse Model of TBI

We first established the levels of calpain-1 activity and protein in a mouse model of TBI. The controlled cortical impact (CCI) model of TBI is a reproducible and well-characterized method to create a localized injury in the brain.[16–18] To assess calpain-1 activity, 150 and 145 kDa breakdown products of the native calpain-1 substrate αII-spectrin were measured, as

described previously.[19] These spectrin breakdown products (SBDPs) were shown to increase to greater than 10-fold in the injured hemisphere at 3 h post injury compared to that in the uninjured brains (Figure 2.1B, C). This increase was sustained up to 96 h post injury. By contrast, the uninjured, contralateral hemisphere did not show a significant elevation of SBDPs. A sham control group that underwent a craniotomy but no injury exhibited similar levels of SBDPs to uninjured mice, confirming that spectrin proteolysis was the result of a direct impact to the brain tissue and not the surgical procedures. We thus establish that calpain-1 activity is increased after CCI and activity is localized to the injured hemisphere, consistent with the previously reported rodent models of CCI.[17,19–21]

To determine that increased spectrin cleavage was due to increased activity of calpain-1 and not increased levels of calpain-1, calpain-1 protein levels were also measured. No significant changes were observed in the protein levels of the 80 kDa large subunit of calpain-1 between injured and uninjured brains (Figure 2.1D, E). Furthermore, assessment of calpain-1 via immunohistochemistry of brain slices showed only a local increase in calpain-1 detected 4 h post injury in the immediate injury area, whereas calpain-1 levels appeared to be unchanged in the uninjured cortex and the greater injury periphery when compared to those in the uninjured brains (Figure 2.2). These results indicate that the observed increase in αII-spectrin proteolysis (Figure 2.1B) is likely due to increased calpain-1 activity and not increased calpain-1 expression. Previous studies have shown that calpain-1 expression can be increased after injury, but its elevation is delayed by ~24 h.[22] Therefore, a sensor to detect calpain-1 activity may be effective in the first few hours after TBI.

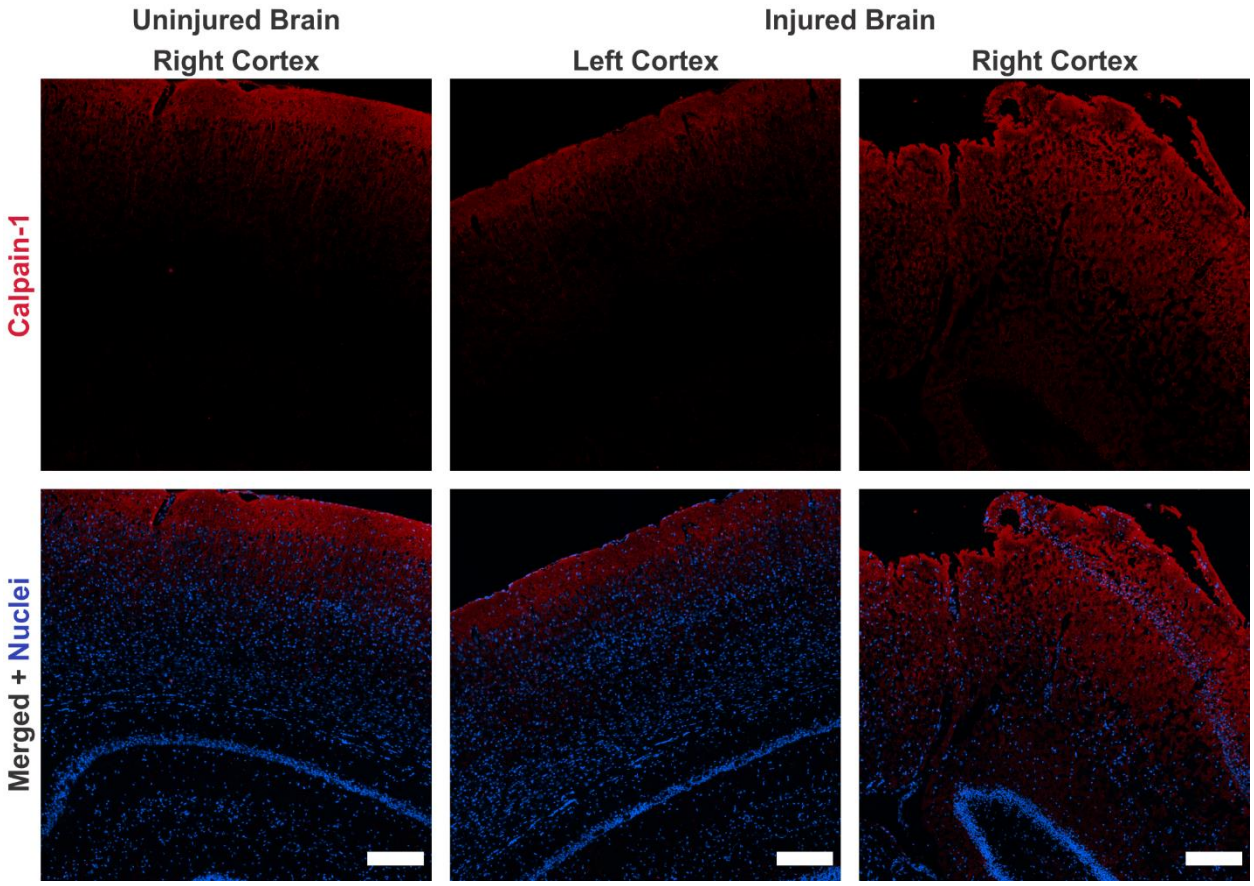

Figure 2.2: Calpain-1 distribution in coronal brain slices 4 hours post injury within injured and uninjured brain tissues (blue, nuclei; red, calpain-1; scale bar = 200 µm).

2.3.2. Large-Molecular-Weight Polymeric Carriers Accumulate in the Site of Injury after CCI

We next focused on a nanoscale delivery carrier for our nanosensor. Shortly after TBI, the vasculature at the site of injury is compromised due to the mechanical damage followed by dysregulation of the neurovascular unit.[23,24] This pathological hallmark of TBI allows for the delivery of nanoscale cargo to the brain within the first 24 h after injury, similar to the enhanced permeability and retention (EPR) effect described for nanoparticles in tumors.[25] On their own, small peptides have a short circulation half-life in vivo due to renal clearance and proteolytic degradation in the bloodstream. We hypothesized that blood circulation time and subsequent tissue retention of the peptide would increase through its conjugation to a larger, neutrally

charged, and minimally immunogenic polymeric carrier such as poly(ethylene glycol) (PEG).[26] While studies have been done on the biodistribution of rigid nanoparticles, including PEGylated polystyrene nanoparticles and liposomes after TBI,[27,28] and polystyrene nanoparticles after microdialysis probe insertion,[29] there has not yet been a study into the distribution of PEG after TBI. To maximize the delivery of the TBI nanosensor through the compromised BBB after injury, we evaluated how the molecular weight of 8-arm PEG affects its accumulation into the injured tissue after CCI injury. 8-arm PEG was chosen as the carrier because it allows for the possibility of multiplexing through the conjugation of ligands to each individual arm. PEG carriers (10, 20, and 40 kDa) were evaluated for distribution into major organs after intravenous injection 2 h after CCI in mice (Figure 2.3A and Figure 2.4). This timeline was chosen to be within the initial 4 h of secondary injury after CCI when a quick diagnosis and intervention of calpain are critical.[17] The highest accumulation for 10 kDa PEG was seen in the kidneys with little accumulation in the brain, whereas the 20 and 40 kDa PEGs had significant accumulation in the injured brain and significantly less accumulation in the kidneys compared to the 10 kDa PEG. In the brain, 20 and 40 kDa PEGs accumulated significantly more in the injured hemisphere than in the contralateral hemisphere by approximately 7- and 5-fold, respectively (Figure 2.3B). The hydrodynamic diameters of each carrier in PBS were measured to be 5.57, 7.89, and 10.25 nm for 10, 20, and 40 kDa PEGs, respectively (Figure 2.3C). The 10 kDa PEG is near the ~5 nm limit for renal filtration,[30,31] which is reflected in its significant accumulation into the kidneys compared to the 20 and 40 kDa sizes. All three carriers are smaller than the 500 nm size range of materials which have been observed to extravasate into the injured tissue following TBI.[28,32] Thus, 8-arm PEG polymer carriers greater than 20 kDa in size can accumulate in the injured brain.

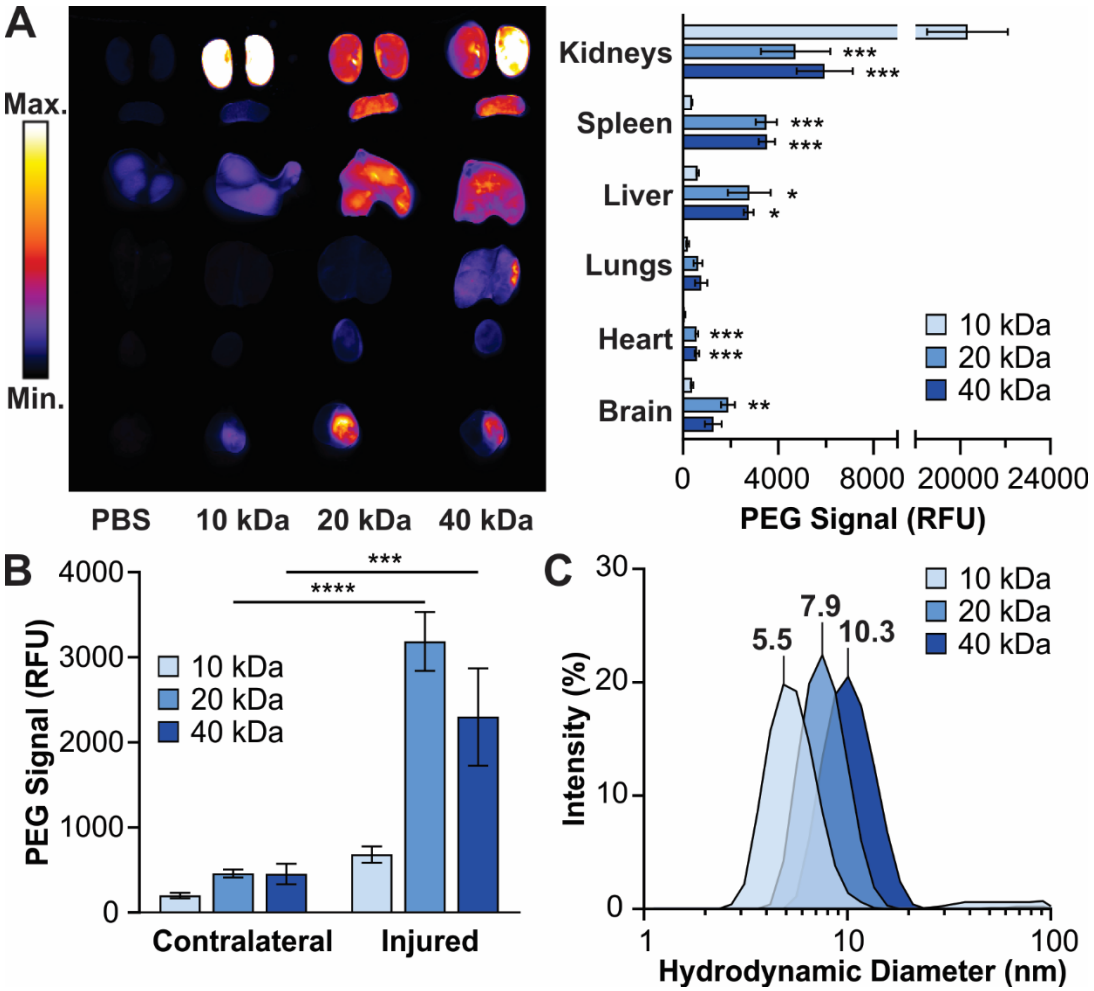

Figure 2.3: Large-molecular-weight PEG carriers localize to the region of injury in a mouse model of TBI. (A) Fluorescence image of major organs after intravenous injection of fluorescently labeled PEG of various sizes (left) was quantified and the signal was normalized to PBS-injected animals (right) (n = 4, mean ± SE, *$p < 0.05$, **$p < 0.01$, ****$p < 0.001$, ordinary one-way ANOVA, and Tukey's post hoc test compared within each organ). (B) PEG distribution in injured or contralateral brain hemispheres (n = 4, mean ± SE, ***$p < 0.001$, ****$p < 0.0001$, two-way ANOVA, and Sidak's post hoc test within each size). (C) Size distribution of 10, 20, and 40 kDa PEGs.

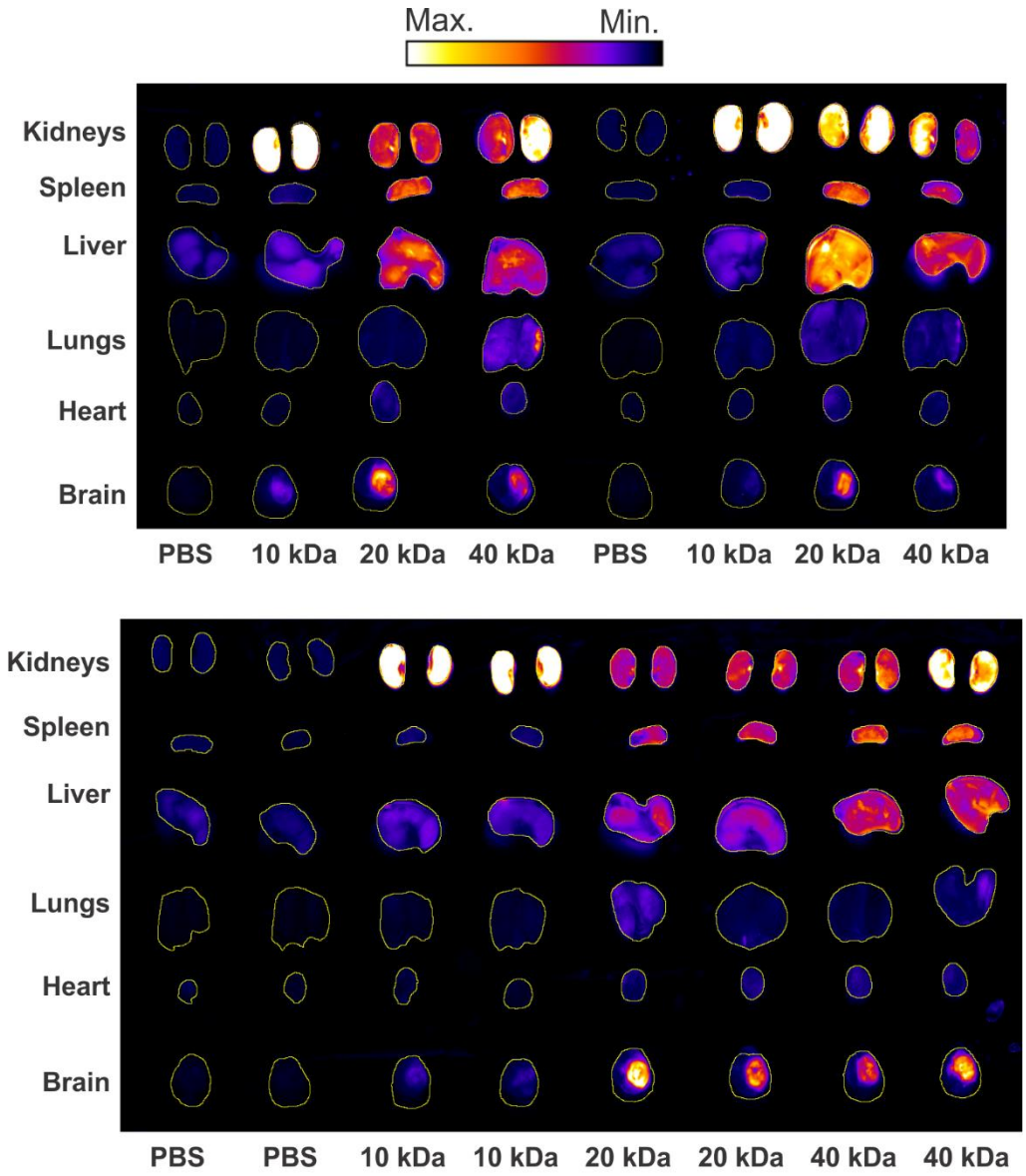

Figure 2.4: Fluorescence images of all organs analyzed for biodistribution. Yellow outlines mark the areas measured for mean fluorescence intensity.

2.3.3. Calpain Substrate Responds to Calpain-1 Activity

To detect calpain-1 activity, we synthesized a calpain-1-responsive peptide composed of the FRET pair Cy5 and QSY21 separated by a calpain-1-specific cleavage sequence (QEVYGAMP) taken from the native mouse αII-spectrin sequence (Figure 2.5A).[33] To measure kinetics of cleavage by calpain-1, several concentrations of peptide were incubated with

recombinant calpain-1 enzyme in vitro, and peptide cleavage was measured by dequenched Cy5 fluorescence (Figure 2.5B). Because blood cleavage is a major concern for a sensor administered intravenously, nonspecific cleavage of our peptide by blood components was examined by incubation with mouse plasma or human α-thrombin. No significant cleavage of our substrate was observed (Figure 2.5C). This peptide was then conjugated to 40 kDa 8-arm PEG to increase its circulation time and retention in the injured brain tissue when applied in vivo (Figure 2.3). The 40 kDa PEG was used over 20 kDa PEG to increase solubility of the peptide, as precipitates were observed with 20 kDa conjugates. Multiple ratios of peptide:PEG were assessed via the same in vitro kinetics assay to optimize for sensor signal in response to calpain-1. It was observed that the conjugation of the peptide:PEG in a 1:1 stoichiometric ratio led to a decrease in the fluorescent signal (Figure 2.5B) as well as maximum cleavage velocity (Figure 2.5D) compared to that of the free peptide. For example, the maximum cleavage velocity of the peptide at an 8 μM concentration decreased from 1677.5 to 692.1 RFU/min with conjugation. This decrease was not observed with the peptide in the presence of free unconjugated PEG (Figure 2.6), suggesting that the direct conjugation of the peptide to PEG impacts peptide cleavage by calpain-1. The addition of multiple peptides:PEG in 2:1 and 4:1 conjugates led to further decreased cleavage velocities compared to that of 1:1 conjugate or free peptide (Figure 2.5D). Conjugates of 8:1 peptide:PEG precipitated out of solution, suggesting that the increased local concentration of peptides created by physical linkage to a polymeric carrier leads to a decrease in solubility. Due to the benefits of brain accumulation afforded by the PEG, a 1:1 stoichiometric ratio of the peptide and PEG carrier was further evaluated in animal models of TBI.

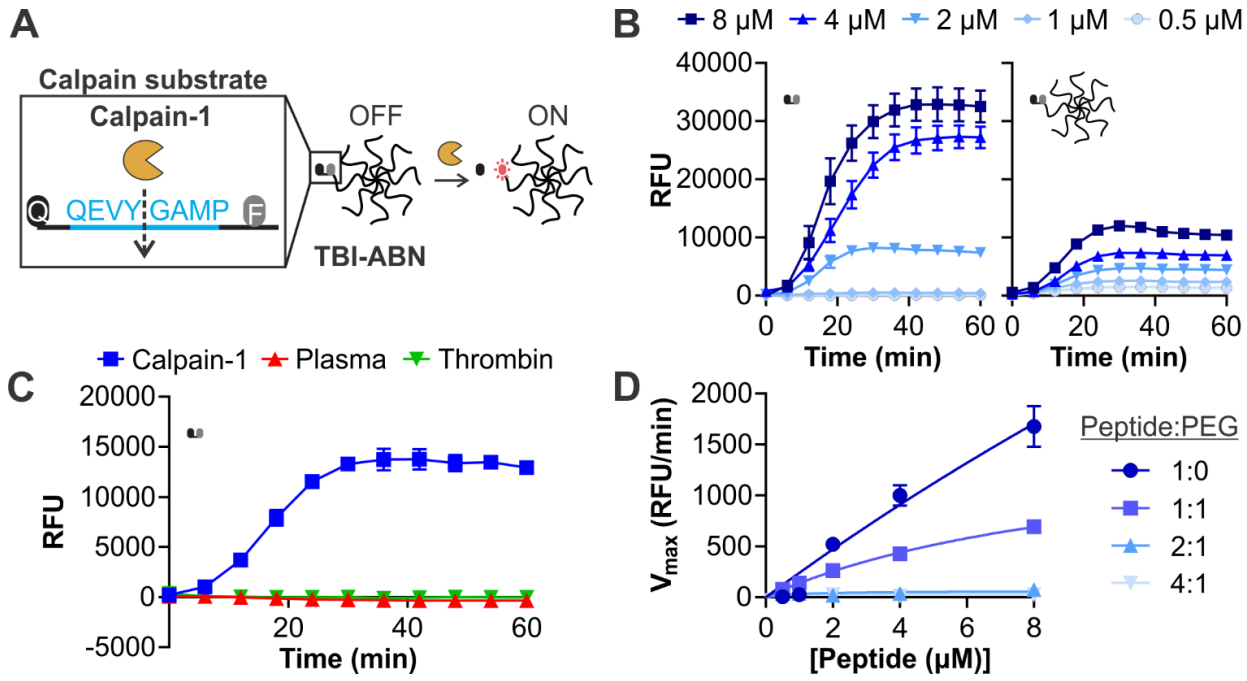

Figure 2.5: Calpain substrate is cleaved by calpain-1 as free peptide and when conjugated to PEG carrier. (A) Schematic of calpain substrate peptide, conjugated to 8-arm PEG to form TBI-ABN (Q = quencher, F = fluorophore). (B) Cleavage of free peptide (left) and 1:1 peptide:PEG (right) with recombinant human calpain-1 (n = 3, mean ± SD). (C) Cleavage of 8 μM peptide with recombinant human calpain-1, mouse plasma, or human α-thrombin (n = 3, mean ± SD). (D) Michaelis–Menten reaction kinetics of peptide:PEG ratios of 1:0, 1:1, 2:1, and 4:1 calpain-1 cleavages (n = 3, mean ± SD).

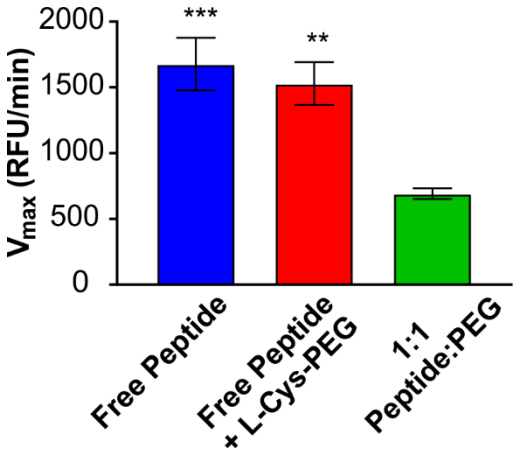

Figure 2.6: Maximal cleavage velocities of peptide with recombinant human calpain-1 as a free peptide, as a free peptide with separate PEG scaffold, and as a peptide conjugated in a 1:1 ratio with PEG scaffold (n = 3, mean ± SD, **p<0.01, ***p<0.001, ordinary one-way ANOVA and Tukey's post-hoc test).

2.3.4. TBI-ABN Activates in Injured Brain Tissue after CCI

Finally, we tested the activation of the TBI nanosensor in a mouse model of TBI. We have established that calpain-1 has an increased activity independent of expression after brain injury, PEG greater than 20 kDa in molecular weight can accumulate in the injury site, and a FRET peptide substrate is cleaved by calpain-1. Extracellular release of calpain-1 and its substrates by necrotic neurons after injury has been observed in previous studies;[5,34] we therefore expect the activation of our nanosensor without the need for cell internalization. Both increased calpain-1 activity and intravenous access to the brain occur within the same 4 h time scale post injury, so we expect that our TBI-ABN can localize and activate in the injured brain. We note that the diagnosis of TBI within this 4 h window has been demonstrated to be crucial to decrease patient morbidity.[2]

Mice were intravenously injected with sensor 2 h after CCI injury and evaluated for sensor activation 2 h after injection. In the first hours after CCI, focal neurodegeneration has been previously shown to extend from the injury site down to the hippocampus;[17] based on these observations, the top 1.5 mm of coronal brain slices was analyzed for sensor activation after fluorescent imaging. The sensor showed significant activation in the injured brain hemisphere with a higher activated sensor signal compared to the background signal from both injured and uninjured brains (Figure 2.7A-C). There was minimal activation of the sensor in uninjured brains, likely due to unchanged calpain-1 activity (Figure 2.1B) and intact BBB. Additionally, there was little difference in signal in uninjured brains and the contralateral hemisphere of injured brains (Figure 2.7D and Figure 2.8). These results provide evidence that the sensor produces a signal in response to injury.

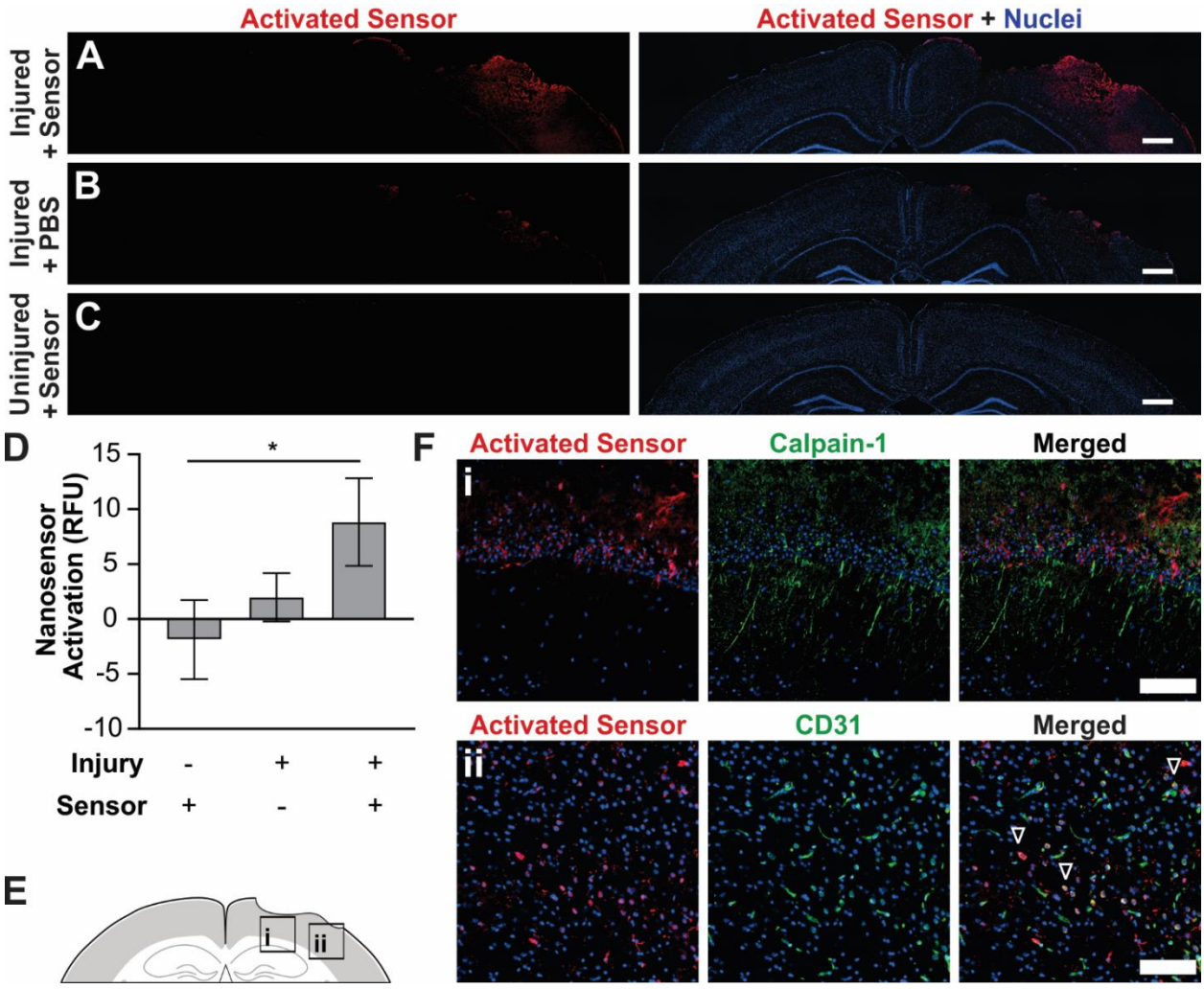

Figure 2.7: Calpain sensor activates in the injured brain tissue after intravenous delivery. (A–C) Representative coronal brain slices from injured and uninjured brains (blue, nuclei; red, activated nanosensor; scale bar = 500 μm). (D) Quantification of mean sensor intensity in the injured hemisphere normalized to uninjured control brains (n = 6, mean ± SE, **p* = 0.0851, ordinary one-way ANOVA, and Sidak's post hoc test). (E) Map and (F) insets from slices adjacent to (A), showing sensor localization relative to (i) calpain-1 and (ii) CD31 in the injury periphery (blue, nuclei; red, activated nanosensor; green, calpain-1 (top) or CD31 (bottom); outlined arrows, overlap of sensor with CD31; scale bar = 100 μm).

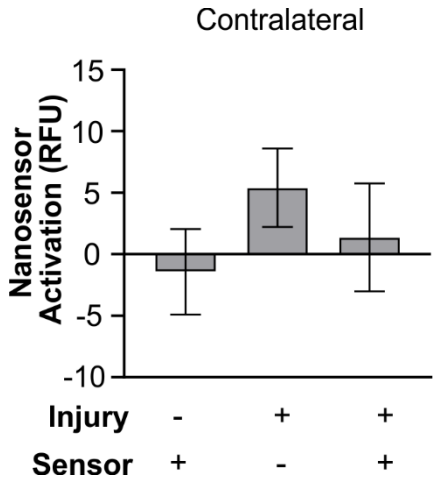

Figure 2.8: Quantification of mean sensor intensity in the contralateral hemisphere normalized to uninjured control brains (n = 6, mean ± SE).

We additionally investigated the cellular distribution of sensor activation. Since the TBI-ABN was delivered through an intravenous injection, we assessed TBI-ABN activation in relation to the vasculature by staining for calpain-1 and the endothelial marker, CD31. In the injury periphery, activated TBI-ABN signal was found in proximity to calpain-1 and some signal was also positively stained for endothelial cells (Figure 2.7E,F). Signal was also detected in the hippocampal CA1 region and dentate gyrus (Figure 2.9), regions that are identified as sites of extravasation and neurodegeneration following CCI.[18,24] Neurons, glia, and endothelial cells populating these regions are known to experience calcium influxes and abnormal calpain activation following injury[6,9] and are therefore potential sources for TBI-ABN signal.

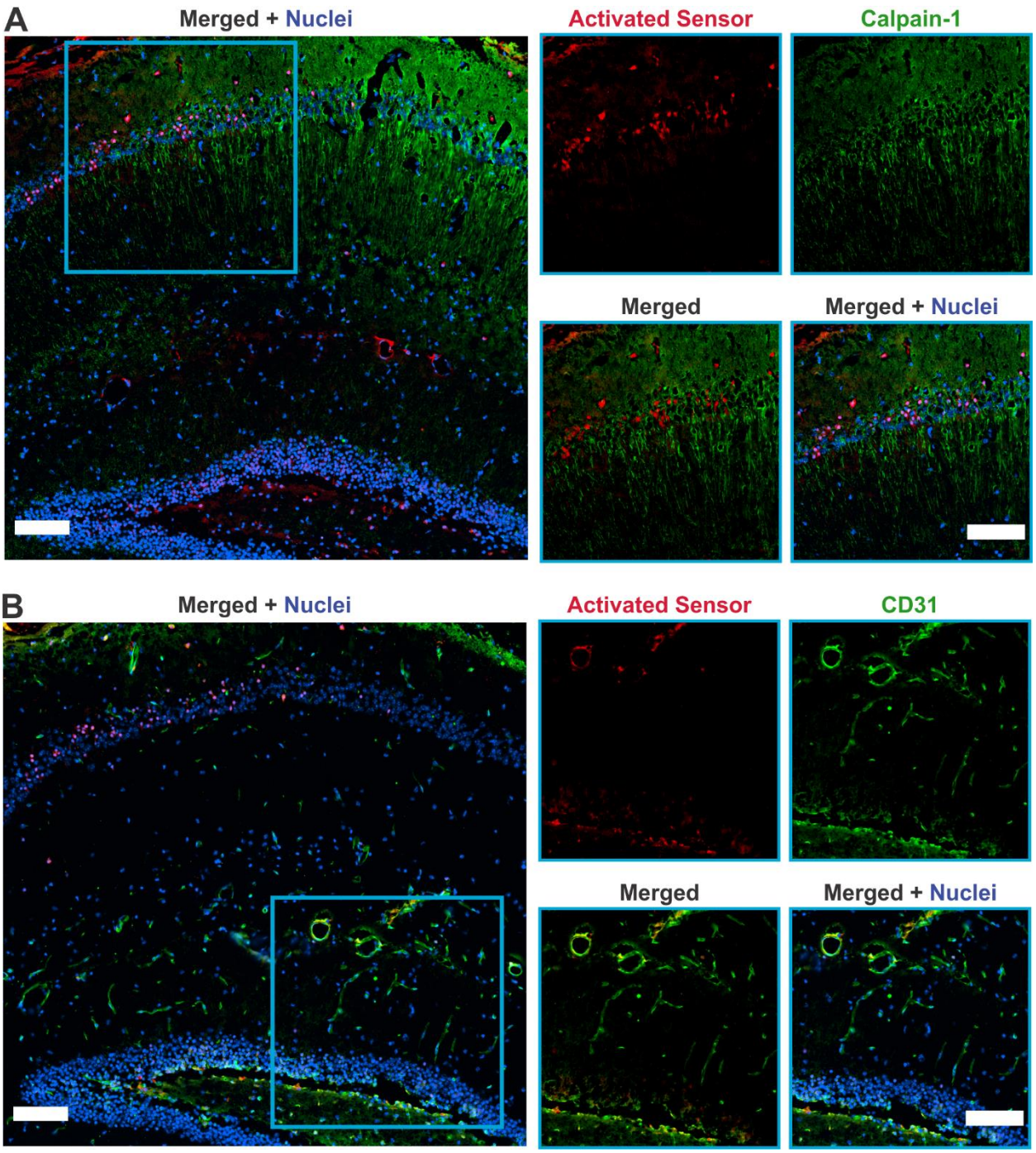

Figure 2.9: Sensor activation in (A) the hippocampal CA1 region and (B) the dentate gyrus in coronal slices from a representative injured brain 4 hours post injury (blue, nuclei; red, activated sensor; green, calpain-1 (top) or CD31 (bottom); scale bar = 100 μm).

2.4. Conclusions

We engineered a TBI activity-based nanosensor, TBI-ABN, which responds to calpain-1 activity, accumulates in the injured brain tissue, and activates in a mouse model of brain injury. To our knowledge, our engineered TBI-ABN is the first sensor to detect enzyme activity in TBI and is a proof-of-concept for the development of future activity-based diagnostics for TBI. Activity-based sensors are gaining significance for their ability to be engineered in response to specific biological stimuli, allowing for the capture of pathological processes that cannot be detected by conventional molecular quantification methods.[35] There are notable examples of activity-based sensors in cancer: fluorescently activated polymers can identify tumor margins during surgical resection,[36,37] and urinary sensors can detect and stratify tumors.[14,15,38] Based on these advances in cancer, measuring protease activity with an activity-based sensor to diagnose TBI is a promising strategy.

Now that we have established that a vascularly delivered sensor can activate in brain injury in response to protease activity, in future work, the TBI-ABN will be engineered to release biomarkers for minimally invasive blood-based detection. Signal specificity can be increased by multiplexing substrates for the detection of proteases such as MMP-9, which has local increases in activity following TBI and contributes to BBB breakdown.[39] To further enhance sensitivity and increase tissue accumulation and retention, we can add active targeting ligands, for example, peptides that bind extracellular matrix components exposed after injury.[40–42] In the long term, TBI-ABN can be paired with inhibitors of protease activity, such as small molecule inhibitors of calpain-1,[11] to create nanotheranostics that can detect and treat TBI.

2.5. Methods

Synthesis of Poly(ethylene glycol) (PEG) Conjugates. Calpain substrate peptide (QSY21-QEVYGAMP-K(Cy5)-PEG2-GC-NH2) was synthesized by CPC Scientific Inc. (Sunnyvale, CA). PEG2 stands for poly(ethylene glycol). 8-arm PEG amine and PEG maleimide (tripentaerythritol) were purchased from Jenkem Technology (Beijing, China). PEG amine was reacted with 1 mol equivalent of VivoTag-S 750 (PerkinElmer, Boston, MA). PEG maleimide was reacted with 1, 2, and 4 mol equivalences of the peptide in the presence of 50 mM triethylamine (TEA) and quenched with an excess of L-cysteine. All conjugates were dialyzed in water, and the final concentrations were determined by absorbance of VivoTag or Cy5 using a Spark multimode microplate reader (Tecan Trading AG, Switzerland). The L-cysteine PEG maleimide control was dissolved by weight. Hydrodynamic diameters of unconjugated PEG amine were measured via dynamic light scattering (DLS) with a Zetasizer Nano (Malvern Panalytical).

In Vitro Reaction Kinetics Assay. Free peptide and conjugates were incubated with 26.6 nM recombinant human calpain-1 (Sigma-Aldrich) in 50 mM *N*-(2-hydroxyethyl)piperazine-*N*′-ethanesulfonic acid (HEPES), 50 mM NaCl, 2 mM ethylenediaminetetraacetic acid (EDTA), 5 mM CaCl2, 5 mM β-mercaptoethanol, 10% mouse plasma in phosphate-buffered saline (PBS), or 13.5 nM human α-thrombin (Haematologic Technologies) in TCNB buffer. Mouse plasma was prepared by centrifuging blood collected with EDTA. Fluorescence readings were taken every 90 s at 37 °C for 1 h. Reaction curves were normalized to controls, and their initial velocities were fitted to a Michaelis–Menten curve in GraphPad Prism (8.1.2).

Controlled Cortical Impact (CCI) Mouse Model of TBI. All mouse protocols were approved by the University of California San Diego's Institutional Animal Care and Use Committee (IACUC). Female C57BL/6J mice of 8–12 weeks old (Jackson Labs) were used for all experiments. Mice were anesthetized with 2.5% isoflurane, and the head was secured in a stereotaxic frame. A midline incision was made to expose the skull, and a 4 mm diameter craniotomy was performed over the right hemisphere between bregma and lambda. The controlled cortical impact was applied to the exposed dura of the cortex with the ImpactOne (Leica Biosystems) fitted with a stainless steel 2 mm diameter probe at a velocity of 3 m/s and a 2 mm depth.

Biodistribution and In Vivo Sensor Activation. Two hours after CCI, 2 nmol of VivoTag-PEG in 100 μL PBS (n = 4 each for biodistribution) or 8 nmol of TBI-ABN in 100 μL PBS (n = 6 for sensor activation analysis) were intravenously administered via the tail vein. Control mice received the same volume of PBS. Two hours after administration, mice were transcardially perfused with USP saline followed by 10% formalin. Fluorescence was measured with an Odyssey scanner (Li-Cor Biosciences) on the same day as collection. The mean fluorescence intensity per area was analyzed using ImageJ.

Immunohistochemistry and Sensor Quantification in Brain Tissue Slices. Organs were fixed with 10% formalin solution at 4 °C overnight, equilibrated in 30% w/v sucrose, and frozen in OCT (Tissue-Tek). Coronal tissue slices 10 μm thick were stained using conventional protocols. The following primary antibodies were used: 1:200 calpain-1 (Abcam, ab108400) and 1:200 CD31 (BD, 553370). Sensor activation was quantified in three tissue slices per brain up to

1.5 mm caudal from the center of the injury. Cy5 signal in each slice extending 1.5 mm down from the top of the cortex was averaged between slices from each brain and then normalized to the signal from uninjured PBS controls using ImageJ. Images were captured with a Nikon Eclipse Ti2 microscope fitted with a Hamamatsu Orca-Flash 4.0 digital camera.

Protein Analysis. At the designated time points after injury, injured and contralateral cortices were harvested and immediately frozen. Sham injured mice received a craniotomy and no injury, and the tissue was harvested 3 h after surgery. Western blots were performed following conventional protocols. The following primary antibodies were used: 1:2000 αII-spectrin (Abcam, ab11755), 1:1000 calpain-1 (Abcam, ab108400), or 1:5000 α-tubulin (Cell Signaling, 3873). Membranes were imaged on a Li-Cor Odyssey scanner, and densitometric analysis of the Western blots was done in ImageJ.

Software and Statistics. All data were analyzed in GraphPad Prism (8.1.2). All post hoc tests were conducted with $p < 0.05$ to identify statistical significance between samples. All images were analyzed with ImageJ (1.52p).

2.6. Acknowledgements

Chapter 2, in full, is reprinted with permission from Kudryashev, Julia A.; Waggoner, Lauren E.; Leng, Hope T.; Mininni, Nicholas H.; Kwon, Ester J. An Activity-Based Nanosensor for Traumatic Brain Injury. ACS Sensors. 2020, 5 (3), 686–692. Copyright 2020 American Chemical Society. The dissertation author was the primary researcher and author of this paper.

J.A.K. is supported by the National Science Foundation (NSF) Graduate Research Fellowship Program under Grant No. DGE-1650112. Any opinions, findings, and conclusions or recommendations expressed in this material are those of the authors and do not necessarily reflect the views of the NSF.

2.7. References

(1) CDC. Surveillance Report of Traumatic Brain Injury-Related Emergency Department Visits, Hospitalizations, and Deaths—United States, 2014; 2019.

(2) Kim, Y. J. The Impact of Time from ED Arrival to Surgery on Mortality and Hospital Length of Stay in Patients With Traumatic Brain Injury. J. Emerg. Nurs. **2011**, 37 (4), 328–333. https://doi.org/10.1016/j.jen.2010.04.017.

(3) Hofman, P. A. M.; Stapert, S. Z.; Kroonenburgh, M. J. P. G. van; Jolles, J.; Kruijk, J. de; Wilmink, J. T. MR Imaging, Single-Photon Emission CT, and Neurocognitive Performance after Mild Traumatic Brain Injury. Am. J. Neuroradiol. **2001**, 22 (3), 441–449.

(4) Maas, A. I. R.; Stocchetti, N.; Bullock, R. Moderate and Severe Traumatic Brain Injury in Adults. Lancet Neurol. **2008**, 7 (8), 728–741. https://doi.org/10.1016/S1474-4422(08)70164-9.

(5) Wang, K. K.; Yang, Z.; Zhu, T.; Shi, Y.; Rubenstein, R.; Tyndall, J. A.; Manley, G. T. An Update on Diagnostic and Prognostic Biomarkers for Traumatic Brain Injury. Expert Rev. Mol. Diagn. **2018**, 18 (2), 165–180. https://doi.org/10.1080/14737159.2018.1428089.

(6) Andriessen, T. M. J. C.; Jacobs, B.; Vos, P. E. Clinical Characteristics and Pathophysiological Mechanisms of Focal and Diffuse Traumatic Brain Injury. J. Cell. Mol. Med. **2010**, 14 (10), 2381–2392. https://doi.org/10.1111/j.1582-4934.2010.01164.x.

(7) Bazarian, J. J.; Biberthaler, P.; Welch, R. D.; Lewis, L. M.; Barzo, P.; Bogner-Flatz, V.; Gunnar Brolinson, P.; Büki, A.; Chen, J. Y.; Christenson, R. H.; Hack, D.; Huff, J. S.; Johar, S.; Jordan, J. D.; Leidel, B. A.; Lindner, T.; Ludington, E.; Okonkwo, D. O.; Ornato, J.; Peacock, W. F.; Schmidt, K.; Tyndall, J. A.; Vossough, A.; Jagoda, A. S. Serum GFAP and UCH-L1 for Prediction of Absence of Intracranial Injuries on Head CT (ALERT-TBI): A Multicentre Observational Study. Lancet Neurol. **2018**, 17 (9), 782–789. https://doi.org/10.1016/S1474-4422(18)30231-X.

(8) Hori, S. S.; Gambhir, S. S. Mathematical Model Identifies Blood Biomarker-Based Early Cancer Detection Strategies and Limitations. Sci. Transl. Med. **2011**, 3 (109), 109ra116-109ra116. https://doi.org/10.1126/scitranslmed.3003110.

(9) Czogalla, A.; Sikorski, A. F. Spectrin and Calpain: A “target” and a “Sniper” in the Pathology of Neuronal Cells. Cell. Mol. Life Sci. **2005**, 62 (17), 1913–1924. https://doi.org/10.1007/s00018-005-5097-0.

(10) Hamakubo, T.; Kannagi, R.; Murachi, T.; Matus, A. Distribution of Calpains I and II in Rat Brain. J. Neurosci. **1986**, 6 (11), 3103–3111. https://doi.org/10.1523/JNEUROSCI.06-11-03103.1986.

(11) Saatman, K. E.; Creed, J.; Raghupathi, R. Calpain as a Therapeutic Target in Traumatic Brain Injury. Neurotherapeutics **2010**, 7 (1), 31–42. https://doi.org/10.1016/j.nurt.2009.11.002.

(12) Siman, R.; Giovannone, N.; Hanten, G.; Wilde, E. A.; McCauley, S. R.; Hunter, J. V.; Li, X.; Levin, H. S.; Smith, D. H. Evidence That the Blood Biomarker SNTF Predicts Brain Imaging Changes and Persistent Cognitive Dysfunction in Mild TBI Patients. Front. Neurol. **2013**, 4, 190–190. https://doi.org/10.3389/fneur.2013.00190.

(13) Gan, Z. S.; Stein, S. C.; Swanson, R.; Guan, S.; Garcia, L.; Mehta, D.; Smith, D. H. Blood Biomarkers for Traumatic Brain Injury: A Quantitative Assessment of Diagnostic and Prognostic Accuracy. Front. Neurol. **2019**, 10 (APR), 446–446. https://doi.org/10.3389/fneur.2019.00446.

(14) Kwong, G. A.; von Maltzahn, G.; Murugappan, G.; Abudayyeh, O.; Mo, S.; Papayannopoulos, I. A.; Sverdlov, D. Y.; Liu, S. B.; Warren, A. D.; Popov, Y.; Schuppan, D.; Bhatia, S. N. Mass-Encoded Synthetic Biomarkers for Multiplexed Urinary Monitoring of Disease. Nat. Biotechnol. **2013**, 31 (1), 63–70. https://doi.org/10.1038/nbt.2464.

(15) Kwon, E. J.; Dudani, J. S.; Bhatia, S. N. Ultrasensitive Tumour-Penetrating Nanosensors of Protease Activity. Nat. Biomed. Eng. **2017**, 1 (4), 0054–0054. https://doi.org/10.1038/s41551-017-0054.

(16) Xiong, Y.; Mahmood, A.; Chopp, M. Animal Models of Traumatic Brain Injury. Nat. Rev. Neurosci. **2013**, 14 (2), 128–142. https://doi.org/10.1038/nrn3407.

(17) Hall, E. D.; Sullivan, P. G.; Gibson, T. R.; Pavel, K. M.; Thompson, B. M.; Scheff, S. W. Spatial and Temporal Characteristics of Neurodegeneration after Controlled Cortical

Impact in Mice: More than a Focal Brain Injury. J. Neurotrauma **2005**, 22 (2), 252–265. https://doi.org/10.1089/neu.2005.22.252.

(18) Chen, Y.; Mao, H.; Yang, K. H.; Abel, T.; Meaney, D. F. A Modified Controlled Cortical Impact Technique to Model Mild Traumatic Brain Injury Mechanics in Mice. Front. Neurol. **2014**, 5, 100–100. https://doi.org/10.3389/fneur.2014.00100.

(19) Pike, B. R.; Flint, J.; Dutta, S.; Johnson, E.; Wang, K. K. W.; Hayes, R. L. Accumulation of Non-Erythroid AII-Spectrin and Calpain-Cleaved AII-Spectrin Breakdown Products in Cerebrospinal Fluid after Traumatic Brain Injury in Rats. J. Neurochem. **2001**, 78 (6), 1297–1306. https://doi.org/10.1046/j.1471-4159.2001.00510.x.

(20) Saatman, K. E.; Bozyczko-Coyne, D.; Marcy, V.; Siman, R.; McIntosh, T. K. Prolonged Calpain-Mediated Spectrin Breakdown Occurs Regionally Following Experimental Brain Injury in the Rat. J. Neuropathol. Exp. Neurol. **1996**, 55 (7), 850–860. https://doi.org/10.1097/00005072-199607000-00010.

(21) Zhao, X.; Posmantur, R.; Kampfl, A.; Liu, S.-J.; Wang, K. K. W.; Newcomb, J. K.; Pike, B. R.; Clifton, G. L.; Hayes, R. L. Subcellular Localization and Duration of μ-Calpain and m-Calpain Activity after Traumatic Brain Injury in the Rat: A Casein Zymography Study. J. Cereb. Blood Flow Metab. **1998**, 18 (2), 161–167. https://doi.org/10.1097/00004647-199802000-00006.

(22) Ringger, N. C.; Tolentino, P. J.; McKinsey, D. M.; Pike, B. R.; Wang, K. K. W.; Hayes, R. L. Effects of Injury Severity on Regional and Temporal MRNA Expression Levels of Calpains and Caspases after Traumatic Brain Injury in Rats. J. Neurotrauma **2004**, 21 (7), 829–841. https://doi.org/10.1089/0897715041526177.

(23) Price, L.; Wilson, C.; Grant, G. Blood–Brain Barrier Pathophysiology Following Traumatic Brain Injury. In Translational Research in Traumatic Brain Injury; Laskowitz, D., Grant, G., Eds.; CRC Press/Taylor and Francis Group: Boca Raton, FL, 2016; pp 85–96. https://doi.org/10.1201/b18959-5.

(24) Hicks, R. R.; Baldwin, S. A.; Scheff, S. W. Serum Extravasation and Cytoskeletal Alterations Following Traumatic Brain Injury in Rats. Mol. Chem. Neuropathol. **1997**, 32 (1–3), 1–16. https://doi.org/10.1007/BF02815164.

(25) Kwon, E. J.; Skalak, M.; Lo Bu, R.; Bhatia, S. N. Neuron-Targeted Nanoparticle for SiRNA Delivery to Traumatic Brain Injuries. ACS Nano **2016**, 10 (8), 7926–7933. https://doi.org/10.1021/acsnano.6b03858.

(26) Caliceti, P.; Veronese, F. M. Pharmacokinetic and Biodistribution Properties of Poly(Ethylene Glycol)–Protein Conjugates. Adv. Drug Deliv. Rev. **2003**, 55 (10), 1261–1277. https://doi.org/10.1016/S0169-409X(03)00108-X.

(27) Boyd, B. J.; Galle, A.; Daglas, M.; Rosenfeld, J. V.; Medcalf, R. Traumatic Brain Injury Opens Blood–Brain Barrier to Stealth Liposomes via an Enhanced Permeability and Retention (EPR)-like Effect. J. Drug Target. **2015**, 23 (9), 847–853. https://doi.org/10.3109/1061186X.2015.1034280.

(28) Bharadwaj, V. N.; Lifshitz, J.; Adelson, P. D.; Kodibagkar, V. D.; Stabenfeldt, S. E. Temporal Assessment of Nanoparticle Accumulation after Experimental Brain Injury: Effect of Particle Size. Sci. Rep. **2016**, 6 (1), 29988–29988. https://doi.org/10.1038/srep29988.

(29) Mitala, C. M.; Wang, Y.; Borland, L. M.; Jung, M.; Shand, S.; Watkins, S.; Weber, S. G.; Michael, A. C. Impact of Microdialysis Probes on Vasculature and Dopamine in the Rat Striatum: A Combined Fluorescence and Voltammetric Study. J. Neurosci. Methods **2008**, 174 (2), 177–185. https://doi.org/10.1016/j.jneumeth.2008.06.034.

(30) Longmire, M.; Choyke, P. L.; Kobayashi, H. Clearance Properties of Nano-Sized Particles and Molecules as Imaging Agents: Considerations and Caveats. Nanomed. **2008**, 3 (5), 703–717. https://doi.org/10.2217/17435889.3.5.703.

(31) Kwong, G. A.; Dudani, J. S.; Carrodeguas, E.; Mazumdar, E. V.; Zekavat, S. M.; Bhatia, S. N. Mathematical Framework for Activity-Based Cancer Biomarkers. Proc. Natl. Acad. Sci. U. S. A. **2015**, 112 (41), 12627–12632. https://doi.org/10.1073/pnas.1506925112.

(32) Habgood, M. D.; Bye, N.; Dziegielewska, K. M.; Ek, C. J.; Lane, M. A.; Potter, A.; Morganti-Kossmann, C.; Saunders, N. R. Changes in Blood-Brain Barrier Permeability to Large and Small Molecules Following Traumatic Brain Injury in Mice. Eur. J. Neurosci. **2007**, 25 (1), 231–238. https://doi.org/10.1111/j.1460-9568.2006.05275.x.

(33) Stockholm, D.; Bartoli, M.; Sillon, G.; Bourg, N.; Davoust, J.; Richard, I. Imaging Calpain Protease Activity by Multiphoton FRET in Living Mice. J. Mol. Biol. **2005**, 346 (1), 215–222. https://doi.org/10.1016/j.jmb.2004.11.039.

(34) Levesque, S.; Wilson, B.; Gregoria, V.; Thorpe, L. B.; Dallas, S.; Polikov, V. S.; Hong, J. S.; Block, M. L. Reactive Microgliosis: Extracellular-Calpain and Microglia-Mediated Dopaminergic Neurotoxicity. Brain **2010**, 133 (3), 808–821. https://doi.org/10.1093/brain/awp333.

(35) Thorek, D. L. J.; Watson, P. A.; Lee, S. G.; Ku, A. T.; Bournazos, S.; Braun, K.; Kim, K.; Sjostrom, K.; Doran, M. G.; Lamminmaki, U.; Santos, E.; Veach, D.; Turkekul, M.; Casey, E.; Lewis, J. S.; Abou, D. S.; van Voss, M. R. H.; Scardino, P. T.; Strand, S.-E.; Alpaugh, M. L.; Scher, H. I.; Lilja, H.; Larson, S. M.; Ulmert, D. Internalization of Secreted Antigen-Targeted Antibodies by the Neonatal Fc Receptor for Precision Imaging of the Androgen Receptor Axis. Sci. Transl. Med. **2016**, 8 (367), 367ra167-367ra167. https://doi.org/10.1126/scitranslmed.aaf2335.

(36) Urano, Y.; Sakabe, M.; Kosaka, N.; Ogawa, M.; Mitsunaga, M.; Asanuma, D.; Kamiya, M.; Young, M. R.; Nagano, T.; Choyke, P. L.; Kobayashi, H. Rapid Cancer Detection by Topically Spraying a -Glutamyltranspeptidase-Activated Fluorescent Probe. Sci. Transl. Med. **2011**, 3 (110), 110ra119-110ra119. https://doi.org/10.1126/scitranslmed.3002823.

(37) Whitley, M. J.; Cardona, D. M.; Lazarides, A. L.; Spasojevic, I.; Ferrer, J. M.; Cahill, J.; Lee, C.-L.; Snuderl, M.; Blazer III, D. G.; Hwang, E. S.; Greenup, R. A.; Mosca, P. J.; Mito, J. K.; Cuneo, K. C.; Larrier, N. A.; O'Reilly, E. K.; Riedel, R. F.; Eward, W. C.; Strasfeld, D. B.; Fukumura, D.; Jain, R. K.; Lee, W. D.; Griffith, L. G.; Bawendi, M. G.; Kirsch, D. G.; Brigman, B. E. A Mouse-Human Phase 1 Co-Clinical Trial of a Protease-Activated Fluorescent Probe for Imaging Cancer. Sci. Transl. Med. **2016**, 8 (320), 320ra4-320ra4. https://doi.org/10.1126/scitranslmed.aad0293.

(38) Dudani, J. S.; Ibrahim, M.; Kirkpatrick, J.; Warren, A. D.; Bhatia, S. N. Classification of Prostate Cancer Using a Protease Activity Nanosensor Library. Proc. Natl. Acad. Sci. U. S. A. **2018**, 115 (36), 8954–8959. https://doi.org/10.1073/pnas.1805337115.

(39) Guilfoyle, M. R.; Carpenter, K. L. H.; Helmy, A.; Pickard, J. D.; Menon, D. K.; Hutchinson, P. J. A. Matrix Metalloproteinase Expression in Contusional Traumatic Brain Injury: A Paired Microdialysis Study. J. Neurotrauma **2015**, 32 (20), 1553–1559. https://doi.org/10.1089/neu.2014.3764.

(40) Costa, C.; Tortosa, R.; Domènech, A.; Vidal, E.; Pumarola, M.; Bassols, A. Mapping of Aggrecan, Hyaluronic Acid, Heparan Sulphate Proteoglycans and Aquaporin 4 in the Central Nervous System of the Mouse. J. Chem. Neuroanat. **2007**, 33 (3), 111–123. https://doi.org/10.1016/j.jchemneu.2007.01.006.

(41) Mummert, M. E.; Mohamadzadeh, M.; Mummert, D. I.; Mizumoto, N.; Takashima, A. Development of a Peptide Inhibitor of Hyaluronan-Mediated Leukocyte Trafficking. J. Exp. Med. **2000**, 192 (6), 769–779. https://doi.org/10.1084/jem.192.6.769.

(42) Mann, A. P.; Scodeller, P.; Hussain, S.; Joo, J.; Kwon, E.; Braun, G. B.; Mölder, T.; She, Z. G.; Kotamraju, V. R.; Ranscht, B.; Krajewski, S.; Teesalu, T.; Bhatia, S.; Sailor, M. J.;

Ruoslahti, E. A Peptide for Targeted, Systemic Delivery of Imaging and Therapeutic Compounds into Acute Brain Injuries. Nat. Commun. **2016**, 7 (1), 11980–11980. https://doi.org/10.1038/ncomms11980.

CHAPTER 3. TARGETING THE EXTRACELLULAR MATRIX IN TRAUMATIC BRAIN INJURY INCREASES SIGNAL GENERATION FROM AN ACTIVITY-BASED NANOSENSOR

3.1. Abstract

Traumatic brain injury (TBI) is a critical public health concern and major contributor to death and long-term disability. After the initial trauma, a sustained secondary injury involving a complex continuum of pathophysiology unfolds, ultimately leading to the destruction of nervous tissue. One disease hallmark of TBI is ectopic protease activity, which can mediate cell death, extracellular matrix breakdown and inflammation. We previously engineered a fluorogenic activity-based nanosensor for TBI (TBI-ABN) that passively accumulates into the injured brain across disrupted vasculature and generates fluorescent signal in response to calpain-1 cleavage, thus enabling in situ visualization of TBI-associated calpain-1 protease activity. In this work, we hypothesized that active targeting to the extracellular matrix of the injured brain would improve nanosensor accumulation in injured brain beyond passive delivery alone and lead to increased nanosensor activation. We evaluated several peptides that bind exposed/enriched ECM constituents in the brain and discovered that nanomaterials modified with peptides that target hyaluronic acid (HA) displayed widespread distribution across the injury lesion, in particular colocalizing with perilesional and hippocampal neurons. Modifying TBI-ABN with HA-targeting peptide led to increases in activation in a ligand valency-dependent manner, up to 6.6-fold in the injured cortex compared to non-targeted nanosensor. This robust nanosensor activation enabled 3D visualization of injury-specific protease activity in a cleared and intact brain. In our work, we establish that targeting brain ECM with peptide ligands can be leveraged to improve the distribution and function of a bioresponsive imaging nanomaterial.

3.2. Introduction

Traumatic brain injury (TBI) affects over 1.5 million Americans per year and an estimated 3.17 million patients live with chronic neurodisability due to TBI.[1,2] After the primary injury, a progressive secondary injury unfolds within the brain over the course of hours to months caused by a complex continuum of pathophysiology characterized by hallmarks such as neuronal apoptosis, excitotoxicity, inflammation, and blood-brain barrier (BBB) dysfunction.[3] One signature of secondary injury pathophysiology is ectopic protease activity; for instance, the calcium-dependent cysteine protease calpain-1 cleaves cytoskeletal proteins and contributes to apoptotic and necrotic cell death,[4] and its activity is correlated with worsened TBI outcome.[5–7] Protease activity measurements have the potential to improve understanding of TBI disease biology and can serve as clinical biomarkers for disease progression,[8,9] but there are few approaches to measure protease activity in the living brain. In order to measure TBI-associated calpain-1 activity, we previously engineered a fluorogenic activity-based nanosensor for TBI (TBI-ABN) comprised of a Förster resonance energy transfer (FRET)-based peptide substrate of calpain-1 conjugated to a polymeric nanomaterial scaffold.[10] When administered intravenously in a TBI mouse model, we demonstrated that TBI-ABN could accumulate into injured brain tissue and activate in the context of injury. To sample ectopic protease activity in the injured tissue, this technology relied on size-dependent accumulation in brain tissue via transient BBB permeability, a hallmark of TBI pathophysiology. This passive accumulation of nanomaterials localized to diseased tissue has been called an "enhanced permeation and retention" (EPR)-like effect,[11,12] and is also described in other diseases such as cancer,[13,14] arthritis,[15] and myocardial infarction.[16,17] However in TBI, reliance on passive targeting alone is generally limited because unlike chronic conditions such as cancer and arthritis, BBB disruption after TBI is transient,

restricting the time window for nanomaterial delivery to hours after injury.[11,18] Furthermore, increased intracranial pressure from ischemia-associated edema creates a pressure gradient that likely limits nanomaterial diffusion across the extracellular space (ECS).[19] Thus, strategies to control the tissue-level distribution of activity-based nanosensors beyond passive targeting have the potential to increase protease-specific signal generation and therefore increase the sensitivity of nanosensors, as was previously demonstrated when the addition of tumor-targeting ligands to an MMP-9-sensitive ABN enabled ultrasensitive detection of low tumor burdens in a urinary readout.[20]

As a complementary approach in addition to passive delivery, active targeting via peptide or protein affinity ligands (e.g., transferrin,[21,22] HER2 antibodies,[23,24] RVG,[18,25] Lyp-1[26,27]) can improve the transport and/or tissue-level distribution of payloads. The extracellular matrix (ECM) represents an attractive biological target for nanomaterials due to its abundance and high density of binding moieties,[28] and therefore has the potential to act as a binding reservoir for exogenously delivered nanomaterials. Active targeting to ECM has been successfully applied to nanoparticle and protein therapeutics within the contexts of cancer[29–32] and arthritis-associated inflammation.[33,34] The dysregulated vasculature associated with cancer and inflammation exposes tissue ECM to materials in systemic circulation. In addition, aberrantly deposited ECM constituents can serve as disease-specific "neo-antigens" to improve distribution and efficacy of therapeutics. For example, the fusion of a collagen binding domain to chemokine CCL4 increased the accumulation of systemically administered CCL4 within collagen-rich tumors, leading to an enhancement of intra-tumor infiltration of immune cells when used in combination with checkpoint inhibitor immunotherapy.[32] In the brain, tissue is largely inaccessible to systemically administered synthetic nanomaterials under physiological conditions due to the

selective and tightly regulated BBB. After TBI, transient BBB disruption initiated by the injury enables unique access to brain parenchyma,[10,11,18,35] including the ECM. In addition, the composition of ECM in the brain is unique compared to that of peripheral organs; the brain is enriched with hyaluronic acid (HA) and sulfate proteoglycans, while fibrillar collagens and elastin are less represented.[36,37] This composition is furthermore changed in disease, with tenascins, laminin, chondroitin sulfate proteoglycans and heparin sulfate proteoglycans focally upregulated in the TBI lesion.[36,37] Local levels of HA are also perturbed due to changes in HA metabolism; hyaluronidases can degrade HA into bioactive fragments,[36,38] and expression of hyaluronic acid synthases are increased after experimental brain injury.[38] In addition to the tissue ECM present in the brain parenchyma, vascular injury leads to fibrin deposition during natural clotting and transient exposure of collagen IV in the basement membrane.[36] Each of these brain ECM components are potential targets for nanomaterials in the context of TBI. The approach of targeting the ECM after brain injury is highlighted by the recent identification of TBI-specific peptides via in vivo phage display.[39] This unbiased screening approach against whole brain tissue after TBI identified a peptide CAQK, whose receptors were discovered to be upregulated tenascin and versican proteoglycans in the ECM. CAQK modification enhanced the accumulation, acute retention, and activity of nanomaterials carrying siRNA payloads in a penetrating brain injury model.[39] Beyond this demonstration, active targeting to the ECM after TBI has been largely unexplored.

In this manuscript, we hypothesized that actively targeting nanomaterials to the brain ECM can increase the bioavailability and therefore activity of a diagnostic payload after systemic delivery in a TBI mouse model. We first performed an in vivo evaluation of nanomaterials modified with a selection of peptides that target major brain ECM constituents:

proteoglycans, collagen IV, fibrin, and HA. In a controlled cortical impact (CCI) model of TBI in mice, nanomaterials modified with peptides that targeted HA led to widespread distribution across cortical and hippocampal perilesional tissue after intravenous administration, and tissue localization was distinct from nanomaterials modified with peptides that targeted other ECM components. To determine whether this ECM-targeting-mediated change in tissue distribution could be harnessed into a functional outcome, we added HA-targeting to TBI-ABN, a nanosensor that activates in response to calpain-1 protease activity. We modified TBI-ABNs with HA-targeting peptide at various levels of substitutions, quantified calpain-1 nanosensor activation in injured brain tissue, and observed that targeting could increase activation up to 6.6-fold over non-targeted nanosensor, which suggests that increasing nanomaterial avidity to the ECM translates into enhanced nanosensor sensitivity. At the tissue level, we observed that the activation of HA-targeted TBI-ABN throughout the perilesional brain tissue colocalized with both neuronal and endothelial cell populations. Finally, light sheet imaging of TBI-ABN in cleared brain revealed nanosensor activation in proximity to the impact lesion in both the hippocampus and cortex. In summary, we establish that targeting an activity-based nanosensor to the brain ECM can significantly increase signal generation when applied to an animal model of TBI after systemic administration, enabling tissue-level visualization of aberrant calpain-1 protease activity in the injured brain.

3.3. Results and Discussion

3.3.1. Nanomaterials targeted to hyaluronic acid have widespread distribution in the injured brain.

In order to generate nanomaterials that interact with the brain ECM after intravenous delivery, we first identified peptide ligands from literature that bind to ECM constituents that are either exposed or enriched in the injured brain.[36] The selected ECM targets and ligand sequences were proteoglycans (CAQK),[39] collagen IV (KLWVLPK),[40] fibrin (CREKA),[41] and hyaluronic acid (STMMSRSHKTRSHHV).[42,43] Throughout the manuscript, these ECM-targeting peptides are referred to as PGpep, CIVpep, FIBpep, and HApep, respectively. These peptides are low molecular weight, linear sequences with comparable physicochemical properties (Table 3.1).

Table 3.1**:** Brain ECM targeting peptides and their properties.

Peptide name	ECM target	Peptide sequence	pI[a]	GRAVY[b]
PGpep	proteoglycans	CAQK[39]	9.13	-0.78
CIVpep	collagen IV	KLWVLPK[40]	10.69	0.21
FIBpep	fibrin	CREKA[41]	9.12	-1.52
HApep	hyaluronic Acid	STMMSRSHKTRSHHV[42]	12.13	-1.27

[a]pI = isoelectric point
[b]GRAVY = grand average of hydropathy

In previous work, we have established that the physiochemical properties of peptides influence nanoparticle pharmacokinetics in a mouse model of TBI.[44] Our nanomaterial scaffold was a 40 kDa 8-arm polyethylene glycol (PEG) which was selected for several reasons. First, each arm can participate in chemical conjugation, thus allowing for multivalent ligand presentation. Second, we previously established that its ~10 nm hydrodynamic diameter facilitates accumulation in the injured brain after intravenous administration[10] since it is larger

than the ~5.5 nm renal filtration limit which prevents rapid kidney excretion,[45] yet smaller than the pores in the extracellular space which allows for diffusion into brain tissue.[19,46] Third, PEG is a component used to extend in vivo circulation half-life in multiple FDA-approved formulations.[47] The ECM-targeting peptides were synthesized with the fluorescent molecule fluorescein (FAM) for quantification and a cysteine for reaction with maleimides on the 8-arm PEG. The PEG scaffold was reacted with one mole equivalence of fluorescent molecule VivoTag S-750 (VivoTag 750) and the remaining moieties were fully reacted with ECM-targeting peptides. The FAM on the peptide was utilized for quantitative biodistribution and histology and VivoTag 750 on the PEG scaffold was utilized for near-infrared surface imaging of organs. A non-targeted nanomaterial control was synthesized by modifying PEG with cysteine (Cys) instead of ECM-targeting peptide. In addition, the linear form of the well-studied peptide RGD[48] was included as a control due to the known elevation of integrin expression in inflammation.[49–51]

We evaluated the biodistribution of nanomaterials modified with each ECM-targeting peptide after intravenous delivery in a controlled cortical impact (CCI) mouse model of TBI (Figure 3.1A). CCI is a well-established model of TBI that has reproducible molecular phenotypes,[52] including elevation of calpain-1 activity.[10,53] Injuries were created by performing a 5 mm craniotomy over the right hemisphere of the brain and impacting the exposed dura with an electromagnetically-driven probe 2 mm in diameter at a speed of 3 m/s and depth of 2 mm. ECM-targeting peptide-modified PEG nanomaterial (25 nmoles of peptide per injection based on FAM absorbance, corresponding to a dosage range of 1136-1389 nmol/kg) was injected intravenously 6 hours post-CCI and mice were perfused and organs harvested 1 hour post-injection, an experimental timeline established by previous work.[39] Surface imaging of the VivoTag 750 label in intact organs shows that nanomaterial accumulation in the brain was

localized to the injured brain hemisphere (Figure 3.1B). This accumulation of intravenously delivered nanomaterials into the injured hemisphere due to local, transient permeability of the dysregulated blood-brain barrier is consistent with previous work from our group[10,18,44] and others.[11,12] Nanomaterials modified with CIVpep had high liver accumulation over all other materials. One potential hypothesis for this observation is the abundance of collagens I, III, IV, and V in the basement membrane of the liver.[54] We also observed significant nanomaterial accumulation in the kidneys, in particular for FIBpep- and PGpep-modified nanomaterials.

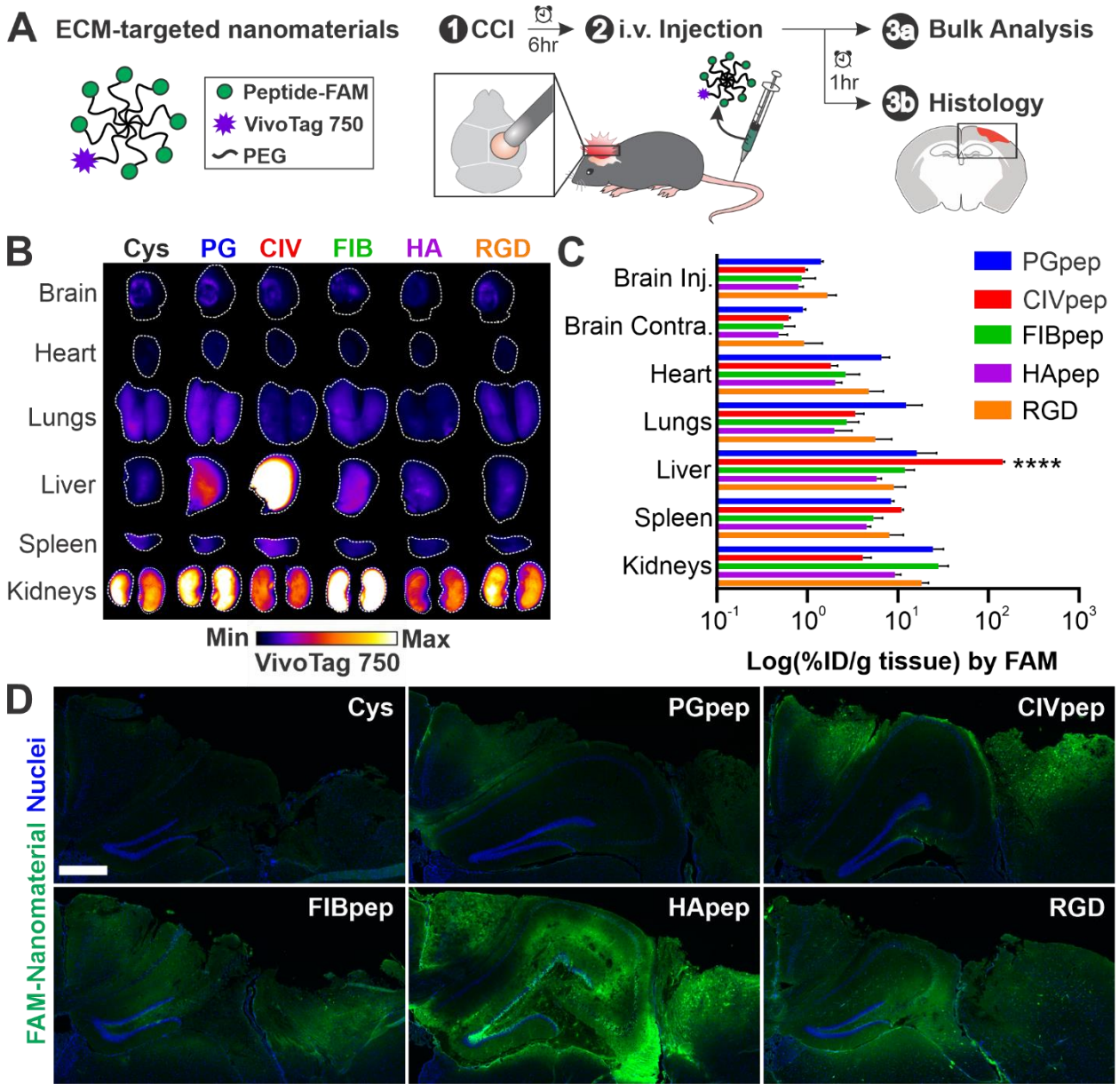

Figure 3.1**:** Nanomaterial modification with HA-targeting peptide leads to widespread distribution in the injured brain after systemic administration.(A) Schematic of ECM-targeted nanomaterials and overview of experimental design. 6 hours post-CCI, ECM-targeted nanomaterials were intravenously administered. After 1 hour, organs were harvested for analysis of nanomaterial biodistribution and histology. (B) Surface imaging of VivoTag 750 from major organs of one representative mouse per nanomaterial (n = 3, white line indicates outline of organ). (C) Bulk quantification of percent injected dose nanomaterial per gram (%ID/g) tissue based on FAM fluorescence (n = 3, mean ± SE, ****$p \leq 0.0001$, two-way ANOVA and Tukey's multiple comparisons post-hoc test within each organ group). (D) Representative images of the injured cortex in coronal brain slices (n = 3; blue, nuclei; green, FAM-labeled ECM-targeting peptide on nanomaterial; scale bar = 500 µm).

While surface imaging gives spatial distribution within an organ, it is limited by imaging depth and we therefore performed a bulk analysis of homogenized organs to quantify nanomaterial accumulation. Bulk quantitative biodistribution analysis was based on fluorescence signal from the FAM label on the peptide which was used to calculate the percent injected dose per gram tissue (%ID/g tissue) from a standard of known peptide concentrations. We observed that bulk quantitative analysis was largely consistent with surface imaging (Figure 3.1C). CIVpep-modified nanomaterials significantly accumulated in the liver over all nanomaterials modified with other ECM peptides (between 8.9-fold and 24.8-fold). Moreover, nanomaterials modified with PGpep and FIBpep had the highest overall kidney accumulation, followed by RGD. The ECM-targeting peptides did not appear to have significant impacts on total accumulation in the injured brain (%ID/g between 0.80 and 1.68), consistent with previous observations that targeting has modest effects on total tissue accumulation.[21,22,24,26] Considering that the targeting peptides we investigated bind to the ECM, we posit that nanomaterials must first encounter the ECM through passive targeting and therefore ECM-targeting peptides would be unlikely to contribute to changes in total brain accumulation. This is further corroborated by similar blood half-lives measured for each ECM-targeted nanomaterial (Figure 3.2); previous work has established that passive accumulation after systemic administration correlates with blood half-life due to a maintenance of a concentration gradient of nanomaterials between the blood and target tissue.[55]

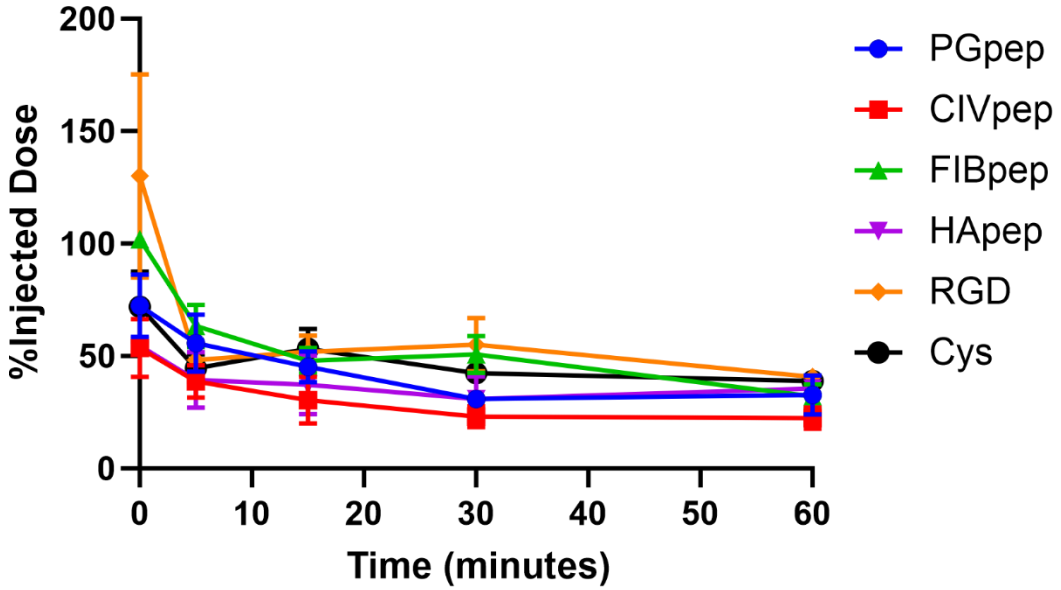

Figure 3.2: Percent injected dose of ECM-targeted nanomaterials in the blood at 0, 5, 15, 30, and 60 minutes after intravenous administration (n = 3, mean ± SE).

To investigate the spatial distribution of nanomaterials in the injured brain at greater depth and resolution than could be achieved with surface imaging, we completed a qualitative comparison of nanomaterial distribution in brain sections following immunostaining with an α-FAM antibody (Figure 3.1D, Table 3.2).

Table 3.2**:** Immunostaining reagents and their dilutions used in this study.

Target and supplier	Dilution	Product #
fluorescein/Oregon Green (ThermoFisher)	2.5 µg/mL	A-889
fluorescein/Oregon Green *(alternate)* (ThermoFisher)	5.0 µg/mL	A-11095
NeuN (Millipore Sigma)	0.6 µg/mL	MAB377
CD31 (BD)	2.5 µg/mL	553370
biotinylated hyaluronic acid binding protein (bHABP) (Sigma)	5.0 µg/mL	385911

We observed a marked increase in the distribution of HApep-modified nanomaterials in the injured area of the brain compared to the other peptide-modified nanomaterials. This observation was consistent across triplicate brains (Figure 3.3). To verify that the FAM-immunostaining was specific, we used an alternate α-FAM antibody and observed the same outcome (Figure 3.4). The non-targeted nanomaterial served as a negative control for non-specific staining since no FAM was present on that nanomaterial. The widespread distribution of HApep-modified nanomaterial in the tissue proximal to the injury was observed despite the lack of appreciable differences measured in bulk analysis of FAM signal. This may be due to the reduced sensitivity of measurement in the bulk analysis since antibody staining was used to image nanomaterial in brain sections. In addition, analysis of brain sections revealed that nanomaterial was largely restricted to the cortical and hippocampal tissue in close proximity to the injury, whereas in bulk quantification the whole hemisphere was homogenized potentially diluting total nanomaterial signal. Our results were also consistent with previous studies that establish active targeting has greater impacts on intra-tissue distribution of nanoparticles over bulk accumulation.[22]

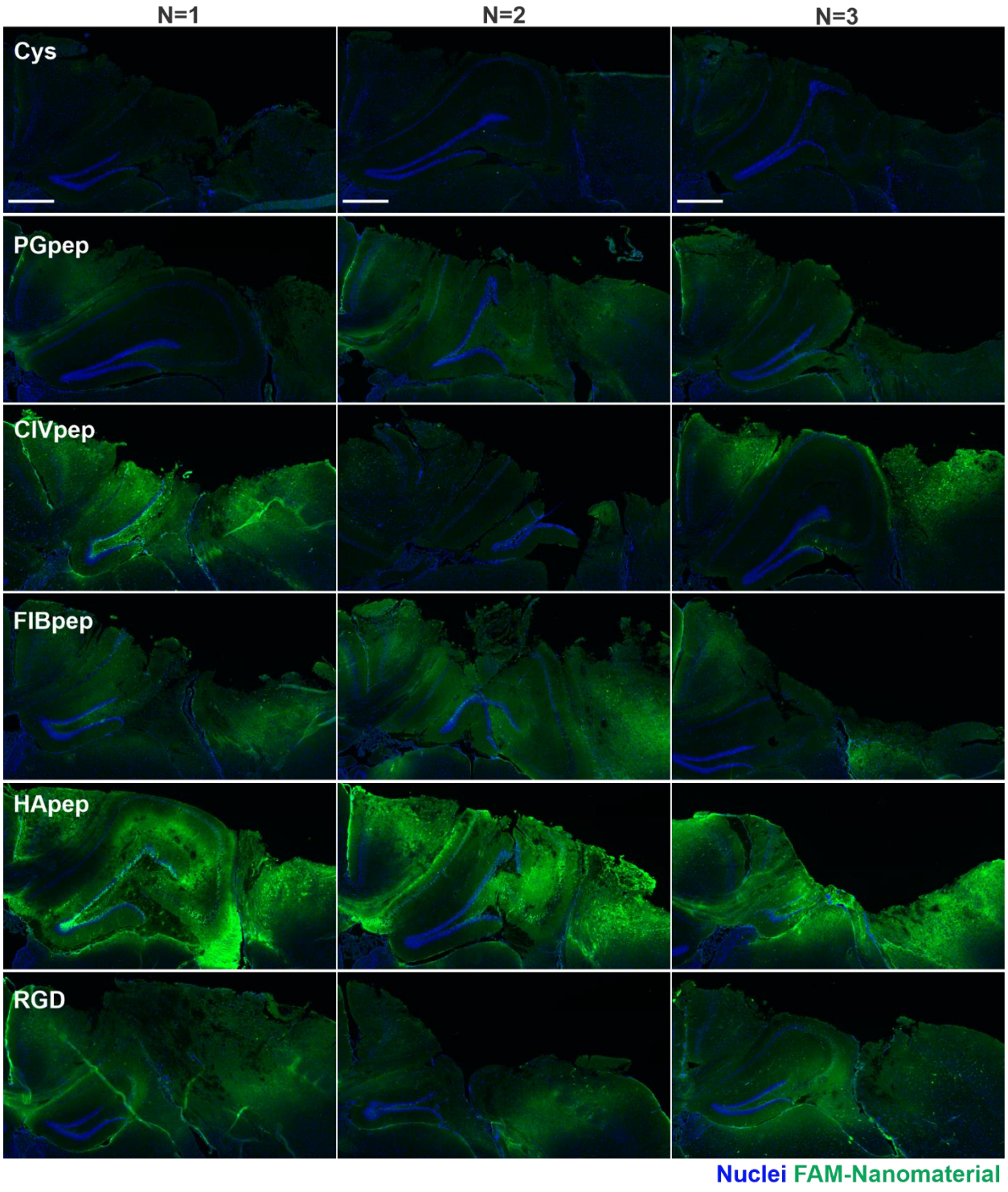

Figure 3.3: Triplicate histology in coronal brain slices of ECM-targeting peptides used in the in vivo screen (blue, nuclei; green, FAM-labeled ECM-targeting peptide on nanomaterial; scale bar = 500 μm).

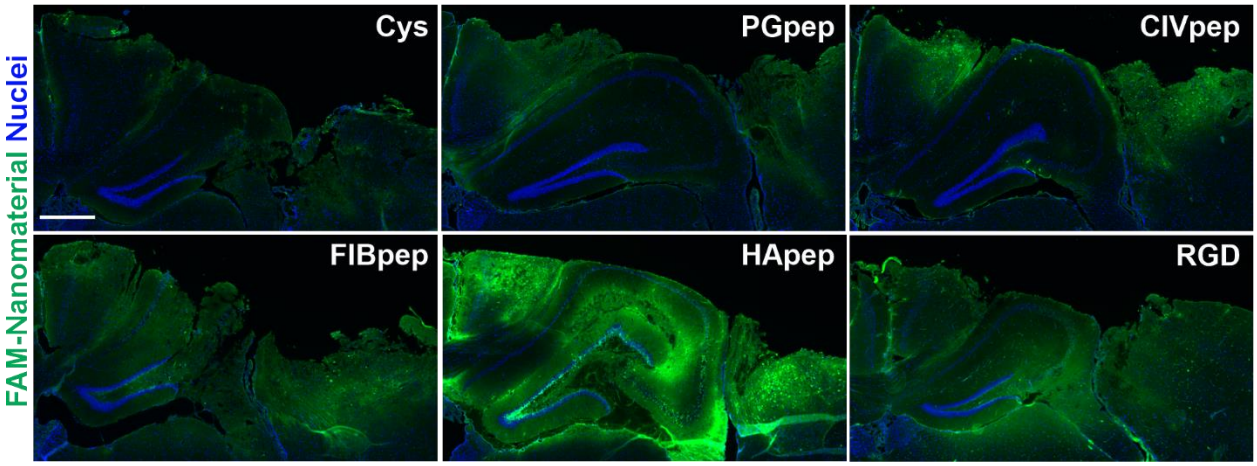

Figure 3.4**:** Coronal brain slices stained with an alternate α-FAM antibody, ThermoFisher A-11095 (blue, nuclei; green, FAM-labeled ECM-targeting peptide on nanomaterial; scale bar = 500 μm).

3.3.2. Hyaluronic acid-targeted nanomaterial accumulates within injured brain tissue and colocalizes with hippocampal and cortical neurons.

Having demonstrated that nanomaterials modified with peptides that target HA have improved distribution within the injured brain over peptides that target other ECM components, we sought to further characterize the tissue-level distribution of this nanomaterial. We stained and imaged both the uninjured contralateral and injured ipsilateral hemispheres in coronal brain sections and observed that nanomaterial localization is specific to the injured hemisphere with minimal signal in the uninjured hemisphere (Figure 3.5A), consistent with our previous observation (Figure 3.1B). Nanomaterial accumulation coincided with areas of tissue trauma in the right hemisphere, where the CCI was applied. Within the injury, there was significant nanomaterial signal in the perilesional cortical and hippocampal regions.

Next, to identify nanomaterial localization around brain cells of interest, we performed immunostaining for neurons — a major source of calpain-1[56,57] and the cellular target for neuroprotective therapeutics.[58] HApep-modified nanomaterial was found to colocalize with

subsets of both cortical and hippocampal neurons (Figure 3.5B). In the perilesional cortex (Figure 3.5Bi), nanomaterial localized to neurons adjacent to tissue trauma and similarly, nanomaterial localized to neurons in the hippocampal region (Figure 3.5Bii).

We next compared the localization of our HA-targeted nanomaterial to the spatial distribution of endogenous HA. A biotinylated hyaluronic acid binding protein (bHABP) was used to visualize native HA, as described previously.[59–62] Consistent with published literature,[60–62] regions with HABP binding were enriched in the hippocampus and cerebral cortex (Figure 3.5C). The staining of bHABP in both the cortex (Figure 3.5Ci) and hippocampus (Figure 3.5Cii) was mainly diffuse, although enrichment was observed around the cell bodies of hippocampal neurons and select neurons in the cortex. This observation is consistent with literature, as HA is a known component of perineuronal nets (PNNs) that surround neuronal cell bodies.[60] In some instances, our HA-targeted nanomaterial colocalized with cells with HABP perineuronal staining in both the cortex and hippocampus (Figure 3.5Ci-ii, arrows). Differences observed between the distribution of HABP staining of brain slices and systemic administration of HApep-modified nanomaterial are likely due to limited access of intravenously administered nanomaterial across the damaged vasculature and extracellular space.[19,46] Additionally, there are likely differences between the specificity of HABP and the short peptide ligand HApep since the modes of discovery and composition are divergent.[42,59]

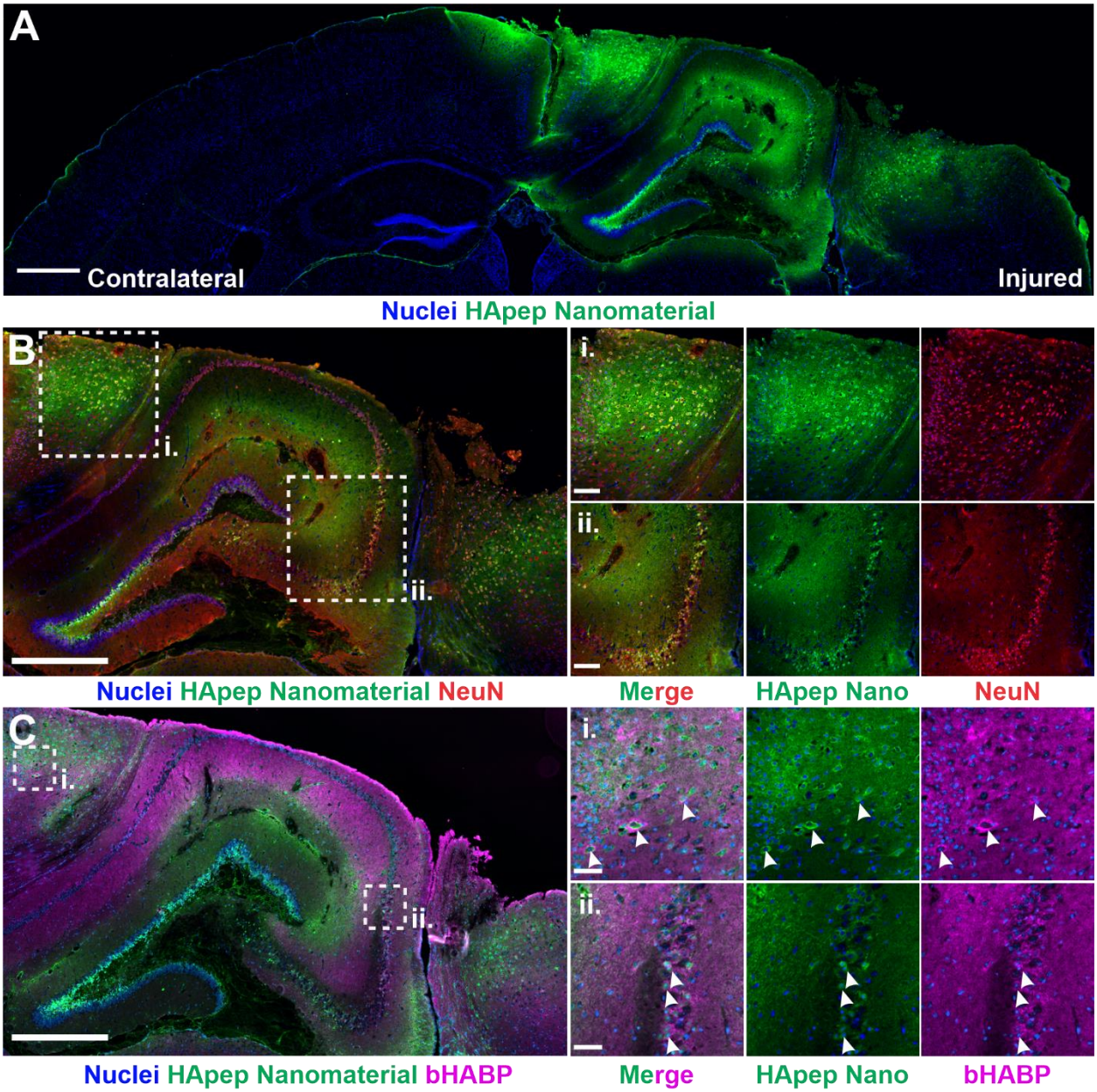

Figure 3.5**:** Hyaluronic acid-targeted nanomaterial distributes across perilesional brain tissue in CCI-injured brains. (A) Coronal brain sections from mice administered i.v. HApep-modified nanomaterial 6 hours post-CCI after 1 hour of circulation (blue, nuclei; green, HApep on nanomaterial; scale bar = 500 µm). (B) HApep-modified nanomaterial in the injured cortex stained for neurons (red, NeuN; scale bar = 500 µm). Insets show (i) perilesional cortex and (ii) hippocampus (scale bar = 100 µm). (C) Injured cortex labeled with biotinylated hyaluronic acid binding protein (magenta, bHABP; scale bar = 500 µm). Insets show (i) perilesional cortex and (ii) hippocampus (scale bar = 50 µm). Arrows note instances of nanomaterial colocalization with HABP staining.

3.3.3. Targeting hyaluronic acid enhances the in vivo sensitivity of an activity based nanosensor for TBI (TBI-ABN).

We previously developed an activity based nanosensor for TBI (TBI-ABN) for detection of calpain-1 protease activity in a mouse model of TBI.[10] The TBI-ABN consists of a FRET pair (fluorophore: Cy5, quencher: QSY21) separated by the calpain-1-cleavable peptide sequence QEVYGAMP, which is derived from a native calpain-1 substrate, αII-spectrin,[63] attached to 40 kDa 8-arm PEG, the same polymeric scaffold that we used to evaluate brain ECM-targeting peptides (Figure 3.1). When active calpain-1 protease is present, the FRET substrate on TBI-ABN is cleaved, leading to dequenching of Cy5 fluorescence. We previously demonstrated that TBI-ABN could passively accumulate in the injured brain and generate fluorescent signal in response to locally activated calpain-1 after systemic administration in CCI-injured mice.[10] As a demonstration that spatial localization in the TBI microenvironment can increase the activity of nanomaterials, we proposed that the addition of active targeting ligands would improve signal generation from TBI-ABN. We previously established that the addition of tumor targeting increased the sensitivity of an activity-based protease nanosensor for cancer via in silico and experimental analyses.[20] In the context of TBI, we hypothesized that the incorporation of HA targeting in our TBI-ABN design would increase nanosensor activation since HA-targeted nanomaterial colocalized within perilesional cortical and hippocampal neurons (Figure 3.5), and neurons are a major cellular source of calpain-1.[56,57]

We synthesized TBI-ABNs with varying degrees of HA targeting in order to investigate the relationship between ligand valency and TBI-ABN activation in vivo. This was motivated by the phenomenon that multivalent molecular interactions confer enhanced overall binding strength (i.e., avidity) and increase the likelihood for binding events to occur.[64] Previous studies have

established the importance of tuning binding avidity for nanomaterial targeting; for example, increasing densities of transferrin targeting ligand on gold nanoparticles led to an increase in nanoparticle localization in tumor cells, although higher ligand density also increased off-target uptake by hepatocytes.[22] In order to create TBI-ABNs with matched amount of calpain-1 FRET substrate peptide and varying levels of targeting for comparison studies, a 1:1 stoichiometry of calpain FRET substrate and 8-arm PEG was reacted, split into three parts, and HApep added at stoichiometric ratios of 0, 4, and 7 to yield non-targeted, moderate-targeted, and high-targeted TBI-ABNs respectively (Figure 3.6A). Absorbance measurements verified that stoichiometric ratios of HApep to calpain FRET peptide on the TBI-ABN were 0, ~3.2, ~8.5 for non-, moderate- and high-targeted TBI-ABNS respectively (Table 3.3). In order to verify that HApep modification of TBI-ABN did not significantly impact nanosensor performance, non-, moderate-, and high-targeted TBI-ABNs were incubated with human calpain-1 enzyme at various concentrations to construct Michaelis-Menten kinetics curves. Maximum cleavage velocities for non-, moderate-, and high-targeted TBI-ABNs were 120.0 RFU/min, 73.72 RFU/min, and 76.13 RFU/min respectively, indicating that the incorporation of HApep moderately decreased calpain-1 cleavage kinetics of TBI-ABN (Figure 3.6B).

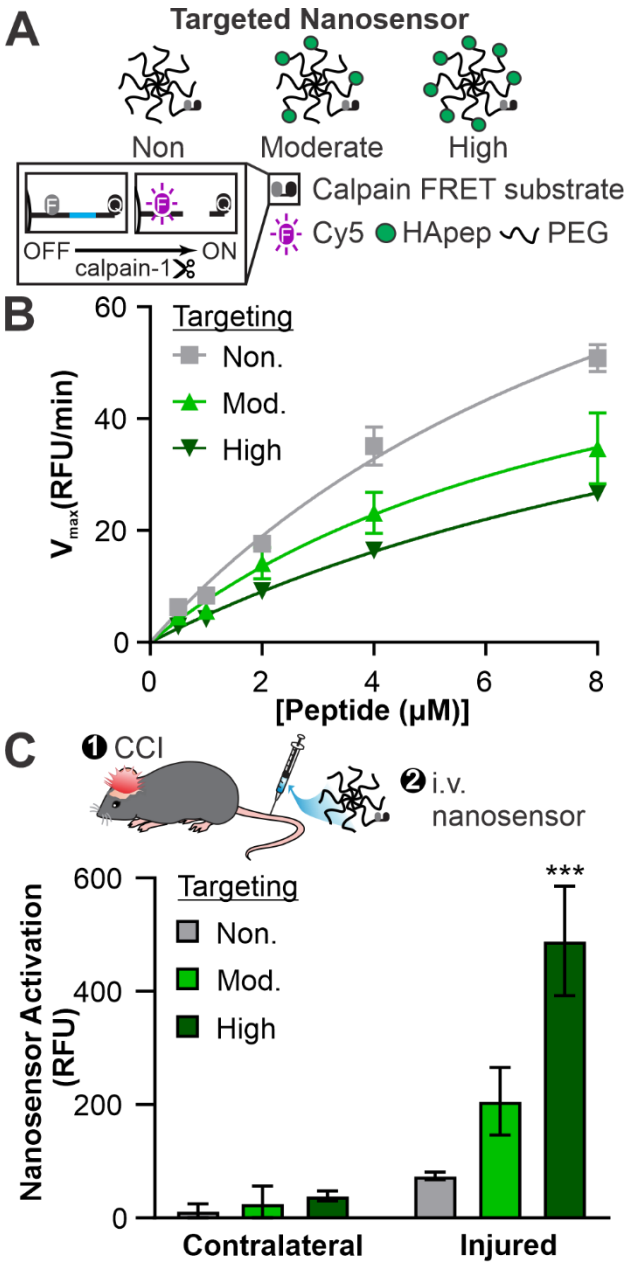

Figure 3.6**:** Hyaluronic acid targeting improves nanosensor signal generation in a CCI mouse model of TBI. (A) Schematic of HApep-modified nanosensors with no, moderate, and high targeting. (B) Michaelis-Menten cleavage kinetics of nanosensors incubated with human calpain-1 (n = 3, mean ± SD). (C) Activated nanosensor signal measured in cortical brain tissue lysate collected from the contralateral and injured hemispheres (n = 3, mean ± SE, ***$p \leq 0.001$, two-way ANOVA with Sidak's multiple comparisons post-hoc test compared to non-targeted groups).

Table 3.3**:** Concentration measurements of calpain substrate peptide[a] and HApep[b] on TBI-ABNs in PBS.

TBI-ABN	Ratio of HApep to calpain substrate
Non-Targeted	N/A
Moderate-targeted	3.2
High-Targeted	8.5

[a]Calpain substrate absorbance measured at $\lambda = 646$ nm, $\varepsilon_{646\ nm} = 112{,}783.33\ (M*cm)^{-1}$
[b]HApep absorbance measured at $\lambda = 495$ nm, $\varepsilon_{495\ nm} = 75{,}000\ (M*cm)^{-1}$

A similar decrease in cleavage kinetics was observed when non-targeted TBI-ABNs were mixed with unconjugated HApep in molar ratios matching the moderate- and high-targeted TBI-ABNs, indicating that the presence of HApep independent of conjugation led to modest decreases in calpain-1 cleavage kinetics **(**Figure 3.7).

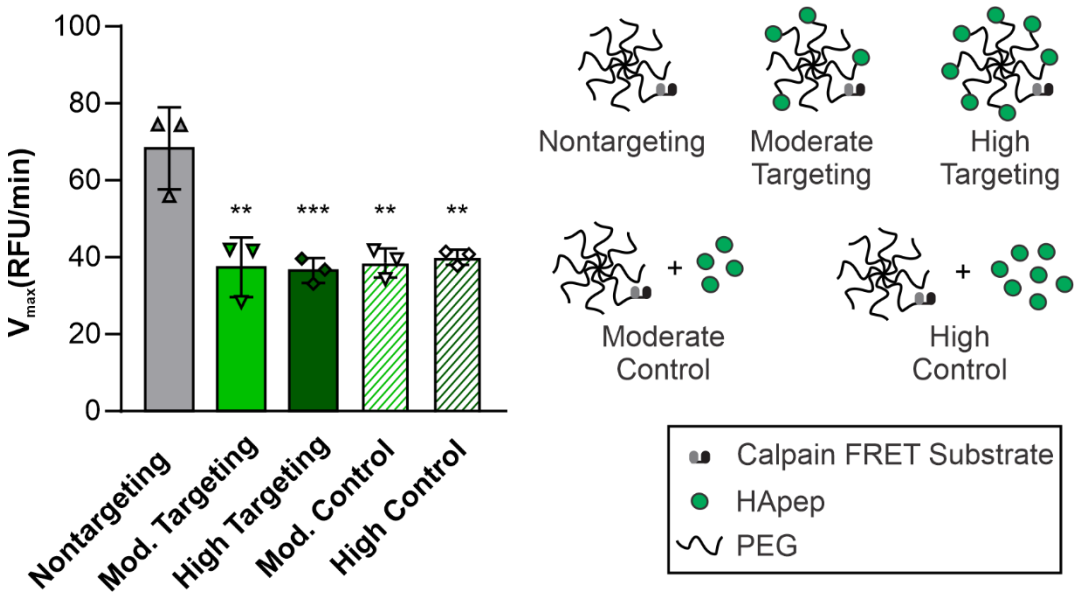

Figure 3.7: Maximal cleavage velocities of TBI-ABNs (8 µM quantified by calpain FRET substrate peptide) incubated with human calpain-1 and different levels of conjugated HApep (for targeting conditions) or unconjugated HApep (for control conditions) (n = 3, mean ± SD, **p ≤ 0.01, ***p ≤ 0.001, ordinary one-way ANOVA and Tukey's post-hoc test).

Next, we quantified TBI-ABN activation after intravenous administration in a mouse model of TBI. Non-, moderate-, and high-targeted nanosensors were administered via tail-vein at matched calpain-1 FRET substrate concentrations three hours after CCI, a time point when calpain-1 activation was measured to be locally increased in injured brain tissue.[10] One hour after nanosensor administration, fresh perilesional tissue and corresponding uninjured tissue from the contralateral hemisphere were collected and homogenized for bulk fluorescence analysis of dequenched FRET substrate from the TBI-ABN. Consistent with our previous observations, nanosensor activation was significantly greater in homogenate isolated from the injured hemisphere over the uninjured contralateral hemisphere by 6.2-fold, 8.1-fold, and 12.5-fold for non-, moderate-, and high-targeted TBI-ABNs respectively (Figure 3.6C). Comparing signal generation in the injured hemisphere across degrees of targeting, moderate and high targeting increased the levels of activated nanosensor signal by approximately 2.8-fold and 6.6-fold, respectively, over the non-targeted control. This increase in signal generation was observed despite the moderately decreased cleavage kinetics of HApep-modified TBI-ABNs measured in vitro with human calpain-1 enzyme (Figure 3.6B). Furthermore, Cy5 signal from activated nanosensor was greater than vehicle control and consistent across triplicate mice within each group (Figure 3.8). These results demonstrate that targeting TBI-ABN to the ECM increases activation within the injured brain in a valency-dependent manner. Although the high-targeted TBI-ABNs resulted in the highest overall signal in the brain, we also observed a concomitant increase in sensor activation in off-target organs compared to moderate- and non-targeted TBI-ABNs (Figure 3.9), suggesting that a moderate level of targeting may be desirable to achieve higher specificity of brain-to-off-target organ signal generation.

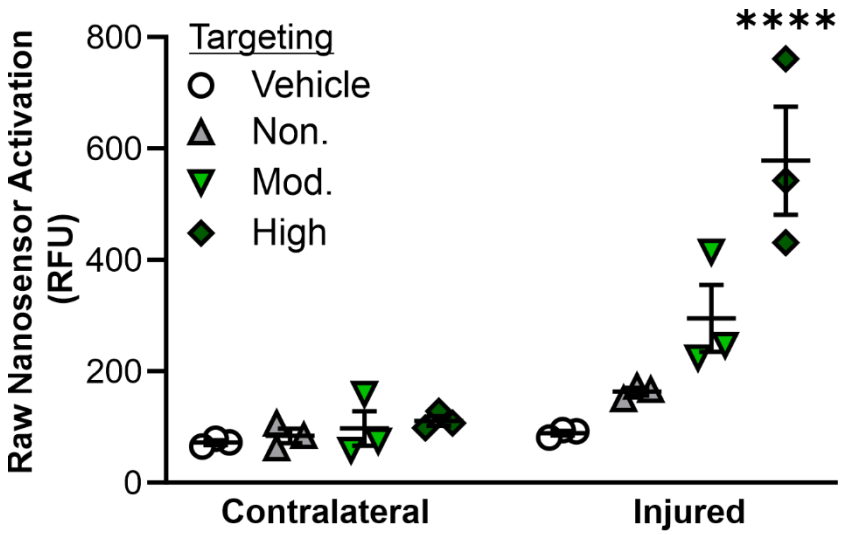

Figure 3.8. Raw activated nanosensor signal for non-, moderate-, and high-targeted TBI-ABN measured in cortical brain tissue lysate collected from contralateral and injured hemispheres, including background tissue signal from vehicle control (n = 3, mean ± SE, ****p ≤ 0.0001, two-way ANOVA with Sidak's multiple comparisons post-hoc test compared to non-targeted; each data point represents one mouse).

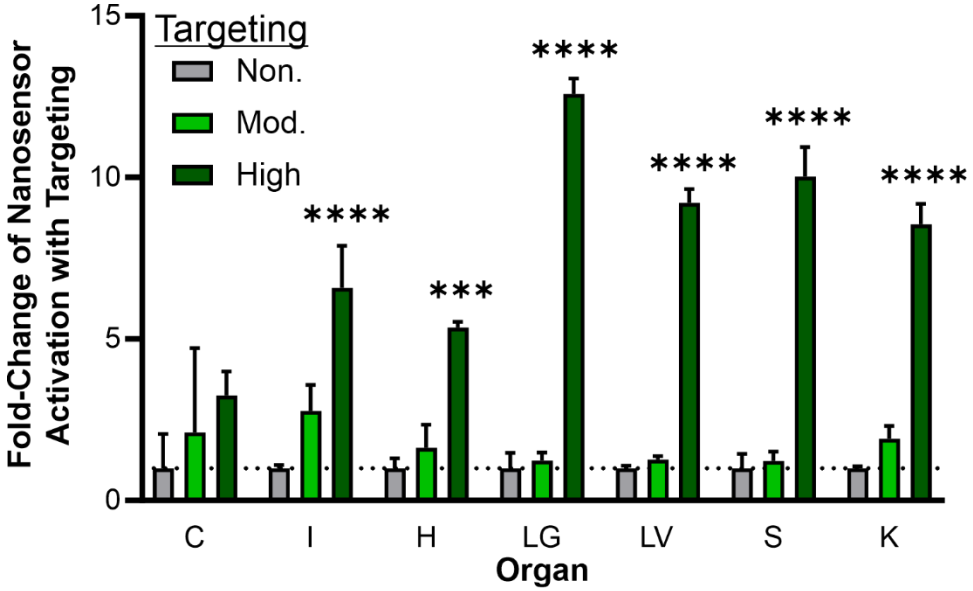

Figure 3.9: Relative fold-change of TBI-ABN activation in brain (C = contralateral cortical tissue; I = injured cortical tissue) and off-target organs (H = heart; LG = lungs; LV = liver; S = spleen; K = kidneys) compared to non-targeted TBI-ABNs (n = 3, mean ± SE, ***p ≤ 0.001, ****p ≤ 0.0001, two-way ANOVA with Dunnett's multiple comparisons post-hoc test compared to non-targeted groups within each organ).

3.3.4. Targeting hyaluronic acid enables widespread TBI-ABN activation in injured brain tissue.

Having established that HApep modification of TBI-ABNs leads to an increase in bulk nanosensor activation in homogenized tissue lysate, we then set out to establish spatial activation of TBI-ABN in the injured brain tissue. The same experimental paradigm was repeated in triplicate, and coronal brain sections were imaged for activated nanosensor via dequenched Cy5 signal and nanosensor localization via the FAM label on HApep. We observed distinct nanosensor activation in all three HApep modification levels (non-, moderate-, and high-targeted) compared to the vehicle control (Figure 3.10), consistent with previous work.[10] In mice administered TBI-ABN with moderate or high HApep valency, there was an observable increase in both nanosensor distribution within the injured cortex and nanosensor activation. The nanosensor tissue distribution resembled that of HApep nanomaterial (Figure 3.5) with accumulation in both the perilesional cortex and hippocampus, indicating the FRET substrate did not have a large impact on distribution, as expected with the low stoichiometry modification (Figure 3.10). The pattern of nanosensor activation in the perilesional cortex and hippocampus were consistent across triplicate brains within each group, although one brain with high-targeting had significantly increased signal generation compared to replicates in the same group (Figure 3.11).

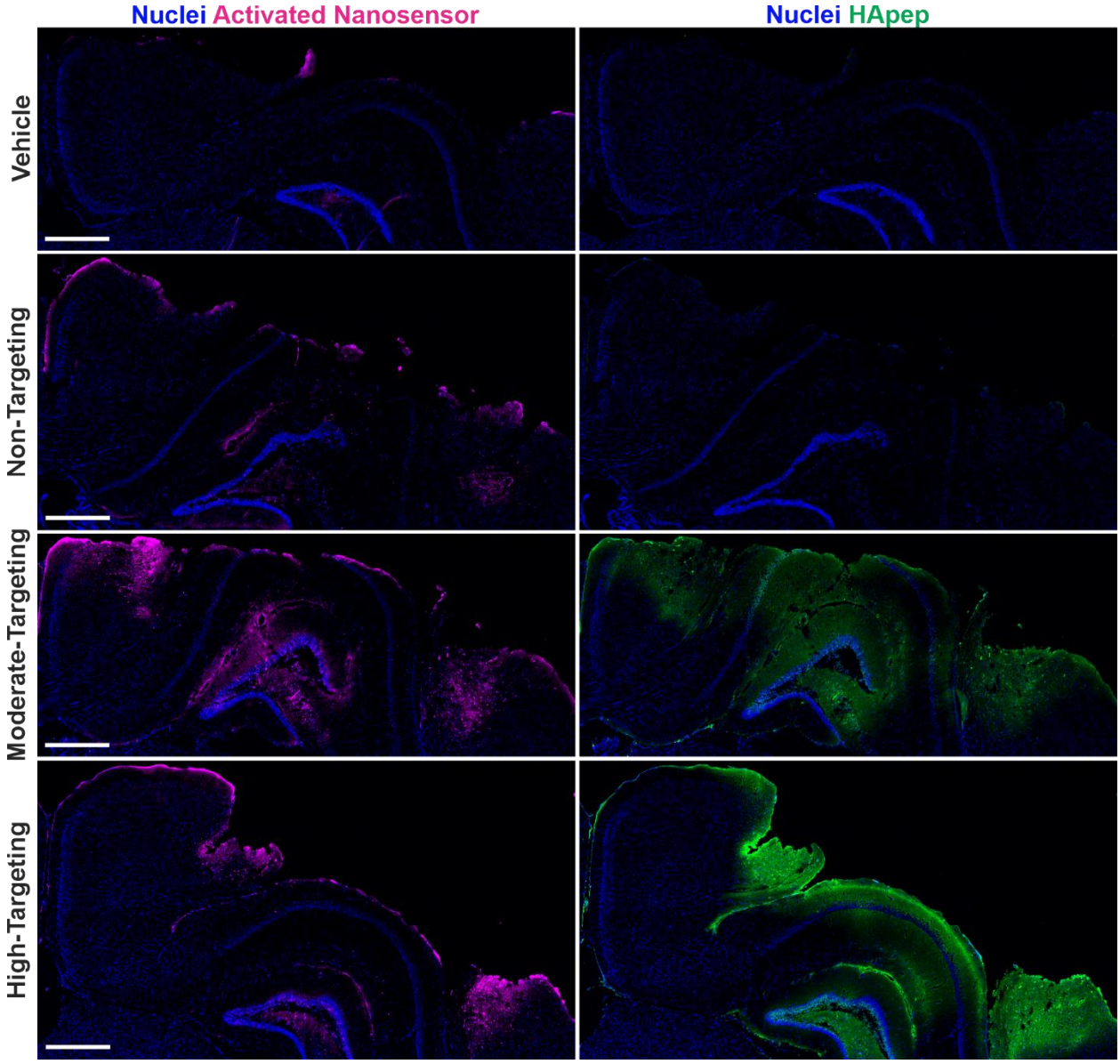

Figure 3.10**:** Hyaluronic acid peptide targeting increases overall TBI-ABN activation and distribution within coronal sections of the injured hemisphere. Injured hemispheres from CCI-injured mice (representative brains from triplicate) after intravenous administration of vehicle or nanosensors with non-, moderate-, or high-targeting modification (blue, nuclei; magenta, activated nanosensor; green, HApep on nanosensor; scale bar = 500 μm).

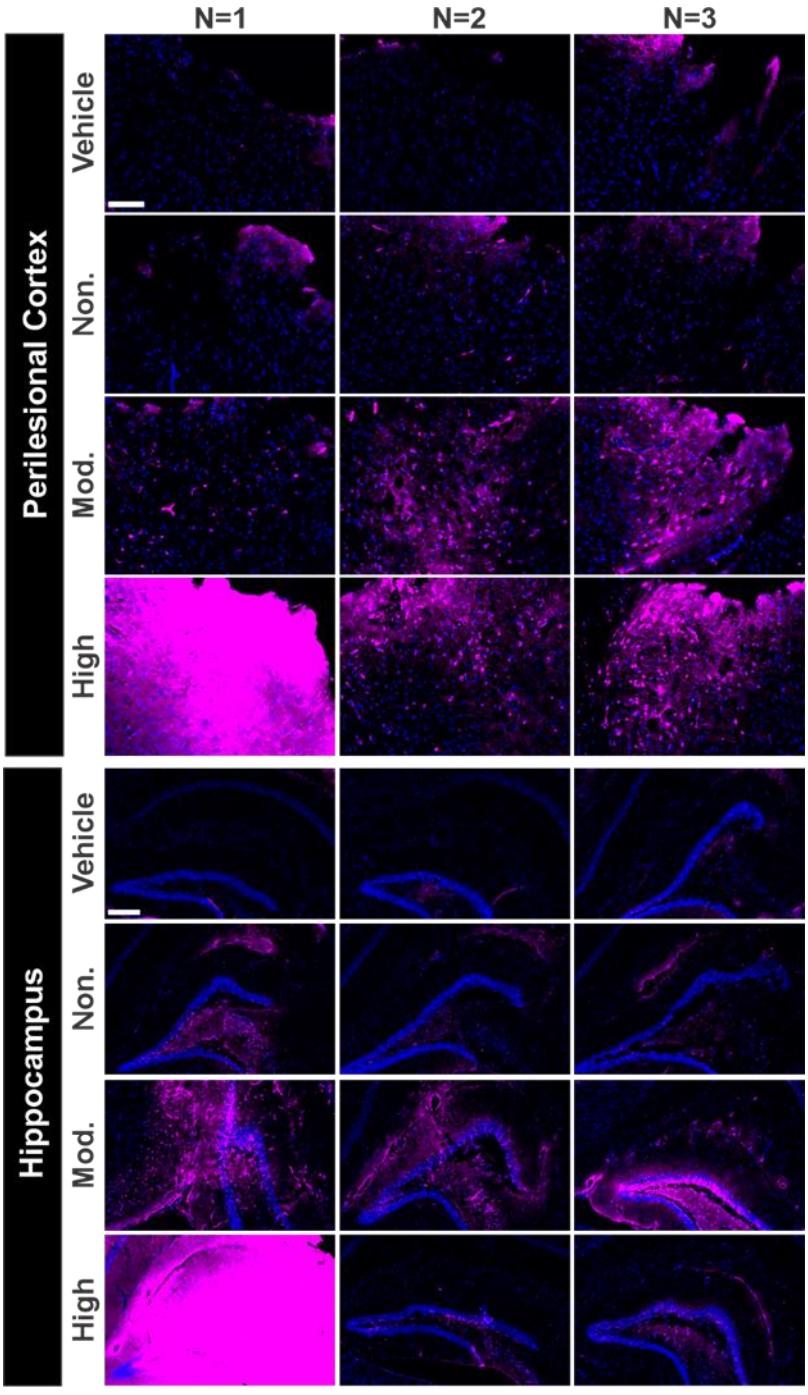

Figure 3.11: Nanosensor activation in triplicate brains for vehicle, non-targeted, moderate HApep-targeted, and high HApep-targeted TBI-ABN in the perilesional cortex and hippocampus (scale bar = 100 µm for perilesional cortex, scale bar = 200 µm for hippocampus; blue, nuclei; magenta, activated nanosensor).

We note that the pattern of nanosensor distribution was distinct from the pattern of nanosensor activation, indicating some level of specificity of nanosensor activation. Overall, the brain sections reflected quantitative measurements made in bulk homogenates (Figure 3.6) and further supported our conclusion that incorporation of HA-targeting ligands increased nanosensor activation in the brain compared to non-targeted control. Since the high-targeted TBI-ABN yielded the maximal fold-increase of nanosensor activation in the brain, subsequent studies were performed with this nanomaterial.

Next, we investigated the distribution of activated TBI-ABN within the brain's cellular milieu because understanding the cellular localization of proteolytic activity could offer insight into TBI pathophysiology. Neurons are a major source of calpain-1 in the brain[56,57] and we have established that HA-targeted nanomaterial predominantly accumulates within cortical and hippocampal neurons proximal to the injury (Figure 3.5). Furthermore, endothelial cells can also contribute to abnormal calpain activation[65,66] and we expected nanosensor to have access to endothelial cells due to the vascular administration route.[10] We therefore investigated the activation of HA-targeted TBI-ABN in the context of neuronal and endothelial cell staining (Figure 3.12). In the perilesional cortex (Figure 3.12A), activated nanosensor signal colocalized with $NeuN^+$ neurons and $CD31^+$ endothelial cells. In the hippocampus (Figure 3.12B), activated nanosensor colocalized mainly with neurons, consistent with HA-targeted nanomaterial accumulation. Importantly, activation of nanosensor was distinct from the presence of nanosensor imaged by the FAM label on HApep in both $NeuN^+$ neurons and $CD31^+$ endothelial cells. Interestingly, the pattern of TBI-ABN activation in perilesional hippocampal and cortical neurons that we observed in our study was accordant with the pattern of neurodegeneration observed in previous studies that stained for degenerating neurons up to ~1 week after injury.[53,67]

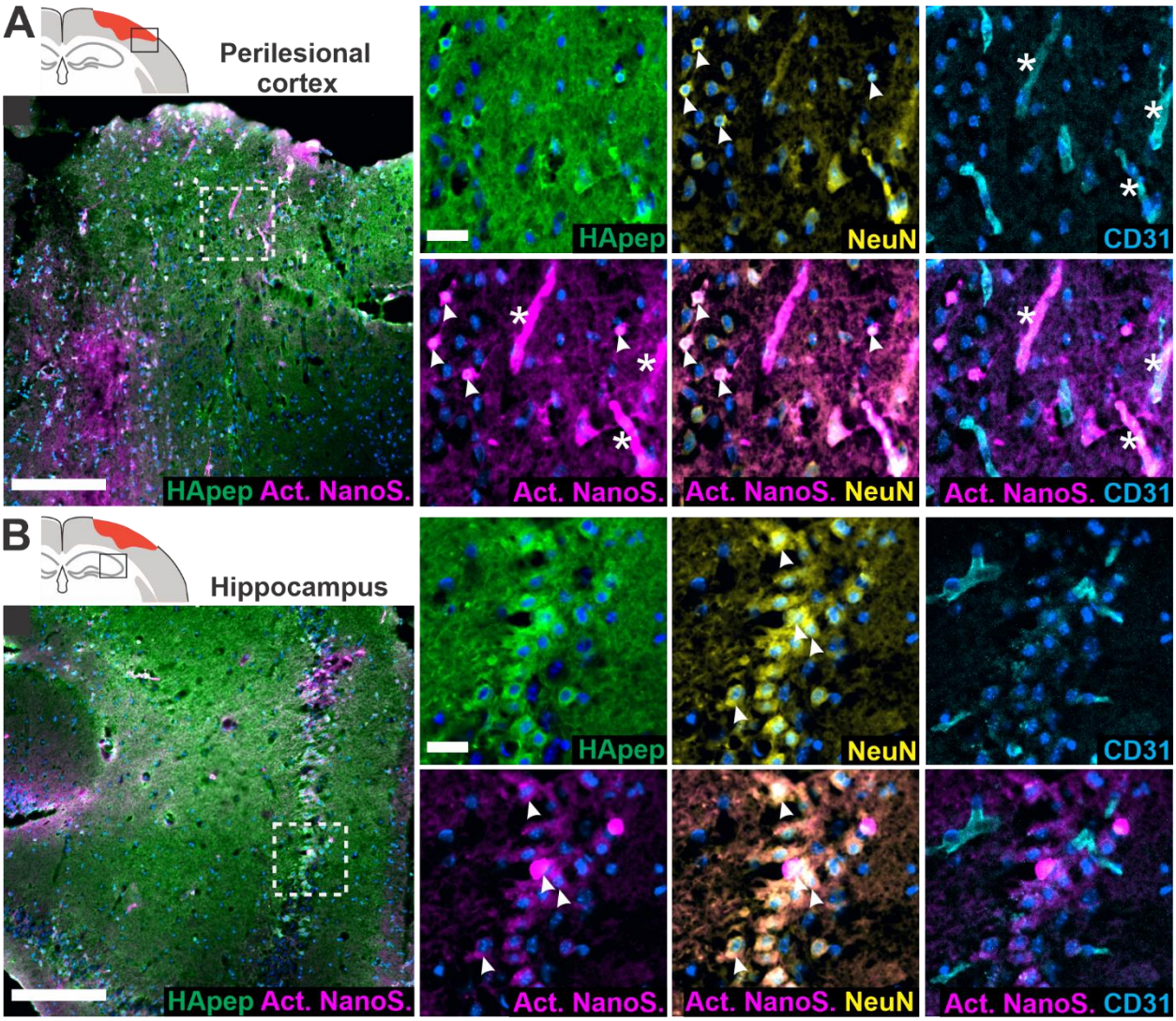

Figure 3.12**:** Hyaluronic acid-targeted nanosensor activates within neuronal and endothelial cells in the perilesional cortex and hippocampus. Images from the (A) perilesional cortex and (B) hippocampus imaged for nanosensor distribution and activated nanosensor (box in schematic indicates imaging location). Immunostaining was performed for HApep (green, FAM), neurons (yellow, NeuN), and endothelial cells (cyan, CD31) (blue, nuclei; magenta, activated nanosensor; scale bar = 200 μm for larger images and 25 μm for insets). Colocalization of nanosensor activation with neurons or endothelial cells are denoted with arrows or stars, respectively.

The robust activation of HA-targeted TBI-ABN enabled the capture of macroscopic 3D spatial heterogeneity of protease activation across the TBI lesion in intact brains. We performed whole brain tissue clearing after TBI-ABN administration in CCI-injured mice with CUBIC (Clear, Unobstructed Brain/Body Imaging Cocktails and Computational analysis),[68] which enabled removal of light scattering components while matching the brain refraction index to the imaging media (Figure 3.13, Figure 3.14A). Cleared brains were imaged with light sheet fluorescence microscopy (LSFM) for TBI-ABN localization and activation (Figure 3.14B-C). The imaged volume was a 9.7 x 4.5 x 3.3 mm rectangular prism that encompassed the injured and contralateral cortices. A 3D rendering was generated of both TBI-ABN localization and activation based on the fluorescence of FAM on HApep and Cy5 on the dequenched FRET substrate, respectively (Figure 3.14B).

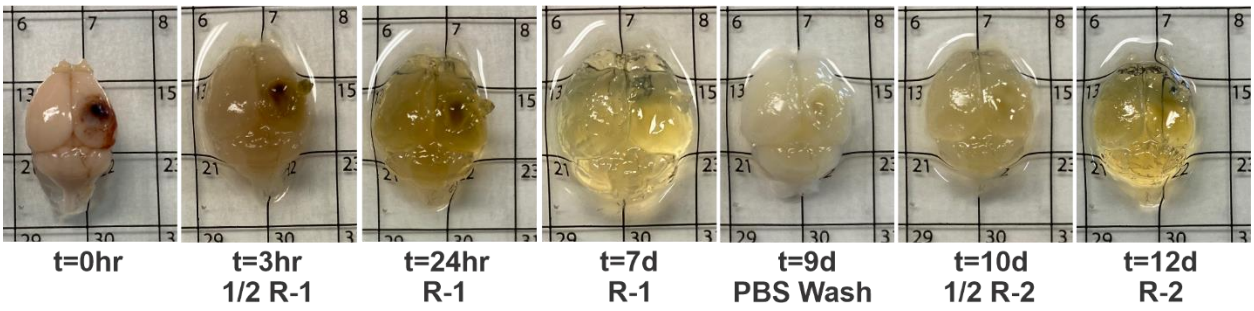

Figure 3.13: CUBIC clearing progress for excised injured brain demonstrating progressive clearing over 12 days following sequential incubations with reagent-1 (R-1) and reagent-2 (R-2).

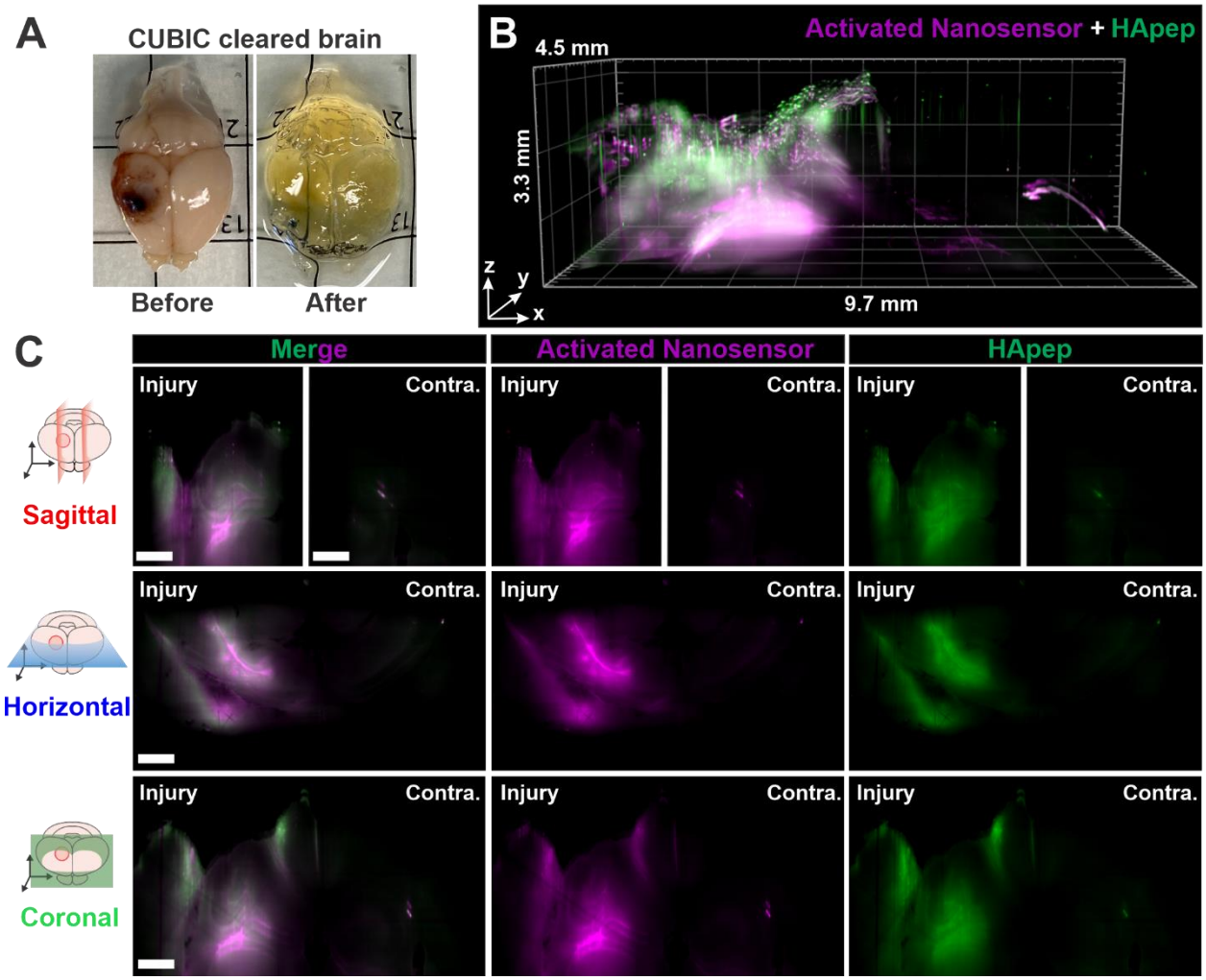

Figure 3.14: Light sheet fluorescence microscopy (LSFM) of cleared tissues enables 3-dimensional (3D) reconstruction of nanosensor activation within the injured brain. (A) Image of injured brain before and after whole brain CUBIC clearing. (B) 3D render view. (C) Sagittal, horizontal, and coronal cross sections (magenta, activated nanosensor; green, HApep on nanosensor; scale bar = 1 mm; Contra. = contralateral hemisphere). See Figure 3.15 for the clipping planes used to generate the cross-sections.

Robust nanosensor activation was observed in the perilesional cortex in all directions from the injury lesion, approximately 2 mm away from the injury epicenter, and in the hippocampal formation directly below the injury. A cylindrical pattern of nanosensor activation around the impact epicenter was observed, as demonstrated by horizontal cross sections at three optical sectioning depths (Figure 3.15). Furthermore, cross-sectional views of the injury (Figure 3.14C), generated using sagittal, horizontal, and coronal clipping planes (Figure 3.16),

demonstrated that robust sensor activation was confined to the area proximal to the injury with minimal nanosensor activation detected in the contralateral hemisphere. Our 3D imaging corroborated the injury-specific activation observed in 2D imaging from brain sections (Figure 3.10 and Figure 3.12). Overall, volumetric optical sectioning of cleared brains enabled spatial visualization of activated nanosensor, showing the extent of calpain-1 protease activity in relation to the injury.

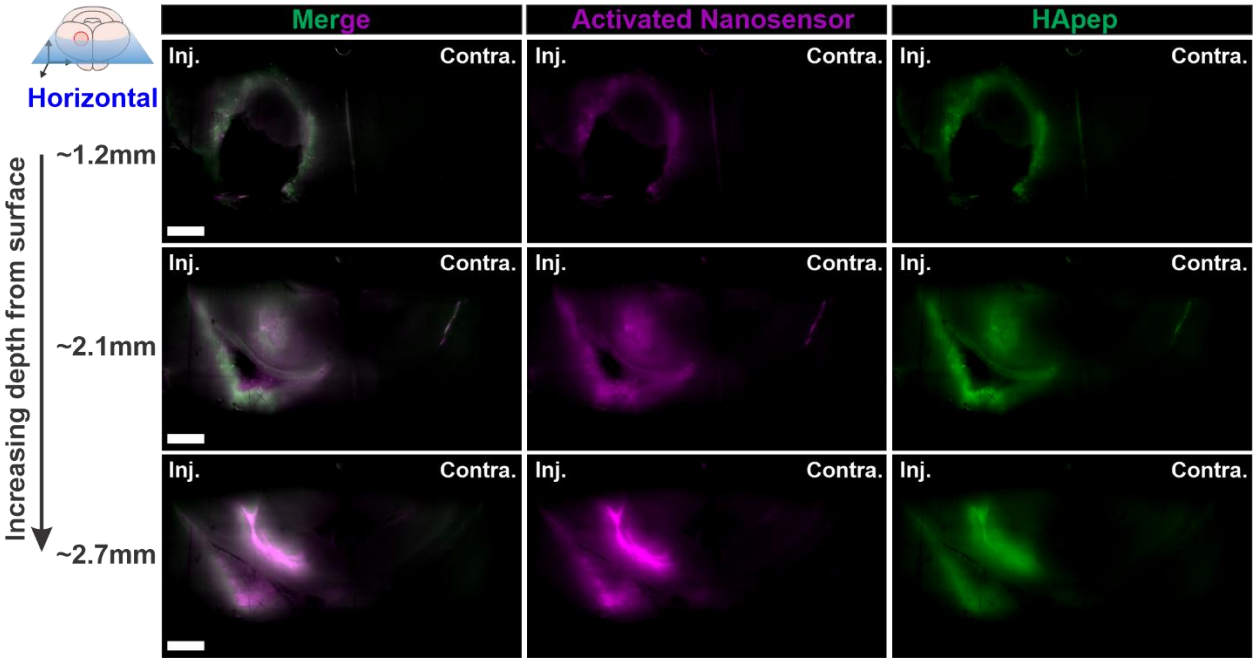

Figure 3.15: Light sheet fluorescence microscopy (LSFM) horizontal cross sections of cleared brain over three imaging depths from the cortical surface (1.2 mm, 2.1 mm, 2.7 mm) (magenta, activated nanosensor; green, HApep on nanosensor; scale bar = 1 mm; Inj. = injured hemisphere; Contra. = contralateral hemisphere).

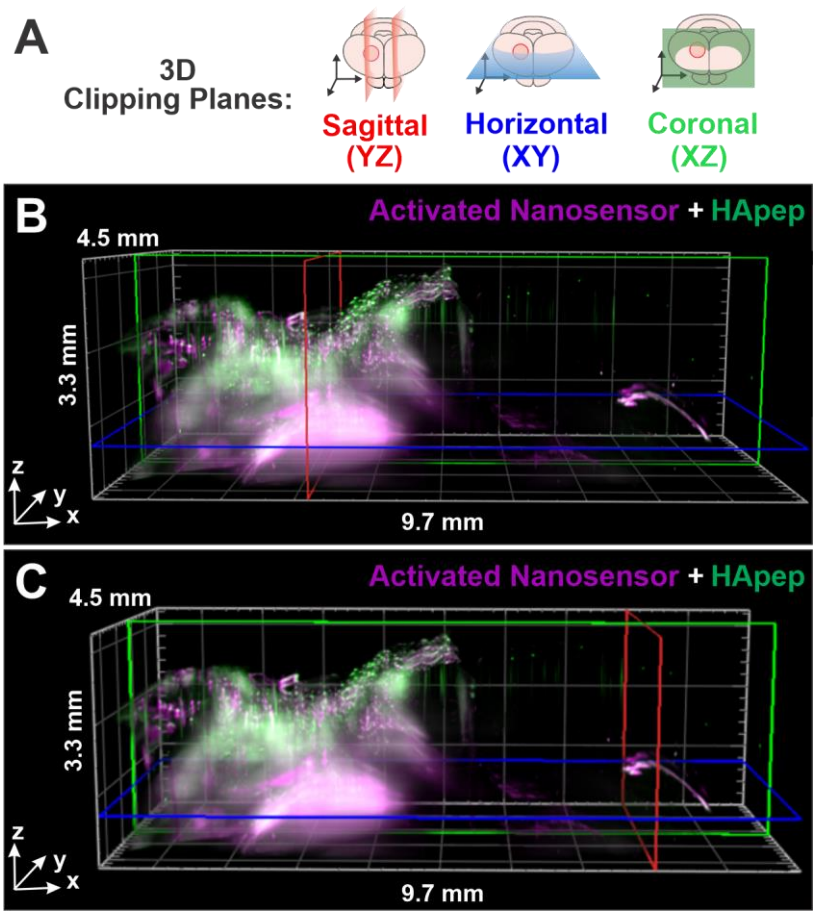

Figure 3.16: 3D rendering of TBI-ABN in the injured brain with clipping planes. (A) Schematic of sagittal (red, YZ), horizontal (blue, XY), and coronal (green, XZ) planes. (B) 3D render showing the three clipping planes with the sagittal plane located in the injured cortex. (C) 3D render showing the same clippling planes but with the sagittal plane in the contralateral cortex. (magenta, activated nanosensor; green, HApep on nanosensor).

3.4. Conclusions

Aberrant protease activity is linked to a worsening of TBI pathophysiology and prognosis[5–7] and tools to measure protease activity in the injured brain would allow for greater understanding of TBI progression. In this manuscript, the addition of HA-targeting peptides to a previously developed activity-based nanosensor for TBI[10] led to a robust signal that enabled visualization of protease activity in an intact brain. The HA-targeting peptide, which is reported to have a dissociation constant between ~0.1-10 µM depending on HA length,[42,43] was selected

following an in vivo screen of ECM-binding peptides.[42] We observed that the addition of HA-targeting peptide increased TBI-ABN activation in a valency-dependent manner, consistent with observations that avidity strengthens with increasing peptide valency.[64] Beyond nanosensors, our results provide impetus to apply ECM targeting as a generalizable strategy to improve nanomaterial distribution and function within the injured brain after systemic administration.

Activity-based nanosensors are useful tools to probe protease activity in various disease states and can thus serve as imaging tools or biomarkers for diagnosis and prognosis.[8,9] We have shown that active targeting to brain ECM is a viable method to improve bioavailability of our nanosensor in the brain post-TBI, and thus increase both protease-dependent signal generation and sensitivity. Beyond improvements in sensitivity, the TBI-ABN design can incorporate the measurement of multiple proteases to further specify TBI-associated protease activity. Multiplexed detection of several disease-specific proteases has enhanced diagnostic specificity of urinary nano-reporters for lung[69] and prostate cancer.[70] In TBI, MMP-9 is a possible candidate for multiplexing as MMP-9 levels are elevated in patients post-TBI, and MMP-9 is implicated in BBB permeability.[71] Tethering substrates for multiple proteases onto a single nanomaterial scaffold and visualization in 3D would allow for the study of spatial activation of proteases in relation to each other; for example, calpain-1 has been shown to activate MMP9 in TBI[72] and stroke.[73] In the future, the TBI-ABN platform could be re-designed for in vivo measurements with quenchable quantum dots[74] and tissue-penetrating near infrared optical imaging through cranial windows, or with superparamagnetic iron oxide nanoparticles[75] and magnetic resonance imaging (MRI). Furthermore, HA-targeting has the potential to be applied to a greater range of nanomaterials, including therapeutic nanomaterials. Our observation that HA-targeted nanomaterial colocalized with hippocampal and perilesional neurons provides motivation for its

use in the delivery of neuroprotective agents, since neuronal apoptosis is a hallmark of secondary injury and hippocampal neurodegeneration is associated with memory deficits after TBI.[76]

3.5. Methods

Synthesis of ECM-targeted and TBI-ABN Poly(ethylene glycol) (PEG) Conjugates. The following targeting peptides were synthesized by Lifetein (Somerset, NJ): PGpep (X(FAM)-CAQK), CIVpep (KLWVLPKGG-K(FAM)-GGC), FIBpep (X(FAM)-CREKA), HApep (X(FAM)-CSTMMSRSHKTRSHHV), and RGD (X(FAM)-CRGD). Calpain substrate FRET peptide (QSY21-QEVYGAMP-K(Cy5)-PEG2-GC-NH2) was synthesized by CPC Scientific Inc. (Sunnyvale, CA). X stands for 6-aminocaproic acid and PEG2 stands for poly(ethylene glycol). The 40kDa 8-arm PEG maleimide (tripentaerythritol) was purchased from Jenkem Technology (Beijing, China). For ECM-targeting peptide screening: PEG maleimide was batch reacted with 1 mol L-cysteine-functionalized VivoTag S-750 (PerkinElmer, Boston, MA). The reaction was then split to ensure matched VivoTag 750 modification for each conjugate and reacted with 8.4 mol equivalencies of each ECM-targeting peptide followed by quenching with an excess of L-cysteine. For HA-targeted TBI-ABNs: 8-arm PEG maleimide was batch reacted with 1 mol equivalent of calpain substrate FRET peptide, split and reacted with 0 mol (non-targeted), 4 mol (moderate targeting), or 8.4 mol (high targeting) equivalents of HApep in the presence of 50 mM triethylamine (TEA), then quenched with an excess of L-cysteine. All conjugates were dialyzed with water, and final concentrations were determined by absorbance of VivoTag 750, FAM, or Cy5 using a Spark multimode microplate reader (Tecan Trading AG, Switzerland).

Controlled Cortical Impact (CCI) TBI Mouse Model. All mouse procedures were approved by the University of California San Diego's Institutional Animal Care and Use Committee (IACUC). A total of 61 8-13 week old female C57BL/6J mice (Jackson Labs) weighing between 18-22 g were used for all in vivo studies. Following anesthetization with 2.5% isoflurane, buprenorphine analgesia was administered. A 5 mm craniotomy was performed over the right hemisphere between bregma and lambda and controlled cortical impact was performed using the ImpactOne (Leica Biosystems) with a 2 mm diameter stainless steel probe at a velocity of 3 m/s, depth of 2 mm, and dwell time of 300 ms. The center of the injury impact was centered around -2.0 mm (± 0.5 mm) lateral from the midline and -2.0 mm (± 0.5 mm) caudal from bregma. Group sizes were n = 3 for each experiment unless noted, based on a type I error rate of 5% and a power of 80% with an anticipated effect size greater than 2 with a 50% variance.

Extracellular Matrix (ECM) Peptide In Vivo Screen. Six hours after CCI, 25 nmoles of ECM-targeting peptide-PEG nanomaterial (quantified via FAM absorbance) in 150 µL 5% dextrose was intravenously administered via the tail-vein. Nanomaterial doses were administered to mice in a weight range of 18-22 g, corresponding to a dosage range of 1136-1389 nmol/kg. Control cysteine mice received a matching dose as quantified by VivoTag 750 absorbance. Triplicate mice were obtained per ECM-targeting peptide. One hour after injection, mice were transcardially perfused with USP saline followed by 10% formalin. Surface fluorescence of organs (brain, heart, lung, liver, spleen, kidneys) was measured with an Odyssey scanner (Li-Cor Biosciences) within 6 hours of collection. For generation of tissue for quantitative biodistribution of homogenized tissue, triplicate mice were perfused with 10 mL of ice-cold PBS. For

quantification of nanomaterial blood half-life, 5-10 µL of blood was collected into heparinized tubes (n = 3), VivoTag 750 signal was detected on a Li-Cor scanner, and %ID of nanomaterial in the blood was calculated based on a standard of known concentrations and estimated blood volume.

HA-targeted TBI-ABN In Vivo Study. Three hours after CCI, 6 nmoles (concentration based on substrate peptide) of non-targeted, moderate targeting, high targeting TBI-ABN in 150 µL 5% dextrose was injected intravenously via the tail vein. Nanomaterial doses were administered to mice with a weight range of 18-22 g, corresponding to a dosage range of 273-333 nmol/kg. Vehicle control received equivolume of 5% dextrose. Following a 1-hour circulation time, mice were sacrificed by transcardial perfusion of either USP saline followed by 10% formalin (for histology) or 10 mL of ice-cold PBS (for whole organ homogenization). Each condition was repeated in triplicate for histology. The study was independently repeated again in triplicate for homogenization tissue generation. A third independent study was performed for CUBIC tissue clearing in one mouse.

Quantitative Biodistribution of Homogenized Tissue. Organ tissue was flash frozen at -80 °C, tissue was minced, and lysis buffer (6% w/v sodium dodecyl sulfate (SDS), 150 mM Tris-HCl pH 7.4, 100 mM dithiothreitol (DTT), and 2 mM ethylenediaminetetraacetic acid (EDTA)) was added to achieve a concentration of 250 mg tissue/mL. Tissue was further processed with a Tissue-Tearor with 4.5 mm probe (Fisher) at medium-high speed for 20-30 seconds until lysate was homogenized. Samples were heated at 90 °C for 10 minutes with agitation at 800 RPM, vortexed to mix, and homogenate measured for FAM fluorescence (ECM-

targeting peptide screen) or Cy5 fluorescence (TBI-ABN activation). Percent injected dose (% ID) per gram of tissue was calculated based on a known nanomaterial concentration standard.

Immunostaining of Brain Tissue Slices. Following transcardial perfusion with 10% formalin, necropsied organs were further fixed in 10% formalin at 4 °C overnight. Organs were washed in PBS, transferred to 30% w/v sucrose-PBS overnight, then frozen in OCT (Tissue-Tek). Coronal tissue slices 10 µm thick were obtained within the 2 mm diameter injury region, then stained using conventional protocols. See Table 3.2 for a list of antibodies and staining reagents. Briefly, tissues were blocked for 1 hour in 2% bovine serum albumin, 5% serum of secondary antibody, and 0.1% Triton X-100. For NeuN staining, blocking buffer included 2µg/mL of donkey anti-mouse Fab. Primary antibody incubations were done in blocking buffer overnight at 4 ˚C. Secondary antibodies were applied for 1 hour at room temperature, washed in PBS, and mounted with Fluoromount-G (Southern Biotech). To probe for endogenous hyaluronic acid, tissues were blocked for 1 hour, incubated overnight with biotinylated hyaluronic acid binding protein (bHABP), incubated for 1 hour with streptavidin AF647 conjugate, washed and mounted. Images were collected on a Nikon Eclipse Ti2 microscope fitted with a Hamamatsu Orca-Flash 4.0 digital camera. Activated TBI-ABN was visualized with imaging settings for Cy5. Images for direct comparison were collected using the same exposure and LED intensity settings.

In Vitro Reaction Kinetics Assay. The calpain-1 reaction kinetics assay was run as previously described.[10] Briefly, conjugates were incubated with 26.6 nM human calpain-1 (Sigma-Aldrich, C6108) in 50 mM N-(2-hydroxyethyl)piperazine-N′-ethanesulfonic acid

(HEPES), 50 mM NaCl, 2 mM EDTA, 5 mM $CaCl_2$, and 5 mM β-mercaptoethanol. Fluorescence readings were taken every 90 s at 37 °C for 1 h. Reaction curves were normalized to controls, and their initial velocities were fitted to a Michaelis−Menten curve in GraphPad Prism (9.2.0).

CUBIC tissue clearing. Brains were cleared following published protocol (Clear, Unobstructed Brain/Body Imaging Cocktails and Computational Analysis or CUBIC).[68] Following transcardial perfusion with 10% formalin, the simple immersion protocol for dissected whole brain tissue was followed without modifications. Tissues were kept static in fresh reagent-2 at room temperature between clearing and imaging, with no longer than 1-1.5 weeks between the last day of clearing and imaging.

3D light sheet fluorescence microscopy (LSFM). Light Sheet Fluorescence Microscopy (LSFM) was accomplished using a Zeiss Lightsheet Z.1. The microscope was fitted with a 2.5x objective, solid-state lasers (excitation wavelengths 488 nm for FAM and 640 nm for sensor) and a PCO.edge 16 bit sCMOS camera for detection. The cleared brain was embedded in low melt 2% agarose (ThermoFisher) then submerged in CUBIC reagent-2 overnight. The next day, magnetic staples were superglued to the agarose-embedded tissue and the sample was hung vertically in front of the LSFM objective (2.5x) using a custom magnetic fixture. The brain was slowly lowered into the imaging chamber filled with reagent-2 for at least 20 minutes prior to image collection. A z-stack (range of 3.258 mm with a 3 µm step size) was obtained. The 3D area, encompassing the injured and contralateral hemispheres, was approximately 9.7 mm (x-

axis) by 4.5 mm (y-axis) by 3.3 mm (z-axis). 3D images and clipping planes were generated in Arivis Vision4D®.

Software and Statistics. GraphPad Prism® (9.2.0) was used to perform statistics. All images were processed in ImageJ (1.53g).

3.6. Acknowledgements

Chapter 3, in full, is reprinted with permission from Kandell, Rebecca M.; Kudryashev, Julia A.; Kwon, Ester J. Targeting the Extracellular Matrix in Traumatic Brain Injury Increases Signal Generation from an Activity-Based Nanosensor. ACS Nano 2021, 15 (12), 20504–20516. Copyright 2021 American Chemical Society. The dissertation author was one of the primary researchers and authors of this paper.

This work was supported by the National Institutes of Health Director's New Innovator Award (1DP2NS111507) and a National Science Foundation (NSF) CAREER Award (2046926). R.M.K acknowledges support from the NHLBI training program Integrative Bioengineering of Heart Vessels Blood (T32 HL105373). J.A.K acknowledges support from the National Science Foundation (NSF) Graduate Research Fellowship Program under Grant No. DGE-1650112. Any opinions, findings, and conclusions or recommendations expressed in this material are those of the authors and do not necessarily reflect the views of the NSF. We also thank the University of California San Diego School of Medicine microscopy core for use of their imaging facilities, supported under NINDS P30NS047101.

3.7. References

(1) Peterson, A. B.; Zhou, H.; Thomas, K. E.; Daugherty, J. Traumatic Brain Injury-Related Hospitalizations and Deaths by Age Group, Sex, and Mechanism of Injury : United States 2016/2017. **2021**.

(2) Maas, A. I. R.; Menon, D. K.; Adelson, P. D.; Andelic, N.; Bell, M. J.; Belli, A.; Bragge, P.; Brazinova, A.; Büki, A.; Chesnut, R. M.; Citerio, G.; Coburn, M.; Cooper, D. J.; Crowder, A. T.; Czeiter, E.; Czosnyka, M.; Diaz-Arrastia, R.; Dreier, J. P.; Duhaime, A.-C.; Ercole, A.; van Essen, T. A.; Feigin, V. L.; Gao, G.; Giacino, J.; Gonzalez-Lara, L. E.; Gruen, R. L.; Gupta, D.; Hartings, J. A.; Hill, S.; Jiang, J.; Ketharanathan, N.; Kompanje, E. J. O.; Lanyon, L.; Laureys, S.; Lecky, F.; Levin, H.; Lingsma, H. F.; Maegele, M.; Majdan, M.; Manley, G.; Marsteller, J.; Mascia, L.; McFadyen, C.; Mondello, S.; Newcombe, V.; Palotie, A.; Parizel, P. M.; Peul, W.; Piercy, J.; Polinder, S.; Puybasset, L.; Rasmussen, T. E.; Rossaint, R.; Smielewski, P.; Söderberg, J.; Stanworth, S. J.; Stein, M. B.; von Steinbüchel, N.; Stewart, W.; Steyerberg, E. W.; Stocchetti, N.; Synnot, A.; Te Ao, B.; Tenovuo, O.; Theadom, A.; Tibboel, D.; Videtta, W.; Wang, K. K. W.; Williams, W. H.; Wilson, L.; Yaffe, K.; Adams, H.; Agnoletti, V.; Allanson, J.; Amrein, K.; Andaluz, N.; Anke, A.; Antoni, A.; van As, A. B.; Audibert, G.; Azaševac, A.; Azouvi, P.; Azzolini, M. L.; Baciu, C.; Badenes, R.; Barlow, K. M.; Bartels, R.; Bauerfeind, U.; Beauchamp, M.; Beer, D.; Beer, R.; Belda, F. J.; Bellander, B.-M.; Bellier, R.; Benali, H.; Benard, T.; Beqiri, V.; Beretta, L.; Bernard, F.; Bertolini, G.; Bilotta, F.; Blaabjerg, M.; den Boogert, H.; Boutis, K.; Bouzat, P.; Brooks, B.; Brorsson, C.; Bullinger, M.; Burns, E.; Calappi, E.; Cameron, P.; Carise, E.; Castaño-León, A. M.; Causin, F.; Chevallard, G.; Chieregato, A.; Christie, B.; Cnossen, M.; Coles, J.; Collett, J.; Della Corte, F.; Craig, W.; Csato, G.; Csomos, A.; Curry, N.; Dahyot-Fizelier, C.; Dawes, H.; DeMatteo, C.; Depreitere, B.; Dewey, D.; van Dijck, J.; Đilvesi, Đ.; Dippel, D.; Dizdarevic, K.; Donoghue, E.; Duek, O.; Dulière, G.-L.; Dzeko, A.; Eapen, G.; Emery, C. A.; English, S.; Esser, P.; Ezer, E.; Fabricius, M.; Feng, J.; Fergusson, D.; Figaji, A.; Fleming, J.; Foks, K.; Francony, G.; Freedman, S.; Freo, U.; Frisvold, S. K.; Gagnon, I.; Galanaud, D.; Gantner, D.; Giraud, B.; Glocker, B.; Golubovic, J.; Gómez López, P. A.; Gordon, W. A.; Gradisek, P.; Gravel, J.; Griesdale, D.; Grossi, F.; Haagsma, J. A.; Håberg, A. K.; Haitsma, I.; Van Hecke, W.; Helbok, R.; Helseth, E.; van Heugten, C.; Hoedemaekers, C.; Höfer, S.; Horton, L.; Hui, J.; Huijben, J. A.; Hutchinson, P. J.; Jacobs, B.; van der Jagt, M.; Jankowski, S.; Janssens, K.; Jelaca, B.; Jones, K. M.; Kamnitsas, K.; Kaps, R.; Karan, M.; Katila, A.; Kaukonen, K.-M.; De Keyser, V.; Kivisaari, R.; Kolias, A. G.; Kolumbán, B.; Kolundžija, K.; Kondziella, D.; Koskinen, L.-O.; Kovács, N.; Kramer, A.; Kutsogiannis, D.; Kyprianou, T.; Lagares, A.; Lamontagne, F.; Latini, R.; Lauzier, F.; Lazar, I.; Ledig, C.; Lefering, R.; Legrand, V.; Levi, L.; Lightfoot, R.; Lozano, A.; MacDonald, S.; Major, S.; Manara, A.; Manhes, P.; Maréchal, H.; Martino, C.; Masala, A.; Masson, S.; Mattern, J.; McFadyen, B.; McMahon, C.; Meade, M.; Melegh, B.; Menovsky, T.; Moore, L.; Morgado Correia, M.; Morganti-Kossmann, M. C.; Muehlan, H.; Mukherjee, P.; Murray, L.; van der Naalt, J.; Negru, A.; Nelson, D.; Nieboer, D.; Noirhomme, Q.; Nyirádi, J.; Oddo, M.; Okonkwo, D. O.; Oldenbeuving, A. W.; Ortolano, F.; Osmond, M.; Payen, J.-F.; Perlbarg, V.; Persona, P.; Pichon, N.; Piippo-Karjalainen, A.; Pili-Floury, S.; Pirinen, M.; Ple, H.; Poca, M. A.; Posti, J.; Van Praag, D.; Ptito, A.; Radoi, A.; Ragauskas, A.; Raj, R.; Real, R. G. L.; Reed, N.;

Rhodes, J.; Robertson, C.; Rocka, S.; Røe, C.; Røise, O.; Roks, G.; Rosand, J.; Rosenfeld, J. V.; Rosenlund, C.; Rosenthal, G.; Rossi, S.; Rueckert, D.; de Ruiter, G. C. W.; Sacchi, M.; Sahakian, B. J.; Sahuquillo, J.; Sakowitz, O.; Salvato, G.; Sánchez-Porras, R.; Sándor, J.; Sangha, G.; Schäfer, N.; Schmidt, S.; Schneider, K. J.; Schnyer, D.; Schöhl, H.; Schoonman, G. G.; Schou, R. F.; Sir, Ö.; Skandsen, T.; Smeets, D.; Sorinola, A.; Stamatakis, E.; Stevanovic, A.; Stevens, R. D.; Sundström, N.; Taccone, F. S.; Takala, R.; Tanskanen, P.; Taylor, M. S.; Telgmann, R.; Temkin, N.; Teodorani, G.; Thomas, M.; Tolias, C. M.; Trapani, T.; Turgeon, A.; Vajkoczy, P.; Valadka, A. B.; Valeinis, E.; Vallance, S.; Vámos, Z.; Vargiolu, A.; Vega, E.; Verheyden, J.; Vik, A.; Vilcinis, R.; Vleggeert-Lankamp, C.; Vogt, L.; Volovici, V.; Voormolen, D. C.; Vulekovic, P.; Vande Vyvere, T.; Van Waesberghe, J.; Wessels, L.; Wildschut, E.; Williams, G.; Winkler, M. K. L.; Wolf, S.; Wood, G.; Xirouchaki, N.; Younsi, A.; Zaaroor, M.; Zelinkova, V.; Zemek, R.; Zumbo, F. Traumatic Brain Injury: Integrated Approaches to Improve Prevention, Clinical Care, and Research. *Lancet Neurol.* **2017**, *16* (12), 987–1048. https://doi.org/10.1016/S1474-4422(17)30371-X.

(3) Kandell, R. M.; Waggoner, L. E.; Kwon, E. J. Nanomedicine for Acute Brain Injuries: Insight from Decades of Cancer Nanomedicine. *Mol. Pharm.* **2021**, *18* (2), 522–538. https://doi.org/10.1021/acs.molpharmaceut.0c00287.

(4) Zhang, Z.; Larner, S. F.; Liu, M. C.; Zheng, W.; Hayes, R. L.; Wang, K. K. W. Multiple AlphaII-Spectrin Breakdown Products Distinguish Calpain and Caspase Dominated Necrotic and Apoptotic Cell Death Pathways. *Apoptosis* **2009**, *14* (11), 1289–1298. https://doi.org/10.1007/s10495-009-0405-z.

(5) Gan, Z. S.; Stein, S. C.; Swanson, R.; Guan, S.; Garcia, L.; Mehta, D.; Smith, D. H. Blood Biomarkers for Traumatic Brain Injury: A Quantitative Assessment of Diagnostic and Prognostic Accuracy. *Front. Neurol.* **2019**, *10* (APR), 446–446. https://doi.org/10.3389/fneur.2019.00446.

(6) Siman, R.; Shahim, P.; Tegner, Y.; Blennow, K.; Zetterberg, H.; Smith, D. H. Serum SNTF Increases in Concussed Professional Ice Hockey Players and Relates to the Severity of Postconcussion Symptoms. *J. Neurotrauma* **2015**, *32* (17), 1294–1300. https://doi.org/10.1089/neu.2014.3698.

(7) Siman, R.; Giovannone, N.; Hanten, G.; Wilde, E. A.; McCauley, S. R.; Hunter, J. V.; Li, X.; Levin, H. S.; Smith, D. H. Evidence That the Blood Biomarker SNTF Predicts Brain Imaging Changes and Persistent Cognitive Dysfunction in Mild TBI Patients. *Front. Neurol.* **2013**, *4*, 190–190. https://doi.org/10.3389/fneur.2013.00190.

(8) Dudani, J. S.; Warren, A. D.; Bhatia, S. N. Harnessing Protease Activity to Improve Cancer Care. *Annu. Rev. Cancer Biol.* **2018**, *2* (1), 353–376. https://doi.org/10.1146/annurev-cancerbio-030617-050549.

(9) Sanman, L. E.; Bogyo, M. Activity-Based Profiling of Proteases. *Annu. Rev. Biochem.* **2014**, *83* (1), 249–273. https://doi.org/10.1146/annurev-biochem-060713-035352.

(10) Kudryashev, J. A.; Waggoner, L. E.; Leng, H. T.; Mininni, N. H.; Kwon, E. J. An Activity-Based Nanosensor for Traumatic Brain Injury. *ACS Sens.* **2020**, *5* (3), 686–692. https://doi.org/10.1021/acssensors.9b01812.

(11) Bharadwaj, V. N.; Lifshitz, J.; Adelson, P. D.; Kodibagkar, V. D.; Stabenfeldt, S. E. Temporal Assessment of Nanoparticle Accumulation after Experimental Brain Injury: Effect of Particle Size. *Sci. Rep.* **2016**, *6* (1), 29988–29988. https://doi.org/10.1038/srep29988.

(12) Boyd, B. J.; Galle, A.; Daglas, M.; Rosenfeld, J. V.; Medcalf, R. Traumatic Brain Injury Opens Blood–Brain Barrier to Stealth Liposomes via an Enhanced Permeability and Retention (EPR)-like Effect. *J. Drug Target.* **2015**, *23* (9), 847–853. https://doi.org/10.3109/1061186X.2015.1034280.

(13) Matsumura, Y.; Maeda, H. A New Concept for Macromolecular Therapeutics in Cancer Chemotherapy: Mechanism of Tumoritropic Accumulation of Proteins and the Antitumor Agent Smancs1. *Cancer Res.* **1986**, *46* (12_Part_1), 6387–6392.

(14) Fang, J.; Nakamura, H.; Maeda, H. The EPR Effect: Unique Features of Tumor Blood Vessels for Drug Delivery, Factors Involved, and Limitations and Augmentation of the Effect. *Adv. Drug Deliv. Rev.* **2011**, *63* (3), 136–151. https://doi.org/10.1016/j.addr.2010.04.009.

(15) Prasad, L. K.; O'Mary, H.; Cui, Z. Nanomedicine Delivers Promising Treatments for Rheumatoid Arthritis. *Nanomed.* **2015**, *10* (13), 2063–2074. https://doi.org/10.2217/nnm.15.45.

(16) Horwitz, L. D.; Kaufman, D.; Keller, M. W.; Kong, Y. Time Course of Coronary Endothelial Healing after Injury Due to Ischemia and Reperfusion. *Circulation* **1994**, *90* (5), 2439–2447. https://doi.org/10.1161/01.CIR.90.5.2439.

(17) Prajnamitra, R. P.; Chen, H.-C.; Lin, C.-J.; Chen, L.-L.; Hsieh, P. C.-H. Nanotechnology Approaches in Tackling Cardiovascular Diseases. *Molecules* **2019**, *24* (10), 2017. https://doi.org/10.3390/molecules24102017.

(18) Kwon, E. J.; Skalak, M.; Lo Bu, R.; Bhatia, S. N. Neuron-Targeted Nanoparticle for SiRNA Delivery to Traumatic Brain Injuries. *ACS Nano* **2016**, *10* (8), 7926–7933. https://doi.org/10.1021/acsnano.6b03858.

(19) Thorne, R. G.; Nicholson, C. In Vivo Diffusion Analysis with Quantum Dots and Dextrans Predicts the Width of Brain Extracellular Space. *Proc. Natl. Acad. Sci.* **2006**, *103* (14), 5567–5572. https://doi.org/10.1073/pnas.0509425103.

(20) Kwon, E. J.; Dudani, J. S.; Bhatia, S. N. Ultrasensitive Tumour-Penetrating Nanosensors of Protease Activity. *Nat. Biomed. Eng.* **2017**, *1* (4), 0054–0054. https://doi.org/10.1038/s41551-017-0054.

(21) Bartlett, D. W.; Su, H.; Hildebrandt, I. J.; Weber, W. A.; Davis, M. E. Impact of Tumor-Specific Targeting on the Biodistribution and Efficacy of SiRNA Nanoparticles Measured by Multimodality in Vivo Imaging. *Proc. Natl. Acad. Sci. U. S. A.* **2007**, *104* (39), 15549–15554. https://doi.org/10.1073/pnas.0707461104.

(22) Choi, C. H. J.; Alabi, C. A.; Webster, P.; Davis, M. E. Mechanism of Active Targeting in Solid Tumors with Transferrin-Containing Gold Nanoparticles. *Proc. Natl. Acad. Sci. U. S. A.* **2010**, *107* (3), 1235–1240. https://doi.org/10.1073/pnas.0914140107.

(23) Park, J. W.; Hong, K.; Kirpotin, D. B.; Colbern, G.; Shalaby, R.; Baselga, J.; Shao, Y.; Nielsen, U. B.; Marks, J. D.; Moore, D.; Papahadjopoulos, D.; Benz, C. C. Anti-HER2 Immunoliposomes: Enhanced Efficacy Attributable to Targeted Delivery1. *Clin. Cancer Res.* **2002**, *8* (4), 1172–1181.

(24) Kirpotin, D. B.; Drummond, D. C.; Shao, Y.; Shalaby, M. R.; Hong, K.; Nielsen, U. B.; Marks, J. D.; Benz, C. C.; Park, J. W. Antibody Targeting of Long-Circulating Lipidic Nanoparticles Does Not Increase Tumor Localization but Does Increase Internalization in Animal Models. *Cancer Res.* **2006**, *66* (13), 6732–6740. https://doi.org/10.1158/0008-5472.CAN-05-4199.

(25) Joo, J.; Kwon, E. J.; Kang, J.; Skalak, M.; Anglin, E. J.; Mann, A. P.; Ruoslahti, E.; Bhatia, S. N.; Sailor, M. J. Porous Silicon–Graphene Oxide Core–Shell Nanoparticles for Targeted Delivery of SiRNA to the Injured Brain. *Nanoscale Horiz.* **2016**, *1* (5), 407–414. https://doi.org/10.1039/C6NH00082G.

(26) Lo, J. H.; Kwon, E. J.; Zhang, A. Q.; Singhal, P.; Bhatia, S. N. Comparison of Modular PEG Incorporation Strategies for Stabilization of Peptide–SiRNA Nanocomplexes. *Bioconjug. Chem.* **2016**, *27* (10), 2323–2331. https://doi.org/10.1021/acs.bioconjchem.6b00304.

(27) Lin, K. Y.; Kwon, E. J.; Lo, J. H.; Bhatia, S. N. Drug-Induced Amplification of Nanoparticle Targeting to Tumors. *Nano Today* **2014**, *9* (5), 550–559. https://doi.org/10.1016/j.nantod.2014.09.001.

(28) Frantz, C.; Stewart, K. M.; Weaver, V. M. The Extracellular Matrix at a Glance. *J. Cell Sci.* **2010**, *123* (24), 4195–4200. https://doi.org/10.1242/jcs.023820.

(29) Zhang, B.; Shen, S.; Liao, Z.; Shi, W.; Wang, Y.; Zhao, J.; Hu, Y.; Yang, J.; Chen, J.; Mei, H.; Hu, Y.; Pang, Z.; Jiang, X. Targeting Fibronectins of Glioma Extracellular Matrix by CLT1 Peptide-Conjugated Nanoparticles. *Biomaterials* **2014**, *35* (13), 4088–4098. https://doi.org/10.1016/j.biomaterials.2014.01.046.

(30) Briquez, P. S.; Hauert, S.; de Titta, A.; Gray, L. T.; Alpar, A. T.; Swartz, M. A.; Hubbell, J. A. Engineering Targeting Materials for Therapeutic Cancer Vaccines. *Front. Bioeng. Biotechnol.* **2020**, *8*.

(31) Ishihara, J.; Ishihara, A.; Sasaki, K.; Lee, S. S.-Y.; Williford, J.-M.; Yasui, M.; Abe, H.; Potin, L.; Hosseinchi, P.; Fukunaga, K.; Raczy, M. M.; Gray, L. T.; Mansurov, A.; Katsumata, K.; Fukayama, M.; Kron, S. J.; Swartz, M. A.; Hubbell, J. A. Targeted Antibody and Cytokine Cancer Immunotherapies through Collagen Affinity. *Sci. Transl. Med.* **2019**, *11* (487), eaau3259. https://doi.org/10.1126/scitranslmed.aau3259.

(32) Williford, J.-M.; Ishihara, J.; Ishihara, A.; Mansurov, A.; Hosseinchi, P.; Marchell, T. M.; Potin, L.; Swartz, M. A.; Hubbell, J. A. Recruitment of CD103+ Dendritic Cells via Tumor-Targeted Chemokine Delivery Enhances Efficacy of Checkpoint Inhibitor Immunotherapy. *Sci. Adv.* **2019**, *5* (12), eaay1357. https://doi.org/10.1126/sciadv.aay1357.

(33) Katsumata, K.; Ishihara, J.; Mansurov, A.; Ishihara, A.; Raczy, M. M.; Yuba, E.; Hubbell, J. A. Targeting Inflammatory Sites through Collagen Affinity Enhances the Therapeutic Efficacy of Anti-Inflammatory Antibodies. *Sci. Adv.* **2019**, *5* (11), eaay1971. https://doi.org/10.1126/sciadv.aay1971.

(34) Katsumata, K.; Ishihara, J.; Fukunaga, K.; Ishihara, A.; Yuba, E.; Budina, E.; Hubbell, J. A. Conferring Extracellular Matrix Affinity Enhances Local Therapeutic Efficacy of Anti-TNF-α Antibody in a Murine Model of Rheumatoid Arthritis. *Arthritis Res. Ther.* **2019**, *21* (1), 298. https://doi.org/10.1186/s13075-019-2075-8.

(35) Price, L.; Wilson, C.; Grant, G. Blood–Brain Barrier Pathophysiology Following Traumatic Brain Injury. In *Translational Research in Traumatic Brain Injury*; Laskowitz, D., Grant, G., Eds.; CRC Press/Taylor and Francis Group: Boca Raton, FL, 2016; pp 85–96. https://doi.org/10.1201/b18959-5.

(36) George, N.; Geller, H. M. Extracellular Matrix and Traumatic Brain Injury. *J. Neurosci. Res.* **2018**, *96* (4), 573–588. https://doi.org/10.1002/jnr.24151.

(37) Lau, L. W.; Cua, R.; Keough, M. B.; Haylock-Jacobs, S.; Yong, V. W. Pathophysiology of the Brain Extracellular Matrix: A New Target for Remyelination. *Nat. Rev. Neurosci.* **2013**, *14* (10), 722–729. https://doi.org/10.1038/nrn3550.

(38) Xing, G.; Ren, M.; Verma, A. Divergent Temporal Expression of Hyaluronan Metabolizing Enzymes and Receptors with Craniotomy vs. Controlled-Cortical Impact Injury in Rat Brain: A Pilot Study. *Front. Neurol.* **2014**, *5*.

(39) Mann, A. P.; Scodeller, P.; Hussain, S.; Joo, J.; Kwon, E.; Braun, G. B.; Mölder, T.; She, Z. G.; Kotamraju, V. R.; Ranscht, B.; Krajewski, S.; Teesalu, T.; Bhatia, S.; Sailor, M. J.; Ruoslahti, E. A Peptide for Targeted, Systemic Delivery of Imaging and Therapeutic Compounds into Acute Brain Injuries. *Nat. Commun.* **2016**, *7* (1), 11980–11980. https://doi.org/10.1038/ncomms11980.

(40) Chan, J. M.; Zhang, L.; Tong, R.; Ghosh, D.; Gao, W.; Liao, G.; Yuet, K. P.; Gray, D.; Rhee, J.-W.; Cheng, J.; Golomb, G.; Libby, P.; Langer, R.; Farokhzad, O. C. Spatiotemporal Controlled Delivery of Nanoparticles to Injured Vasculature. *Proc. Natl. Acad. Sci. U. S. A.* **2010**, *107* (5), 2213–2218. https://doi.org/10.1073/pnas.0914585107.

(41) Simberg, D.; Duza, T.; Park, J. H.; Essler, M.; Pilch, J.; Zhang, L.; Derfus, A. M.; Yang, M.; Hoffman, R. M.; Bhatia, S.; Sailor, M. J.; Ruoslahti, E. Biomimetic Amplification of Nanoparticle Homing to Tumors. *Proc. Natl. Acad. Sci.* **2007**, *104* (3), 932–936. https://doi.org/10.1073/pnas.0610298104.

(42) Tolg, C.; Hamilton, S. R.; Zalinska, E.; McCulloch, L.; Amin, R.; Akentieva, N.; Winnik, F.; Savani, R.; Bagli, D. J.; Luyt, L. G.; Cowman, M. K.; McCarthy, J. B.; Turley, E. A. A RHAMM Mimetic Peptide Blocks Hyaluronan Signaling and Reduces Inflammation and Fibrogenesis in Excisional Skin Wounds. *Am. J. Pathol.* **2012**, *181* (4), 1250–1270. https://doi.org/10.1016/j.ajpath.2012.06.036.

(43) Faust, H. J.; Sommerfeld, S. D.; Rathod, S.; Rittenbach, A.; Ray Banerjee, S.; Tsui, B. M. W.; Pomper, M.; Amzel, M. L.; Singh, A.; Elisseeff, J. H. A Hyaluronic Acid Binding

Peptide-Polymer System for Treating Osteoarthritis. *Biomaterials* **2018**, *183*, 93–101. https://doi.org/10.1016/j.biomaterials.2018.08.045.

(44) Waggoner, L. E.; Madias, M. I.; Hurtado, A. A.; Kwon, E. J. Pharmacokinetic Analysis of Peptide-Modified Nanoparticles with Engineered Physicochemical Properties in a Mouse Model of Traumatic Brain Injury. *AAPS J.* **2021**, *23* (5), 100. https://doi.org/10.1208/s12248-021-00626-5.

(45) Soo Choi, H.; Liu, W.; Misra, P.; Tanaka, E.; Zimmer, J. P.; Itty Ipe, B.; Bawendi, M. G.; Frangioni, J. V. Renal Clearance of Quantum Dots. *Nat. Biotechnol.* **2007**, *25* (10), 1165–1170. https://doi.org/10.1038/nbt1340.

(46) Nance, E. A.; Woodworth, G. F.; Sailor, K. A.; Shih, T.-Y.; Xu, Q.; Swaminathan, G.; Xiang, D.; Eberhart, C.; Hanes, J. A Dense Poly(Ethylene Glycol) Coating Improves Penetration of Large Polymeric Nanoparticles Within Brain Tissue. *Sci. Transl. Med.* **2012**, *4* (149), 149ra119-149ra119. https://doi.org/10.1126/scitranslmed.3003594.

(47) Suk, J. S.; Xu, Q.; Kim, N.; Hanes, J.; Ensign, L. M. PEGylation as a Strategy for Improving Nanoparticle-Based Drug and Gene Delivery. *Adv. Drug Deliv. Rev.* **2016**, *99*, 28–51. https://doi.org/10.1016/J.ADDR.2015.09.012.

(48) Pierschbacher, M. D.; Ruoslahti, E. Cell Attachment Activity of Fibronectin Can Be Duplicated by Small Synthetic Fragments of the Molecule. *Nature* **1984**, *309* (5963), 30–33. https://doi.org/10.1038/309030a0.

(49) Mezu-Ndubuisi, O. J.; Maheshwari, A. The Role of Integrins in Inflammation and Angiogenesis. *Pediatr. Res.* **2021**, *89* (7), 1619–1626. https://doi.org/10.1038/s41390-020-01177-9.

(50) Abumiya, T.; Lucero, J.; Heo, J. H.; Tagaya, M.; Koziol, J. A.; Copeland, B. R.; del Zoppo, G. J. Activated Microvessels Express Vascular Endothelial Growth Factor and Integrin Avβ3 During Focal Cerebral Ischemia. *J. Cereb. Blood Flow Metab.* **1999**, *19* (9), 1038–1050. https://doi.org/10.1097/00004647-199909000-00012.

(51) Ward, P. A. Inflammation and Avβ3 Integrin. *Am. J. Respir. Crit. Care Med.* **2012**, *185* (1), 5–6. https://doi.org/10.1164/rccm.201110-1859ED.

(52) Xiong, Y.; Mahmood, A.; Chopp, M. Animal Models of Traumatic Brain Injury. *Nat. Rev. Neurosci.* **2013**, *14* (2), 128–142. https://doi.org/10.1038/nrn3407.

(53) Hall, E. D.; Sullivan, P. G.; Gibson, T. R.; Pavel, K. M.; Thompson, B. M.; Scheff, S. W. Spatial and Temporal Characteristics of Neurodegeneration after Controlled Cortical Impact in Mice: More than a Focal Brain Injury. *J. Neurotrauma* **2005**, *22* (2), 252–265. https://doi.org/10.1089/neu.2005.22.252.

(54) Natarajan, V.; Harris, E. N.; Kidambi, S. SECs (Sinusoidal Endothelial Cells), Liver Microenvironment, and Fibrosis. *BioMed Res. Int.* **2017**, *2017*, e4097205. https://doi.org/10.1155/2017/4097205.

(55) Perrault, S. D.; Walkey, C.; Jennings, T.; Fischer, H. C.; Chan, W. C. W. Mediating Tumor Targeting Efficiency of Nanoparticles Through Design. *Nano Lett.* **2009**, *9* (5), 1909–1915. https://doi.org/10.1021/nl900031y.

(56) Hamakubo, T.; Kannagi, R.; Murachi, T.; Matus, A. Distribution of Calpains I and II in Rat Brain. *J. Neurosci.* **1986**, *6* (11), 3103–3111. https://doi.org/10.1523/JNEUROSCI.06-11-03103.1986.

(57) Czogalla, A.; Sikorski, A. F. Spectrin and Calpain: A "target" and a "Sniper" in the Pathology of Neuronal Cells. *Cell. Mol. Life Sci.* **2005**, *62* (17), 1913–1924. https://doi.org/10.1007/s00018-005-5097-0.

(58) Xiong, Y.; Mahmood, A.; Chopp, M. Emerging Treatments for Traumatic Brain Injury. *Expert Opin. Emerg. Drugs* **2009**, *14* (1), 67–84. https://doi.org/10.1517/14728210902769601.

(59) Heinegård, D.; Hascall, V. C. Aggregation of Cartilage Proteoglycans: III. CHARACTERISTICS OF THE PROTEINS ISOLATED FROM TRYPSIN DIGESTS OF AGGREGATES. *J. Biol. Chem.* **1974**, *249* (13), 4250–4256. https://doi.org/10.1016/S0021-9258(19)42509-X.

(60) Ueno, H.; Suemitsu, S.; Murakami, S.; Kitamura, N.; Wani, K.; Matsumoto, Y.; Aoki, S.; Okamoto, M.; Ishihara, T. Hyaluronic Acid Is Present on Specific Perineuronal Nets in the Mouse Cerebral Cortex. *Brain Res.* **2018**, *1698*, 139–150. https://doi.org/10.1016/j.brainres.2018.08.011.

(61) Arranz, A. M.; Perkins, K. L.; Irie, F.; Lewis, D. P.; Hrabe, J.; Xiao, F.; Itano, N.; Kimata, K.; Hrabetova, S.; Yamaguchi, Y. Hyaluronan Deficiency Due to Has3 Knock-Out Causes Altered Neuronal Activity and Seizures via Reduction in Brain Extracellular Space. *J. Neurosci.* **2014**, *34* (18), 6164–6176. https://doi.org/10.1523/JNEUROSCI.3458-13.2014.

(62) Kochlamazashvili, G.; Henneberger, C.; Bukalo, O.; Dvoretskova, E.; Senkov, O.; Lievens, P. M.-J.; Westenbroek, R.; Engel, A. K.; Catterall, W. A.; Rusakov, D. A.; Schachner, M.; Dityatev, A. The Extracellular Matrix Molecule Hyaluronic Acid Regulates Hippocampal Synaptic Plasticity by Modulating Postsynaptic L-Type Ca2+ Channels. *Neuron* **2010**, *67* (1), 116–128. https://doi.org/10.1016/j.neuron.2010.05.030.

(63) Stockholm, D.; Bartoli, M.; Sillon, G.; Bourg, N.; Davoust, J.; Richard, I. Imaging Calpain Protease Activity by Multiphoton FRET in Living Mice. *J. Mol. Biol.* **2005**, *346* (1), 215–222. https://doi.org/10.1016/j.jmb.2004.11.039.

(64) Jeong, W.; Bu, J.; Kubiatowicz, L. J.; Chen, S. S.; Kim, Y.; Hong, S. Peptide–Nanoparticle Conjugates: A next Generation of Diagnostic and Therapeutic Platforms? *Nano Converg.* **2018**, *5* (1), 38. https://doi.org/10.1186/s40580-018-0170-1.

(65) Vindis, C.; Elbaz, M.; Escargueil-Blanc, I.; Augé, N.; Heniquez, A.; Thiers, J.-C.; Nègre-Salvayre, A.; Salvayre, R. Two Distinct Calcium-Dependent Mitochondrial Pathways Are Involved in Oxidized LDL-Induced Apoptosis. *Arterioscler. Thromb. Vasc. Biol.* **2005**, *25* (3), 639–645. https://doi.org/10.1161/01.ATV.0000154359.60886.33.

(66) Smith, M. A.; Schnellmann, R. G. Calpains, Mitochondria, and Apoptosis. *Cardiovasc. Res.* **2012**, *96* (1), 32–37. https://doi.org/10.1093/cvr/cvs163.

(67) Chen, Y.; Mao, H.; Yang, K. H.; Abel, T.; Meaney, D. F. A Modified Controlled Cortical Impact Technique to Model Mild Traumatic Brain Injury Mechanics in Mice. *Front. Neurol.* **2014**, *5*, 100–100. https://doi.org/10.3389/fneur.2014.00100.

(68) Susaki, E. A.; Tainaka, K.; Perrin, D.; Yukinaga, H.; Kuno, A.; Ueda, H. R. Advanced CUBIC Protocols for Whole-Brain and Whole-Body Clearing and Imaging. *Nat. Protoc.* **2015**, *10* (11), 1709–1727. https://doi.org/10.1038/nprot.2015.085.

(69) Kirkpatrick, J. D.; Warren, A. D.; Soleimany, A. P.; Westcott, P. M. K.; Voog, J. C.; Martin-Alonso, C.; Fleming, H. E.; Tammela, T.; Jacks, T.; Bhatia, S. N. Urinary Detection of Lung Cancer in Mice via Noninvasive Pulmonary Protease Profiling. *Sci. Transl. Med.* **2020**, *12* (537). https://doi.org/10.1126/scitranslmed.aaw0262.

(70) Dudani, J. S.; Ibrahim, M.; Kirkpatrick, J.; Warren, A. D.; Bhatia, S. N. Classification of Prostate Cancer Using a Protease Activity Nanosensor Library. *Proc. Natl. Acad. Sci. U. S. A.* **2018**, *115* (36), 8954–8959. https://doi.org/10.1073/pnas.1805337115.

(71) Guilfoyle, M. R.; Carpenter, K. L. H.; Helmy, A.; Pickard, J. D.; Menon, D. K.; Hutchinson, P. J. A. Matrix Metalloproteinase Expression in Contusional Traumatic Brain Injury: A Paired Microdialysis Study. *J. Neurotrauma* **2015**, *32* (20), 1553–1559. https://doi.org/10.1089/neu.2014.3764.

(72) Knopp, R. C.; Jastaniah, A.; Dubrovskyi, O.; Gaisina, I.; Tai, L.; Thatcher, G. R. J. Extending the Calpain–Cathepsin Hypothesis to the Neurovasculature: Protection of Brain Endothelial Cells and Mice from Neurotrauma. *ACS Pharmacol. Transl. Sci.* **2021**, *4* (1), 372–385. https://doi.org/10.1021/acsptsci.0c00217.

(73) Tsubokawa, T.; Solaroglu, I.; Yatsushige, H.; Cahill, J.; Yata, K.; Zhang, J. H. Cathepsin and Calpain Inhibitor E64d Attenuates Matrix Metalloproteinase-9 Activity After Focal Cerebral Ischemia in Rats. *Stroke* **2006**, *37* (7), 1888–1894. https://doi.org/10.1161/01.STR.0000227259.15506.24.

(74) Samanta, A.; Zhou, Y.; Zou, S.; Yan, H.; Liu, Y. Fluorescence Quenching of Quantum Dots by Gold Nanoparticles: A Potential Long Range Spectroscopic Ruler. *Nano Lett.* **2014**, *14* (9), 5052–5057. https://doi.org/10.1021/nl501709s.

(75) Shin, T. H.; Kang, S.; Park, S.; Choi, J. sil; Kim, P. K.; Cheon, J. A Magnetic Resonance Tuning Sensor for the MRI Detection of Biological Targets. *Nat. Protoc.* **2018**, *13* (11), 2664–2684. https://doi.org/10.1038/s41596-018-0057-y.

(76) Girgis, F.; Pace, J.; Sweet, J.; Miller, J. P. Hippocampal Neurophysiologic Changes after Mild Traumatic Brain Injury and Potential Neuromodulation Treatment Approaches. *Front. Syst. Neurosci.* **2016**, *10*.

CHAPTER 4. BLOOD- AND URINE-BASED MEASUREMENT OF A TARGETED ACTIVITY-BASED NANOSENSOR FOR TRAUMATIC BRAIN INJURY

4.1. Abstract

Traumatic brain injury (TBI) affects millions of people annually in the United States. Current treatments for TBI are palliative and do not address the secondary injury which can lead to long-term side effects in physical and cognitive function. Part of the challenge in addressing secondary injury is that current diagnostic tools such as the Glasgow Coma Scale and medical imaging (e.g. computed tomography, magnetic resonance imaging) are limited to patient response and structural imaging and cannot detect the biological processes that unfold in the damaged brain. Breakdown products released into the blood as biomarkers are one potential strategy to measure the progression of secondary injury, and many of these biomarkers are produced by proteases. Aberrant protease activity is one of the hallmarks of secondary injury after TBI and a driver of disease progression, therefore technologies that measure protease activity have the potential to complement current diagnostics by supplying readouts on the active progression of injury. In this study, we developed an activity-based nanosensor for TBI (TBI-ABN) which can release a synthetic biomarker into the blood or urine for minimally-invasive measurement after cleavage by the TBI-associated protease calpain-1, which is a target of therapeutics for TBI. We established that the synthetic biomarker can be detected from the blood and urine via fluorescence and immunoassays after systemic administration in a mouse model of TBI. The sensitivity of the TBI-ABN in both blood and urine was improved by targeting the nanosensor to the extracellular matrix component hyaluronic acid with a peptide ligand, and this improvement was dependent on ligand valency. In a diagnostic evaluation within female and male mice, we observed sex-specific differences in urine signal but not in blood signal or organ

signal; in the urine of female mice, the TBI-ABN was able to identify severe TBI with a strong performance that was not observed in male mice. Blood- and urine-based detection of protease activity has the potential to provide tools to understand protease activity in TBI and supplement TBI diagnosis by providing readouts of potential therapeutic targets.

4.2. Introduction

TBI affects approximately 2.8 million people annually in the United States and leads to the hospitalization of over 200,000 patients per year.[1] Current diagnostics for TBI rely on the Glasgow Coma Scale which can be subjective, or on medical imaging (e.g. MRI, CT) which can be time- and resource-intensive.[2–4] More recently, there has been the identification of biomarkers that can be detected in the blood or cerebrospinal fluid. These biomarkers are breakdown products which are released during degenerative processes after TBI.[5] Measurement of these biomarkers can help identify processes that otherwise could not be captured by medical imaging, and provide additional information for the triage, treatment, and prognostication of TBI patients. Moreover, they can be sampled through minimally-invasive collection of biofluids and can be quantified relatively quickly compared to imaging. However, there are some limitations to the measurement of endogenous biomarkers. The levels of most blood-based biomarkers for TBI are so low that their measurement requires extremely sensitive assays; until the recent developments of more sensitive instruments such as the Abbot i-Stat device,[6,7] this had limited the development of rapid point-of-care diagnostics.[8] Moreover, it has been difficult to identify biomarkers that are unique to the brain, as some levels of TBI biomarkers can change in response to poly-trauma or other stressors.

As an alternative to the measurement of endogenous biomarkers, synthetic sensors have been developed which can directly sample the activity of the proteases producing these biomarkers.[9,10] Proteases, enzymes which can selectively identify and cleave sequences in other proteins, are involved in critical cellular processes such as signal transduction, protein processing, and transcriptional control.[11] In disease, these proteases can be ectopically expressed or activated, which can then drive central hallmarks of disease such as inflammation and extracellular matrix remodeling. Direct readouts of these pathological processes can aid in diagnosis and identify direct targets for therapeutic intervention.[9] In addition, activity-based sensors are engineered from the ground up and therefore can be selectively tuned to optimize the sensitivity and specificity of measurement.[12,13] Many of the endogenous biomarkers currently being investigated for TBI diagnosis (e.g. SNTF) are produced by ectopic protease activity including the calcium-dependent protease calpain-1.[5] Calpain-1 is expressed within neurons, astrocytes, and endothelial cells in the brain, and is locally activated within injured brain tissue after TBI as part of secondary injury.[14–19] Calpain-1 activity is implicated in cellular death and worsened prognosis after TBI,[20–22] and it is a target of therapeutics for TBI.[23] Thus, tools to measure calpain-1 activity may useful in diagnostic measurement of injury progression, predicting patient prognosis, and informing precision treatments after TBI.

In previous work, we developed an imaging-based nanosensor for calpain-1 activity which could accumulate within the injured brain tissue and produce a fluorescent signal after systemic administration in a mouse model of TBI.[19] The sensitivity of this calpain-1 nanosensor was improved by incorporating targeting to the brain extracellular matrix component hyaluronic acid (HA).[24] In this study, we designed an activity-based nanosensor for TBI (TBI-ABN) which instead of generating fluorescent signal in situ, releases a synthetic biomarker into the blood and

urine for a minimally-invasive measurement of calpain-1 activity after TBI. We demonstrate that this nanosensor can produce signals in the blood and urine in a mouse model of TBI and that activated sensor can be quantified both via fluorescence and immunoassays. The addition of targeting ligands to HA improved the sensitivity of both blood and urine measurement in a ligand valency-dependent manner. Finally, a targeted form of the TBI-ABN was assessed for diagnostic efficacy in both female and male mice, where sex-based differences were observed in urine signal but not in blood or organ signal. This minimally-invasive measurement of protease activity after TBI has the potential to supplement current diagnostics by providing directly-actionable readouts which can inform patient treatment.

4.3. Results and Discussion

4.3.1. TBI-ABN allows for two detection modalities.

We designed a calpain-1 nanosensor that allows for measurement by both direct fluorescence and immunoassay quantification in the blood or urine (Figure 4.1 and Figure 4.2). Direct fluorescence measurement was desirable as a simple method to validate the engineering design of the nanosensor, while immunoassay quantification was desirable both for an increased dynamic range and sensitivity and as a format more relevant to clinical diagnostics. This nanosensor contains a calpain substrate peptide from native substrate αII-spectrin[25] flanked by a fluorescein (FAM) fluorophore and CPQ2 quencher FRET pair (Biotin-GGSGG-K(5FAM)-QEVYGAMP-K(CPQ2)-C-NH2). To prolong circulation time in the blood and improve passive accumulation into the injured brain, the calpain substrate peptide was conjugated via a C-terminal cysteine to an 8-arm 40 kDa poly(ethylene glycol) (PEG) scaffold.[19] The multi-arm PEG scaffold was chosen because a single scaffold can carry multiple functional moieties, and

because PEG is biocompatible and a component of many FDA-approved materials;[26] moreover, it has a hydrodynamic diameter of ~10 nm[19] which is both above the renal filtration limit of ~5.5 nm[27] and below the estimated pore size of the brain extracellular matrix.[28,29] Nanoscale materials are able to passively accumulate within injured brain tissue in the first 24 hours after TBI due to an enhanced permeation and retention-like effect.[19,24,30–33] The peptide was designed such that upon calpain-1 cleavage, the quencher remains attached to the PEG scaffold while the FAM-labeled cleaved peptide (c-Peptide) is released (Figure 4.2A). The c-Peptide also contains an N-terminal biotin connected to the FAM via a short peptide linker to create a heterobifunctional synthetic biomarker for downstream analysis.[34] This biomarker can be quantified with sandwich immunoassays using α-FAM antibodies to capture the FAM end of the peptide and labeled streptavidin to detect the biotin end of the peptide.

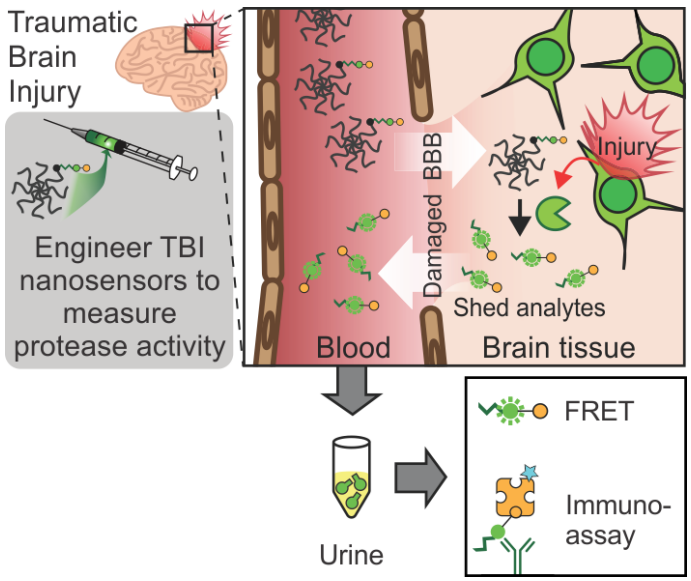

Figure 4.1: Overview of redesigned TBI-ABN. After systemic administration, the ABN accumulates in injured brain tissue where it is cleaved by calpain-1. The cleaved peptide (c-Peptide) can then shed back into the blood and urine for minimally-invasive measurement of protease activity via fluorescence or ELISA.

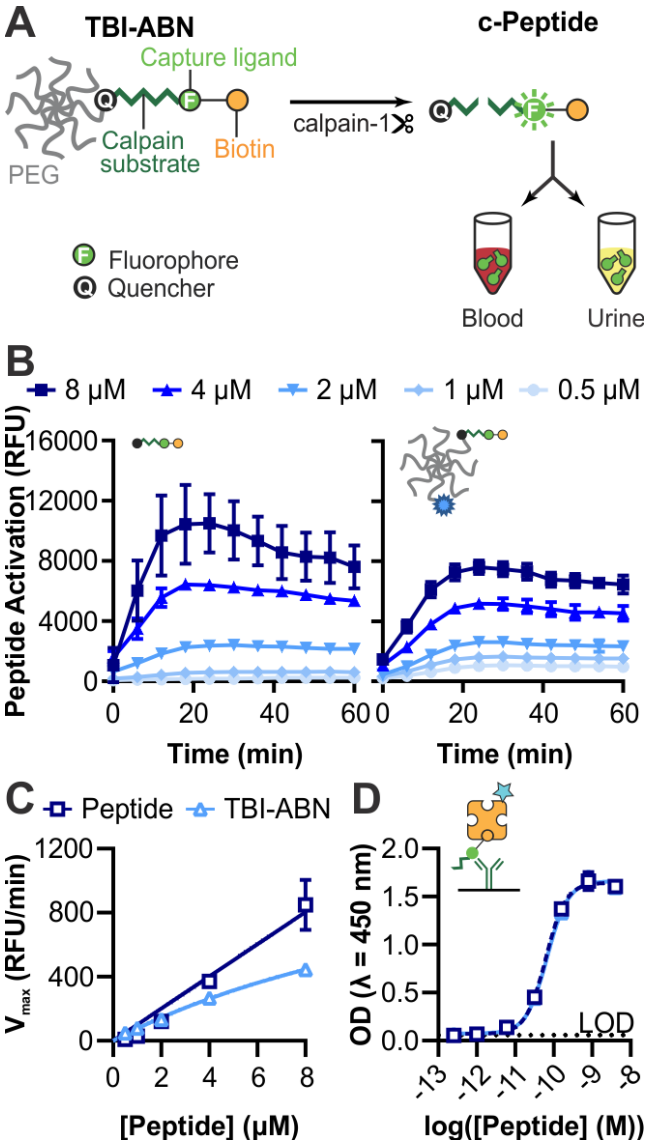

Figure 4.2: (A) TBI-ABN contains a calpain-1 FRET substrate peptide that can be quantified via fluorescence and ELISA. (B) In vitro cleavage kinetics of free peptide (left) and peptide conjugated to PEG to form TBI-ABN (right), incubated with human calpain-1 (n = 3, mean ± SD). (C) Michaelis-Menten curves derived from the maximal velocities of cleavage (n = 3, mean ± SD). (D) Dynamic range of free peptide and TBI-ABN on a sandwich ELISA, with α-FAM as the capture antibody and streptavidin-HRP as the detection molecule. (n = 3, mean ± SD, dashed line denotes the limit of detection (LOD)).

For initial kinetics and pharmacokinetics tests, TBI-ABN was synthesized by reacting 40 kDa 8-arm PEG maleimide with 1 mol equivalence of calpain substrate peptide and 1 mol equivalence of cysteine-functionalized fluorescent tag VivoTag S-750 (VT750). We verified that the calpain substrate peptide undergoes FAM dequenching after cleavage by human calpain-1 in vitro, and that conjugation of the peptide to the PEG scaffold minimally impacted cleavage kinetics (Figure 4.2B). At 8 µM peptide, the maximal velocity of cleavage decreased from ~850 RFU/min to ~445 RFU/min with conjugation. However, at lower concentrations of peptide the difference in cleavage rates was less pronounced between free peptide and conjugate (Figure 4.2C). We investigated whether the decrease in maximal velocity was due to the presence of PEG, or due to the conjugation of peptide to PEG, and found that the conjugation of peptide to PEG led to the decrease in kinetics (Figure 4.3).

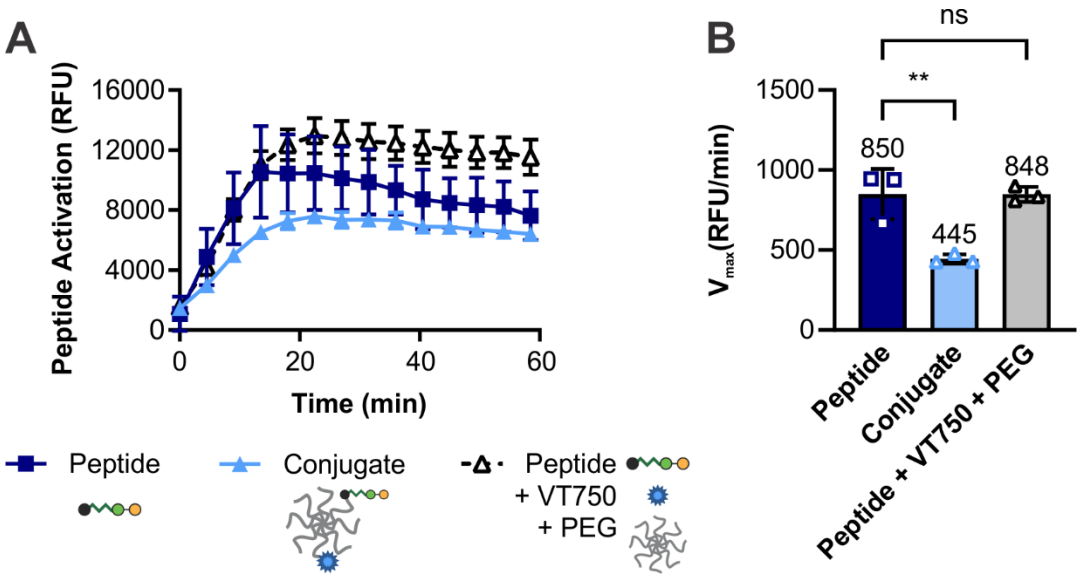

Figure 4.3: (A) Kinetic curves and (B) Vmax at 8 µM peptide for calpain substrate peptide, TBI-ABN conjugate, and TBI-ABN conjugate components (n = 3, mean ± SD, Ordinary one-way ANOVA with Dunnett's multiple comparisons post-hoc test against peptide, **p<0.005).

Previous studies have shown that the attachment of peptide substrates to PEG change cleavage specificity and kinetics.[13] The specificity of calpain substrate was assessed by incubating free peptide with two off-target proteases: α-thrombin, an abundant blood protease that is involved in the clotting cascade and can extravasate from the blood into the brain parenchyma in brain injury,[35–37] and MMP9, a protease that has also been found to activate within injured brain tissue after TBI.[38–41] The calpain substrate peptide did not activate after incubation with either α-thrombin or MMP9 at the concentrations tested (Figure 4.4). Lastly, in order to validate that the designed peptide could be sensitively measured in immunoassays, we developed a sandwich ELISA immunoassay. The ELISA uses α-FAM antibodies to capture the FAM end of the peptide and streptavidin-HRP to detect the biotin end of the peptide. This allows for a more sensitive measurement of calpain substrate peptide with a limit of detection down to ~1 pM peptide (Figure 4.2D). The α-FAM antibody binds with equal affinity to both free peptide and conjugate, thus the accurate measurement of biological samples would require the removal of conjugate carrying uncleaved peptide prior to measurement.

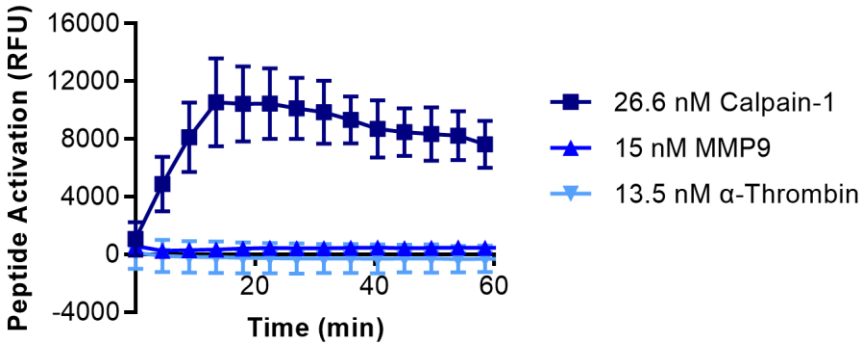

Figure 4.4: Specificity assay of 8 μM calpain substrate peptide after incubation with calpain-1, MMP9, or α-thrombin (n = 3, mean ± SD).

4.3.2. TBI-ABN produces fluorescent signal in the blood and urine in a TBI mouse model.

The pharmacokinetics and activation of calpain substrate peptide and TBI-ABN were then evaluated in vivo in a mouse model of TBI (Figure 4.5A). First, the blood circulation time and urine clearance were investigated to determine the time-dependent boundaries for sampling TBI-ABN activity. In uninjured mice, free peptide was intravenously administered followed by blood collection from the tail-vein at 1, 3, 7, 15, 30, 60, and 120 minutes post-injection or urine collection at 1 hour post-injection. Peptide was quantified via ELISA and compared to a standard to obtain the percent injected dose (%ID) for each sample. Free calpain substrate peptide was found to have a distribution half-life of 1.49 minutes, and a clearance half-life of 18.8 minutes (Figure 4.5B). At 1 hour post-injection, ~5% of the peptide remained in blood circulation, while the greater majority of peptide was recovered from the urine (Figure 4.5B-C). This suggests that the peptide can clear into the urine after 1 hour of circulation. This was expected based on the small molecular weight of the peptide, which is ~2.6 kDa when uncleaved and ~1.5 kDa when cleaved.

To track the circulation of the larger TBI-ABN construct, the PEG scaffold was conjugated with the fluorophore VT750. Uninjured mice were intravenously given TBI-ABNs followed by blood collection at 0, 1, 2, 4, 8, and 24 hours post-injection and urine collection at 1 hour post-injection. Blood and urine samples were both measured for the fluorophore and compared to a standard to determine %ID. TBI-ABNs were found to have a much longer circulation time in the blood compared to free peptide, with a distribution half-life of 16.8 minutes and a clearance half-life of 29.6 hours (Figure 4.5D). At 1 hour post-injection, ~1.8% of PEG was recovered from urine (Figure 4.5E). The observed clearance was comparable to previous observations on renal clearance of 40 kDa 8-arm PEG in mice,[12] and is over an order of

magnitude lower than the observed clearance of free peptide. The 40 kDa 8-arm PEG scaffold has a hydrodynamic diameter of ~10.3 nm,[19] which is above the renal filtration limit of ~5.5 nm.[27] Thus, the kidney acts as a natural size filter to allow c-Peptide to accumulate in the urine while excluding uncleaved, intact TBI-ABNs. This property allows for quantification of c-Peptide in the urine using both fluorescence and ELISA without the need to separate uncleaved from cleaved TBI-ABN. Due to the inability to separate uncleaved and cleaved TBI-ABN in blood, TBI-ABN activation in the blood was only measured through fluorescence of activation. The combined rates of TBI-ABN extravasation into the injured brain, calpain-1 cleavage of the substrate, and shedding of c-Peptide back into the bloodstream will likely be similar to the clearance rate of c-Peptide from the blood. Thus, the accumulation of signal with injury is expected to take more time to be apparent in blood, which provides a snapshot of activity, compared to urine, which can integrate the accumulation of signal over time.[12]

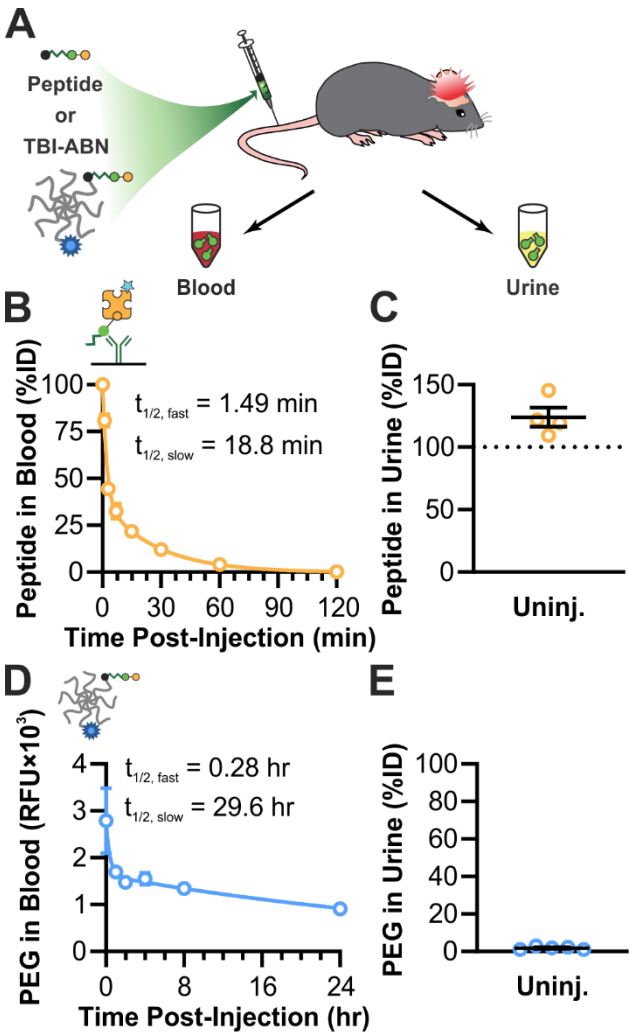

Figure 4.5: Pharmacokinetics of TBI-ABN in mice. (A) Nanosensor was intravenously administered at 3 hours post-injury, and blood and urine samples were collected at multiple time-points after injection. (B) Blood circulation half-life of free calpain substrate in the blood of uninjured mice, as measured by ELISA (n = 2-4, mean ± SE, two-phase decay). (C) Estimated accumulation of free calpain substrate in the urine of uninjured mice at 1 hour post-injection, as measured by ELISA (n = 4, mean ± SE). (D) Blood circulation half-life of TBI-ABN tagged with VT750 in injured and uninjured mice, as measured by fluorescence of VT750 (n = 5, mean ± SE). (E) Accumulation of TBI-ABN tagged with VT750 in urine at 1 hour post-injection, as measured by fluorescence of VT750 (n = 5, mean ± SE).

4.3.3. Targeting the TBI-ABN to hyaluronic acid improves sensitivity of TBI-ABN.

Next, we sought to improve on the sensitivity of blood and urine measurement by incorporating active targeting ligands to the extracellular matrix component, hyaluronic acid (HA). The brain parenchyma is highly abundant in HA, which can be accessed via passive accumulation after disruption of the BBB in TBI.[24,30,42] Thus, targeting to HA could improve the accumulation of systemically administered material in the injured brain tissue and therefore improve sampling of TBI-associated proteases. The addition of targeting ligands has previously shown to improve sensitivity of a cancer nanosensor, as supported by predictions of a mathematical framework.[13] In previous work, we employed an HA-targeting peptide (HApep)[43] on our imaging nanosensor and were able to increase signal generation in the injured tissue by 6.6-fold over untargeted nanosensor.[24] We hypothesized that this increased signal generation observed in the injured brain tissue with our imaging nanosensor would translate to increased signal in the blood and urine from our redesigned diagnostic TBI-ABN.

We investigated how the valency of targeting ligand impacted blood and urine signal generated from our diagnostic TBI-ABN. In order to create conjugates with matched levels of sensor peptide, 40 kDa 8-arm PEG-maleimide and calpain substrate peptide were first reacted in equimolar concentrations then split into 3 reactions with different inputs of HApep with an N-terminal cysteine (CWSTMMSRSHKTRSHHV). The resulting conjugates for non-targeted, moderate targeted, and high targeted TBI-ABNs had molar ratios of 0, ~2.5, and ~3.9 HApep per calpain substrate, respectively, as measured by absorbance (Table 4.1, Figure 4.6). The addition of HApep on the TBI-ABNs did not significantly affect cleavage kinetics of the calpain substrate peptide between conjugates (Figure 4.7 and Figure 4.8).

Table 4.1**:** Concentration measurements of calpain substrate peptide[a] and HApep[b] on TBI-ABNs in PBS.

TBI-ABN	Ratio of HApep to calpain substrate
Non-Targeted	N/A
Moderate-targeted	2.5
High-Targeted	3.9

[a]Calpain substrate absorbance measured by FAM absorbance at λ = 495 nm, concentration calculated from a standard of free peptide in PBS

[b]HApep absorbance measured by tryptophan content at λ = 280 nm, $\varepsilon_{280\ nm}$ = 5,500 $(M*cm)^{-1}$ after correcting for the contribution to absorbance from calpain substrate

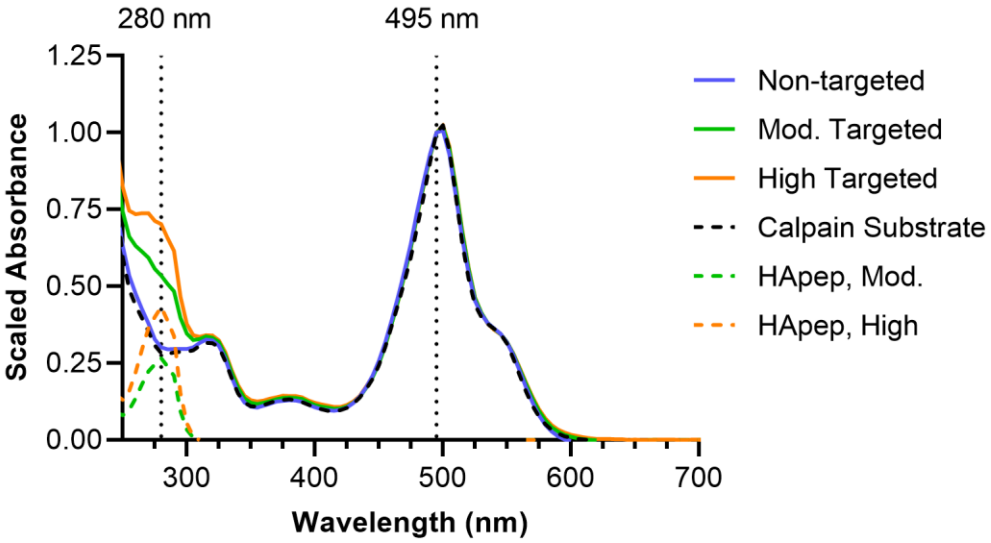

Figure 4.6: Absorbance spectra of targeted TBI-ABNs show peaks at 280 nm for HApep and 495 nm for calpain substrate.

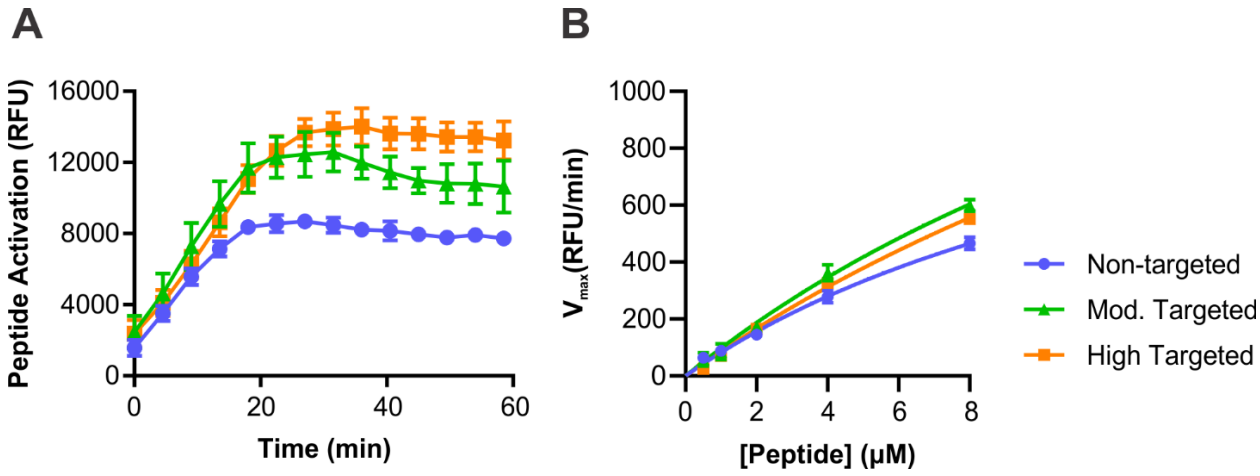

Figure 4.7: (A) Kinetic curves at 8 μM calpain substrate peptide of targeted TBI-ABNs incubated with human calpain-1 (n = 3, mean ± SD). (B) Michaelis Menten curves derived from the maximal velocities of cleavage (n = 3, mean ± SD).

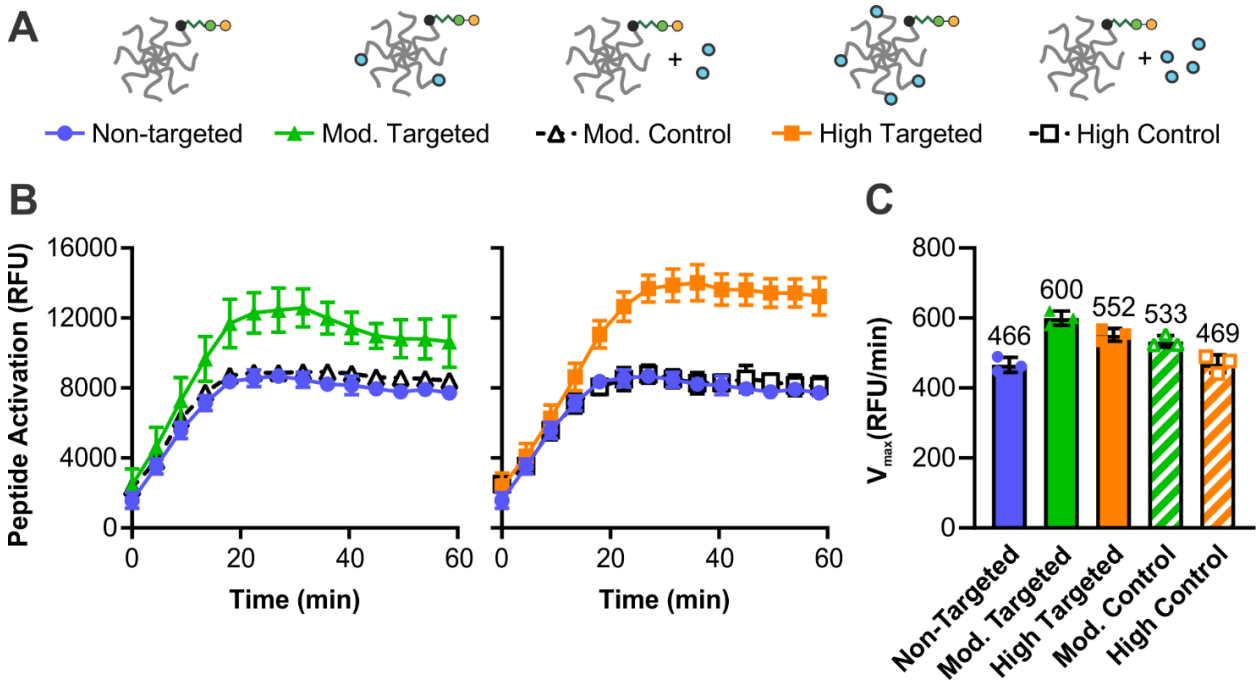

Figure 4.8: (A) Non-targeted TBI-ABN was incubated with unconjugated HApep at equal ratios to the HApep in moderate and high targeted TBI-ABNs as controls for conjugation. (B) Deconstructed conjugate control curves and (C) bar graph of V_{max} for moderate and high targeted conjugates at 8 μM calpain substrate peptide with human calpain-1 (n = 3, mean ± SD, Ordinary one-way ANOVA with Dunnett's multiple comparisons post-hoc test against non-targeted).

Conjugates were evaluated in a controlled cortical impact (CCI) model of TBI. CCI is a well-characterized model of focal TBI[44] and has shown to recapitulate human-relevant features of TBI, such as locally increased calpain-1 activity within injured brain tissue.[18,19] Uninjured mice and CCI-injured mice were each intravenously administered one of the three targeted TBI-ABNs at 3 hours post-injury, following previous observations in increased calpain activity in injured brain tissue at that time-point.[19] Blood collection was performed at 0, 1, 2, 4, and 8 hours post-injection and urine collection was performed at 1 hour post-injection (Figure 4.9A). In fluorescence readings of calpain substrate cleavage from blood samples, non- and moderate targeted TBI-ABNs showed an increased activation of signal in injured mice relative to the baseline activation seen in uninjured mice (Figure 4.9B). In contrast, the high targeted TBI-ABNs showed minimal differences in blood signal between injured and uninjured mice. For further analysis, we generated receiver operating characteristic (ROC) curves for each time point based on the ability to distinguish signal between uninjured and CCI-injured mice and calculated the area under the curve (AUC) as a measure of diagnostic performance (Figure 4.10). Based on ROC AUC values, the ability of each TBI-ABN to classify injury through blood samples increased over time from 1 hour through 4 hours before plateauing (Figure 4.9C). The moderate targeted TBI-ABN outperformed the non-targeted TBI-ABN at classifying injury through blood samples from 1 hour post-injection, while the high targeted TBI-ABN could only classify injury from 4 hours post-injection.

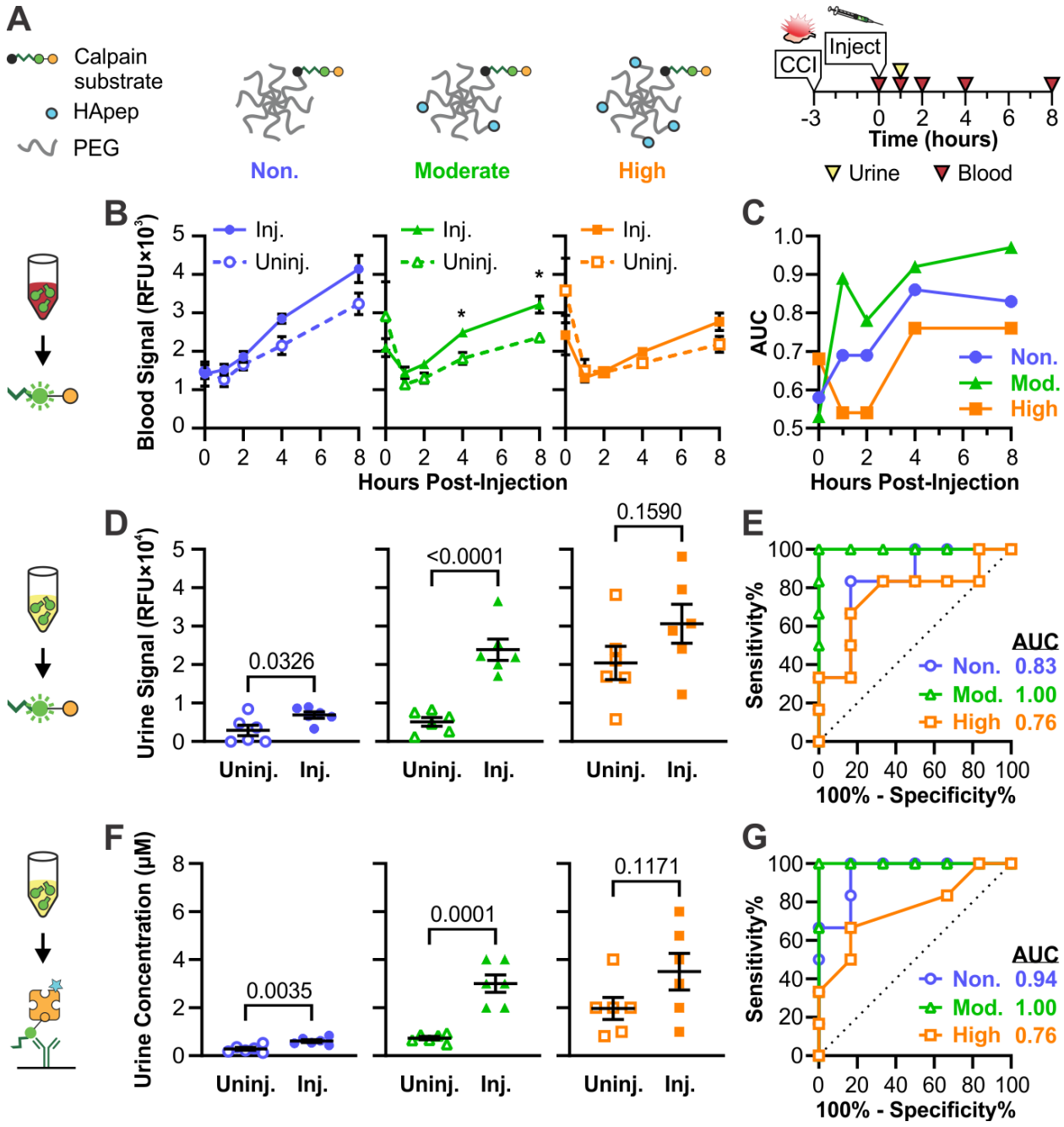

Figure 4.9: Targeting to hyaluronic acid improves the sensitivity of TBI-ABN in both blood and urine. (A) Schematic of HA-targeted TBI-ABNs with non-, moderate, and high targeted ABNs. (B) Activation of sensor in the blood of injured and uninjured mice at multiple time-points post-injection as measured by fluorescence (n = 6, mean ± SE, Two-way RM ANOVA with Sidak's multiple comparisons post-hoc test for each time point, *p<0.05). (C) AUCs for blood ROCs taken at each time point (n = 6). (D,F) Accumulation of activated sensor in the urine of mice 1 hour post-injection as measured by fluorescence and ELISA respectively (n = 6, mean ± SE, Unpaired t-test). (E,G) ROC curves and calculated AUCs from fluorescence and ELISA measurements of urine, respectively (n = 6).

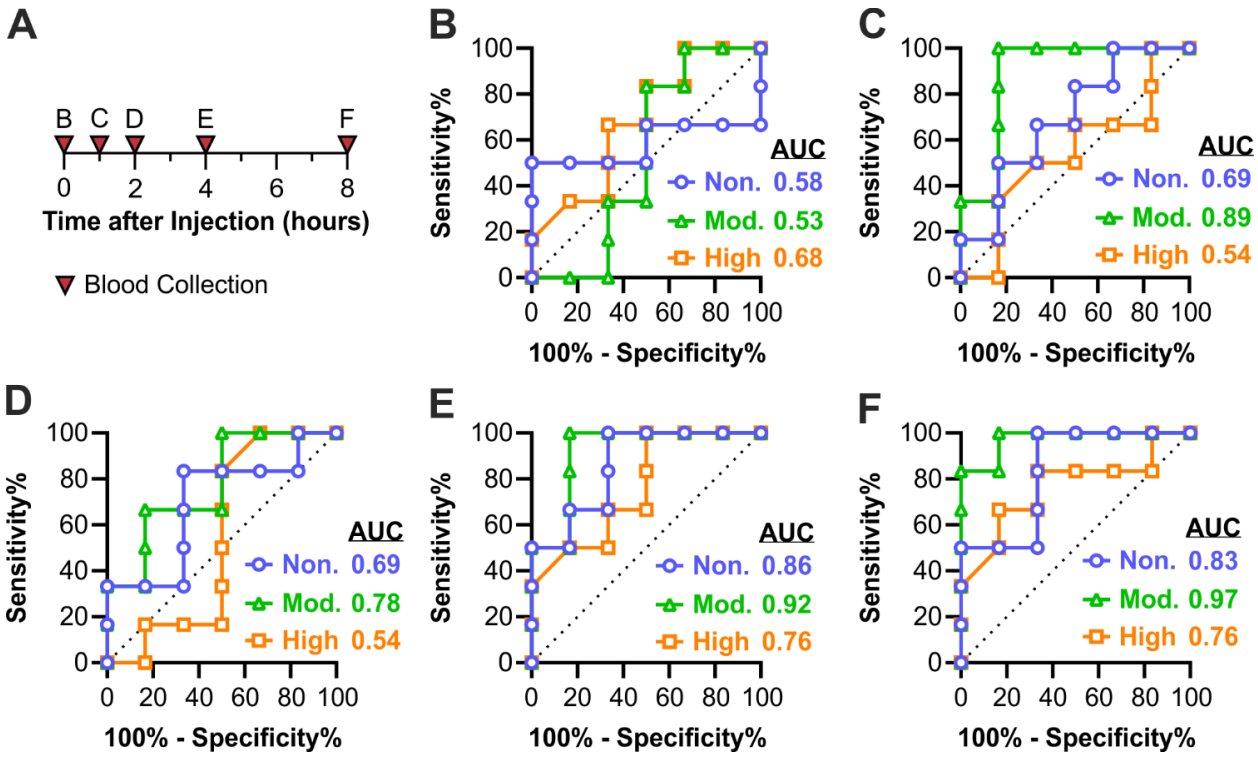

Figure 4.10**:** (A) Time points of blood collection and (B-F) ROC curves classifying injured from uninjured mice using TBI-ABN fluorescence from blood samples at 0, 1, 2, 4, and 8 hours post-injection, respectively (n = 6).

Consistent with measured blood activation, the moderate targeted TBI-ABN showed the greatest increase in urine signal between injured and uninjured conditions compared to the non- and high targeted TBI-ABNs (Figure 4.9D). Interestingly, while the absolute fluorescent signal in urine increased with ligand valency in injured mice, high targeted TBI-ABN yielded substantially elevated signal accumulation in the urine of uninjured mice. The moderate targeted TBI-ABNs yielded the highest signal-to-noise ratio of 4.7, significantly outperforming the signal-to-noise ratios of 2.4 and 1.5 for non- and high targeted TBI-ABNs, respectively. These observations are consistent to previous observations with targeting with the imaging TBI-ABN,[24] where the sensitivity of TBI-ABN signal within injured brain tissue was the highest for the high targeted TBI-ABN, at the cost of high accumulation and activation in off-target organs. In that

study, the moderate targeted TBI-ABN yielded the highest specificity with minimal accumulation or activation within off-target organs. The specificity advantage of moderate levels of targeting were recapitulated in the diagnostic TBI-ABN; moderate targeted TBI-ABN was able to discriminate injury with an ROC AUC of 1.00, compared to non-targeted and high targeted TBI-ABNs with ROC AUCs of 0.83 and 0.76, respectively (Figure 4.9E). Signal was not correlated with the collected urine volume, indicating that the differences in signal were primarily due to targeting (Figure 4.11A). In order to establish that signal from the urine could also be measured with more clinically-relevant immunoassays, an ELISA was performed to quantify the concentration of c-Peptide in urine samples (Figure 4.9F). The c-Peptide concentration quantified by ELISA correlated closely with fluorescence measurements with a Pearson correlation of $r = 0.9686$, confirming that an immunoassay accurately reflected peptide cleavage as measured by the direct fluorescent measurement (Figure 4.11B). The ELISA measurements resulted in signal-to-noise ratios of 2.1, 4.1, and 1.8 for non-, moderate, and high targeted TBI-ABNs, respectively (Figure 4.9F). The ROC curves based on ELISA measurements likewise were comparable to the ROC curves based on fluorescence, with ROC AUCs of 0.94, 1.00, and 0.76 for non-, moderate, and high targeted TBI-ABNs, respectively (Figure 4.9G).

The difference in diagnostic performance between the nanosensors with various targeting valencies highlights the importance of tuning targeting valency in nanomaterial interactions. The overall binding strength of nanomaterials to their targets can be enhanced by increasing targeting valency.[45] However, too high of an avidity can disrupt transport of materials to their desired target,[46] and changes in pharmacokinetic properties such as charge can affect cellular uptake in off-target organs such as the liver, spleen, or kidneys.[33,47] This was observed with HA-targeting of a calpain nanosensor in our previous study, where increasing valencies of targeting led to

increased nanosensor activation within both the target brain tissue and in off-target organs.[24] Thus, the relative contribution of off-target activation is likely increased with high targeted TBI-ABNs, leading to the reduced difference in both blood and urine signal between injured and uninjured mice. From these results, the moderate targeted TBI-ABN yielded the highest combination of sensitivity and specificity for both blood and urine measurements. One possible reason for this enhanced sensitivity is that HA is a component of peri-neuronal nets, which surround the cell bodies of neurons.[48] Neurons are a major source of calpain-1 within the brain, and therefore the physical localization of nanosensor to neurons may increase sampling of ectopic calpain-1 activity after TBI.[49,50] The 4-hour time point was selected for blood sampling in subsequent experiments based on statistical significance seen in the time-course of injured signal relative to uninjured controls (Figure 4.9A).

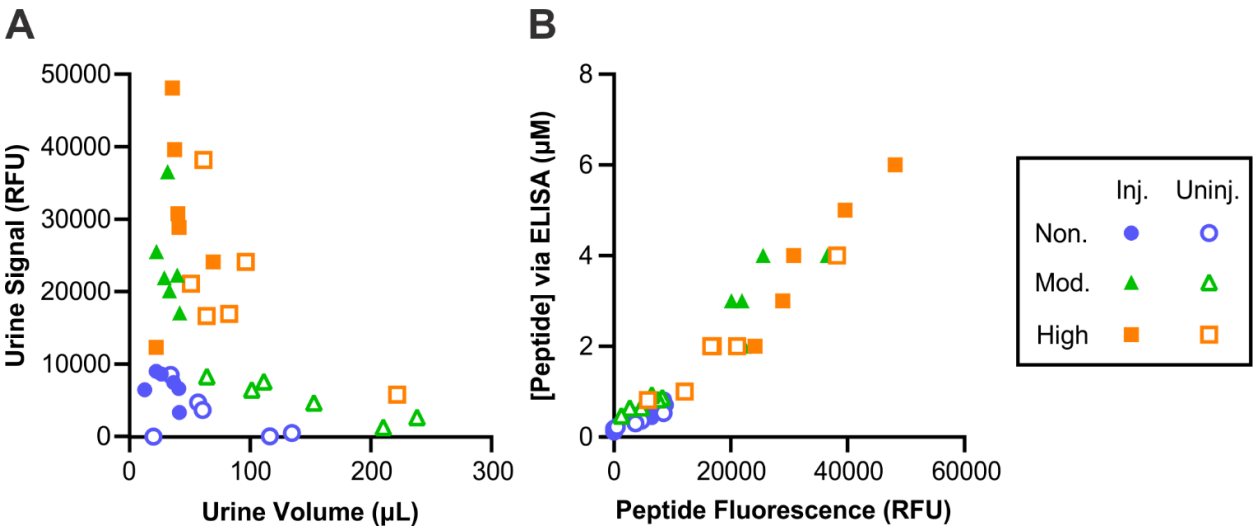

Figure 4.11: Measurement of peptide via ELISA yields similar results to measurement via fluorescence. (A) Scatterplot of activated nanosensor signal in urine against collected urine volume in female mice with different targeted TBI-ABNs (n = 36). (B) Scatterplot, fluorescence vs. ELISA concentration of cleaved TBI-ABN in urine collected at 1 hour post-injection (n = 36, Pearson correlation analysis: r = 0.9686, p<0.0001).

4.3.4. Sex- and severity-dependent performance of targeted TBI-ABN.

After establishing the optimal valency of HA targeting and identifying the 1-hour urine and 4-hour blood collection time points, we further evaluated the diagnostic efficacy of the moderate targeted TBI-ABN in a larger cohort of both female and male mice. Our next goal was to evaluate performance of our nanosensor based on sex and injury severity. Sex-based differences in cellular responses and outcome after TBI have been observed in both human patients and animal models,[51,52] and these differences could extend to calpain-1 activity. For example, the spatial distribution and time course of calpain-1 activation in the brain was found to differ after diffuse head injury in female and male mice.[53] Thus, we investigated whether the TBI-ABN could detect sex-based differences in calpain-1 activation. We also investigated whether the TBI-ABN could discriminate between different severities of injury, as the serum levels of calpain-specific breakdown products have previously been observed to increase with severity of injury in human patients.[22] Two severities of injury were investigated based on previously established studies[54] by varying the depth of impact and speed of impact to produce mild and severe TBI. For mild injuries, impact depth was 0.5 mm and impact speed was 1 m/s while for severe injuries, impact depth was 2 mm and impact speed as 5 m/s. TBI-ABN was administered at 3 hours post-injury and urine was collected at 1 hour post-injection and blood was collected at 4 hours post-injection (Figure 4.12A).

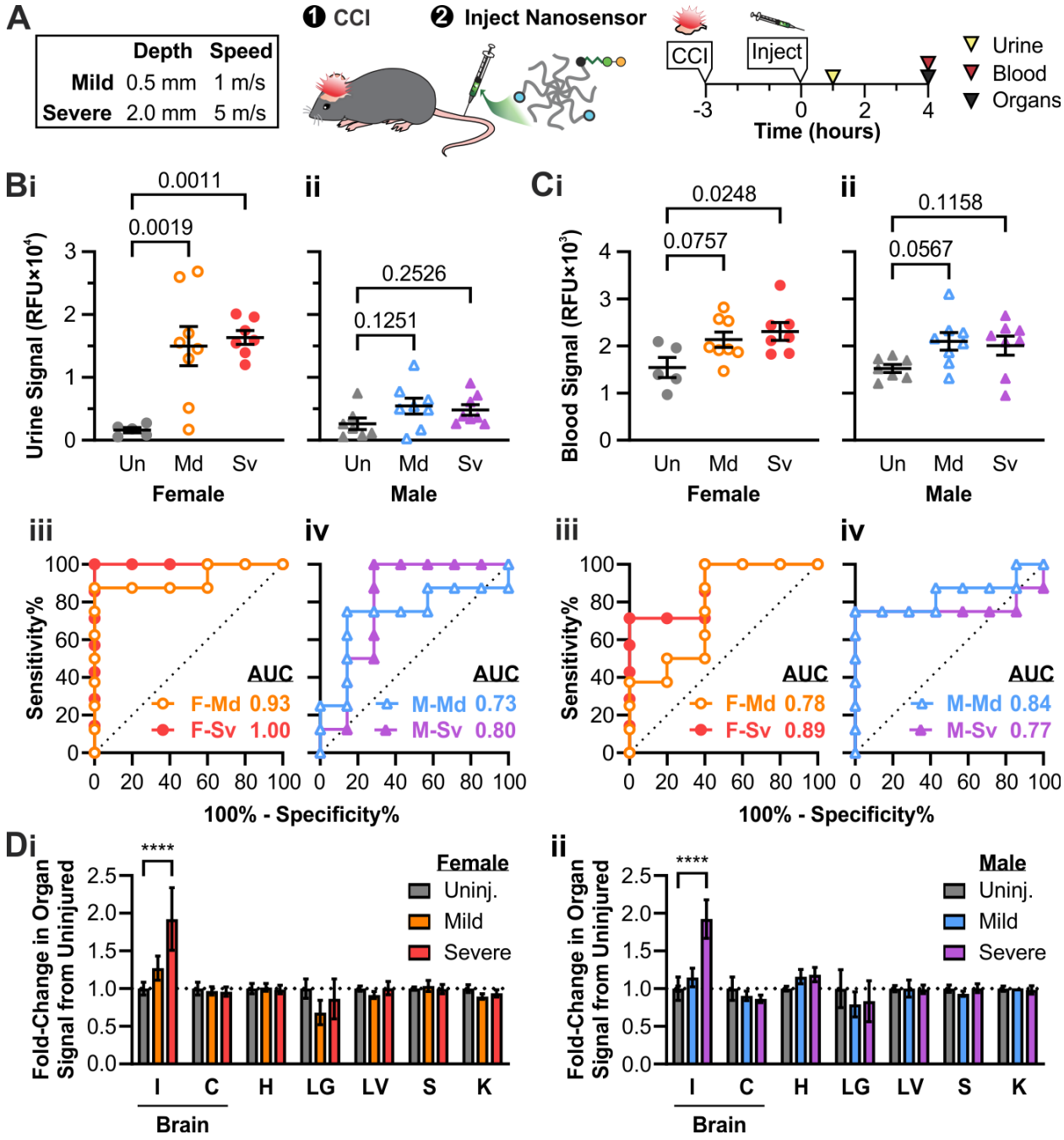

Figure 4.12: Moderate targeted TBI-ABNs show different patterns of signal with injury in female vs. male mice. TBI-ABN activation in (B) urine at 1 hour post-injection and (C) blood at 4 hours post-injection in (i) female and (ii) male mice as measured by fluorescence, and corresponding ROC curves in (iii) female and (iv) male mice (Un = uninjured; Md = mild CCI; Sv = severe CCI; F = female; M = male; n = 5-8, mean ± SE, ordinary one-way ANOVA with Dunnett's multiple comparisons post-hoc test against uninjured control). (D) Relative fold-change of TBI-ABN activation in the brain (I = injured cortical tissue, C = contralateral cortical tissue, with I+C pooled for uninjured control) and in off-target organs (H = heart; LG = lungs; LV = liver; S = spleen; K = kidney) in (i) female and (ii) male mice with mild or severe CCI compared to uninjured controls (n = 5-8, mean ± SE, two-way ANOVA with Dunnett's multiple comparisons test compared to uninjured within each organ, ****p<0.0001).

In urine samples collected at 1 hour post-injection, female mice produced strong fluorescent signals with both mild and severe injury, with a ~9-10-fold higher signal compared to uninjured female mice (Figure 4.12Bi). Curiously, signal measured in injured male mice was lower in magnitude than what was measured in female mice, with a ~2-fold higher signal in injured male mice compared to uninjured male mice despite producing similar urine volumes to female mice within each injury group (Figure 4.12Bii and Figure 4.13).

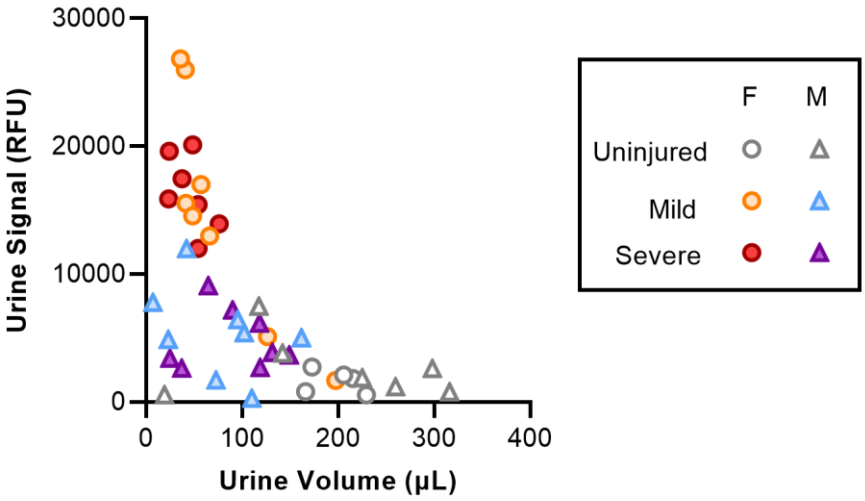

Figure 4.13: Scatterplot of activated nanosensor signal in urine against collected urine volume in female and male mice and different severities of CCI (n = 43).

No differences in overall signal generation were observed between mild and severe injury conditions within either sex, although signal generation for mild injuries were more variable. The TBI-ABN was able to discriminate injury in female mice with higher performance in mice with severe (ROC AUC 1.0) compared to mild (ROC AUC 0.93) injuries (Figure 4.12Biii). In male mice, the diagnostic performance was somewhat reduced, with ROC AUCs of 0.73 for mild injury and 0.80 for severe injury (Figure 4.12Biv). In blood samples taken 4 hours post-injection,

the measured signal was similar in female and male mice across injury severities (Figure 4.12Ci-ii). Accordingly, the diagnostic performances were similar between female and male mice within each group, with ROC curve AUCs of 0.78 and 0.84 for female and male mice with mild injury, and 0.89 and 0.77 for female and male mice with severe injury, respectively (Figure 4.12Ciii-iv). The urine ROC curve in female mice, and the blood ROC curves in both sexes of mice are comparable to AUCs seen for diagnosis of TBI with blood-based measurement of GFAP and UCHL-1 in human patients.[55]

To determine whether the observed sex-based differences in urine signal were due to differences in overall sensor activation in the injured brain, cortical brain tissue and off-target organs were collected for homogenization from each mouse at 4-5 hours post-injection. Sensor fluorescence was measured from organ homogenates to characterize the biodistribution of activated nanosensor. Overall nanosensor activation was comparable across organs between female and male mice (Figure 4.12D and Figure 4.14). A severity-dependent increase in fluorescence was observed within the ipsilateral cortical brain tissue in injured mice, with a slight increase in mild injury and significant increase in severe injury relative to uninjured mice. Within each sex and injury condition, there was no difference in the relative distribution of signal across organs. This suggests that the overall activation of sensor is independent of sex, and that the differences measured in urine signals could be due to differences in transport of c-Peptide.

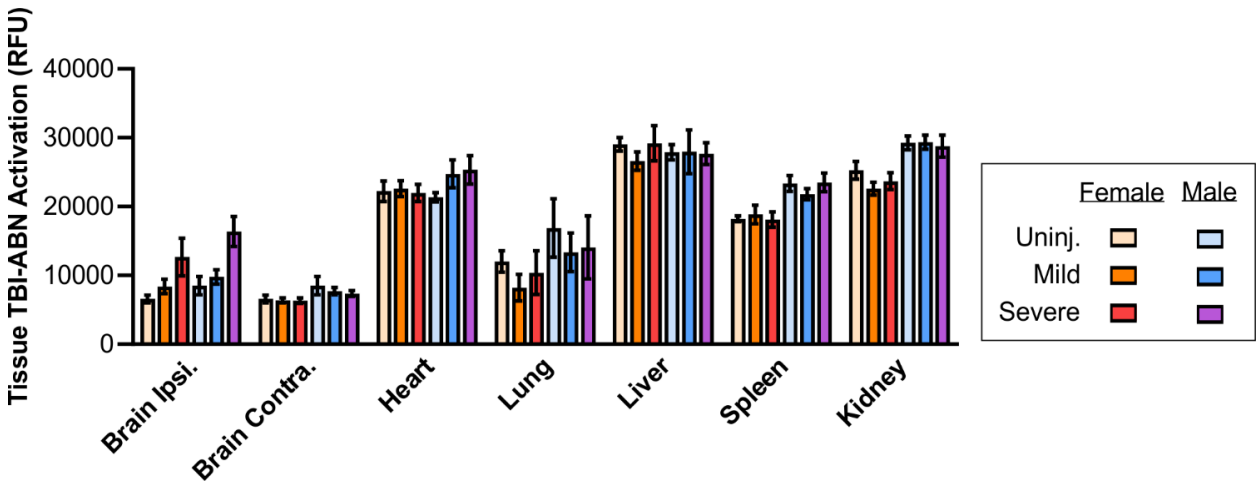

Figure 4.14: TBI-ABN activation in the brain (Ipsi. = injured cortical tissue, Contra. = contralateral cortical tissue, with Ipsi.+Contra. pooled for uninjured control) and in off-target organs in female and male mice with no, mild, or severe CCI (n = 5-8, mean ± SE).

In the context of TBI, it has previously been shown that there are sex-dependent differences in the extravasation of nanoparticles to the injured brain 24 hours after TBI, but not at 3 hours after TBI.[56] The lack of sex-based differences in nanosensor activation within injured brain tissue and the shorter time-frame of this study both suggest that the observed differences in urine signal were not due to sex-dependent changes in nanosensor extravasation. The difference in transport could instead be due to intrinsic differences in renal function between sexes. Sex-based differences in the renal transport of different compounds, and in the expression of peptide transporters within the kidneys have been identified within multiple animal models and within humans.[57–60] Initial characterization of the TBI-ABN was done only in female mice, so it's likely that a different time point could be more optimal for urine collection in male mice. These observations bring up interesting questions on sex-dependent changes in renal physiology after TBI, which are out of scope of the current study.

4.4. Conclusions

In summary, we have developed a protease-responsive nanosensor which can produce quantifiable signals in response to TBI that can measured through minimally-invasive sampling of the blood and urine. We established that in a mouse model of TBI, systemically administered nanosensor released a synthetic biomarker which could be quantified from biological samples via fluorescence and immunoassay modalities. The addition of targeting ligands to hyaluronic acid led to enhancement in detection sensitivity of the synthetic biomarker in both the blood and urine, and this enhancement of sensitivity was dependent on the valency of targeting ligands. Within urine samples, the signal-to-noise ratio relative to uninjured mice was increased from 2.4 with no targeting to 4.7 with moderate targeting. Finally, we evaluated the diagnostic efficacy of this optimized TBI-ABN in female and male mice across two severities of TBI. The TBI-ABNs were unable to discriminate between TBI severities in blood or urine, but showed differences in activation within homogenized brain tissues. Interestingly, sex-based differences were observed in the urine transport of c-Peptide, with injured female mice showing a ~3-fold-higher urine signal compared to injured male mice at 1 hour post-injection.

In urine samples from female mice, the TBI-ABNs could identify severe injury with an AUC of 1.00. In blood samples from both female and male mice, injury could be identified with an AUC of ~0.77-0.89 depending on sex and injury severity. The urine diagnosis with our engineered nanosensor are comparable to the top-performing biomarker-based diagnostics that are currently being developed for TBI.[8] In one major study that led to the first FDA approval of a blood-based diagnostic assay for TBI, the serum levels of UCHL-1 and GFAP were quantified from TBI patients via ELISA and used to determine whether the patients would be CT positive or negative with a sensitivity of 0.973 and negative predictive value of 0.996.[55] More recently, a

rapid point-of-care version of the assay was developed by Abbot, termed the i-Stat, which can quantify plasma levels of GFAP and UCHL-1 in 15 minutes.[6,7]

Further work can be done to optimize the diagnostic performance of the TBI-ABN by tuning different transport rates for its components.[12] For example, the speed of signal detection in the blood could be increased by using substrate sequences that were optimized for maximal cleavage rate by calpain-1.[61] The rate of c-Peptide clearance into the urine could also be increased by incorporating ligands optimized for renal clearance, such as glutamate-fibrinopeptide B or cyclodextrin.[62,63] Finally, it is known that calpain-1 activation occurs across other diseases such Alzheimer's and ischemia-reperfusion injury;[64–66] the specificity of TBI detection can be enhanced by multiplexing for other proteases that are activated in TBI, such as MMP9 and cathepsin B.[38–41,67,68] All of these parameters should be considered in the context of different demographic groups to ensure that the sensor can work in as many patients as possible. With these improvements, TBI-ABNs have the potential to provide a quantitative readout of TBI pathology specific to each patient, allowing for a greater understanding of injury progression and for the development of more targeted therapies against TBI-associated proteases through precision medicine.[69]

4.5. Methods

Synthesis of TBI-ABN Poly(ethylene glycol) (PEG) Conjugates. Calpain substrate FRET peptide (Biotin-GGSGG-K(5FAM)-QEVYGAMP-K(CPQ2)-C-NH2) was synthesized by CPC Scientific Inc. (Sunnyvale, CA). HApep (CWSTMMSRSHKTRSHHV) was synthesized by Lifetein (Somerset, NJ). The 40kDa 8-arm PEG maleimide (tripentaerythritol) was purchased from Jenkem Technology (Beijing, China). For the initial kinetics and pharmacokinetics studies:

PEG maleimide was reacted with 1 mol equivalence of calpain substrate peptide and 1 mol equivalence of L-cysteine-functionalized VivoTag S-750 (PerkinElmer, Boston, MA), followed by quenching with an excess of L-cysteine. For the targeting comparison and diagnostic evaluation: PEG maleimide was batch reacted with 1 mol equivalence of calpain substrate peptide to ensure matched substrate peptide modification for each targeting group. The reaction was then split and reacted with 0 mol (non-targeted), 4 mol (moderate targeted), or 7 mol (high targeted) equivalencies of HApep followed by quenching with an excess of L-cysteine. All conjugates were dialyzed with water, and final concentrations were determined by absorbance of VivoTag 750, FAM, or tryptophan using a Spark multimode microplate reader (Tecan Trading AG, Switzerland).

In Vitro Reaction Kinetics Assay. The calpain-1 reaction kinetics assay was run as previously described.[19] Briefly, conjugates were incubated with 26.6 nM human calpain-1 (Sigma-Aldrich, C6108) in 50 mM N-(2-hydroxyethyl)piperazine-N′-ethanesulfonic acid (HEPES), 50 mM NaCl, 2 mM EDTA, 5 mM $CaCl_2$, and 5 mM β-mercaptoethanol. Fluorescence readings were taken every 90 s at 37 °C for 1 h. Reaction curves were normalized to controls, and their initial velocities were fitted to a Michaelis−Menten curve in GraphPad Prism.

Quantification of Peptide from Urine and Blood via ELISA. 96-well plates were coated overnight with polyclonal α-FAM antibody (Invitrogen, A-11095) at 0.5 μg/mL in PBS. Coated plates were then blocked with blocking buffer (PBS, 0.05% Tween-20, 1% BSA) for 2 hours, incubated with sample in blocking buffer for 1 hour, then incubated with 1:200

streptavidin-HRP (R&D Systems, DY998) for 1 hour. In between each incubation, the plate was washed with PBS + 0.05% Tween-20. TMB substrate (Thermo Scientific, 34021) was then added to develop signal for 5-10 minutes, followed by quenching with 1 N HCl. The final plate was quantified by absorbance at 450 nm. For the half-life study, blood and urine samples were quantified against a dilution ladder of injected material in PBS. For the targeting study, urine samples were quantified against a dilution ladder of free peptide in PBS.

Controlled Cortical Impact (CCI) TBI Mouse Model. All mouse procedures were approved by the University of California San Diego's Institutional Animal Care and Use Committee (IACUC). Female C57BL/6J mice (Jackson Labs) at 8-12 weeks old were used for all in vivo studies. Male C57BL/6J mice (Jackson Labs) at 8-12 weeks old were used only in the last diagnostic evaluation. Following anesthetization with 2.5% isoflurane, buprenorphine analgesia was administered. A 5 mm craniotomy was performed over the right hemisphere between bregma and lambda, and controlled cortical impact was performed using the ImpactOne (Leica Biosystems) with a 2 mm diameter stainless steel probe and a dwell time of 300 ms. For the targeting comparison study, severe CCIs were performed with a velocity of 5 m/s and impact depth of 2 mm. In the diagnostic evaluation, an additional mild CCI condition was included with a velocity of 1 m/s and impact depth of 0.5 mm. The center of the injury impact was centered around -2.0 mm (± 0.5 mm) lateral from the midline and -2.0 mm (± 0.5 mm) caudal from bregma.

Blood Collection and TBI-ABN Measurement. At each time point, 10 µL of blood was collected from the tail vein into EDTA-coated tubes, then diluted 1:5 in PBS with a final

concentration of 2 µM EDTA. Blood samples were centrifuged at 2,000 x g at 4 °C for 15 minutes to pellet cells and platelets, then the plasma supernatant was collected into clean tubes. Samples were immediately measured for fluorescence before storing at -80 °C. For blood pharmacokinetics of free peptide, the blood was diluted by 1:12,500 in PBS and quantified via ELISA.

Urine Collection and TBI-ABN Measurement. After TBI-ABN injection, mice were given 200 µL subcutaneous USP saline to induce urine production, then placed in a urine collection box for 1 hour. After 1 hour, the bladders were gently pressed to expel all available urine and the mice were returned to their housing. Collected urine was weighed to estimate volume, then spun down at 20,000 x g at 4 °C for 2 minutes to pellet solid particles. Clean supernatant was transferred to a clean tube, diluted 1:25 in PBS for fluorescence measurement, then stored at -80 °C. For ELISA measurement, urine samples were diluted 1:50,000 in PBS.

Peptide and PEG Half-Life and Urine Accumulation Studies. To assess the pharmacokinetics of calpain substrate peptide, uninjured mice were administered peptide in 1xPBS at a dose of 50 nmol calpain substrate / kg through the tail vein. In one set of mice, blood was collected at 1, 3, 7, 15, 30, 60, and 120 minutes post-injection for quantification via ELISA (n = 4). In a separate group of mice, urine was collected at 1 hour post-injection for quantification via ELISA (n = 4). For the percent injected dose (%ID) of peptide, blood volume was estimated to be of 8% / kg. Blood half-life was estimated with two-phase decay after assuming 100 %ID at 0 minutes. Urine volume was estimated based on urine weight with a specific gravity of 1.0058. The % accumulation of peptide into urine was estimated by

multiplying the quantified concentration of peptide in urine by the volume to obtain the moles recovered, then dividing that value by the injected dose. To assess PEG biodistribution, uninjured mice were administered fluorescently-tagged TBI-ABN in 1xPBS at 50 nmol calpain substrate / kg through the tail vein (n = 5). Urine was collected at 1 hour post-injection to assess PEG accumulation via fluorescence of VT750. Blood was collected at 0, 1, 2, 4, 8, and 24 hours post-injection and measured for PEG via fluorescence of VT750. The % accumulation of PEG into urine was similar to the calculation for % accumulation of peptide, except that the concentration of PEG was based on a fluorescence standard of TBI-ABN.

TBI-ABN In Vivo Studies. For comparison of targeted TBI-ABNs, non-, moderate, or high targeted TBI-ABN in 1xPBS was administered through the tail vein at 50 nmol calpain substrate / kg and at 3 hours post-injury. Uninjured mice and mice with severe CCI were compared for each targeting group (n = 6). Urine was collected at 1 hour post-injection and blood was collected at 0, 1, 2, 4, and 8 hours post-injection for quantification of TBI-ABN activation via FAM fluorescence. Urine was additionally measured for concentration of c-Peptide via a sandwich ELISA against FAM and biotin. In the final diagnostic evaluation, female and male mice were compared with uninjured mice, mice with mild CCI, and mice with severe CCI for each sex (n = 5-8). Moderate targeted TBI-ABNs were administered at 50 nmol calpain substrate / kg through the tail vein at 3 hours post-injury. Urine was collected at 1 hour post-injection and blood was collected at 4 hours post-injection for quantification of TBI-ABN activation via FAM fluorescence. At 4-5 hours post-injection, mice were transcardially perfused with ice cold PBS and the organs were collected for homogenization to assess biodistribution of activated TBI-ABN.

Quantitative Biodistribution of Sensor Activation in Homogenized Tissue.

Homogenization was performed as previously described.[24] The collected organ tissue was flash frozen at -80 °C. The heart, lungs, spleen, and kidney were minced, and homogenization buffer (6% w/v sodium dodecyl sulfate (SDS), 150 mM Tris-HCl pH 7.4, 100 mM dithiothreitol (DTT), and 2 mM ethylenediaminetetraacetic acid (EDTA)) was added to all organs to a final concentration of 250 mg tissue / mL buffer. Tissue was further processed with a Tissue-Tearor with a 4.5 mm probe (Fisher) until lysate was fully homogenized. Samples were heated at 90 °C for 10 minutes with agitation at 800 RPM, vortexed to mix, and homogenate measured for FAM fluorescence to quantify relative activation of TBI-ABN.

Software and Statistics. GraphPad Prism® (9.4.1) was used to perform statistics.

4.6. Acknowledgements

Chapter 4, in full, is currently being prepared for submission for publication of the material. Kudryashev, Julia A.; Madias, Marianne I.; Kandell, Rebecca M.; Lin, Queenie X.; Kwon, Ester J. The dissertation author was the primary researcher and author of this material.

4.7. References

(1) CDC. Surveillance Report of Traumatic Brain Injury-Related Emergency Department Visits, Hospitalizations, and Deaths—United States, 2014; 2019.

(2) Saatman, K. E.; Duhaime, A.-C.; Bullock, R.; Maas, A. I. R.; Valadka, A.; Manley, G. T. Classification of Traumatic Brain Injury for Targeted Therapies. J. Neurotrauma **2008**, 25 (7), 719–738. https://doi.org/10.1089/neu.2008.0586.

(3) Edlow, B. L.; Rosenthal, E. S. Diagnostic, Prognostic, and Advanced Imaging in Severe Traumatic Brain Injury. Curr. Trauma Rep. **2015**, 1 (3), 133–146. https://doi.org/10.1007/s40719-015-0018-7.

(4) Bramlett, H. M.; Dietrich, W. D. Long-Term Consequences of Traumatic Brain Injury: Current Status of Potential Mechanisms of Injury and Neurological Outcomes. J. Neurotrauma **2014**, 32 (23), 1834–1848. https://doi.org/10.1089/neu.2014.3352.

(5) Wang, K. K.; Yang, Z.; Zhu, T.; Shi, Y.; Rubenstein, R.; Tyndall, J. A.; Manley, G. T. An Update on Diagnostic and Prognostic Biomarkers for Traumatic Brain Injury. Expert Rev. Mol. Diagn. **2018**, 18 (2), 165–180. https://doi.org/10.1080/14737159.2018.1428089.

(6) Okonkwo, D. O.; Puffer, R. C.; Puccio, A. M.; Yuh, E. L.; Yue, J. K.; Diaz-Arrastia, R.; Korley, F. K.; Wang, K. K. W.; Sun, X.; Taylor, S. R.; Mukherjee, P.; Markowitz, A. J.; Jain, S.; Manley, G. T.; Adeoye, O.; Badjatia, N.; Boase, K.; Bodien, Y.; Bullock, R.; Chesnut, R.; Corrigan, J.; Crawford, K.; Dikmen, S.; Duhaime, A.-C.; Ellenbogen, R.; Feeser, V.; Ferguson, A. R.; Foreman, B.; Gardner, R.; Gaudette, E.; Giacino, J.; Goldman, D.; Gonzalez, L.; Gopinath, S.; Gullapalli, R.; Hemphill, C.; Hotz, G.; Kramer, J.; Kreitzer, N.; Levin, H.; Lindsell, C.; Machamer, J.; Madden, C.; Martin, A.; McAllister, T.; McCrea, M.; Merchant, R.; Nelson, L.; Ngwenya, L. B.; Noel, F.; Palacios, E.; Perl, D.; Rabinowitz, M.; Robertson, C.; Rosand, J.; Sander, A.; Satris, G.; Schnyer, D.; Seabury, S.; Sherer, M.; Stein, M.; Temkin, N.; Toga, A.; Valadka, A.; Vassar, M.; Vespa, P.; Zafonte, R. Point-of-Care Platform Blood Biomarker Testing of Glial Fibrillary Acidic Protein versus S100 Calcium-Binding Protein B for Prediction of Traumatic Brain Injuries: A Transforming Research and Clinical Knowledge in Traumatic Brain Injury Study. J. Neurotrauma **2020**, 37 (23), 2460–2467. https://doi.org/10.1089/neu.2020.7140.

(7) Korley, F. K.; Datwyler, S. A.; Jain, S.; Sun, X.; Beligere, G.; Chandran, R.; Marino, J. A.; McQuiston, B.; Zhang, H.; Caudle, K. L.; Wang, K. K. W.; Puccio, A. M.; Okonkwo, D. O.; Yue, J. K.; Taylor, S. R.; Markowitz, A.; Manley, G. T.; Diaz-Arrastia, R. Comparison of GFAP and UCH-L1 Measurements from Two Prototype Assays: The Abbott i-STAT and ARCHITECT Assays. Neurotrauma Rep. **2021**, 2 (1), 193–199. https://doi.org/10.1089/neur.2020.0037.

(8) Wang, K. K. W.; Kobeissy, F. H.; Shakkour, Z.; Tyndall, J. A. Thorough Overview of Ubiquitin C-Terminal Hydrolase-L1 and Glial Fibrillary Acidic Protein as Tandem Biomarkers Recently Cleared by US Food and Drug Administration for the Evaluation of Intracranial Injuries among Patients with Traumatic Brain Injury. Acute Med. Surg. **2021**, 8 (1), e622. https://doi.org/10.1002/ams2.622.

(9) Dudani, J. S.; Warren, A. D.; Bhatia, S. N. Harnessing Protease Activity to Improve Cancer Care. Annu. Rev. Cancer Biol. **2018**, 2 (1), 353–376. https://doi.org/10.1146/annurev-cancerbio-030617-050549.

(10) Sanman, L. E.; Bogyo, M. Activity-Based Profiling of Proteases. Annu. Rev. Biochem. **2014**, 83 (1), 249–273. https://doi.org/10.1146/annurev-biochem-060713-035352.

(11) López-Otín, C.; Bond, J. S. Proteases: Multifunctional Enzymes in Life and Disease. J. Biol. Chem. **2008**, 283 (45), 30433–30437. https://doi.org/10.1074/jbc.R800035200.

(12) Kwong, G. A.; Dudani, J. S.; Carrodeguas, E.; Mazumdar, E. V.; Zekavat, S. M.; Bhatia, S. N. Mathematical Framework for Activity-Based Cancer Biomarkers. Proc. Natl. Acad. Sci. U. S. A. **2015**, 112 (41), 12627–12632. https://doi.org/10.1073/pnas.1506925112.

(13) Kwon, E. J.; Dudani, J. S.; Bhatia, S. N. Ultrasensitive Tumour-Penetrating Nanosensors of Protease Activity. Nat. Biomed. Eng. **2017**, 1 (4), 0054–0054. https://doi.org/10.1038/s41551-017-0054.

(14) Liu, J.; Liu, M. C.; Wang, K. K. W. Calpain in the CNS: From Synaptic Function to Neurotoxicity. Sci. Signal. **2008**, 1 (14), re1–re1. https://doi.org/10.1126/stke.114re1.

(15) Bevers, M. B.; Neumar, R. W. Mechanistic Role of Calpains in Postischemic Neurodegeneration. J. Cereb. Blood Flow Metab. Off. J. Int. Soc. Cereb. Blood Flow Metab. **2008**, 28 (4), 655–673. https://doi.org/10.1038/sj.jcbfm.9600595.

(16) Zhang, Z.; Larner, S. F.; Liu, M. C.; Zheng, W.; Hayes, R. L.; Wang, K. K. W. Multiple AlphaII-Spectrin Breakdown Products Distinguish Calpain and Caspase Dominated Necrotic and Apoptotic Cell Death Pathways. Apoptosis **2009**, 14 (11), 1289–1298. https://doi.org/10.1007/s10495-009-0405-z.

(17) Levesque, S.; Wilson, B.; Gregoria, V.; Thorpe, L. B.; Dallas, S.; Polikov, V. S.; Hong, J. S.; Block, M. L. Reactive Microgliosis: Extracellular-Calpain and Microglia-Mediated Dopaminergic Neurotoxicity. Brain **2010**, 133 (3), 808–821. https://doi.org/10.1093/brain/awp333.

(18) Hall, E. D.; Sullivan, P. G.; Gibson, T. R.; Pavel, K. M.; Thompson, B. M.; Scheff, S. W. Spatial and Temporal Characteristics of Neurodegeneration after Controlled Cortical Impact in Mice: More than a Focal Brain Injury. J. Neurotrauma **2005**, 22 (2), 252–265. https://doi.org/10.1089/neu.2005.22.252.

(19) Kudryashev, J. A.; Waggoner, L. E.; Leng, H. T.; Mininni, N. H.; Kwon, E. J. An Activity-Based Nanosensor for Traumatic Brain Injury. ACS Sens. **2020**, 5 (3), 686–692. https://doi.org/10.1021/acssensors.9b01812.

(20) Gan, Z. S.; Stein, S. C.; Swanson, R.; Guan, S.; Garcia, L.; Mehta, D.; Smith, D. H. Blood Biomarkers for Traumatic Brain Injury: A Quantitative Assessment of Diagnostic and Prognostic Accuracy. Front. Neurol. **2019**, 10 (APR), 446–446. https://doi.org/10.3389/fneur.2019.00446.

(21) Siman, R.; Giovannone, N.; Hanten, G.; Wilde, E. A.; McCauley, S. R.; Hunter, J. V.; Li, X.; Levin, H. S.; Smith, D. H. Evidence That the Blood Biomarker SNTF Predicts Brain Imaging Changes and Persistent Cognitive Dysfunction in Mild TBI Patients. Front. Neurol. **2013**, 4, 190–190. https://doi.org/10.3389/fneur.2013.00190.

(22) Siman, R.; Shahim, P.; Tegner, Y.; Blennow, K.; Zetterberg, H.; Smith, D. H. Serum SNTF Increases in Concussed Professional Ice Hockey Players and Relates to the Severity of Postconcussion Symptoms. J. Neurotrauma **2015**, 32 (17), 1294–1300. https://doi.org/10.1089/neu.2014.3698.

(23) Saatman, K. E.; Creed, J.; Raghupathi, R. Calpain as a Therapeutic Target in Traumatic Brain Injury. Neurotherapeutics **2010**, 7 (1), 31–42. https://doi.org/10.1016/j.nurt.2009.11.002.

(24) Kandell, R. M.; Kudryashev, J. A.; Kwon, E. J. Targeting the Extracellular Matrix in Traumatic Brain Injury Increases Signal Generation from an Activity-Based Nanosensor. ACS Nano **2021**, 15 (12), 20504–20516. https://doi.org/10.1021/acsnano.1c09064.

(25) Stockholm, D.; Bartoli, M.; Sillon, G.; Bourg, N.; Davoust, J.; Richard, I. Imaging Calpain Protease Activity by Multiphoton FRET in Living Mice. J. Mol. Biol. **2005**, 346 (1), 215–222. https://doi.org/10.1016/j.jmb.2004.11.039.

(26) Suk, J. S.; Xu, Q.; Kim, N.; Hanes, J.; Ensign, L. M. PEGylation as a Strategy for Improving Nanoparticle-Based Drug and Gene Delivery. Adv. Drug Deliv. Rev. **2016**, 99, 28–51. https://doi.org/10.1016/J.ADDR.2015.09.012.

(27) Soo Choi, H.; Liu, W.; Misra, P.; Tanaka, E.; Zimmer, J. P.; Itty Ipe, B.; Bawendi, M. G.; Frangioni, J. V. Renal Clearance of Quantum Dots. Nat. Biotechnol. **2007**, 25 (10), 1165–1170. https://doi.org/10.1038/nbt1340.

(28) Thorne, R. G.; Nicholson, C. In Vivo Diffusion Analysis with Quantum Dots and Dextrans Predicts the Width of Brain Extracellular Space. Proc. Natl. Acad. Sci. **2006**, 103 (14), 5567–5572. https://doi.org/10.1073/pnas.0509425103.

(29) Nance, E. A.; Woodworth, G. F.; Sailor, K. A.; Shih, T.-Y.; Xu, Q.; Swaminathan, G.; Xiang, D.; Eberhart, C.; Hanes, J. A Dense Poly(Ethylene Glycol) Coating Improves Penetration of Large Polymeric Nanoparticles Within Brain Tissue. Sci. Transl. Med. **2012**, 4 (149), 149ra119-149ra119. https://doi.org/10.1126/scitranslmed.3003594.

(30) Kwon, E. J.; Skalak, M.; Lo Bu, R.; Bhatia, S. N. Neuron-Targeted Nanoparticle for SiRNA Delivery to Traumatic Brain Injuries. ACS Nano **2016**, 10 (8), 7926–7933. https://doi.org/10.1021/acsnano.6b03858.

(31) Bharadwaj, V. N.; Lifshitz, J.; Adelson, P. D.; Kodibagkar, V. D.; Stabenfeldt, S. E. Temporal Assessment of Nanoparticle Accumulation after Experimental Brain Injury: Effect of Particle Size. Sci. Rep. **2016**, 6 (1), 29988–29988. https://doi.org/10.1038/srep29988.

(32) Boyd, B. J.; Galle, A.; Daglas, M.; Rosenfeld, J. V.; Medcalf, R. Traumatic Brain Injury Opens Blood–Brain Barrier to Stealth Liposomes via an Enhanced Permeability and Retention (EPR)-like Effect. J. Drug Target. **2015**, 23 (9), 847–853. https://doi.org/10.3109/1061186X.2015.1034280.

(33) Waggoner, L. E.; Madias, M. I.; Hurtado, A. A.; Kwon, E. J. Pharmacokinetic Analysis of Peptide-Modified Nanoparticles with Engineered Physicochemical Properties in a Mouse Model of Traumatic Brain Injury. AAPS J. **2021**, 23 (5), 100. https://doi.org/10.1208/s12248-021-00626-5.

(34) Warren, A. D.; Kwong, G. A.; Wood, D. K.; Lin, K. Y.; Bhatia, S. N. Point-of-Care Diagnostics for Noncommunicable Diseases Using Synthetic Urinary Biomarkers and Paper Microfluidics. Proc. Natl. Acad. Sci. U. S. A. **2014**, 111 (10), 3671–3676. https://doi.org/10.1073/pnas.1314651111.

(35) Xi, G.; Reiser, G.; Keep, R. F. The Role of Thrombin and Thrombin Receptors in Ischemic, Hemorrhagic and Traumatic Brain Injury: Deleterious or Protective? J. Neurochem. **2002**, 84 (1), 3–9. https://doi.org/10.1046/j.1471-4159.2003.01268.x.

(36) Chen Bo; Cheng Qun; Yang Kai; Lyden Patrick D. Thrombin Mediates Severe Neurovascular Injury During Ischemia. Stroke **2010**, 41 (10), 2348–2352. https://doi.org/10.1161/STROKEAHA.110.584920.

(37) Chen, B.; Friedman, B.; Whitney, M. A.; Winkle, J. A. V.; Lei, I.-F.; Olson, E. S.; Cheng, Q.; Pereira, B.; Zhao, L.; Tsien, R. Y.; Lyden, P. D. Thrombin Activity Associated with Neuronal Damage during Acute Focal Ischemia. J. Neurosci. **2012**, 32 (22), 7622–7631. https://doi.org/10.1523/JNEUROSCI.0369-12.2012.

(38) Jia, F.; Pan, Y.; Mao, Q.; Liang, Y.; Jiang, J. Matrix Metalloproteinase-9 Expression and Protein Levels after Fluid Percussion Injury in Rats: The Effect of Injury Severity and Brain Temperature. J. Neurotrauma **2010**, 27 (6), 1059–1068. https://doi.org/10.1089/neu.2009.1067.

(39) Lo, E. H.; Wang, X.; Cuzner, M. L. Extracellular Proteolysis in Brain Injury and Inflammation: Role for Plasminogen Activators and Matrix Metalloproteinases. J. Neurosci. Res. **2002**, 69 (1), 1–9. https://doi.org/10.1002/jnr.10270.

(40) Vilalta, A.; Sahuquillo, J.; Poca, M. A.; De Los Rios, J.; Cuadrado, E.; Ortega-Aznar, A.; Riveiro, M.; Montaner, J. Brain Contusions Induce a Strong Local Overexpression of MMP-9. Results of a Pilot Study. In Acta Neurochirurgica Supplements; Steiger, H.-J., Ed.; Acta Neurochirurgica Supplementum; Springer: Vienna, 2009; pp 415–419. https://doi.org/10.1007/978-3-211-85578-2_81.

(41) Vafadari, B.; Salamian, A.; Kaczmarek, L. MMP-9 in Translation: From Molecule to Brain Physiology, Pathology, and Therapy. J. Neurochem. **2016**, 139, 91–114. https://doi.org/10.1111/jnc.13415.

(42) Price, L.; Wilson, C.; Grant, G. Blood–Brain Barrier Pathophysiology Following Traumatic Brain Injury. In Translational Research in Traumatic Brain Injury; Laskowitz, D., Grant, G., Eds.; CRC Press/Taylor and Francis Group: Boca Raton, FL, 2016; pp 85–96. https://doi.org/10.1201/b18959-5.

(43) Tolg, C.; Hamilton, S. R.; Zalinska, E.; McCulloch, L.; Amin, R.; Akentieva, N.; Winnik, F.; Savani, R.; Bagli, D. J.; Luyt, L. G.; Cowman, M. K.; McCarthy, J. B.; Turley, E. A. A RHAMM Mimetic Peptide Blocks Hyaluronan Signaling and Reduces Inflammation and Fibrogenesis in Excisional Skin Wounds. Am. J. Pathol. **2012**, 181 (4), 1250–1270. https://doi.org/10.1016/j.ajpath.2012.06.036.

(44) Xiong, Y.; Mahmood, A.; Chopp, M. Animal Models of Traumatic Brain Injury. Nat. Rev. Neurosci. **2013**, 14 (2), 128–142. https://doi.org/10.1038/nrn3407.

(45) Jeong, W.; Bu, J.; Kubiatowicz, L. J.; Chen, S. S.; Kim, Y.; Hong, S. Peptide–Nanoparticle Conjugates: A next Generation of Diagnostic and Therapeutic Platforms? Nano Converg. **2018**, 5 (1), 38. https://doi.org/10.1186/s40580-018-0170-1.

(46) Yu, Y. J.; Zhang, Y.; Kenrick, M.; Hoyte, K.; Luk, W.; Lu, Y.; Atwal, J.; Elliott, J. M.; Prabhu, S.; Watts, R. J.; Dennis, M. S. Boosting Brain Uptake of a Therapeutic Antibody by Reducing Its Affinity for a Transcytosis Target. Sci. Transl. Med. **2011**, 3 (84), 84ra44-84ra44. https://doi.org/10.1126/scitranslmed.3002230.

(47) Choi, C. H. J.; Alabi, C. A.; Webster, P.; Davis, M. E. Mechanism of Active Targeting in Solid Tumors with Transferrin-Containing Gold Nanoparticles. Proc. Natl. Acad. Sci. U. S. A. **2010**, 107 (3), 1235–1240. https://doi.org/10.1073/pnas.0914140107.

(48) Ueno, H.; Suemitsu, S.; Murakami, S.; Kitamura, N.; Wani, K.; Matsumoto, Y.; Aoki, S.; Okamoto, M.; Ishihara, T. Hyaluronic Acid Is Present on Specific Perineuronal Nets in the Mouse Cerebral Cortex. Brain Res. **2018**, 1698, 139–150. https://doi.org/10.1016/j.brainres.2018.08.011.

(49) Hamakubo, T.; Kannagi, R.; Murachi, T.; Matus, A. Distribution of Calpains I and II in Rat Brain. J. Neurosci. **1986**, 6 (11), 3103–3111. https://doi.org/10.1523/JNEUROSCI.06-11-03103.1986.

(50) Czogalla, A.; Sikorski, A. F. Spectrin and Calpain: A “target” and a “Sniper” in the Pathology of Neuronal Cells. Cell. Mol. Life Sci. **2005**, 62 (17), 1913–1924. https://doi.org/10.1007/s00018-005-5097-0.

(51) Gupte, R. P.; Brooks, W. M.; Vukas, R. R.; Pierce, J. D.; Harris, J. L. Sex Differences in Traumatic Brain Injury: What We Know and What We Should Know. J. Neurotrauma **2019**, 36 (22), 3063–3091. https://doi.org/10.1089/neu.2018.6171.

(52) Zagni, E.; Simoni, L.; Colombo, D. Sex and Gender Differences in Central Nervous System-Related Disorders. Neurosci. J. **2016**, 2016, 1–13. https://doi.org/10.1155/2016/2827090.

(53) Kupina, N. C.; Detloff, M. R.; Bobrowski, W. F.; Snyder, B. J.; Hall, E. D. Cytoskeletal Protein Degradation and Neurodegeneration Evolves Differently in Males and Females Following Experimental Head Injury. Exp. Neurol. **2003**, 180 (1), 55–73. https://doi.org/10.1016/S0014-4886(02)00048-1.

(54) Siebold, L.; Obenaus, A.; Goyal, R. Criteria to Define Mild, Moderate, and Severe Traumatic Brain Injury in the Mouse Controlled Cortical Impact Model. Exp. Neurol. **2018**, 310, 48–57. https://doi.org/10.1016/j.expneurol.2018.07.004.

(55) Bazarian, J. J.; Biberthaler, P.; Welch, R. D.; Lewis, L. M.; Barzo, P.; Bogner-Flatz, V.; Gunnar Brolinson, P.; Büki, A.; Chen, J. Y.; Christenson, R. H.; Hack, D.; Huff, J. S.; Johar, S.; Jordan, J. D.; Leidel, B. A.; Lindner, T.; Ludington, E.; Okonkwo, D. O.; Ornato, J.; Peacock, W. F.; Schmidt, K.; Tyndall, J. A.; Vossough, A.; Jagoda, A. S. Serum GFAP and UCH-L1 for Prediction of Absence of Intracranial Injuries on Head CT (ALERT-TBI): A Multicentre Observational Study. Lancet Neurol. **2018**, 17 (9), 782–789. https://doi.org/10.1016/S1474-4422(18)30231-X.

(56) Bharadwaj, V. N.; Copeland, C.; Mathew, E.; Newbern, J.; Anderson, T. R.; Lifshitz, J.; Kodibagkar, V. D.; Stabenfeldt, S. E. Sex-Dependent Macromolecule and Nanoparticle Delivery in Experimental Brain Injury. Tissue Eng. Part A **2020**, 26 (13–14), 688–701. https://doi.org/10.1089/ten.tea.2020.0040.

(57) Sabolić, I.; Asif, A. R.; Budach, W. E.; Wanke, C.; Bahn, A.; Burckhardt, G. Gender Differences in Kidney Function. Pflüg. Arch. - Eur. J. Physiol. **2007**, 455 (3), 397–429. https://doi.org/10.1007/s00424-007-0308-1.

(58) Melis, M.; Krenning, E. P.; Bernard, B. F.; de Visser, M.; Rolleman, E.; de Jong, M. Renal Uptake and Retention of Radiolabeled Somatostatin, Bombesin, Neurotensin, Minigastrin and CCK Analogues: Species and Gender Differences. Nucl. Med. Biol. **2007**, 34 (6), 633–641. https://doi.org/10.1016/j.nucmedbio.2007.05.002.

(59) Qi, Z.; Whitt, I.; Mehta, A.; Jin, J.; Zhao, M.; Harris, R. C.; Fogo, A. B.; Breyer, M. D. Serial Determination of Glomerular Filtration Rate in Conscious Mice Using FITC-Inulin Clearance. Am. J. Physiol.-Ren. Physiol. **2004**, 286 (3), F590–F596. https://doi.org/10.1152/ajprenal.00324.2003.

(60) Ruetten, H.; Wegner, K. A.; Zhang, H. L.; Wang, P.; Sandhu, J.; Sandhu, S.; Mueller, B.; Wang, Z.; Macoska, J.; Peterson, R. E.; Bjorling, D. E.; Ricke, W. A.; Marker, P. C.; Vezina, C. M. Impact of Sex, Androgens, and Prostate Size on C57BL/6J Mouse Urinary Physiology: Functional Assessment. Am. J. Physiol. - Ren. Physiol. **2019**, 317 (4), F996–F1009. https://doi.org/10.1152/ajprenal.00270.2019.

(61) Cuerrier, D.; Moldoveanu, T.; Davies, P. L. Determination of Peptide Substrate Specificity for μ-Calpain by a Peptide Library-Based Approach: The Importance of Primed Side Interactions. J. Biol. Chem. **2005**, 280 (49), 40632–40641. https://doi.org/10.1074/jbc.M506870200.

(62) Kwong, G. A.; von Maltzahn, G.; Murugappan, G.; Abudayyeh, O.; Mo, S.; Papayannopoulos, I. A.; Sverdlov, D. Y.; Liu, S. B.; Warren, A. D.; Popov, Y.; Schuppan,

D.; Bhatia, S. N. Mass-Encoded Synthetic Biomarkers for Multiplexed Urinary Monitoring of Disease. Nat. Biotechnol. **2013**, 31 (1), 63–70. https://doi.org/10.1038/nbt.2464.

(63) Loftsson, T.; Brewster, M. E. Pharmaceutical Applications of Cyclodextrins: Basic Science and Product Development. J. Pharm. Pharmacol. **2010**, 62 (11), 1607–1621. https://doi.org/10.1111/j.2042-7158.2010.01030.x.

(64) Mahaman, Y. A. R.; Huang, F.; Kessete Afewerky, H.; Maibouge, T. M. S.; Ghose, B.; Wang, X. Involvement of Calpain in the Neuropathogenesis of Alzheimer's Disease. Med. Res. Rev. **2019**, 39 (2), 608–630. https://doi.org/10.1002/med.21534.

(65) Inserte, J.; Hernando, V.; Garcia-Dorado, D. Contribution of Calpains to Myocardial Ischaemia/Reperfusion Injury. Cardiovasc. Res. **2012**, 96 (1), 23–31. https://doi.org/10.1093/cvr/cvs232.

(66) Potz, B. A.; Abid, M. R.; Sellke, F. W. Role of Calpain in Pathogenesis of Human Disease Processes. J. Nat. Sci. **2016**, 2 (9).

(67) Boutté, A. M.; Hook, V.; Thangavelu, B.; Sarkis, G. A.; Abbatiello, B. N.; Hook, G.; Jacobsen, J. S.; Robertson, C. S.; Gilsdorf, J.; Yang, Z.; Wang, K. K. W.; Shear, D. A. Penetrating Traumatic Brain Injury Triggers Dysregulation of Cathepsin B Protein Levels Independent of Cysteine Protease Activity in Brain and Cerebral Spinal Fluid. J. Neurotrauma **2020**, 37 (13), 1574–1586. https://doi.org/10.1089/neu.2019.6537.

(68) Hook, G.; Jacobsen, J. S.; Grabstein, K.; Kindy, M.; Hook, V. Cathepsin B Is a New Drug Target for Traumatic Brain Injury Therapeutics: Evidence for E64d as a Promising Lead Drug Candidate. Front. Neurol. **2015**, 6.

(69) Soleimany, A. P.; Bhatia, S. N. Activity-Based Diagnostics: An Emerging Paradigm for Disease Detection and Monitoring. Trends Mol. Med. **2020**, 26 (5), 450–468. https://doi.org/10.1016/j.molmed.2020.01.013.